Miniaturised Experimental Simulation of Ingot-to-Billet Conversion

A dissertation submitted for the degree of
Doctor of Philosophy at the University of Strathclyde

Author:
Mr. David James Connolly
Strathclyde University

Supervisor:
Dr. Vassili Vorontsov

May 17, 2024

Preface

This dissertation is submitted for the degree of Doctor of Philosophy at the University of Strathclyde. It describes the research carried out in the Department of Design, Manufacture, and Engineering Management (DMEM) at the Advanced Forming Reseach Centre (AFRC) between October 2019 and April 2023 under the supervision of Dr. Vassili Vorontsov. Except where appropriately referenced, this work is original and has not been the result of collaboration. No part of this dissertation has been, or is currently being, submitted for any other degree, diploma or other qualification. It does not exceed 60,000 words in length.

Parts of this dissertation have been published or submitted for publication in:

D. J. Connolly, G. Sivaswamy, S. Rahimi, and V. Vorontsov. Miniaturised experimental simulation of open-die forging. *Journal of Materials Research and Technology*, Vol. 26, p. 3146-3161, 2023.

D. J. Connolly, M. Fabris, G. Sivaswamy, S. Rahimi, and V. Vorontsov. Miniaturised experimental simulation and combined modelling of open-die forging of Ti-6Al-4V titanium alloy. *Journal of Materials Research and Technology*, Vol. 30, p. 3622-3639, 2024.

D. J. Connolly
May 17, 2024

Acknowledgements

First and foremost, I would like to greatly thank my academic supervisor, Dr. Vassili Vorontsov, for educating me in the art and science of metallurgy, processing, and much more, letting me work with a great degree of independence but at the same time providing impeccable guidance and discussion on a number of occasions when it proved most invaluable. A great thanks should be extended to Dr. Salaheddin Rahimi for his help with reviewing, and general support in engaging my work with customers of the AFRC and encouraging me to share my work.

I would also like to acknowledge that this research would not have been possible without the financial funding provided by the University of Strathclyde and Advanced Forming Research Centre (AFRC). Dr. Giribaskar Sivaswamy for taking a great interest in my work and supporting and helping to guide me through improving experimentation, analysis, and publishing and being a co-author on my first publications. Special thank you to Dr. Dorothy Evans for kickstarting this journey for me by bringing me into the postgraduate world, for the continuous support over the years and help in securing essential funding. Dr. Ioannis Violatos for taking me on in a part time role at the end of my funding and providing me with valuable training and opportunities.

I'd also like to thank Mr. Jose Hernandez and Mr. Gregor Cranstoun for the opportunity to work part time in a different role with the National Manufacturing Institute (NMIS) during my research allowing for the break up of monotony of lockdown study which was greatly appreciated. An extension of thanks to Dr. Andrzej Rosochowski and Dr. Paul Blackwell for asking the difficult questions during the annual review sessions for my first and second year.

Mr. Thomas Condie and Mr. Scott Gubbins in the DMEM workshop who manufactured essential tooling and rig components for the project. Miss. Kornelia Kondziolka - Mr. Ryan O'Neill - Miss. Liza Hall - Miss. Jacqueline Shramm, Mr. Martin Ogilby, Mr. Michael McCracken - Mr. Adam Robbins and all the apprentices in the workshop. The late Mr. Ian MacKenzie in stores, who helped me greatly at a crucial time, and made the best rocky road.

Mr. Tony Fry, Dr. Ken Mingard, and the advanced materials team for making me feel extremely welcome and a part of the team for my short stay with them at NPL. Dr. Vivian Tong my NPL Supervisor, for help with MTEX analysis work. Dr. Sam Johnston in the Photon Science Institute at the University of Manchester, for their help and instruction with DCT grain mapping and analysis.

Research, Science, and Engineering should be a social affair. With that in mind, I would like to greatly thank Mrs. Leah Chapman, Mrs. Linden Fradet, Dr. Ben Webster, and Prof. Richard Burguete at the Postgraduate Institute of Measurement Science (PGI) at the NPL for providing me with incredible and unique opportunities, through conference hosting and ambassador roles, for which I feel were instrumental in my growth and confidence in being a researcher. A huge thank you also to the many other ambassadors and friends that came and went throughout my time with the PGI who kept me grounded over the years of lockdowns with ample banter and distractions during our weekly meetings.

A great thank you to the PhD cohort of students & staff at the AFRC, John, Gulsum, Angus, Beatrice, Michael, Michail, Matthew, Mathieu, Mauro, Constantinos, Georgios, Luis, Amy, Rory, Calum, Sean, Ahmed, and Elen who helped immeasurably through introductions, guidance, materials knowledge, interesting conversations and laughs. A big thanks to Mr. John Reid for answering my many questions and helping with C++ UI/menu coding and integration for the electronic controller.

I owe a great gratitude to my friends that have supported me over my time of study. And for making it all come together as some of the best years of my life. Last but certainly not least, I owe the greatest debt to my parents as they have offered the support and guidance that is impossible to repay.

Abstract

Ingot-to-billet conversion processing, one process of which is known as "cogging", is an important production step in high-value metallurgical manufacturing. It is necessary to homogenise and refine the microstructure of high-performance alloys before they proceed to subsequent processing stages. Despite its importance, the process is still not very well understood for many modern advanced alloys and few published studies exist. The limited knowledge of the deformation and microstructure evolution leads to difficulties in achieving the desired accuracy in microstructural control. Traditional uni-axial testing is not fully representative of the forging processes seen in industry, and does not capture different elements of open-die forging parameters. Given significant costs of large multi-tonne workpiece ingots and the difficulties with their non-destructive evaluation, it is crucial to develop a laboratory-scale evaluation for the cogging process so that scrapping and re-processing can be avoided.

The "Micro Future Forge" has been developed as a reproducible laboratory-scale experimental method for exploring the various thermo-mechanical process mechanisms of hot open die forging. This novel methodology employs a purpose-built apparatus, that has been designed to be cost-effective and portable. The test set-up uses a remotely operated manipulator assembly constructed predominantly from standard off-the-shelf components in conjunction with a conventional uni-axial load frame. This combination allows for high operational scalability. Multi-directional open-die forging (cogging) of single and dual-phase alloys has been successfully accomplished using the described apparatus, demonstrating an ability to attain the desired beneficial refinement of the microstructure. Application of this experimental approach provides precisely controlled conditions and allows high research specimen throughput to discover new insights into the structural transformations that occur in industry-scale forgings, while offering savings in energy, material, time and capital investment. The obtained experimental data can be used for thermo-mechanical process optimisation of high-performance alloys, guiding larger scale testing and manufacturing trials (*e.g.,* AFRC Catapult Future Forge), as well as informing the development of digital-twins for various high-value metallurgical manufacturing processes.

Contents

1 Introduction

Precise control of microstructure evolution is of paramount importance during all metallurgical manufacturing processes, and is essential for achieving optimal mechanical properties in the final manufactured components. Thermomechanical processing used for ingot-to-billet conversion of high-performance alloys is no exception. The high-temperature plastic deformation must be sufficient to promote complete recrystallisation of the coarse-grained as-cast ingot structure into a final billet with refined grains. The success of this process is fundamental in the production of high-value metallurgical components, since any inhomogeneities in the resulting microstructure are inherited during all subsequent processing steps (*e.g.,* closed-die forging) and are ultimately carried forward into the final product. Therefore, understanding the phenomenology of microstructural transformations during the ingot-to-billet conversion stage is key for the overall manufacturing route.

Progression in the field of design of jet turbine engine components has been largely due to advancements in the performance capability of titanium alloys and nickel-based superalloys [1]. Refinement in these materials is due to the advancements in material processing in the range of stages between initial mining and the final product. Improvement in temperature and stress capabilities in these materials, allows for increased operating temperatures and engine speeds, ultimately leading to increased fuel efficiency [2–7]. Efficacy of advanced engineering alloy products is of high interest from an engineering, economic, and environmental perspective as continuous improvement of these materials has led to savings in energy, material, time, and money. For commercial airlines to remain competitive, it is necessary for components to be made from materials that can maintain high mechanical strength at elevated temperatures whilst remaining comparatively low in cost, alongside the trend for custom application specific materials being developed.

Conventional ingot-to-billet conversion is an expensive and challenging operation, requiring numerous steps to break up the coarse as-cast structure and interdendritic regions. Achieving a uniformly high level of strain for recrystallisation is challenging due to the large size of conventional, multi-tonne ingots. Non-recrystallised regions that retain large unrecrystallised grains are often seen post-processing and are detrimental to the properties of the part.

Grain size is one of the primary parameters controlling properties in these materials. An ideal microstructure, for example in a nickel superalloy, would consist of small, recrystallised γ grains, with a fine and dense concentration of γ' precipitates. After ingot-to-billet conversion of AD730 nickel superalloy, instead of this desired microstructure, what is being found are several large deformed grains are present alongside small recrystallised grains. This inhomogeneous structure is not only detrimental in terms of mechanical properties throughout the products lifetime, but also causes the alloy to fail industry standard ultrasonic testing; which is used to find flaws in the billet such as porosity, cracks, and large inclusions, and also defects in the final component [8]. The occurrence of these large, deformed grains has attracted some attention in the literature, but as yet there are no theories concerning their formation, or more importantly, their elimination. Similarly, in α+β titanium alloys millimetre long clusters of α grains with, nearly or, the same crystallographic orientation. These areas, named macrozones, are known to have a negative effect on the fatigue performance of the alloy. What remains unknown with these features is how to sufficiently break them down at an industrial scale, owing to the large primary β grain size.

When investigating microstructural evolution of alloys throughout a manufacturing process, there are two scientific approaches: experimental techniques and computer simulation. A combination of both techniques would be optimal in any circumstance for comparison between numerical models and experimental data. For this work, the focus remains on the experimental data and observations using characterisation techniques such as: electron backscatter diffraction (EBSD); scanning electron microscopy (SEM); light microscopy; X-ray computed tomography (XCT), and Vickers microhardness testing. These analysis methods provide an insight into the deformation processes that occur and hence physical evidence of their mechanisms. Basic simulation studies were

completed for proof of concept design work. Further modelling was completed using DEFORM™ software, in order to obtain comparable strain distributions to the test specimens.

In this work, an attempt is made to experimentally simulate the cogging process used in ingot-to-billet conversion and to understand the primary deformation and recrystallisation behaviour of advanced alloys during ingot-to-billet conversion. It should be considered a novel miniaturised scale experimental approach that can give some indication of industrial scale bulk properties. Experimental methodology and rig design, which is the major research output and challenge of this work, will be discussed.

This work is, foremost, a design and manufacture research project with a capability study of the novel laboratory-scale method of replicating the microstructural mechanisms seen during the open-die forging process known as "cogging." Fundamentally, microstructures from cogging are inherited for all subsequent processing steps, meaning that inhomogeneities from any ingot-to-billet conversion process will be carried forward into the final product. Thus, understanding of this stage in production is of key interest, as the primary objective is to obtain a high standard of quality in forgings, *i.e.,* optimal properties for product life in service and functional characteristics at the required shape and dimensional tolerance. Ingot-to-billet conversion of titanium and nickel alloys and simulation of ingot-to-billet conversion relies on a number of upsetting and cogging steps. For proof of concept of the proposed design, a combination of both single and dual-phase alloys were selected and their microstructural evolution studied after cogging. These first trials have helped to establish the foundations of appropriate experimental techniques for laboratory open-die forging, and hopefully the beginning of many similar studies.

Initially, this research work set out to experimentally simulate the cogging process on nickel-based superalloy AD730. As the project moved forward, and the design was generated, it became clear moving into the experimental stage that it was essential for the design and method development process to begin with lower temperature, and softer, materials as a benchmark for proof of concept. For this, copper alloy C101 and aluminium alloy Al6060 were selected as lower temperature materials to be tested and studied with the novel experiement, with Ti-6Al-4V titanium alloy selected for a higher temperature study, which is of interest to metallurgists in the context of ingot-to-billet conversion. From these benchmarks, it would allow for the operation, tool-life, deformation level capability, method, and software to be developed and improved. This then allows further development and preparation for higher temperature tests on superalloys to be explored,

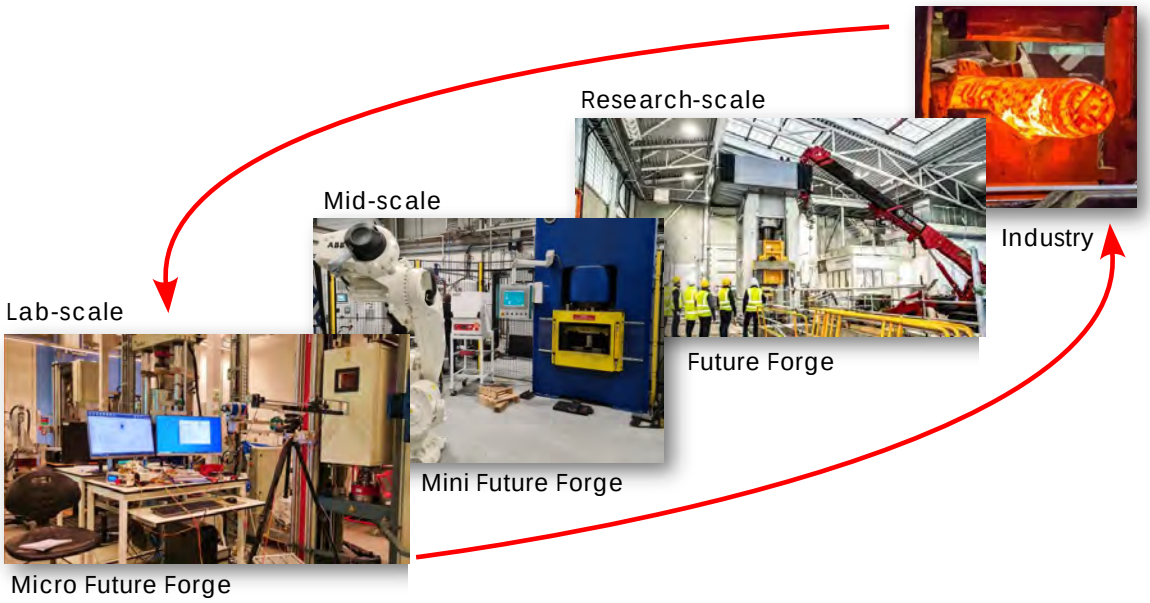

Figure 1.1: Collection of photographs demonstrating the current forging research scales being explored, showing where the newly designed apparatus (named the Micro Future Forge) fits into forging research.

and to have a stronger knowledge for the future research studies that are of higher material research interest.

Future work from this research is also crucial, as one would hope that this is the first of a high number of research projects that will help underpin the large and expensive state-of-the-art Future Forge press recently launched at the AFRC. As this is important for the UK forging and forming community, it is critical to highlight the avenues for new and exciting work that this new design has opened for exploration. Figure 1.1 highlights the current different scales of forging research and how they feed into industry knowledge, and how they can all be used to cross reference and inform each other with regard to process parameters and resultant material characteristics.

2 Literature Review

2.1 Metallurgy of Advanced Alloys

2.1.1 Introduction to Processing Route

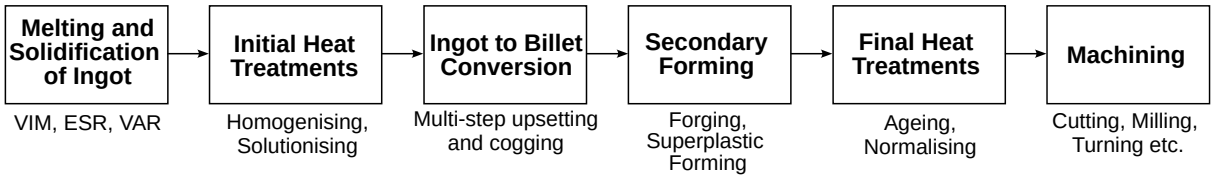

Figure 2.1: High-level processing route for wrought advanced alloys, with examples of specific processes within each stage.

Before dedicating to any greater level of detail, it is necessary to understand the processes and control schemes undergone by advanced alloys throughout their production lifespan as each prior processing stage can greatly impact the final part. It is also important to distinguish the relevant processing stages surrounding those pertinent to this work, to develop an understanding of the overall manufacturing process. Figure 2.1 presents an overview of the processing route discussed throughout this work. These stages are often broken down into further discrete stages. For example, in $\alpha + \beta$ titanium alloy manufacture the ingot-to-billet conversion stage is broken into 3 sub-stages: β hot working, initial α/β hot working (with intermittent heat treatments), and secondary α/β hot working.

2.1.2 Overview of the Triple Melting Process

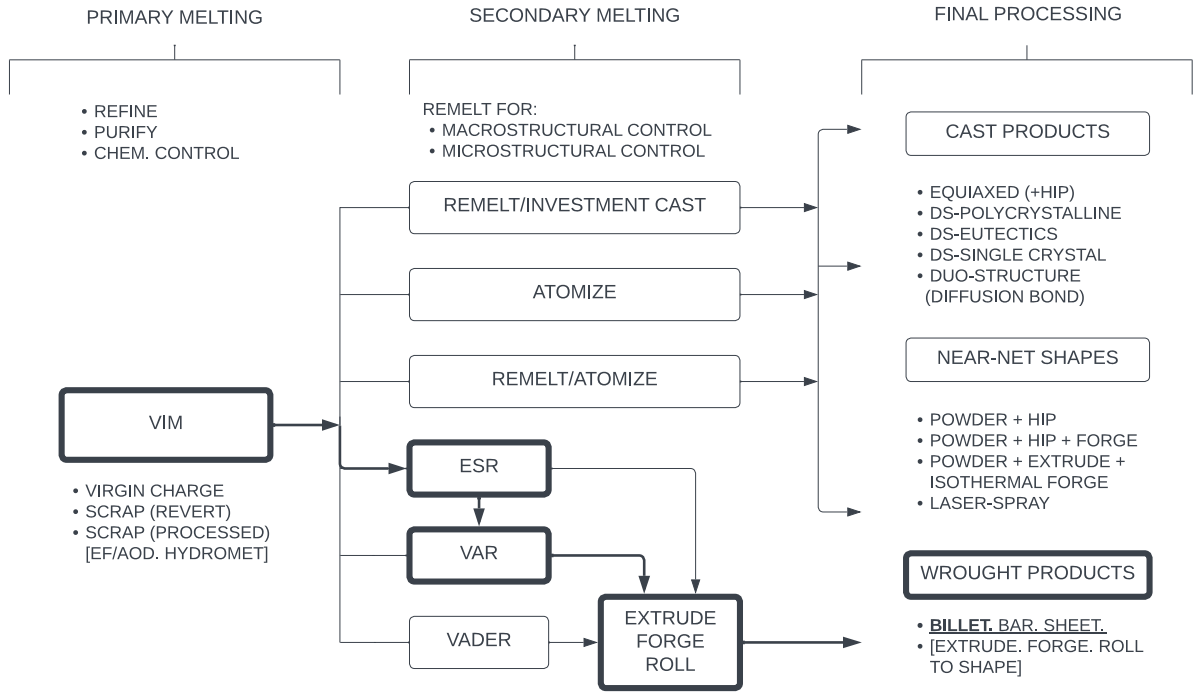

Figure 2.2: Processing routes for products cast from VIM-ingots or electrodes with route of interest highlighted. Adapted from Choudhury *et al.* [9]

Table 2.1: Common ranges of main alloying elements and their effects in superalloys [10]

Element	Range in wt.% FeNi- and Ni- base	Range in wt.% Co- base	Effects
Cr	5-25	19-30	Oxidation and hot corrosion resistance; carbides; solution hardening
Mo, W	0-12	0-11	Carbides; solution hardening
Al	0-6	0-4.5	Precipitation hardening; oxidation resistance
Ti	0-6	0-4	Precipitation hardening; carbides affects
Co	0-20	-	amount of precipitate
Ni	-	0-22	Stabilises austenite; forms hardening precipitates
Cb	0-5	0-4	Carbides; solution hardening; precipitation hardening (FeNi- and Ni- base)
Ta	0-12	0-9	Carbides; solution hardening; oxidation resistance

It has been identified that metallurgy can be split into three distinct categories: Process Metallurgy; Physical Metallurgy; and Mechanical Metallurgy. [11] The first of these stages, Process Metallurgy, is focused on the extraction of metals from their ores and their refinement, the main category of where the triple melting process is concerned. Physical Metallurgy would also encompass early melting processes, as it is primarily concerned with composition processing and environmental conditions that affect the physical and mechanical properties of metals [12]. Mechanical Metallurgy, the last stage, is the area of knowledge which is concerned with behaviour and response of metals to applied forces [13].

The triple melting process that is composed of: Vacuum Induction Melting (VIM); Electro-slag Remelting (ESR); and Vacuum Arc Remelting (VAR), highlighted in Figure 2.2 is the collective name of a commercial key processing route of modern superalloys and titanium alloys for purification and compositional control. Specifically, superalloys are produced using all of the processes in this route for the purpose of meeting the growing demands for both cleanliness and structural homogeneity. Industrial challenges of achieving lighter, higher strength, and oxidation resistant materials at high working temperatures are constant. Thus, a significant amount of research been done into comparing ESR and VAR processes [14], as well as publications discussing triple melting [15–19]. To achieve microstructures that inherit these beneficial qualities amongst others is a balancing act of chemical composition that includes various alloying elements of different concentrations that remains quite complex. Table 2.1 shows the main alloying elements in superalloys and their effects.

Concentrations of trace elements and impurities and their roles are widely known in the literature to have been studied by Holt and Wallace. [20] The constituents of nickel-base superalloys were then classified into solid solution formers, precipitate formers, carbide formers, and surface stabilizers by Jena and Chaturvedi [21]. Considerable progress has been made since this publication in the understanding of achieving stability, including the occurrence of Ni_3X type compounds and their structure and various roles in alloying additions.

Alloying elements in titanium are typically categorised as α or β stabilisers, based on whether they raise or lower the α/β transformation temperature of 882 °C of pure titanium [22].

Al and the interstitial elements O, N, and C act as robust α stabilisers, raising the transus temperature as the solute content increases, as demonstrated in the schematic phase diagram presented in Figure 2.3. Aluminium stands out as the predominant alloying element in titanium alloys due to its unique ability to elevate the transition temperature and exhibit substantial solubility in both the α and β phases. From the interstitial elements, oxygen may be regarded as an alloying component in titanium, particularly when its content is manipulated to achieve the desired strength levels. This is particularly relevant for various grades of commercially pure (CP) titanium. Additional α

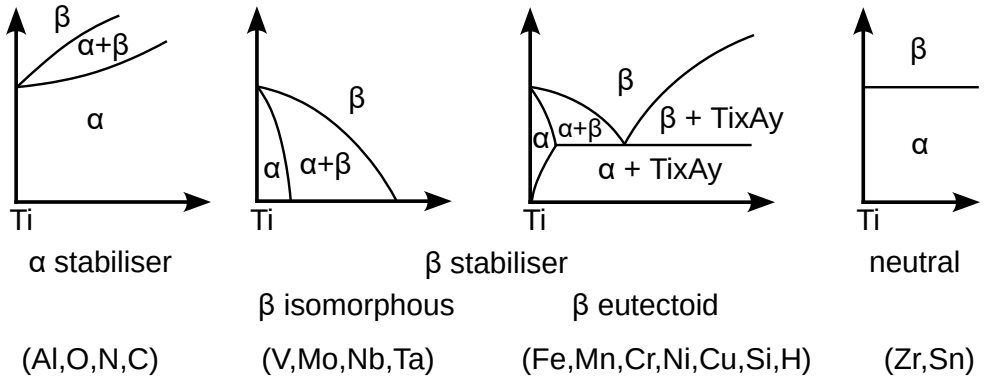

Figure 2.3: Effect of alloying elements on phase diagrams of titanium alloys (schematically). Adapted from L´utjering and Williams [22]

stabilising elements comprise B, Ga, Ge, and the rare earth elements. However, their solid solubilities are considerably lower when compared to aluminum or oxygen, and none of these elements are commonly employed as alloying constituents.

The β stabilising elements are categorised into β isomorphous elements and β eutectoid forming elements, based on the specific binary phase diagrams they form. Both types of diagrams are outlined schematically in Figure 2.3. The commonly employed β isomorphous elements in titanium alloys include V, Mo, and Nb. When present in sufficient concentrations, these elements can stabilise the β phase at room temperature. There are other elements in this group, such as Ta and Re, but they are seldom used or not used at all due to considerations of density.

Among the β eutectoid forming elements, Cr, Fe, and Si find extensive use in various titanium alloys. On the other hand, Ni, Cu, Mn, W, Pd, and Bi have very limited applications, restricted to just one or two specialised alloys. Certain elements like Co, Ag, Au, Pt, Be, Pb, and U, which fall into the β eutectoid forming category, are not used in titanium alloys. [22]

Furthermore, certain elements like Zr, Hf, and Sn demonstrate relatively neutral behavior, as illustrated in Figure 2.3. They marginally decrease the α/β transformation temperature and then, at higher concentrations, raise it once more. Zr and Hf share isomorphic characteristics with titanium, leading to identical β to α allotropic phase transformations. These elements have full solubility in both the α and β phases of titanium. In contrast, Sn falls under the category of β eutectoid forming elements but exerts negligible influence on the α/β transformation temperature.

For the scope of developing an improved understanding of the processes and effects that alloys are subjected to prior to the ingot to billet conversion stage, each stage of the triple melting process is critically assessed.

VIM

Vacuum Induction Melting (VIM) is a process which involves the melting of metals through electromagnetic induction under vacuum. Induction melting is completed through inducing eddy currents in the metal being processed. The eddy current heats and melts the charge. The process provides an end product that is clean and homogenous by removing dissolved and chemically bonded impurities. Melting processes, most frequently VIM, have been review and described many times in the literature [23–37]. Typically, the vacuum levels during the refining phase fall between 10^{-1} - 10^{-4} mbar range, this level varies depending on the metallurgical process and final product.

VIM is said to be the most versatile melting process for the production of speciality alloys [9]. As a whole, the process provides excellent control over the chemistry of each alloy for both harmful and beneficial trace elements, leading to great reproducibility of composition, as shown in Table 2.2 for IN718. Component elements for any speciality alloy are of utmost importance for determining its material properties, their concentration must be kept within a narrow compositional range to

Table 2.2: Chemical composition control of IN718 based on 100 heats *Analytical frequency *e.g.,* 95% means that the chemical composition of 95% of the melts are within the final range [9]

Element	Specific range in wt%	Final range in wt%	Analytical frequency in wt%*	Analytical Accuracy in wt%*	
				1971 data	1980 data
C	0.02-0.08	0.04-0.05	95	0.0006	0.003
Ti	0.80-1.15	0.90-1.10	97	0.05	0.03
Cb	4.75-5.50	5.05-5.40	99	0.12	0.08
Al	0.30-0.70	0.50-0.60	95	0.04	0.02

ensure the desired material properties remain reproducible.

Consequently, during melting, caution must be taken to avoid any unwanted reactions, such as oxidation with air, increasing loss of these elements, deterioration in oxide, and nitride cleanliness. Thus, it makes sense for the melting of superalloys to be carried out under vacuum or in an inert gas atmosphere. VIM is occasionally performed in an inert gas atmosphere instead of under vacuum to stop the vaporisation of alloying elements. Similar to inert gas heat treatments, in this case the chamber is backfilled most commonly with argon after reaching a state of vacuum, prior to melting.

Another alternative for some steel, nickel, cobalt, and cast-iron alloys is standard air induction melting. This conventional method will drastically reduce costs involved in melting; however the quality and mechanical properties of the final part will suffer. One step for improvement of this method has been the development of argon blanketing methods that protect the liquid metal and furnace lining at a lower cost. [34] The first most well-known argon blanketing method is surface protection air liquid (SPAL), where liquid argon is added to the furnace and expands to a gaseous state 800 times its liquid volume improving the liquid metal protection. In the second process, laminar barrier inerting (LBI), argon gas is added into the plenum and flows through the porous face to form a laminar barrier on top of the furnace. Both SPAL and LBI methods have been reported to enhance cleanliness, gas content and alloy element recovery over standard air melting.

The three key challenges of VIM that have been realised by Edwards Vacuum, a world leader in vacuum systems, are: the handling of high-volume chambers with highly dusty environments; the fast roughing pump-down time and resistance to dust involving coarse and fine particles; and the pumping of high argon concentrations ($> 70\%$) in the range 5 - 45 kPa. [38]

On top of the achievement of very closely reproducible compositional tolerances there are a number of additional special features of vacuum induction melting. These features can be summarised as follows:

1. flexibility due to small batch sizes.
2. faster change of melt programme.
3. isolation of the melt from air contamination.
4. gas atmosphere can be selected at will.
5. resulting in low loss of reactive elements due to oxidation.
6. and control of pressure above the melt.
7. control of pressure-dependant chemical reactions.
8. precise temperature control.
9. excellent homogenisation due to inductive stirring.
10. removal of undesired trace elements with high vapour pressure.

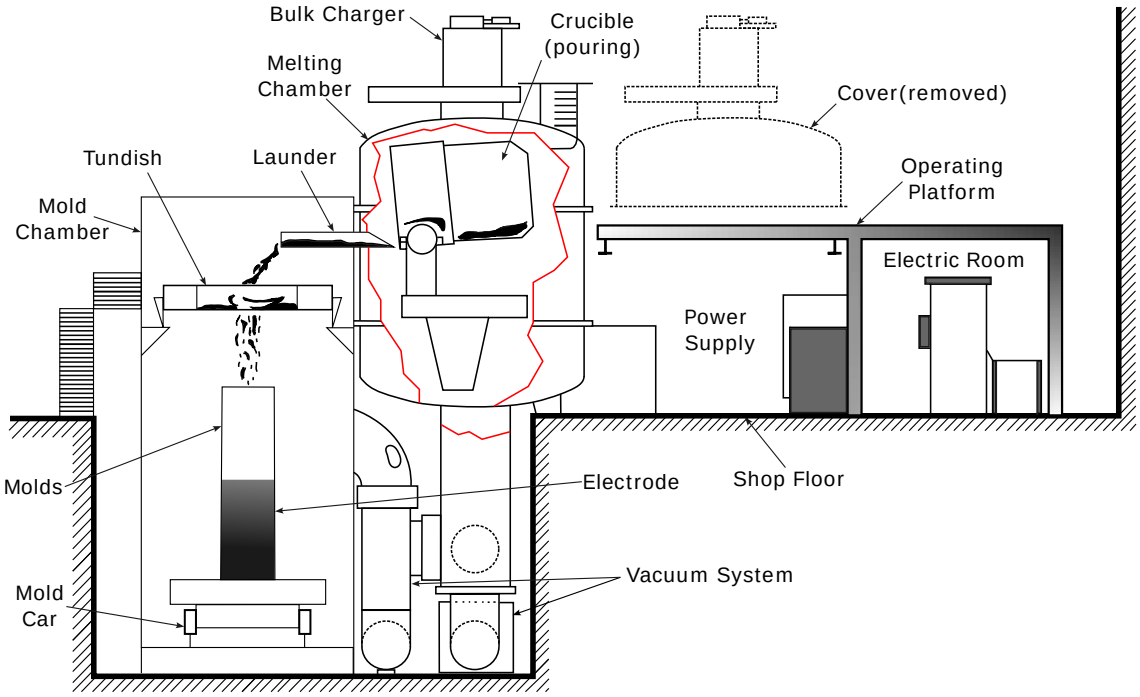

Figure 2.4: Schematic diagram of Vacuum Induction Melting furnace. Adapted from ASM Handbook Volume 15 [39].

11. removal of dissolved gases like hydrogen and nitrogen.

12. removal of oxide inclusions.

13. low level of environment pollution from dust output.

A schematic of a typical VIM furnace is presented in Figure 2.4, where the key components are listed. Some features, such as sampling ports, casting chambers, tilt and pour mechanisms, and mould handling facilities may be added depending on furnace size. Conventionally, the VIM furnace consists of an air-tight water-cooled steel jacket, capable of holding the vacuum requirements for processing and a crucible housed in a water-cooled induction coil where the metal is melted.

Fashu *et al.* concluded from a review on crucible design for induction melting of titanium alloys, that among a range of various techniques for melting, vacuum induction is promising due to its, "simplicity, flexibility and the ability to produce homogeneous ingots." [40] On the other hand, from the review, they identified that selecting an appropriately designed crucible is another major key challenge for VIM. The selected crucible must be fit for the purpose of being both able to withstand aggressive melt at high temperature and being resistant to thermal shock.

As an essential component in the VIM process, crucible improvement relies on the combination of having the following features: low contamination of the ingot, long service lifetime, high tolerance towards attack, stability at high temperatures, high thermal shock resistance, and low wettability under melting conditions. In the end, this study found that upscaling of the parts made in the laboratory up to the industrial scale to be the final hurdle for the titanium alloy melting. [9, 40]

In another study by Kamyshnykova *et al.* of VIM and solidification of a TiAl-based alloy (Ti-46.6Al-5Nb-0.2B-0.2C *at.*%) in graphite crucibles, it was seen that varying the vacuum pressure greatly varied the content of the alloying elements. [35] At $1x10^4$ Pa (low vacuum) it led to an increase of carbon content to 0.49 *at.%* without affecting the Ti, Al, Nb, and B alloying elements. Whereas a vacuum presure of 6.8 Pa (medium vacuum) led to an increase of carbon content to 0.68 *at.*% due to evaporation loss and decrease of Al content to 45.5 *at.*% in turn increasing Ti and

Nb content. Overall, it was found that the vacuum pressure affects cooling rates, solidification behaviour, macrostructure, and microstructure. Medium vacuum results in lower cooling rates during solidification and solid phase transformations, and coarser columnar grain structure compared to those under low vacuum preparation. Lastly, it was concluded that the Vickers microhardness of the lamellar microstructure and hardness of the metals from the medium vacuum were higher than their low vacuum counterparts. This was also respectively true for the compression yield stress and peak flow stress at temperatures of 800 and 900 °C. Studies that include changing vacuum pressure to achieve desired removal and balance of alloying elements, material properties, and their kinetics can be seen throughout literature [23, 26, 27, 32, 36, 37, 41–43].

Finally, although it is more than a century old and with decades of experience, the VIM process is still being iterated upon with new set-ups and products. This includes the novel vacuum induction melting furnace designed by Chen *et al.* in 2019 [31]. With this iteration they have aimed to overhaul and improve upon:

1. the high energy consumption
2. complex overall structure
3. long heating time of the device
4. low heating efficiency
5. unreasonable structure design of the induction heating coil
6. and the length of time in which the furnace can be used

For this, a new cooling system, high frequency induction machine, insulating baffle, high frequency induction heating coil, valves amongst many other components have been redesigned for process improvement. Another re-design of the horizontal VIM furnace by Hongqiang *et al.* in 2020 [44], improved the filling ability of casting workpieces, which resulted in the improvement of the casting yield of both special-shaped workpieces and thin-walled workpieces. The last example of redesign improvement of the VIM process is on the traditional observation window, allowing the user to view the heating and melting of the workpiece in the crucible and prevent any processing faults or issues. This patent [30] from Yu, has a clever design to avoid the issue of the quartz glass lenses requiring to be dismounted and cleaned when contaminated, demonstrating how small design changes can improve work efficiency in VIM processes. There are many further such designs that can be found and explored in the literature. [45–47]

In the triple melting process, as well as VIM, the second process, electro-slag remelting is also widely used in alloy refinement processing.

ESR

Electro-slag remelting (ESR) is a critical process in the production of special steels (most notably tool steels) and nickel-based alloys when aiming for cleanliness and homogenity in the microstructure. [48] There are a wide variety of processing avenues and combinations, however for triple melting ESR is the intermediate stage of achieving high quality ingots. ESR can produce round shape, square section, slabs, hollow, and composite materials after remelting.

Titanium is a reactive metal with high affinity for oxygen and nitrogen and reacts with almost all oxides at high temperature. Therefore, the electroslag remelting of titanium requires the furnace atmosphere to be free from oxygen and nitrogen (*e.g.,* an inertgas atmosphere must be secured to avoid additional pick up of undesired elements), and the slag must be free from oxides. ESR is usually not carried out on titanium ingots, due to it's reactive nature, requirement for additional set up, and that single melting is sufficient for further working in most cases [9].

ESR works by the new ingot being built-up in a water cooled mould by melting a consumable electrode, also known as the VIM ingot, immersed in a superheated slag usually under normal

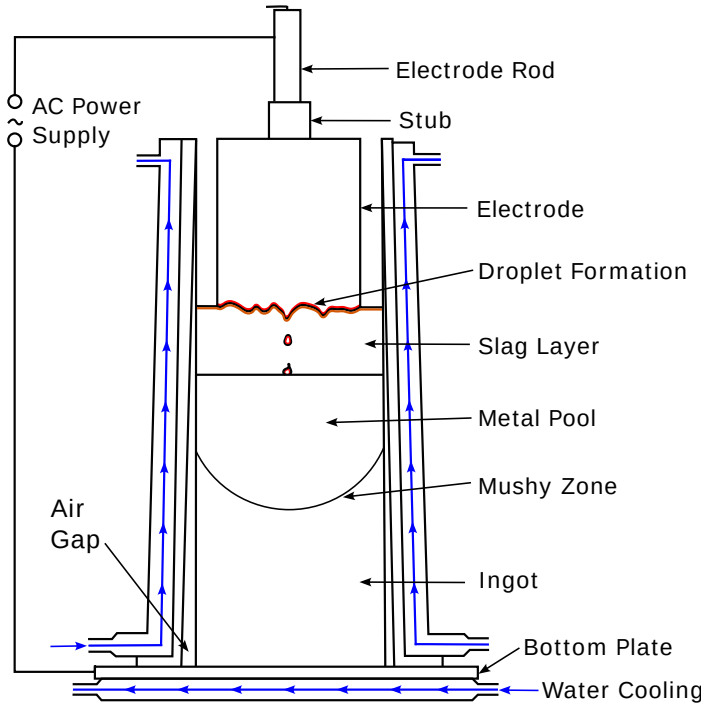

Figure 2.5: Schematic representation for Electro-slag Remelting process. Adapted from Choudhury *et al.* [9].

atmosphere [9]. The heat required is usually supplied from an AC supply current flowing through the liquid slag, which provides the electrical resistance. As the temperature of the slag surpasses the liquidus temperature of the alloy, the electrode tip melts. The now molten metal falls through the liquid slag and collects in the cool mould. The slag pool slowly rises as the new ingot of refined material builds up from the bottom of the mould. During this formation of the liquid film, the metal is refined and cleaned of contaminants, such as oxide and sulphide particles. The metal/slag-interface surface area is greatly increased as the metal is in the form of droplets at this stage. Concentrated reactions between metal and slag results in a significant reduction in sulphur and non-metallic inclusions. The schematic and principle of the ESR process is presented in Figure 2.5.

- With proper process control any additional pick up of undesired elements, eg. oxygen and nitrogen, can be completely avoided.

ESR provides continuous transport of liquid metal through the slag, during which both compositions change according to the kinetic and thermodynamic conditions. For this, the slag must meet the following requirements:

1. The melting point must be lower than that of the electrode.
2. The composition should allow for favourable reactions, *e.g.,* desulphurisation and removal of oxides.
3. It must have a suitable viscosity at the remelting temperature.

Typically, slags for ESR are composed of (CaF_2), lime (CaO) and alumina (Al_2O_3). Furthermore, magnesia (MgO), titania (TiO_2) and silica (SiO_2) can be added, depending on the alloys being remelted. Currently, the main challenge with ESR is in the cleanliness of the output ingot, however a main advantage of the ESR process has always been the good desulphurisation of the metal, which is determined by two reactions. The first is the metal/slag reaction, where the sulphur is transferred from the electrode to the slag:

$$[S] + (CaO) = (CaS) + [O] \tag{2.1}$$

The second reaction is in the slag/gas phase. Here, the sulphur that has been absorbed by the slag transitions into sulphur oxide by oxygen that is present in the gas phase:

$$(CaS) + \frac{3}{2}O_{2gas} = (CaO) + SO_{2gas} \tag{2.2}$$

The desulphurisation capacity of the slag remains intact throughout the entire remelting process as the slag is not saturated with sulphur. As mentioned previously, ESR is usually carried out at normal air atmosphere. Oxidation of the metal is unavoidable. The metal can pick up oxygen in several ways:

1. Oxidation of the slag surface of elements with different valences, *e.g.,* iron and maganese.
2. Oxidation of the electrode surface above the slag bath.
3. Oxide attached to the electrode outer surface.
4. Desulphurisation causing the transfer of oxygen seen in Eq. 2.1.

In summary of decades of literature on ESR research relating to cleanliness, several variables can be seen to have an influence. These being, the deoxidation of the electrode, ESR repeated with the same ingot/electrode [49], pressure [50], or protective gas electroslag remelting (PESR) (*e.g.,* [51–55]), the size of the inclusions present in the electrode [56, 57], and the composition and viscosity of the slag (*e.g.,* [58–60]).

Moreover, the process parameters must be considered. The melt rate, current, voltage, and the power supply (AC, DC, and frequency) have an impact in the removal of non-metallic inclusions. As highlighted in more depth by Paar *et al.* [50] a lower melt rate typically generates a shallow melt bath, a better solidification structure, and improved removal of non-metallic inclusions. A lower melt rate also allows more reaction time between the slag and the metal, which is better for the vertical solidification, decreasing the "freezing" of the non-metallic inclusions during solidification.

Whereas, as Paar [50] highlights, the literature also reports a positive effect of a higher melt rate. This is due to that increasing the electrode speed increases electrode-slag immersion depth, which reduces the chance of any oxidation at the electrode tip. As ESR is typically carried out at normal atmosphere, it leads to the loss of easily oxidisable elements, *e.g.,* titanium, aluminium, and silicon.

During the remelting of Fe-based alloys this is counterbalanced by the slag being simultaneously deoxidised, preferably by aluminium. For superalloys with relatively high titanium and aluminium content, the deoxidation of CaF_2-CaO-Al_2O_3-slag is of no benefit in achieving the desired analytical range in the remelted ingot. Introduction of oxygen into any superalloy melt is mainly due to the ESR-slag constituents FeO, SiO_2, and Al_2O_3.

The slag reactions between titanium and the oxides (FeO and SiO_2), are often of minor importance due to their low content, the oxidation of titanium can be represented with the equation:

$$3[Ti] + 2(Al_2O_3) = 3(TiO_2) + 4[Al] \tag{2.3}$$

Where applying the law of mass action, the equilibrium condition can be simplified to the expression:

$$\frac{[Ti]^3}{[Al]^4} = K\frac{(TiO_2)^3}{(Al_2O_3)^2} \tag{2.4}$$

To avoid the loss of titanium in the melt, the TiO_2-content should be adjusted for the Al_2O_3-content of the slag to achieve the equilibrium to match the [Ti]/[Al]-ratio of the superalloy that is being formed.

Similar to VIM, there are many studies in the literature regarding ESR, for example in Yang *et al.*'s 2017 article [61], the distribution behaviour of Al and Ti between Ni-based alloys and molten

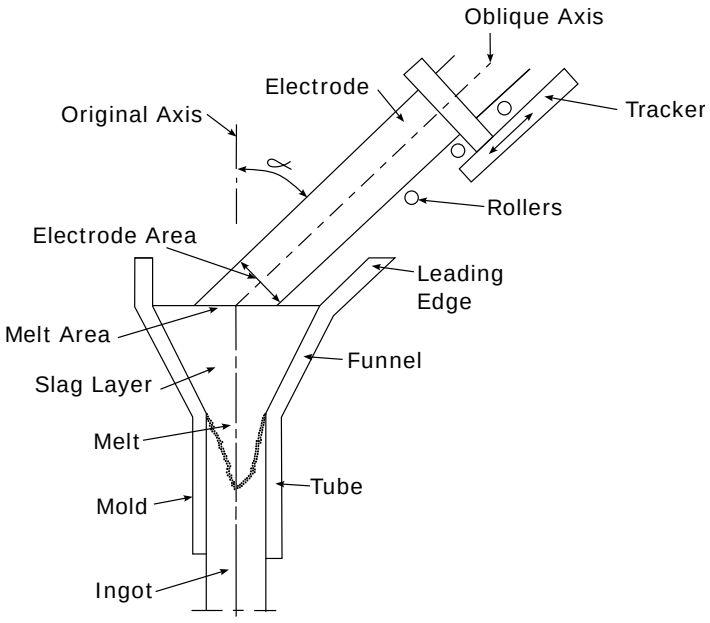

Figure 2.6: Schematic for novel ESR installation setup. Adapted from Harald *et al.* [64].

slags during ESR was studied. They concluded that the temperature dependence of the activity-composition relationship of TiO_2 and Al_2O_3 in the slag showed good linear correlations and the equilibrium content ratio of TiO_2 to Al_2O_3 at a fixed activity ratio increases with increasing temperature. This indicates that the oxidation of Ti occurred more compared to Al as the temperature increased. Proving that for higher operating temperatures in the ESR process, the volume of TiO_2 should be increased.

In another example, Prasad [62] found that Electro-slag crucible melting (ESCM), which is another form of ESR that reduces chromium oxide, is a viable alternative production route for Cu-Cr alloys. Typically, Cu-Cr alloys are difficult to melt by conventional techniques, additionally the process serves the dual purpose of recycling copper scrap and alloying remelted copper by chromium simultaneously. This study was the first time that direct reduction had been employed during an ESR process.

Pribulová *et al.* [63] aimed to determine the optimal slag composition for the ESR of steel, ensuring the resulting chemical composition aligns with the specified standard. That is the remelted steel had to meet criteria for minimum sulfur content, minimal presence of oxide and sulphide inclusions, and mechanical properties in accordance with the STN 14 109 standard. The authors discovered that the fractions of C and P do not change after ESR, *i.e.,* it does not cause chrome loss. However, remelting does result in significant Si loss, and Probulová recommends the maximum permissible Si content value in the remelted electrode, due to which a reduction of sulphide inclusions was also observed. Manganese content was seen to increase post-ESR also. Overall, the study optimised the steel electrode through ESR by removing undesired elements and improving mechanical properties, while remaining within the required standard.

Harald *et al.* invented a novel ESR set-up in 2018 that aimed to increase the melt rate without an increase in cross-sectional area of the consumable electrode [64]. This was achieved through introducing the electrode at an angle into the mould (preferably between 20° and 60°, especially 45°), resulting in the consumable surface being increased, which in turn increases the melting rate. The arrangement has a number of other small advantages, *e.g.,* rapid replacement of the electrode being made easier with roller bearings. A diagram of the novel ESR set-up is presented in Figure 2.6.

In summary, ESR is an essential process for the refinement, homogeneity, and cleanliness of several different quality alloys. Some variations of the typical setup have been adapted for specific alloys (*i.e.,* titanium alloys), and in recent years for iterative improvement of the main parameters

affecting the efficiency of the process. The final part of the triple melt process (VAR) is often comparable to ESR, however has an entirely different operating principle. Due to the difference in operating principle, VAR is the main melting process of titanium ingots.

VAR

Vacuum-arc remelting (VAR) is the last industrial refinement process of triple melting. Just like the other melting and remelting processes, VAR is used to improve the cleanliness, chemical homogeneity, and mechanical properties of metals [65, 66]. On the other hand, inappropriate melting parameters may result in metallurgical defects, such as macrosegregation, porosities, tree ring patterns, and beta flecks (also known as white spots) [67–69]. A primary feature of VAR is the continuous melting of a consumable electrode by means of a DC under vacuum [9]. The molten material solidifies in a watercooled copper mould, similar to ESR. A schematic diagram is presented in Figure 2.7. Although comparatively similar in some respects, there are fundamental differences between ESR and VAR, such as:

1. In VAR, heat for remelting is generated by a DC vacuum between the electrode and resultant ingot, this arc is unstable and has no thermal buffer. Whereas, as described before, ESR is an AC current passing between the electrode and ingot through the resistive slag.

2. In VAR, the atmosphere surrounding the forming ingot is a low pressure mixture of metal vapours and gases. For ESR, this is nominally air atmosphere above the slag, where the slag is a physical barrier for the forming ingot.

3. In VAR, the ingot solidifies directly onto the water cooled crucible, creating a chill cast layer In ESR, a layer of 'slag skin' is formed between the water cooled crucible and the solidifying metal.

4. In VAR, the molten metal droplets transfer at a high rate from the electrode to the ingot. In ESR, the metal droplets often react chemically and thermally with the molten flux, while slowly sinking through the slag.

5. In VAR, the stability of the arc and the heat distribution are dependant on the length of the arc. A long arc gap typically concentrates the heat in the centre of the new ingot. In ESR, the electrode tip placement and position relative to the slag pool surface greatly affects the heat distribution throughout the slag. If the electrode is only immersed in the slag by a few millimetres it will cause a thicker slag skin, due to the high heat in the centre of the slag surface.

Similar to VIM and ESR, there has been abundant research into the process improvement and parameters of VAR techniques. A great deal of these have been through simulation studies. For example, Delzant *et al.* [71] established two separate models to calculate the thermal radiation at the top of the VAR ingot. One model only considered the heat exchanges from radiation between the electrode tip and the ingot, whereas the second method further involved the crucible wall heat transfer interactions. Delzant found that heat transfer between the ingot top was greatly dependant on the arc gap length and the electrode radius. In another example, Kondrashov *et al.* [72] developed a simple heat model for VAR in 2007 which predicted the molten pool depth from different current strengths, however it did not consider the magnetohydrodynamic phenomena in the molten pool. Kou *et al.* [73] in 2014 determined the fluid flow, temperatures, and solidification structure of Ti-6Al-4V during VAR. The experimental data correlated well with the simulated columnar grains of the ingot when radiative heat was considered. Kemanpur *et al.* [74] established a multi-scale model which combined the modelling of grain growth and nucleation with the larger macroscopic heat transfer, fluid flow, and electromagnetism. The focus of melt rate, arc power, and arc focus on the grain structure and their effects were studied. Similarly, Atwood *et al.* [75] also developed

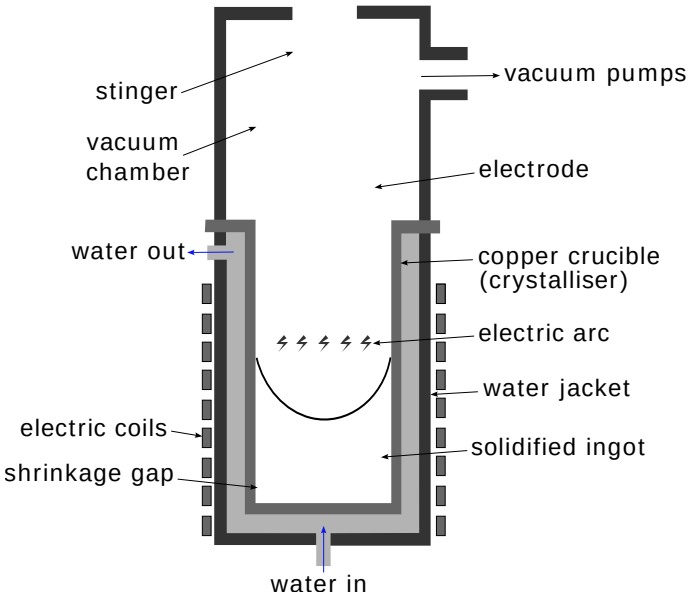

Figure 2.7: Schematic representation for Vacuum Arc Remelting setup. Adapted from Cui *et al.* [70].

a multiscale model, which was used to study the effect of stirring and grain nucleation on the morphology of the columnar dendrites. Huang *et al.* [76] simulated the entire VAR process of high alloy bearing steel ingots, and found that when the overall smelting power increased, the depth of the molten pool became deeper. Additionally, the primary and secondary dendrites and dendrite spacing increased considerably, as well as the percentage of columnar crystals.

More recently, Wang *et al.* [77] used the finite element method to investigate the effect of melting rate and current intensity on the solidification structure, depth of the molten pool, and equiaxed crystal rate in VAR. The direct correlation between current intensity and melt rate is presented in Figure 2.8, where the VAR process is broken into three discrete stages: current increasing, remelting, and feeding periods.

The melt rate is also controlled by the gas pressure inside the vacuum chamber and gap length [78, 79]. Cracks on the electrode can also have an impact on the behaviour of the arc and thus, the melt rate of the electrode.

VAR is a highly researched process, with a lot of investigation into the solidification structure and macrosegregation of VAR ingots [80–85]. Where all previously mentioned solidification defects are all reported. It was discovered that the use of an external magnetic field helps to diminish the solidification defects, particularly macrosegregation [86].

Non-metallic inclusion (NMI) cleanliness greatly influences the mechanical properties and characteristics of metal alloys, *e.g.,* fatigue strength [87]. Descotes *et al*'s work found that inclusion size was heterogeneous along the radius, with the largest inclusions being localised to the centre of the ingot, and that the melt rate influences the inclusion size, as it influences the local solidification time.

Among other conclusions, Seongi *et al.* [88] concluded when studying high entropy alloys with equiatomic, or near equiatomic, compositions that a different solidification rate as a function of melting temperature resulted in the micro-segregation in the dendrite arms and inter-dendritic regions enriched with Ta & Mo, and V & Ti respectively.

Similarly to the other melting processes, there has been significant improvements in VAR design from its initial basic conceptualisation in 1892, to the first VAR research in 1928, definitive work in 1935, patent in 1940, and popular use in the 1950's and 1960's [89]. Even in recent years there have been improvements, in creating a more compact structure, minimising uncontrollable magnetic field

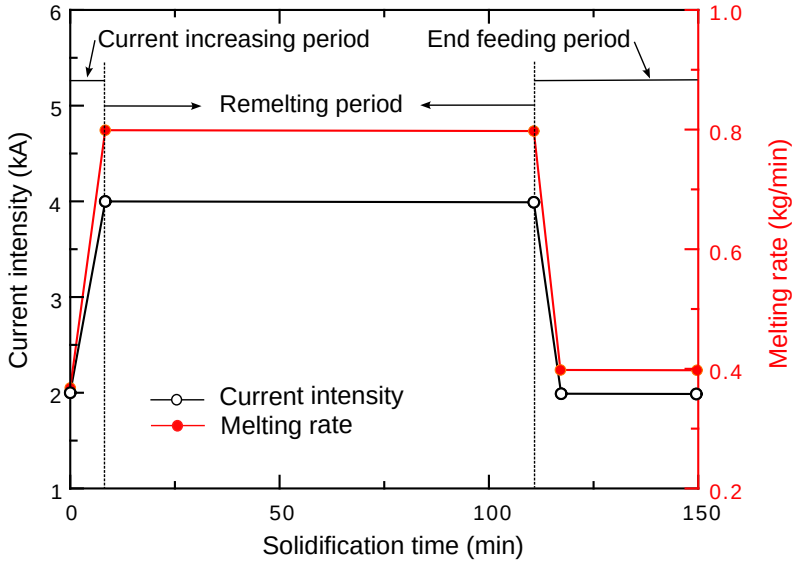

Figure 2.8: The current intensity and melting rate during the VAR process. Adapted from Wang *et al.* [77].

stirring during the process of vacuum smelting, and improving the accuracy of metal smelting [90]. Shipu *et al.* designed a utility model of a VAR setup to improve overall work efficiency, *i.e.,* reduce the labour times lifting crystallisers from the furnace heads, perform de-spinning, inspection *etc.* [91] The design provides improved support for placement of the crystalliser of the VAR furnace, solving the problem of poor bearing capacity and single structure supports, as well as saving space, and having convenient detection and maintenance. In a final example, Patel *et al.* [92] designed compact coil assemblies to ensure the magnetic field generated by the electromagnetic energy source during remelting is confined to the arc region.

In summary, the triple melting process is the combination of VIM, ESR, and VAR in the processing of various high value alloys and tool steels. Each individual process has its own strengths and weaknesses for improving the quality of the metal. This is where many variations of routes and processes themselves are sought to achieve the desired characteristics for the final ingot component before further processing. The processing stages employed by industry for speciality alloys prior to cogging is summarised in Figure 2.9. One further processing stage, beyond melting and remelting, to achieve the desired microstructure for many alloys and steels is through heat treatment, which improve the compositional homogeneity and purity of the ingot prior to ingot-to-billet conversion.

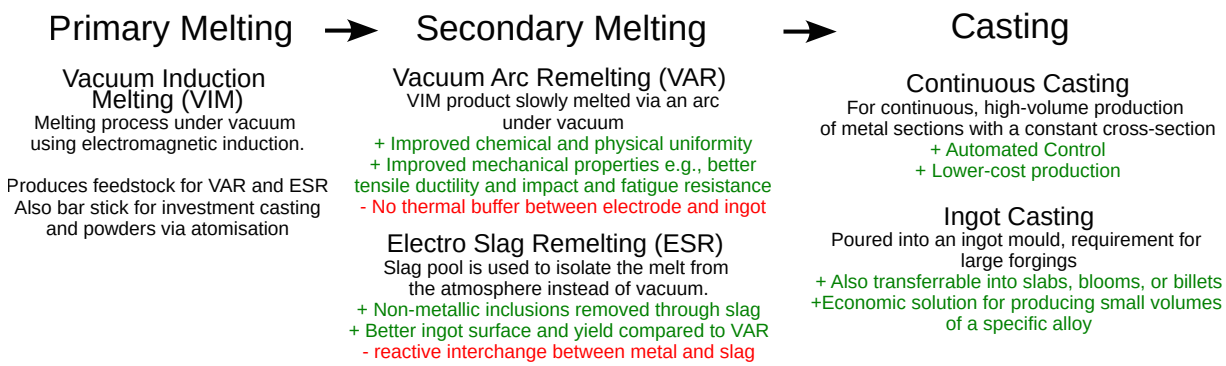

Figure 2.9: Summary of melting stages employed in industry for the production of speciality alloy ingots prior to cogging.

2.1.3 Heat Treatments of Advanced Alloys

Heat treatments are necessary throughout thermomechanical processing of advanced alloys and fulfil a number of important roles focusing upon compositional processing and environmental conditions. They can be used to homogenise cast alloys, improving their hot workability, to soften material before, and during, hot and cold operations, or to alter their microstructure in such a way as to achieve the desired mechanical properties.

Annealing

Annealing, in general terms, refers to a heat treatment where a material undergoes exposure to a high temperature environment (above its recrystallisation temperature) for an extended time, that is then cooled. [93] The two key parameters in an annealing process are temperature and time, this includes the rates at which temperature is increased and decreased. Annealing is commonly used to: increase softness, ductility, and toughness; relieve stresses; and/or produce a desired microstructure [93]. All annealing processes are made up of three discrete stages:

1. **Heating cycle** (heating to a specific temperature).
2. **Soaking cycle** (held at the specific temperature for a period of time).
3. **Cooling cycle** (cooled, usually at a slow rate to room temperature).

As previously mentioned, time is a crucial factor in any annealing process. There can be large differences between the interior and exterior of any workpiece, known as temperature gradients, which can vary depending on the part size and geometry. If the rate of change of temperature is too high, it may introduce unwanted internal stresses into the workpiece that may lead to warping or even cracking. Annealing time must also account for the necessary transformation reactions to take place. [93] Equally temperature plays a key role, annealing is accelerated as temperature is raised since diffusional processes are usually involved. An example of this is presented in Figure 2.10, where it can be observed as temperature increases, the number of coarse recrystallised grains increases. Annealing follows diffusional processes seen throughout both Avrami equations (in cases of constant temperature) and Arrhenius type relationships (derived from Fick's laws of diffusion) where variance in temperature is found, *i.e.,* where diffusion rates fluctuate. More discussion on diffusion and recrystallisation kinetics can be found later in this review.

For titanium alloys, heat treatments are used throughout thermomechanical processing, and variations are used depending on the titanium alloy type, (*e.g.,* β-alloys). Some examples, given by Boyer *et al.* [95] of these include:

1. **Stress relief** - A low temperature treatment, typically used to removed residual stress and will not change the microstructure.
2. **Anneal or mill anneal** - Most common treatment for α and α+β Ti alloys (typically between 650-790 °C) result in a completely stress free part with an elongated or equiaxed primary α structure.
3. **Duplex anneal** - This heat treatment is used to provide a duplex (or bimodal) microstructure with transformed β and equiaxed α. A bimodal structure may have lower ductility than an equiaxed structure however, will have better fracture toughness, creep resistance, and fatigue properties.
4. **Recrystallisation anneal** - A slow cool from a high temperature anneal resulting in coarse equiaxed α with isolated β at triple points. Done precisely, this method offers the best combination of tensile, endurance, and damage tolerance properties.

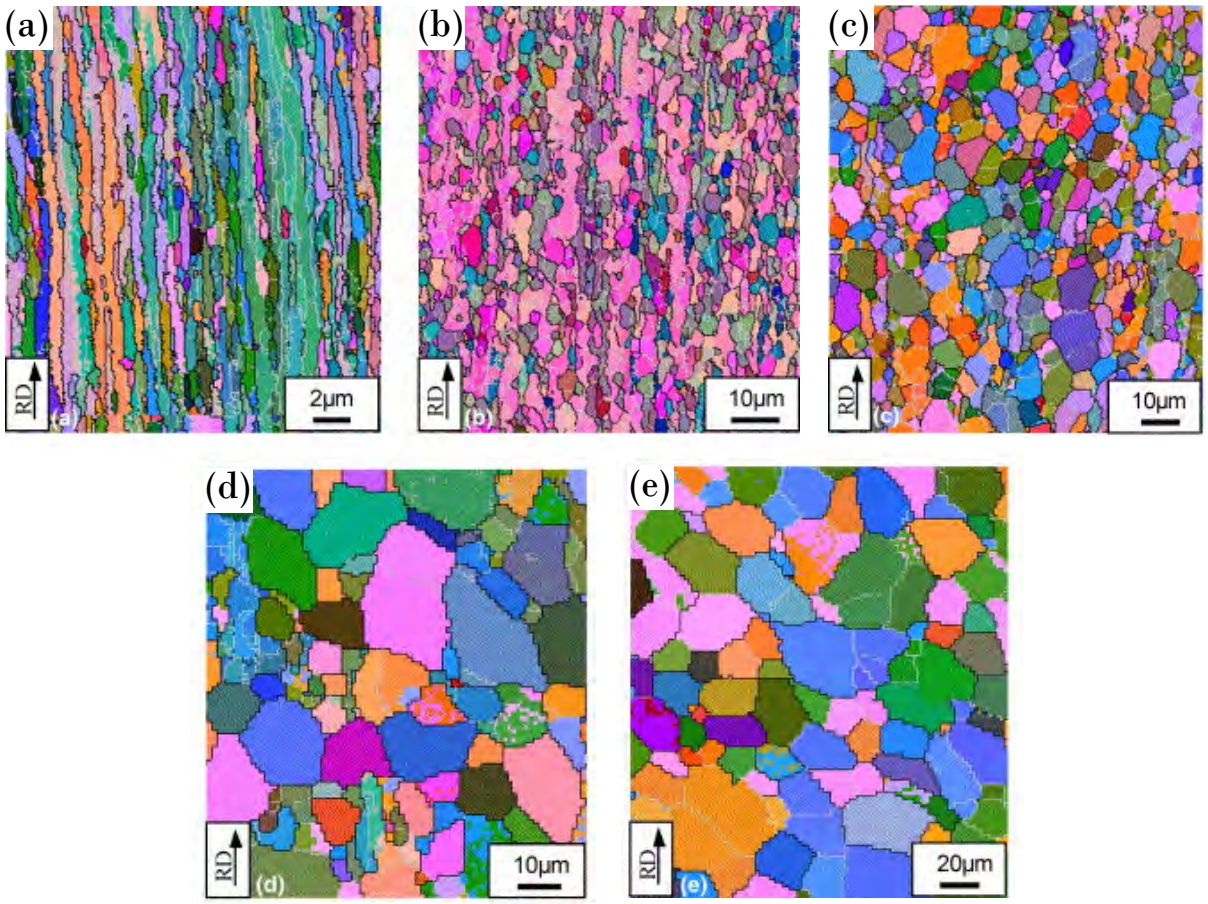

Figure 2.10: EBSD maps showing continuous recrystallisation in small-grained Al-0.1Mg deformed to $\varepsilon = 2.6$. (a) As deformed and annealed for 1h at (b) 200°C, (c) 225°C, (d) 250°C, and (e) 300°C. Captured from Jazaeri *et al.* [94].

5. **Solution treat and age** - $\alpha+\beta$ will usually be solution treated high in the α/β-phase field and β alloys above the β transus. Solution treatments in these cases will often be followed by rapid cooling. Ageing of these alloys will result in α precipitation.

6. β **anneal** - A β anneal is carried out above the β transus. As lamellar α structure begins to form when the temperature below the β transus, the aim of this heat treatment is to control the thickness of the α platelets, or lamallae through cooling rate. β annealing is followed by a mill anneal to finish to remove residual stress.

7. **Triplex anneal** - A 3 stage annealing process, firstly solution treated above β transus with controlled cooling, then solution treated high in the α/β-phase field with controlled cooling, and then a final mill anneal. This technique was developed specifically for Ti62222 alloy (Ti-6Al-2Sn-2Zr-2Mo-2Cr).

Stabilisation annealing is another specific treatment designed to produce a stable β-phase in titanium alloys capable of resisting further transformation when exposed to elevated temperatures in service. Seo *et al.* found when studying cooling rates and stabilisation annealing of β-annealed and β-quenched Ti-6Al-4V, that stabilisation annealing had no noticeable microstructural effect on the material [96]. Additionally, it was seen that the change in high cycle fatigue (HCF) and fatigue crack propagation (FCP) tensile behaviours on the β-annealed vs non β-annealed Ti-6Al-4V was negligible, which indicated it may not be necessary for fatigue-critical structures in ambient service temperature. However, the β-quenched Ti-6Al-4V after stabilisation annealing tended to decrease the materials resistance to HCF and FCP. Therefore, from this study it can be concluded that heat

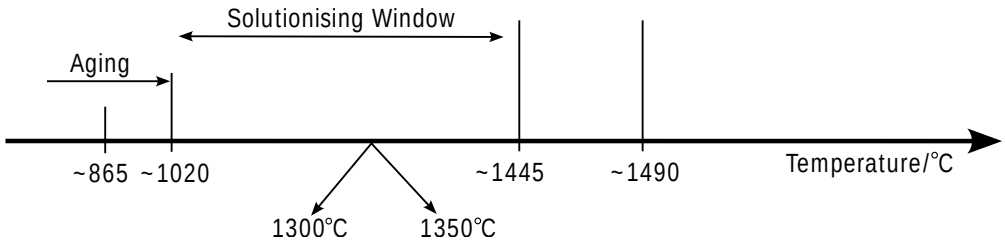

Figure 2.11: Schematic of transition temperatures in γ-γ' Co-9Al-9W alloy. Adapted from Tomaszewska *et al* [103].

treatments for each alloy should be carefully considered, as a specific treatment or no treatment may be required to achieve the desired properties for the materials service-life.

Although it falls out with the scope of ingot-to-billet conversion, it is worth mentioning there are a great deal of studies in the literature dedicated to annealing treatments of additively manufactured (AM) and selective laser melted (SLM) metals, *e.g.,* [97–101].

Overall, it is clear that annealing is a widely studied topic in the literature. As it is a general process that is carried out with regularity in metal and alloy processing at different stages, it is of crucial importance to understand its various effects at all levels of metallurgy. There are other heat treatments undergone by advanced alloys that are under the scope of annealing with slight variances, such as homogenisation and solutionising.

Homogenisation and Solutionising

Homogenisation is one form of annealing, often known as uniform, or diffusion, annealing which is an important step prior to ingot-to-billet conversion. The intent of the homogenisation process is to produce a homogenous structure through diffusion (*i.e.,* dissolve intermetallic particles into a matrix), and/or to reduce the effects of microsegregation [102]. A similar process and term, known as solutionising, is sometimes used synonymously [103] but its intent is to reduce the number of phases (usually to a single phase), with no precipitates which in turn typically makes the structure more homogenous.

In the work of Tomaszewska *et al.* [103], thermal analysis was carried out on homogenised, solutionised, and aged Co-9Al-9W (at.%). Different metals have different transition temperatures. The transition schematic in γ-γ' Co-9Al-9W alloy can be seen in Figure 2.11. The effect of solutionising on the microstructure of this material can be seen in Figure 2.12, where the impact of an increase in temperature and time can be observed. The example presented in Figure 2.12 again reinforces the fundamental relationships on diffusion, typical of all materials seen throughout heat treatment processing.

In Wang *et al.*'s work [104], the effect of heating rate on the mechanical properties, microstructure and texture of Al-Mg-Si-Cu during solution treatment was studied. It was concluded that the recrystallisation microstructure of the alloys is greatly influenced by the heating rate. Where the higher heat rate resulted in almost equiaxed grains, whereas the slower heat rate sample had elongated grains with a high length/width ratio. Again, this reinforces that during solutionising, the effect of heating rate has a great effect on the product outcome.

In Peng *et al.*'s work [105], second phase particle evolution during the heating cycle of solution treatment of Al-Zn-Mg-Cu alloy was investigated. In this study, during solution treatment the alloy was subjected to a few different technical phenomena. It was found that the alloy experienced precipitation, coarsening, and dissolution during the heating cycle of solution treatment. They also found through SEM and TEM characterisation that the coarsening of the S phase particles has two forms; aggregation coarsening and Ostwald ripening [105]. Moreover, a slow heating process at a medium temperature resulted in S phase coarsening, degrading the mechanical properties. Thus, proving that one outcome of the homogenisation process is grain coarsening.

Deng *et al.*'s work [102] highlights the requirement of specialised homogenisation techniques to

be used for 7000 series Al alloys. As homogenisation causes precipitation of the Al_3Zr dispersoid (which are finely divided particles throughout the alloy) with added zirconium [106–109]. Single-stage homogenisation promotes Al_3Zr particles to be precipitated at the centre of the grains by homogenous nucleation, where these new precipitates remain at a smaller grain size. In the meantime, the Al_3Zr particles are heterogeneously nucleated on residual second-phase particles at the grain boundaries. After this, in two-stage homogenisation schemes, where the process is repeated at a slightly higher temperature, the new centre-grain precipitates grow further, whilst the residual second-phase particles at the grain boundaries are dissolved back into the matrix [102]. Thus, resulting in a greater homogeneous distribution of Al_3Zr particles throughout the matrix. Jia *et al.*'s work [110] is another example of a two-stage homogenisation process being utilised to achieve a desired effect. In the study, Sc is added into Al-Cu-Li alloy, which leads to the formation of the W-phase only when under homogenisation annealing.

Interestingly, Osman *et al.* [111] proposed a new two-stage homogenisation practice in 2007, which was designed to dissolve as much as possible of the fine second phase particles that slow recrystallisation by using the phenomena of pinning grain boundaries in Al-Mg-Mn alloy AA5454. This technique is now used commercially, which has led to greater levels of recrystallisation during self-annealing, improving ductility and formability.

For subsequent forging, and post forging, of many advanced alloys, achieving a homogenous structure is an important step for metallurgists. As the physical metallurgy of the part at this stage is impactful to the parts future processing and eventually time in service. Ageing is one final heat treatment process that is imperative to understand for hardening and strength properties in advanced alloy processing.

Ageing

Ageing, otherwise known as age hardening or precipitation hardening [13], refers to the thermal treatments that increase strength, and sometimes ductility, of a material subjected to prior heat treatment. Specimens aged beyond peak hardness are referred to as overaged [112].

Diffusion, including diffusion rates, is a critical factor in all heat treatment processes, whereby

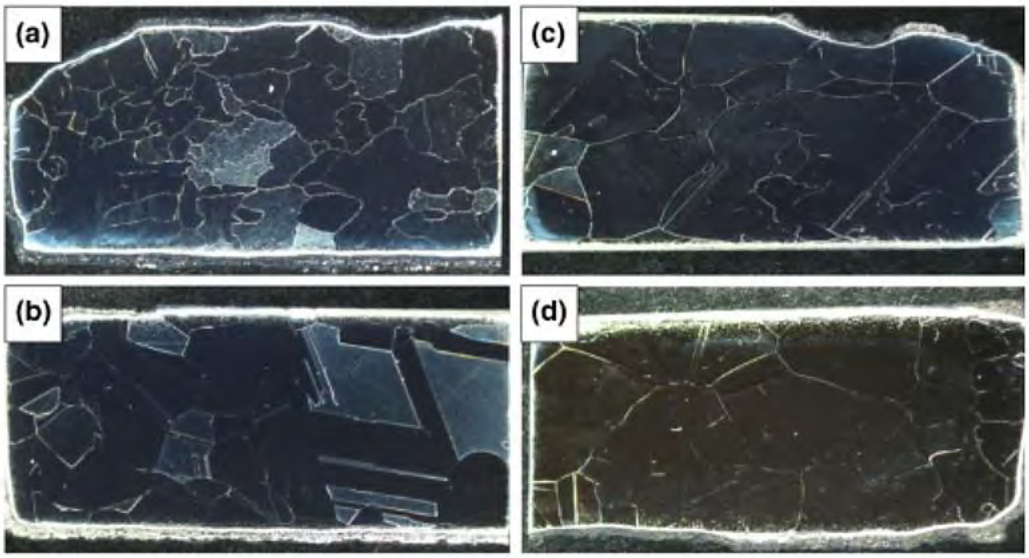

Figure 2.12: Macrographs of Co-9Al-9W alloy specimens: (a) solutionised at 1300°C for 5 h; (b) solutionised at 1300°C for 24 h; (c) solutionised at 1350°C for 5 h; (d) solutionised at 1350°C for 24 h. [103]

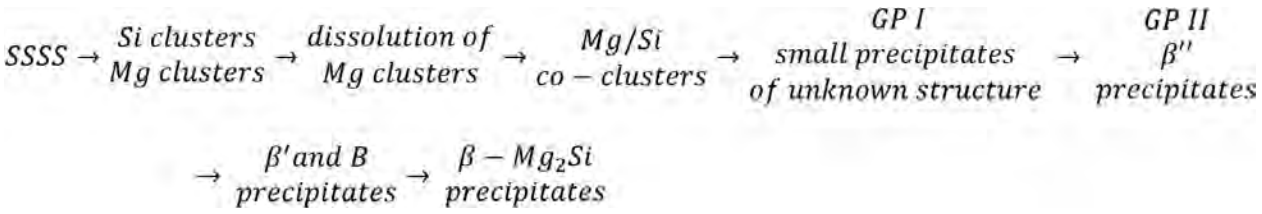

Figure 2.13: The precipitation sequence during the precipitation hardening process in the Al6061 alloy, adopted from Edwards *et al.* [121].

alloying elements and their difference in diffusion rates can play a role in the final alloy outcome after processing. For example, microstructural features of two novel titanium alloys Ti-6Al-4Cr and Ti-6Al-4Mo, based on the makeup of Ti-6Al-4V, after solutionising and ageing are compared in Cong Li *et al.*'s work [113]. After ageing, both alloys show a typical Widmanstätten microstructure, however with the increasing ageing temperature, the size of the α platelets in Ti-6Al-4Cr alloy coarsened more evidently as compared to the Ti-6Al-4Mo alloy. Also, in Ti-6Al-4Cr alloy, samples aged at 600°C, TiCr2 Laves phase was seen at the α/β interface, and within the α phase, Cr solid solution bands were observed. Ultimately, this meant that due to differing diffusion rates of Cr and Mo elements, Ti-6Al-4Cr alloy had a more uniform resultant microstructure than the Ti-6Al-4Mo alloy.

Research is also being completed in the fine-tuning of ageing processes. In one example, Gao *et al.* [114] investigated the Cu- and Sc-precipitation sequences and their interactions at different temperature ranges in an Al-Cu-Sc alloy, developed an isochronal ageing technique with a continuously increasing temperature. From the outcomes of this study they discovered they could use the dual precipitates of θ'-Al_2Cu and Al_2Sc in the alloy to artificially tune and optimise the precipitate dispersion, in turn raising the ageing hardening response, and improving the creep resistance. Proving again the intricacies of heat treatments, with ageing alone and their variety from alloy to alloy.

Different ageing schemes can form different precipitates, which can lead to different hardening and strengthening properties in alloys [115–118]. In Hillel *et al.*'s article [119], the initial stages of precipitation hardening of Al6061 aluminium alloy was studied under direct observation . Typically, in Al-based alloys, they fall short with their relatively low hardness. Precipitation hardening is used widely to combat this shortcoming. However, the route for hardening is complex due to the many phase changes of the precipitates during ageing after quenching from the supersaturated solid solution state (SSSS), as shown in Figure 2.13. The precipitation sequence starts with Si or Mg cluster, then creating co-clusters of both. Then, small precipitates with an unknown structure and precipitates are formed. These are often known as Guinier-Preston (GP) zones: GP-I and GP-II, respectively. Then, if ageing is allowed to continue after this, other precipitates can form, such as rod-like β, β', and β-Mg_2Si [120]. Overall, it is key to understand, from these examples, the complexity and precision that is required in ageing and other heat treatment processing to achieve the desired result. The diffusion mechanisms taking place can be controlled by the metallurgist seeking particular features, yet many different research avenues remain to explore further improvements to these processes.

In summary, amongst all other heat treatments, ageing plays an important role in the physical metallurgy of advanced alloys and their processing. The thermal history continues to have a strong influence on strength observed throughout the alloy's lifetime. Ageing can take place during thermo-mechanical processing and ingot-to-billet conversion. Whereby precipitates affect grain boundaries and dislocation mobilities and hence, final microstructure. Ageing also is used to produced duplex structures with grain boundary precipitates. Mechanisms, such as nucleation, growth, ostwald ripening *etc.,* mentioned in this section will be discussion in greater detail later in the review. Heat treatments of new metals and alloys are of constant interest both in industry and in the literature as understanding of these materials continues to be at the forefront of research. Both before and

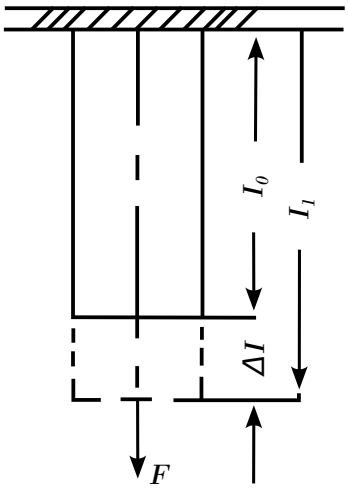

Figure 2.14: Tension test bar - change in length under stress, adopted from Tschaetsch *et al.* [123].

after heat treatments, advanced alloys also undergo forging which also a wide variety of scope in terms of setups, with novel advancements in technology being investigated today.

2.1.4 Forging

Forging comes under the window of the final area of metallurgy, mechanical metallurgy, which is concerned with responsive behaviour of metals to applied forces. Metal forging refers to a collection of manufacturing methods where the metal, usually shapeless or of a simple geometry, is converted into a useful part without change in the mass or composition of the material. The new part typically has a geometry of well-defined (a) shape, (b) size, (c) accuracy and tolerances, (d) appearance, and (e) properties [122]. This change in geometry is achieved through plastic deformation. These fundamentals are imperative to the understanding of ingot to billet conversion and will be discussed briefly.

Unlike elastic deformation, where, for example, a bar under tension (seen in Figure 2.14) returns to its original length as long as the materials defined value (elastic limit of the material, $R_{p0,2}$ limit) is not exceeded. A material which is plastically deformed retains its changed shape permanently.

For the elastic range, the following applies:

$$\sigma_z = \varepsilon \cdot E \tag{2.5}$$

$$\varepsilon = \frac{\Delta l}{l_0} = \frac{l_0 - l_1}{l_0} \tag{2.6}$$

where σ is tensile stress, ε is elongation, l_0 is initial length, l_1 is length under the influence of force F, Δl is lengthening, and E is modulus of elasticity.

In the plastic range, a permanent deformation is caused by a shear stress that exceeds the elastic limit. This makes the atoms in row A_1 of Figure 2.15 change their state of equilibrium in relation to row A_2. The extent of the displacement is proportional to the extent of the shear stress τ [123]. Therefore, for elastic deformation, the effective shear stress is less than τ_f (the yield shear stress) and after removal of the stress, the atoms return to their original position. This can also be denoted as $m < a/2$ (where m is the atom displacement, and a is the atom spacing).

However, for plastic deformation, the yield shear stress limit is exceeded, meaning $m > a/2$ or $m > n$, moving the atoms in A_1 into the fields of new adjacent atoms in A_2, creating a new permanent state of equilibrium.

The limit which must be exceeded is also known as the plasticity criterion, and the associated resistance as the flow stress, k_{str} [123].

Flow stress k_{str}, in cold forming depends only on the extent of the deformation φ_p (principal strain) and the material. Flow stress curves can be represented by:

$$k_{str} = k_{str100\%} \cdot \varphi^n = c \cdot \varphi^n \tag{2.7}$$

where n is the strain hardening exponent, c is the equivalent to k_{str_1} when $\varphi = 1$ or when $\varphi = 100\%$, and k_{str_0} is the flow stress before forming for $\varphi = 0$.

The mean flow stress is also often necessary to calculate the force and work in an operation. It can be approximately found from:

$$k_{str_m} = \frac{k_{str_0} + k_{str_1}}{2} \tag{2.8}$$

where k_{str_m} is the mean flow stress, k_{str_0} is the mean flow stress for $\varphi = 0$, and k_{str_1} is the flow stress at the end of forming ($\varphi_p = \varphi_{max}$).

On the other hand, in hot forming above the recrystallisation temperature, k_{str} does not depend on the level of deformation φ. Instead, k_{str} depends on the temperature, material being deformed, and the strain rate $\dot{\varphi}$. This can be seen represented in Figure 2.16.

As the strain rate k_{str} rises when hot forging, the cohesion-reducing processes which occur due to recrystallisation no longer take place completely. To calculate the flow-stress for semi-hot forging (500 - 600°C) the following equation is used:

$$k_{str_{sh}} = c \cdot \varphi_p^n \cdot \dot{\varphi}^m \quad c = \frac{1400 - T}{3} \tag{2.9}$$

where $k_{str_{sh}}$ is the flow stress, T is the temperature, c is the empirical calculation coefficient, φ_p is the principal strain, n is the exponent of φ_p, $\dot{\varphi}$ is the strain rate, and m is the exponent of φ. Of course, when any of this cold or hot work is undertaken there is a counteracting force which is known as the "resistance to flow," which is constituted by both the flow stress and the friction resistances in the tool [123].

$$k_r = k_{str} + p_{fl} \tag{2.10}$$

where k_r is the deformation resistance, k_{str} is the flow stress, and p_{fl} is the resistance to flow. p_{fl} can be calculated for rotationally symmetric pieces with:

$$p_{fl} = \frac{1}{3}\mu \cdot k_{str}\frac{d_1}{h_1} \tag{2.11}$$

where k_{str_1} is the flow stress at the end of operation, d_0 is the diameter before forming, h_0 is the height before forming, μ is the coefficient of friction ($\mu = 0.15$), d_1 = diameter after forming, h_1 =

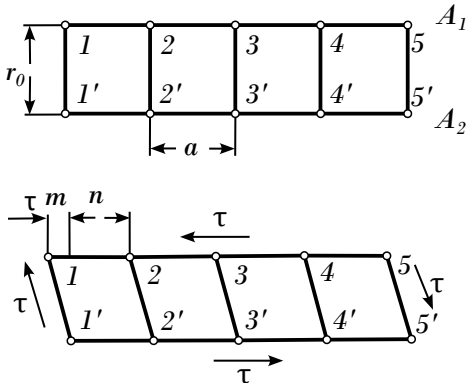

Figure 2.15: Ideal process of atom positional changes, adopted from Tschaetsch *et al.* [123].

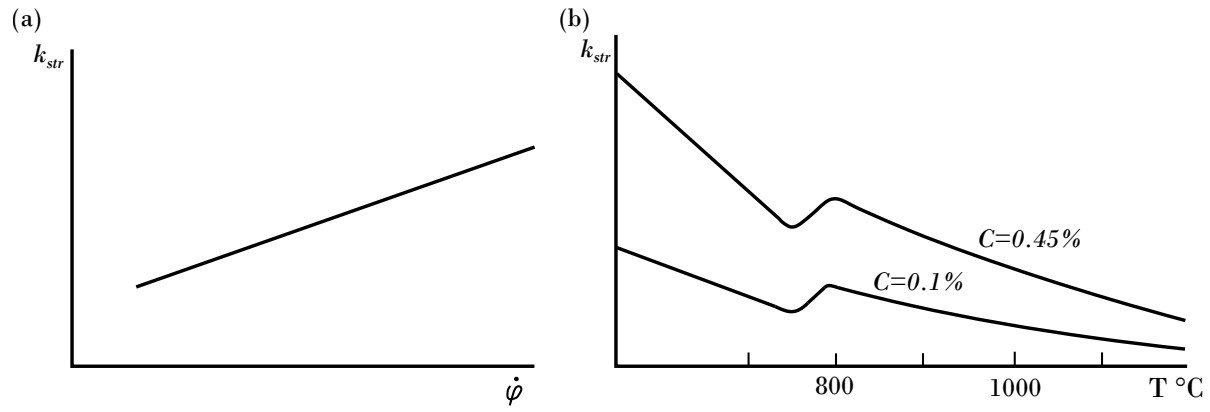

Figure 2.16: (a) $k_{str} = f(\dot{\varphi})$ in hot forming, (b) $k_{str} = f$ (temperature and material) in hot forming, where C denotes carbon content. With higher carbon steels, k_{str} decreases at a faster rate than lower carbon steels - adopted from Tschaetsch *et al.* [123].

height after forming. Following this, the deformation resistance k_r can be defined as:

$$k_r = k_{str_1}(\frac{1}{3}\mu \cdot \frac{d_1}{h_1}) \tag{2.12}$$

For asymmetric workpieces, which are far more complex to study mathematically, the deformation resistance is determined with assistance of the deformation efficiency, η_F:

$$k_r = \frac{k_{str_1}}{\eta_F} \tag{2.13}$$

Understanding of the degree of deformation and principal strain is crucial for engineers working on material processing and especially with metals and alloys. The calculation is generally made from the relation between an extremely small measurement difference, dx, and an existing measurement x. By integrating it into the limits x_0 to x_1 this produces:

$$\varphi_x = \int_{x_0}^{x_1} \frac{dx}{x} = ln\frac{x_1}{x_0} \tag{2.14}$$

for cases where it can be assumed that the volume of body to be deformed remains constant throughout deformation:

$$V = l_0 \cdot\ w_0 \cdot\ h_0\ = l_1 \cdot\ w_1 \cdot\ h_1 \tag{2.15}$$

Figure 2.17 shows the general measurements of a cuboid before and after forming, according to the highest change in dimension, a difference is made between:

$$\text{Degree of upsetting } \varphi_1 = ln\frac{h_1}{h_0} \tag{2.16}$$

$$\text{Degree of lateral flow } \varphi_2 = ln\frac{w_1}{w_0} \tag{2.17}$$

$$\text{Degree of elongation } \varphi_3 = ln\frac{l_1}{l_0} \tag{2.18}$$

If, however, the dominant value change is between the cross section or wall thickness, φ can also be calculated with:

$$\text{for change of wall thickness, } \varphi = ln\frac{s_1}{s_0} \tag{2.19}$$

$$\text{for change of cross section, } \varphi = ln\frac{A_1}{A_0} \tag{2.20}$$

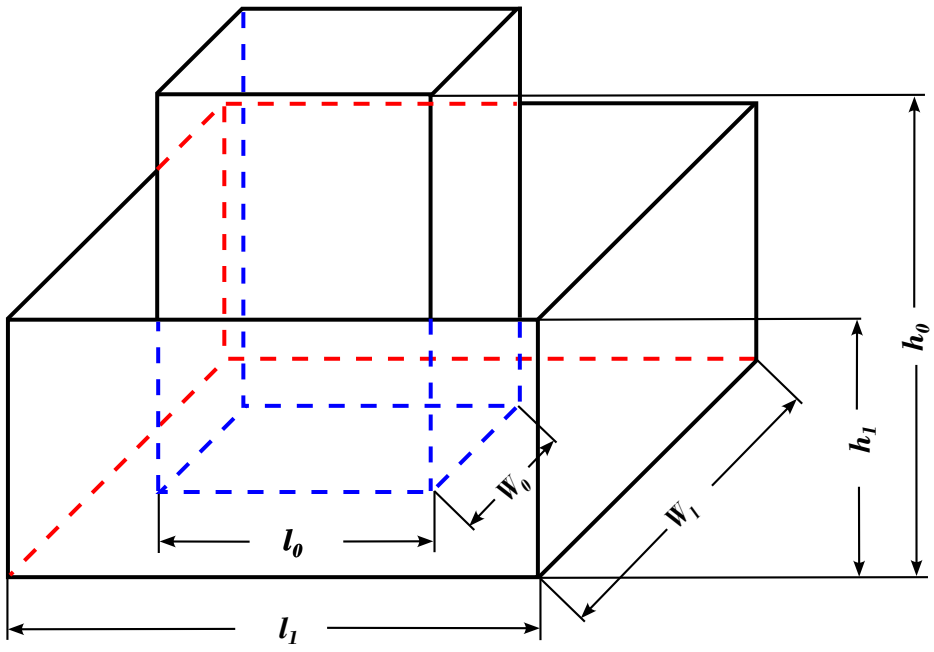

Figure 2.17: Cuboid before forming with the measurements h_0, w_0, l_0 and after forming with the measurements, h_1, w_1, l_1, adopted from Tschaetsch *et al.* [123].

Still assuming that the volume will be retained throughout deformation, it can be said that the sum of the changes in the three dimensions (l, w, h) is equal to 0. Any reduction in height will result in a gain in width and length:

$$\varphi_1 + \varphi_2 + \varphi_3 = 0 \tag{2.21}$$

Thus, each one of these three deformation dimensions is equal to the negative sum of the two others, for example:

$$\varphi_1 = -(\varphi_2 + \varphi_3). \tag{2.22}$$

The greatest deformation here is the principal strain φ_p.

The strain rate, $\dot{\varphi}$, is a crucial parameter for forging operations. The mean strain rate for a deformation over time t can be represented as:

$$\dot{\varphi_m} = \frac{\varphi}{t} \tag{2.23}$$

The strain rate can also be calculated from the die/ram velocity v over the initial height of the workpiece h_0:

$$\dot{\varphi} = \frac{v}{h_0} \tag{2.24}$$

Throughout forging there are numerous and varied techniques for metal forming. These techniques and their applications are discussed. The first of these is the well-documented and very widely utilised closed-die forging.

Closed-die Forging

Closed-die, or impression-die, forging is a hot bulk precision forming process. It is a pressure forming process where two or more shaped dies compress material, which adopts the shape of the die cavities. Impression-die forging is known as a precision forming process as it often requires specially designed tooling and dies to be manufactured for any given part geometry.

Closed-die forging, covering a range of materials, is well researched and documented in the liter-

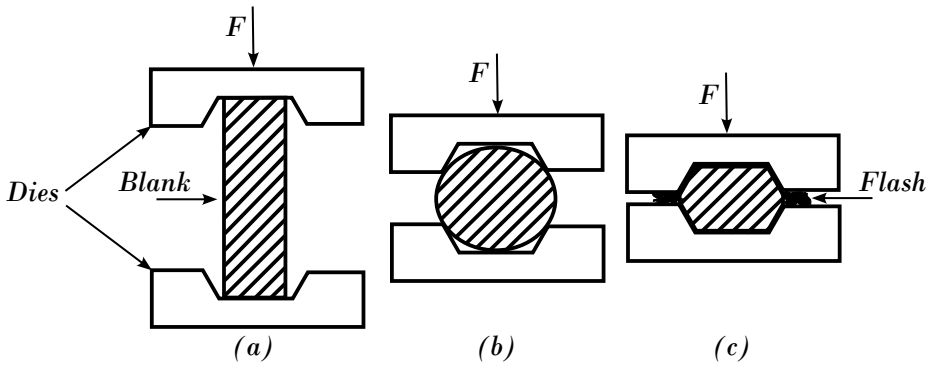

Figure 2.18: Impression-die forging process, (a) Forging start, (b) Forging in process, (c) Forging finish, adapted from Chandrasekaran *et al.* [124].

ature. In Skubisz *et al.*'s work [125], the hot and warm closed-die forging of a range of magnesium wrought alloys was investigated. It was found that through appropriate design of die geometry, elimination of shearing zones, as well as proper selection of workpiece proportions results in the possibility of a reduction of the forging temperature to the warm-working range.

Billet reheating can have a major effect on the extent of recrystallisation. Gupta *et al.* [126] studied the effect of variants of thermomechanical working and annealing on Ti-6Al-4V closed die forgings. Full recrystallisation was found in the first route which allowed for both dynamic and static recrystallisation due to multiple forging and reheating cycles. Whereas in the second route only partial recrystallisation was realised due to only limited dynamic recrystallisation in less reheating-forging cycles.

The weight of the component is a determining factor for the homogeneity of deformation, deformation energy, and die life. In Kaur *et al.*'s work [127], closed-die forging input parameter optimisations are investigated as these inputs define the metal flow and forming within the cavity. A uniform rate of change of effective strain during deformation is optimal. It was also concluded that the size of the cavity was the main factor of the uniformity of the flow. With larger cavities not providing as uniform a flow as smaller cavities, which are generally filled at a steadier rate.

Axial closed-die rolling is another closed-die forming technique that is economical due to its high precision and flexibility [128]. It brings together the advantages of reduced forces and more precise parts, which are seen in incremental forming, with closed-die forging tolerances. This forming process uses less input material and offers reduced machining allowances, meaning it is more economically favourable to conventional closed-die processes, and is typically used to form disk-shaped parts (*e.g.,* sprocket wheels, bearing rings *etc*). During Zheng *et al.*'s work on the microstructure evolution of Ti-6Al-4V during axial closed-die rolling, the gradient distribution for strain and temperature observed was similar across the alloy throughout deformation, except for the strain distribution at the centre axis where it was seen to be linear [129]. It was also shown from this study that the effect of the irregular plastic flow and multidirectional plastic deformation from this technique results in efficient α-spheroidisation [129].

Closed-die forging, only covered briefly here, remains widely used and widely researched throughout industry. However, for this study the primary forging route that is of interest is open-die forging. The advantages and disadvantages between these two forging techniques has been highlighted in Table 2.3.

Open-die Forging

Open-die forging is typically a hot forming process that uses a range of dies in presses. Die geometries range standard flat, to V-shaped, concave, or convex [130]. This forming method is used to form an effectively limitless range of component sizes, limited only to press size. The workpiece is heated to reduce the force required to work the metal by improving the plastic flow characteristics.

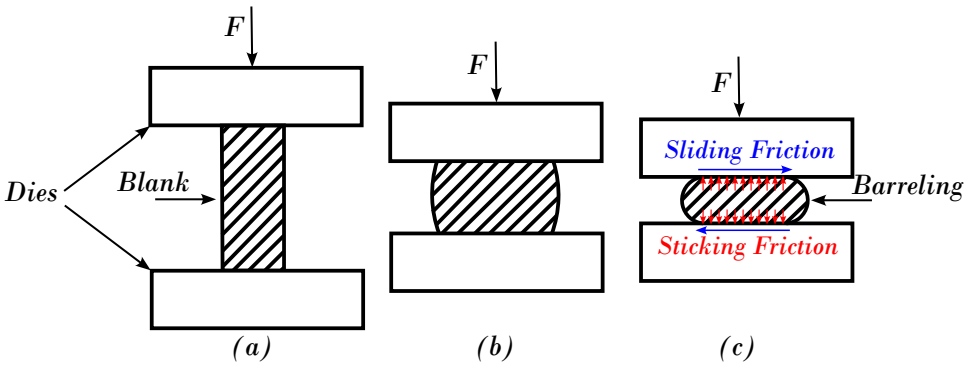

Figure 2.19: Open-die forging process, (a) Forging start, (b) Forging in process, (c) Forging finish, highlighting frictional forces and barrelling effect, adapted from Chandrasekaran *et al.* [124].

Then the workpiece is systematically deformed and manipulated throughout a series of strokes or bites from the upper die while being supported on the lower die [130].

Open-die forging allows the freedom of the workpiece to move in one or two directions. Typically the workpiece is compressed along the axial direction (direction of movement of the upper die) with no lateral constraint [130]. The most common open-die forging operations are listed: drawing; piercing; punching; saddening and hot trepanning; hollow forging; closing in; ring forging; upsetting; and cogging. The latter of which is the key focus of this work. As well as these individual procedures, they are also often combined to produce complex geometries in a wide range of sizes. In general, open-die forging is specially suited for very large, complex forgings, usually beyond the capabilities of closed-die forging. Table 2.3 shows the advantage and disadvantage comparison between open-die forging and closed-die forging. The basic principle of open-die forging can be seen in Figure 2.19.

During open-die forging, defects such as cavities, porosities, and segregation induced from casting are removed by guaranteeing a sufficient yet homogenous strain inside the workpiece [131]. This leads to a defect-free microstructure and, thus, to the key industrial goal of reaching a homogenous distribution of mechanical properties for the alloy. Due to each individual stroke in open-die forging typically introducing an inhomogenous distribution of the equivalent strain into the workpiece, reaching the homogeneous distribution becomes the key challenge for this type of thermomechanical

Table 2.3: Advantage and disadvantage comparison of open-die and closed-die forging

Open-die forging	Closed-die forging
Advantages	
Better fatigue resistance and improved microstructure	Internal grain structure formation increases strength
Continous grain flow and finer grain size	Economic for product reproducibility
Increased strength and longer part life	No material limitation
Less material waste	Better surface finish
Reduced chance of voids	Less or no machining required for finishing
Valuable cost savings	Tighter tolerances and net shapes can be achieved
Disadvantages	
Close tolerances more difficult for high precision parts	High cost of die production
Machining often required to finish	Introduces a dangerous working environment

processing. The collective effect of individual strokes from an incremental technique such as this can ultimately cause an inhomogenous distribution of strain and therefore microstructure. To combat this phenomenon and achieve a balanced structure, specific pass recipes are calculated through 3D modelling and numerical simulations, which are carried out prior to the forging process [132].

Since open-die forging processes are typically carried out with large ingots of metals and alloys, in small batches or unique pieces, developing recipes for materials takes a great deal of time and experience from engineers and metallurgists [131]. Similarly, even repeat manufactured parts can have small deviations in homogenity due to microstructural evolution, pre-processing homogenities, and many varied recrystallisation phenomena all playing a role. Thus, open-die-forging is a widely studied subject throughout industry and academia over a variety of materials [132, 133].

One of the earliest publications on computer simulation of forging was from Biswas *et al.* in 1972 [134], where a simulation was used to estimate load and energy for axisymmetric closed-die forging. A few years later, Appleton *et al.* completed an experimental study using an industrial robot as a manipulator for open-die forging [135]. In 1993, Aksakal *et al.* explored the introduction of automation into batch open-die forging [136]. In Kim *et al.*'s work in 2002, this technology evolved into forging pass algorithms to manage and schedule forming operations, and manage strokes delivered to the material through neural networks and data acquisition. Recent studies are still exploring this area and level of control [137].

It is crucial to highlight and understand open-die forging technology studies, material studies, and simulation studies that have been carried out in the literature. However as this is a key focus of this work, the literature of this will be further expanded upon in section 2.3 when reviewing ingot to billet conversion and the state of the art of cogging investigations.

Rotary Forging

Rotary forging, also known as orbital forging, is a dual-die process that deforms one small section of the workpiece at a time continuously. [138] It is often compared quite closely to other open-die forging processes. A representation of the rotary forging process is presented in Figure 2.20, displaying the key principles of the rotary forge operation. The key difference with rotary forging is that the workpiece is only partially in contact with the conical tool, meaning that the forging loads necessary for forming are relatively low [139]. A representation of the difference in forces and torque between conventional upsetting and cold rotary forging can be seen in Figure 2.21. Both the rotational movement and lateral movement of the upper die gradually deforms the part until a final geometry is formed [140]. This technique can achieve near net shape geometries in one operation, leading to a reduction of both material and tooling costs [141, 142].

Semiatin [138], Han and Hua [143], and Nowak *et al.* [142] both summarised the advantages of rotary forging over more conventional forging techniques as:

1. High level of accuracy in a single operation.
2. Precise geometrical tolerances.
3. Better surface finish.
4. Reduced friction between workpiece and dies.
5. Reduced tool wear.
6. Faster production rate.
7. Reduced energy consumption.

In modern manufacturing, axisymmetric components, such as disks, rings, and gears, are increasingly being fabricated using the rotary forging technique. [144–147] Rotary forging is currently

a well-studied technique and discussed topic in the industry due to the great commercial benefits. In Mandal *et al.*'s work [148] on the cold rotary forging of Inconel 718 the microstructure and mechanical propety development was investigated. Through characterisation of the rotary forged samples, severe deformation was observed in the 90 degree bend zone, which resulted in the formation of refined but elongated grains. As highlighted by Mandal, this grain behaviour is reflected by the refinement theory seen in the first pass of an Equal Channel Angular Pressing (ECAP) process. ECAP or Incremental ECAP (I-ECAP) are processes that press material billet into most commonly a 90 degree bend channel, from which the orientation of the microstructure is refined through each pass [149]. Through Mandal *et al.*'s 2019 study it is also confirmed that Inconel 718 can be rotary forged into a near net-shape axisymmetric component, meaning from the commercial perspective rotary forging is a far more desirable route for material, time, and cost effectiveness. This is highly interesting, as in Han and Hua's work [143] in 2009, 10 years prior, it was concluded that cold rotary forging was not an axisymmetric process, but was, in fact, an asymmetrical deformation process.

Plancak *et al.* has completed an extensive general description of rotary forging technology [150]. Standring *et al.* investigated the plastic deformation introduced during the indentation stage of rotary forging [151], who then did further analysis on the importance of the nutation angle [152] (seen in Figure 2.20), from which the characteristic features of this process was studied [144]. Jin *et al.* [153] studied preform design for the rotary forging of a flange gear. Other papers focus on researching rotary forging, like other forging technologies, through process modelling and numerical analysis. For example, Liu *et al.* [154] completed numerical analysis of the flange formation in a cylinder. Similarly, the effect of the cylindrical workpiece on rotary forging was analysed by Hua *et al.* [140]. The same authors later further studied the behaviours of the plastic deformation with different imposed contact patterns [155].

This phenomenon is discussed by Hua *et al.* later where the authors describe the "*mushroom*" effect in deformed cylindrical workpieces being a key characteristic of rotary forging deformation, where an inhomogenous strain distribution is developed across the flange [140]. This idea is discussed in Pérez's work, where the rotary forged flanged samples present an inverted "*mushroom shape*," with asymmetrical bulging in the early stage of the forging operations, whereby this changes at the end of the operation to the same "*mushroom shape*," but with an axisymmetrical bulge [156]. Pérez describes that initially due the contact area at the bottom die being smaller than the upper die, higher axial pressure metal near the bottom die is observed. Thus, less force is required to achieve plastic deformation. This explains why initially deformation is localised close to the bottom tool

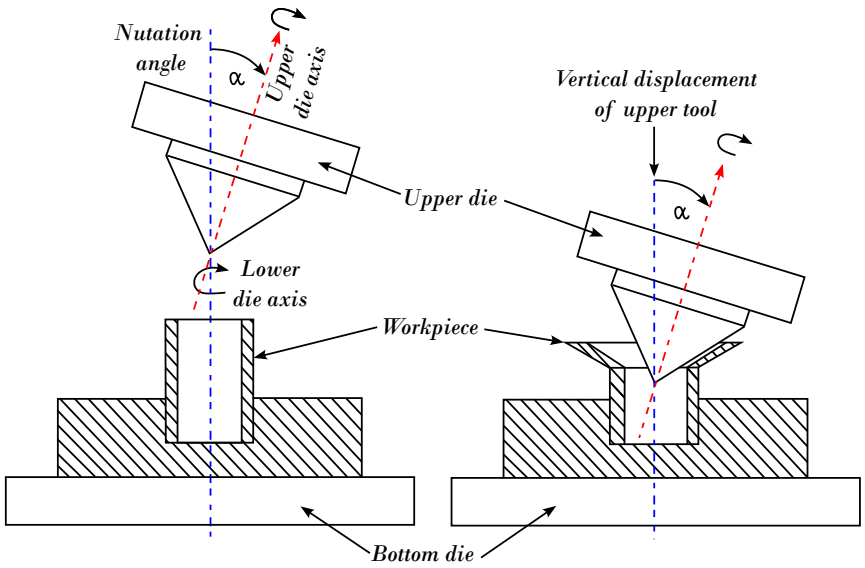

Figure 2.20: Schematic representation of rotary forging process. Adapted from Pérez *et al.* [139].

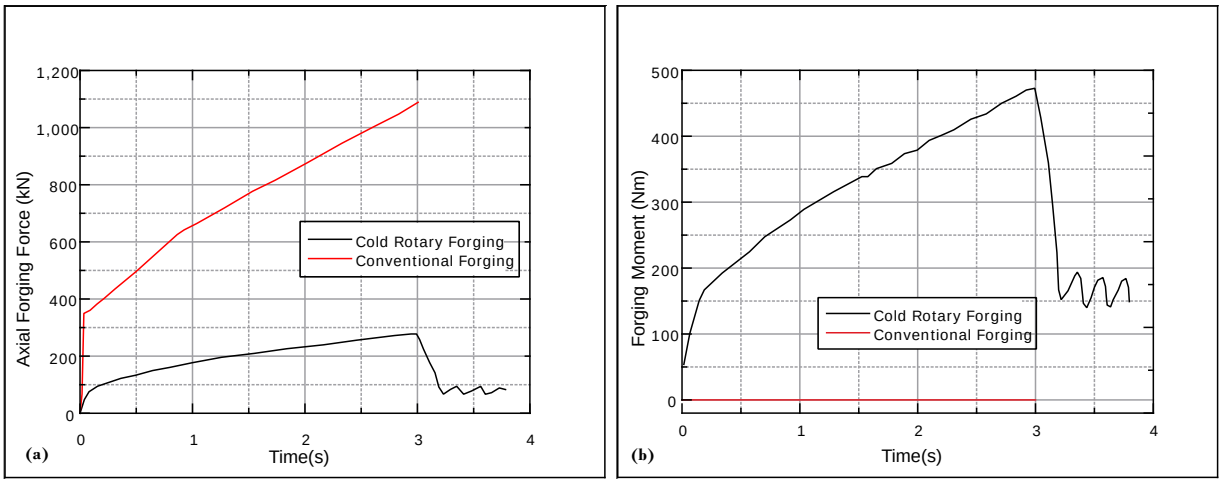

Figure 2.21: Graphs comparing conventional and cold rotary forging. (a) Comparison of axial forging force between conventional forging and cold rotary forging, (b) Comparison of forging moment between conventional forging and cold rotary forging. Adapted from Han and Hua [143].

but also why this inverted "*mushroom shape*" is being formed.

Semiatin [138] also highlights that rotary forging can often be confused with the term radial forging, which is more alike to the cogging operation, however, radial forging can also be known as swaging.

Swaging

Rotary swaging, or radial forging, is a near net shape bulk forming process, most commonly carried out cold, but can also be done at elevated temperature [158,159]. The diameter of the workpiece is reduced incrementally by oscillating movement of the tools [157]. This reduction is not dissimilar to open-die forging operations such as cogging. This reduction in diameter of rods results in improved tensile strength as well as undisturbed fibre flow, and allows for adjustable wall thicknesses to be manufactured in hollow shafts to optimise material use [160].

The principle set-up is presented in Figure 2.22. The workpiece is inserted axially into the swaging head with the feeding force F_f. Due to the radial forming force F_{RI} in the reduction zone (I) and the tool angle α, an axial reaction force F_A counteracts F_f. F_A increases as the there is a decrease in friction. Thus, the conventional tooling used is coated with a thermally sprayed layer of tungsten carbide at the reduction zone [157], which increases the effective friction due to

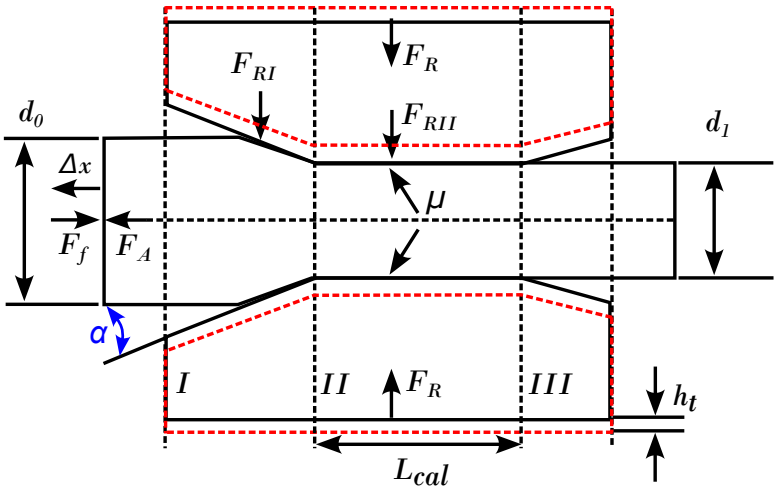

Figure 2.22: Principle setup of infeed rotary swaging process. Adapted from Herrmann *et al.* [157].

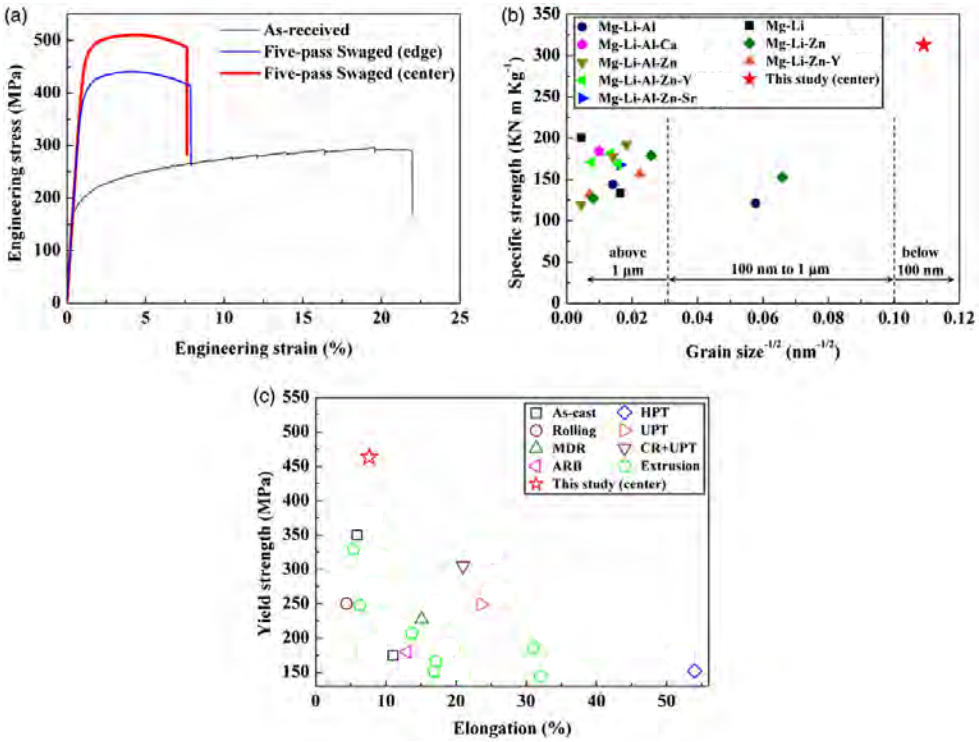

Figure 2.23: **(a)**Room temperature tensile stress-strain curves of the as received and five-pass swaged samples. **(b)** Comparison of specific strength with various MgLi alloys in the published literature [163–176]. **(c)** Comparison of yield strength with various high strength MgLi alloys in the published literature. [166, 168–171, 175–182] MDR: multidirection rolling; ARB: accumulative roll bonding; UPT: ultrahigh pressure treatment; and CR & UPT: cryorolling + ultrahigh pressure treatment. Captured from Chen *et al.* [162].

these coatings having high roughness. The four oscillating tools are placed concentrically around the workpiece. Through each tool stroke h_T at a stroke frequency f_{St} the incremental reduction of the workpiece diameter d_0 begins. Rotary swaging becomes unstable if F_A exceeds F_f. In the calibration zone (II) the final diameter d_1 is reached. Due to the driving feed having limited stiffness, it undergoes a back motion Δx at each stroke [160]. Once completed, the final workpiece is expelled through the exit zone (III).

During the swaging operation, intense lubrication is necessary to reduce the coefficient of friction μ. Without the heavy use of a lubricant the softer workpiece is prone to sticking to the tooling which may cause galling phenomena after a number of cycles [161]. Degreasing agents used before subsequent processing are solvent-based and therefore usually toxic, so there has be great interest, ecologically and economically, for creating a lubricant-free swaging process. The results from Hasselbruch *et al.*'s study proved that swapping to an unlubricated swaging design has great potential of improving the CO_2 balance, and could even shorten subsequent processing.

Near-net shape methodologies, including rotary swaging, are also a widely researched topic in the literature. For example, in Chen *et al.*'s experimental work [162], studied the results of the central and edge regions of the alloy after rotary swaging at room temperature. It was seen that after five-pass swaging, the central region had the best improvement in microhardness 68 → 119 HV (75% increase), yield strength 179 → 463 MPa (159% increase), and ultimate tensile strength 296 → 511 MPa (73% increase) over the original as-received material. Improvement was also found in the edge of the alloy after five-pass swaging, however with a lower microhardness 68 → 103 HV (51% increase), yield strength 179 → 380 MPa (112% increase), and ultimate tensile strength 296 →441 MPa (49% increase) than the centre of the alloy. Significant grain refinement can be achieved in the central region of the alloy bar. An excellent representation of the properties changes of the material, alongside other materials in the literature is highlighted by Wan *et al.* and can be seen in Figure 2.23.

In Toenjes *et al.*'s work [183], a two-stage eccentric rotary swaging process was studied using

eccentric flat shaped dies. The focus was the influence of changing the feed direction, and the addition of a heat treatment between two consecutive forming steps. It was discovered that the change of feed direction presented a more homogenous structure, with an increased hardness. It was also seen that this increase in hardness was only expanded with the introduction of the intermediate stage heat treatment between subsequent forming processes. [183] Cracks introduced by the first forming step are opened and deepend by the typical cold-form swaging heat treatment, which leads to further poor interactions in the following forming step, this route is undesired. Toenjes concluded that this novel method provides an opportunity to produce rods with a fine grain structure homogeneously across the transverse cross-section [183].

There are also some non-conventional forming methods that have not been discussed as they fall outside the strict scope of forging, nevertheless are worthy of mention, such as non-conventional extrusion [184], thermo-forming and mould injection [185], hot-isostatic pressing (HIP) with additive manufacturing of powder metals [186, 187] and flow forming [188]. Before discussing the cogging process, which is of key interest in this work, it is also important to understand and discuss the mechanisms and phenomena that occur throughout the ingot-to-billet conversion process.

2.2 Recovery, Recrystallisation, and Grain Growth

2.2.1 Introduction

Understanding of the mechanics and kinetics that take place within different advanced alloys is of fundamental importance when designing equipment for the processing of such alloys. This understanding goes beyond the deformation in forging into the microstructural changes undergone by the material throughout thermomechanical forming. Of course, there is a great breadth of knowledge on the various forms of recrystallisation, grain growth, and related phenomena for all materials and is continually a broadly studied field in the literature. A key goal of this section is to highlight and demonstrate knowledge of these underlying principles.

This section details the key aspects of recovery, recrystallisation, and grain growth with a focus on both single and dual-phase alloys that will be used in this study. These three phenomena are described as "core elements" of thermomechanical processing by Humphreys and Hatherly [189]. Additionally, it will demonstrate the methods for modelling the phenomena and discuss studies from the literature on recrystallisation.

2.2.2 Background

Early discoveries of the parameters affecting recrystallisation are as follows:

1. **Kinetics** - Ewing and Rosenhain [190] first wrote of the relationship between the recrystallisation temperature to the melting temperature, and Humphrey showed that the rate of recrystallisation increased with increasing annealing temperature.

2. **Strain** - The relationship between prior strain and grain size was first reported by Charpy in 1910, and it was found that there was a critical strain for recrystallisation in 1912 by Sauveur, both effects were validated by Carpenter and Elam at the end of the same decade [189].

3. **Grain Growth** - Jeffries in 1916 wrote during his study on the control of microstructure during annealing that abnormal grain growth in thoriated tungsten was promoted in specimens where normal grain growth had been constrained.

As highlighted by Humphreys and Hatherly [189], further understanding of recrystallisation was slowed until a greater understanding of the deformed state and dislocation theory was developed.

For further discussion into these phenomena, it is crucial to highlight the importance of the basic principles of free energy and compare the energy changes which occur during the various annealing processes. It is key to understand that the defect content of a material drives the three processes of recovery, recrystallisation, and grain growth [189]. If we consider a small part of the microstructure of a single-phase crystalline material as seen in Figure 2.24, which consists of two regions A and B separated by a boundary and position X. If the separate regions contain different

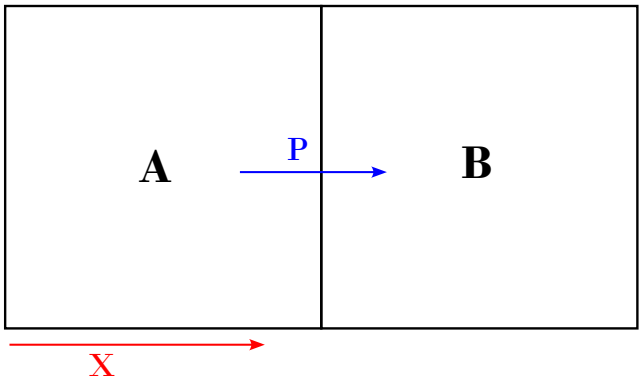

Figure 2.24: The pressure on a boundary. Adapted from Humphreys and Hatherly [189]

defect concentrations and that the free energies of these regions per unit volume are G^A and G^B respectively.

The boundary will move if the Gibbs free energy of the system is lowered, and if an area a of the boundary moves a distance dx, then the change in free energy of the system is:

$$dG = dx \left(G^A - G^B\right) a \tag{2.25}$$

The force, F, on the boundary is given by dG/dx, and the pressure, P, on the boundary, is given by F/a, so:

$$P = -\frac{1}{a}\frac{dG}{dx} = G^A - G^B = \Delta G \tag{2.26}$$

If ΔG in equation 2.26 is given in units of Jm^{-3}, then Nm^{-2} are the units for the pressure on the boundary, P. A summary of the different driving forces for each phenomena stage is highlighted also in Humphreys and Hatherly's book [189].

The first of these being that for recrystallisation the driving force comes from the elimination of the dislocations introduced during deformation. The stored energy due to a dislocation number density ρ is $0.5\rho Gb^2$, where b is the Burgers vector length of the dislocations and G is the shear modulus.

The second being for both recovery and grain growth following recrystallisation being governed by the elimination of boundary area. If the boundary energy is γ per unit area and the boundaries form a 3D network of spacing D, then the driving pressure for growth is approximately given as $3\gamma/D$.

Overview of the Deformed State

Throughout deformation of a metallic material the majority of the work is expended as heat, with only a small ~1% of the energy remains stored, also known as work, in the material [189]. Most commonly, almost all the energy in worked material is derived from the accumulation of dislocations. Each stage of the annealing process can be seen in Figure 2.25. Each stage involves some loss of the work in the material with a relative change in microstructure. The release of work provides

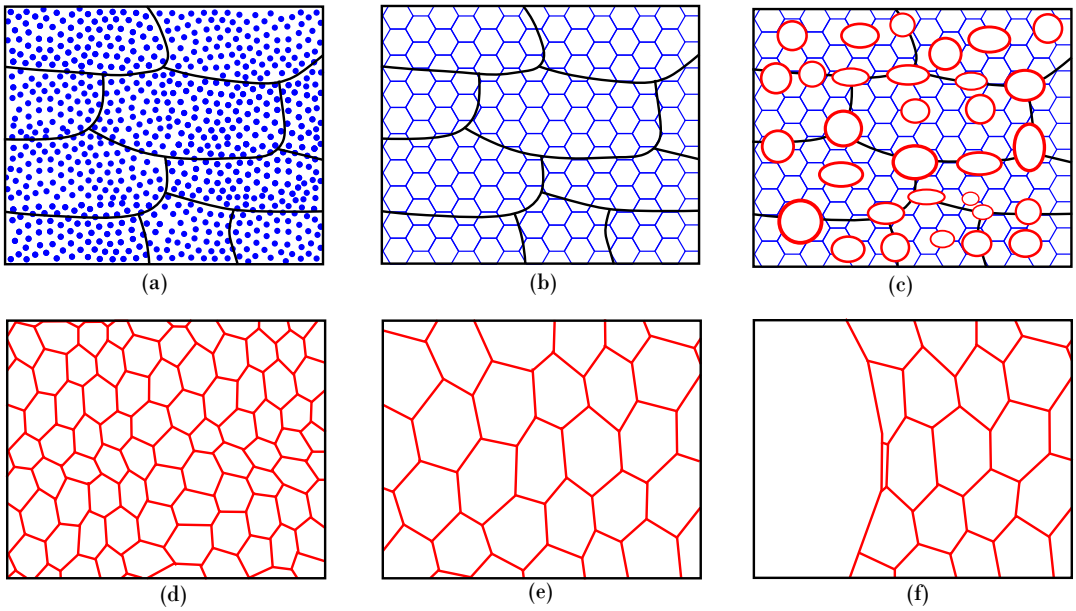

Figure 2.25: Schematic diagram of the main annealing processes: (a) Deformed state, (b) Recovered (metastable state), (c) Partially recrystallised, (d) Fully recrystallised, (e) Grain growth, and (f) Abnormal grain growth. Black lines represent original grain size in the deformed material, blue dots/lines represent dislocations/dislocation structure, and red lines represent different stages of recrystallised (dislocation-free) grains. Adapted from Humphreys and Hatherly [189].

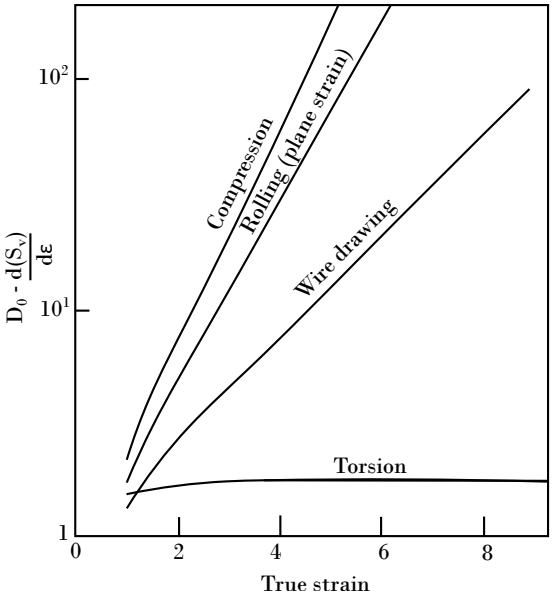

Figure 2.26: Rate of growth of grain boundary per unit volume (S_v) for different modes of deformation assuming an initial cubic grain size D_0. Adapted from Humphreys and Hatherly [189].

the input force for recovery and recrystallisation, but it is the nature of the microstructure that ultimately controls the development and growth of the nuclei that will become recrystallised grains, as well as their orientation evolution. Thus, microstructural analysis is a widely researched topic, as A.H. Cottrell said, "Few problems of crystal plasticity have proved more challenging than work hardening. It is a spectacular effect, for example enabling the yield strength of pure copper and aluminium crystals to be raised a hundredfold." [189].

The key difference between an annealed and deformed material is the dislocation content and arrangement. Due to this, discussion of deformation microstructure during recovery and recrystallisation in the literature is based on the density, distribution, and arrangement of dislocations in the material [189]. The dislocation density increase is due to the continued trapping of new mobile dislocations from the existing dislocations and their incorporation into the various microstructural features. During deformation, the dislocations (of Burgers vector $\boldsymbol{b}$) move an average distance L, and the dislocation density (ρ) is related to the true strain (ε) by:

$$\varepsilon = \rho b L \tag{2.27}$$

Also, throughout the deformation of a polycrystalline material, the grains change their shape in relation to the macroscopic shape change. Consequently, the grain boundary area is increased [189].

The rate of increase of the grain boundary area per unit volume depends on how the material is deformed, *e.g.,* torsion, compression, drawn, *etc.* The grain shape also follows the mode of deformation, for example, rolled sheet grains become laths, drawn wire become needles, and compressed material becomes disc shaped. The calculated increase in boundary area as a function of strain is shown in Figure 2.26. Boundary area increase is a crucial factor in promoting continuous recrystallisation after large strain deformation [189]. A second result from the increase in the number of dislocations is that an internal structure is generated within the grains. The sum of the energy of all the dislocations and new interfaces represents the work from deformation, except for any vacancies and interstitials that remain. Furthermore, during the deformation the orientations of single crystals and of the individual grains of a polycrystalline metal change relative to the direction(s) of the applied stress(es) [189]. These rotational changes are correspondent to the crystallography of the material and the deformation directions tend to an optimal alignment, or texture, which increases in commonality as deformation continues.

Understanding of dislocations and dislocation movement within crystalline structures is fundamental to discuss. Screw and edge are the two key dislocation types. An edge dislocation occurs

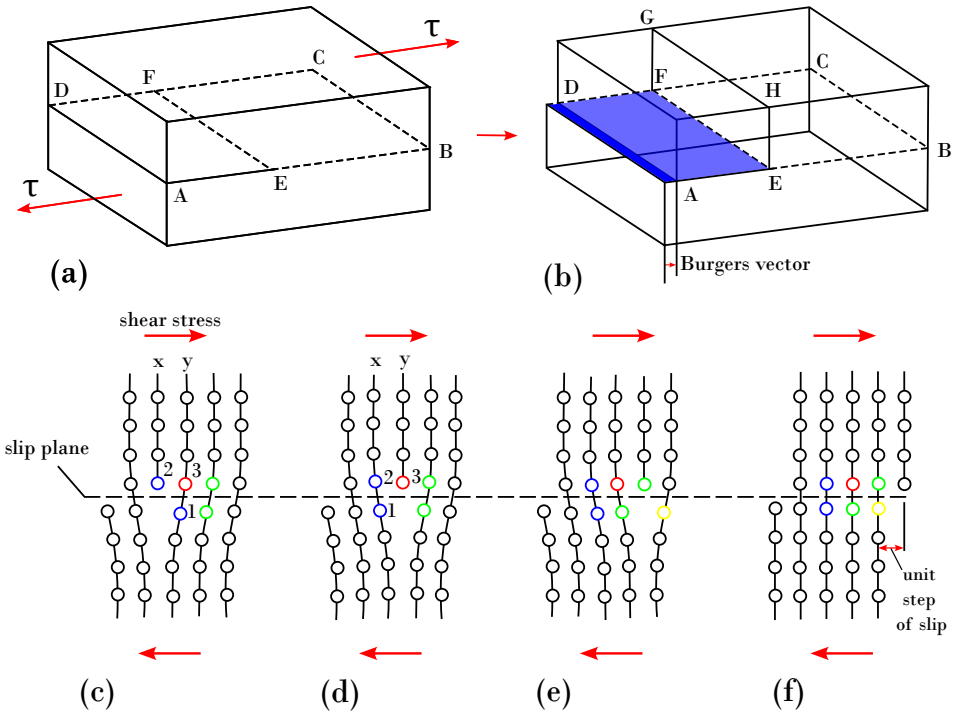

Figure 2.27: (a) & (b) - Formation of a pure edge dislocation FE. (c), (d), (e), and (f) - Formation of an edge dislocation. Adapted from Hull and Bacon [191]

when there is a localised lattice distortion along the end of an extra half-plane of atoms, which defines its dislocation line, seen in Figure 2.27. Whereas a screw dislocation results from shear distortion, where it's dislocation line passes through the centre of a spiral, atomic plane ramp, seen in Figure 2.28. Most dislocations in crystalline materials have both screw and edge components, which are known as mixed dislocations [192]. Plastic deformation through dislocation motion is known as slip, and the crystallographic plane along which the dislocation line traverses is known as the slip plane.

On top of stored energy in a deformed metal, spatial distribution also plays a crucial role. Locally, work inhomogeneity in the material will affect the nucleation of recrystallisation, and larger-scale heterogeneity will impact the growth of the new grains. To be able to predict the annealing behaviour, it is important to determine the distribution of defects resulting from deformation [189].

Whenever a materials dislocation content is high and cannot be easily measured experimentally through transmission electron microscopy (TEM), it can be estimated through the mechanical properties of the material. As an example, a relationship between dislocation density and flow stress:

$$\sigma = c_1 G b \rho^{1/2} \tag{2.28}$$

where c_1 is a constant of the order of 0.5 ad G is the shear modulus, has been shown to work for a

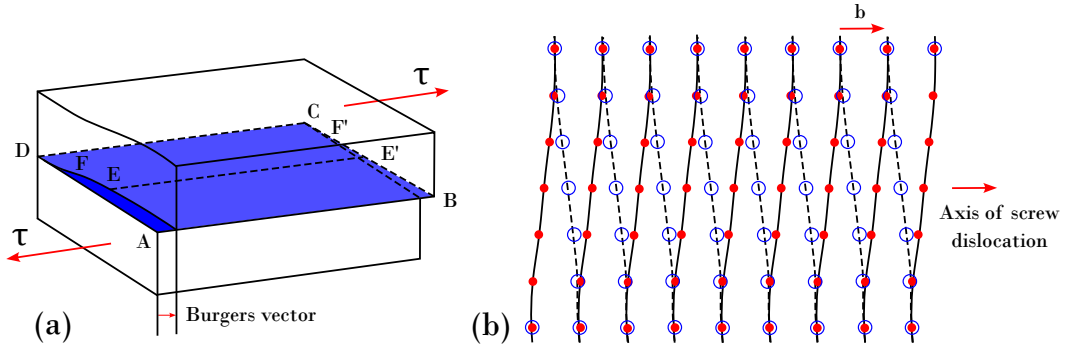

Figure 2.28: (a) Formation and movement of a pure screw dislocation AA' to BB' by slip. Adapted from Hull and Bacon [191].

variety of materials [189].

If the energy of the dislocation core is ignored and if isotropic elasticity is assumed, the energy (E_{dis}) per unit length of dislocation line is given approximately by:

$$E_{dis} = \frac{Gb^2 f(v)}{4\pi} ln\left(\frac{R}{R_0}\right) \tag{2.29}$$

where R is the upper cut-off radius (typically taken to be the separation of dislocations, $\rho^{-1/2}$), R_0 is the inner cut-off radius (usually taken as between b and 5b), $f(v)$ is a function of Poisson's ratio (v), which, for an average population of edge and screw dislocations is ~(1 - v/2)/(1 - v).

For the dislocation density ρ, the stored energy can be expressed as:

$$E_D = \rho E_{dis} \tag{2.30}$$

this expression is viable when the dislocations are particularly arranged that the stress fields of other dislocations are screened. Dislocations in worked material are often quite uneven, with pile-ups and intricate tangles [189]. The environment of the dislocation influences the dislocation energy, *e.g.,* highest in a pile-up and lowest in a cell or subgrain wall. When only approximating the dislocation energy, equation 2.29 can be simplified to:

$$E_{dis} = c_2 Gb^2 \tag{2.31}$$

where c_2 is a constant of ~0.5. The stored energy can then be expressed as:

$$E_D = c_2 \rho Gb^2 \tag{2.32}$$

If the deformed microstructure consists of well-defined, equiaxed subgrains, the work in the material may be estimated from the diameter of the subgrains (D) and the specific energy (γ_s) of the low angle grain boundaries that constitute the subgrain walls. The area of low angle boundary per unit volume is ~3/D and hence the approximate energy per unit volume (E_D) is given by:

$$E_D \approx \frac{3\gamma_s}{D} \approx \frac{\alpha\gamma_S}{R} \tag{2.33}$$

where α is a constant of ~1.5.

The boundary energy (γ_s) is directly related to the misorientation angle (θ) across the boundary, which therefore means equation 2.33 may be given in terms of D and θ, where both can be measured experimentally:

$$E_D = \frac{3\gamma_s\theta}{D\theta_m}\left(1 - ln\frac{\theta}{\theta_m}\right) \approx \frac{K\theta}{D} \tag{2.34}$$

where K is a constant and θ_m is defined by:

$$\gamma = \gamma_m \frac{\theta}{\theta_m}\left(1 - ln\frac{\theta}{\theta_m}\right) \tag{2.35}$$

equation 2.34 can be used for boundaries in which the dislocation spacing, and content are close to their equilibrium values. If the dislocation boundaries were less organised, which is more common in deformed materials, it is unlikely to be an accurate calculation. Therefore, it is also important to consider the cell/subgrain size and misorientation. Both of which, may be dependent on the grain orientation. Thus, the work in the material varies depending on the different texture components of the material. These texture components also play an important role in recrystallisation behaviour of the material [189].

Before discussing the more imperative aspects of recovery, recrystallisation, and regrowth for this project, it is also important to discuss the phenomena involved in crystal plasticity.

Crystal Plasticity

Slip and twinning are the two most basic mechanisms of plastic deformation in cubic metals, and the value of the stacking fault energy (γ_{SFE}) is a key material parameter that determines which of the two mechnanisms dominates [189]. Deformation twinning may occur in metals with a low γ_{SFE}, as cross-slip is more difficult meaning that it is, in turn, more difficult to plastically deform by slip alone [189].

The two basic types of dislocation movement are glide (otherwise known as conservative motion), and climb (non-conservative motion) [191]. Glide occurs when the dislocation moves in the surface/plane which contains both its line and Burgers vector. Climb occurs when the dislocation moves out of the glide surface, and thus normal to the Burgers vector. Slip occurs when many dislocations undergo glide, which is the most common deformation mode. It can be depicted as successive displacement of one plane of atoms over another on what is known as slip planes. Further deformation occurs either by the activation of new slip planes or by more movement on existing slip planes [191].

Tables 2.4 & 2.5 show the planes and directions of both processes which are a function of the crystal structure. Slip is more likely to take place on the most densely packed planes and directions. With these factors combined, the slip system $\{111\}\langle 110\rangle$ is defined for FCC metals. The literature demonstrates that other systems can operate at high temperatures, usually in metals with high γ_{SFE} values, and typically take the form to slip on $\{100\}$, $\{110\}$, $\{112\}$, and $\{122\}$ planes [193].

In BCC structures, slip occurs along the close-packed $\langle 111\rangle$ directions, but the slip plane may be any of the planes $\{110\}$, $\{112\}$, or $\{123\}$; each of these planes contains the close-packed slip direction, $\langle 111\rangle$. The temperature of deformation influences the plane in which slip occurs in BCC materials. At temperatures under $T_m/4$, $\{112\}$ slip occurs; between $T_m/4$ and $T_m/2$, $\{110\}$ is preferred and at temperatures above $T_m/2$, $\{123\}$ is observed.

A characteristic shear stress is required for slip [191]. When considering the crystal illustrated in Figure 2.29 which is being deformed through tension by force F along the cylindrical axis. If the cross sectional area is A, then the tensile stress parallel to F can be expressed as $\sigma = F/A$. The force has a component $Fcos\lambda$ in the slip direction, where λ is the angle between F and the slip direction. This force acts across the slip surface, area $A/cos\theta$, where θ is the angle between F and the normal to the slip plane. So, the shear stress τ, resolved on the slip plane in the slip direction can be expressed as:

$$\tau = \frac{F}{A} cos\theta cos\lambda \tag{2.36}$$

If the critical force required for slip to occur is known as F_c, the relative value of shear stress τ_c

Table 2.4: Crystallography of slip in cubic metals. Adapted from Humphreys and Hatherly [189]

Structure	Slip system	
	Plane	Direction
FCC	$\{111\}$	$\langle 110\rangle$
BCC	$\{110\}$	$\langle 111\rangle$
	$\{112\}$	$\langle 111\rangle$
	$\{123\}$	$\langle 111\rangle$

Table 2.5: Crystallography of twinning in cubic metals. Adapted from Humphreys and Hatherly [189]

Structure	Twinning Shear	Twinning Plane	Twinning Direction
FCC	0.707	$\{111\}$	$\langle 112\rangle$
BCC	0.707	$\{112\}$	$\langle 111\rangle$

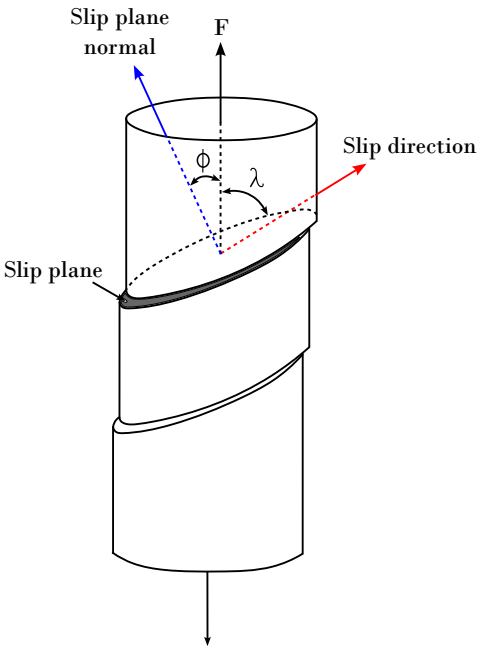

Figure 2.29: Illustration of the geometry of slip in a cylindrical crystal. Note that $(\phi + \lambda) \neq 90°$. Adapted from Hull and Bacon [191].

at this force is known as the critical resolved shear stress (CRSS) for slip [191]. However, the theoretical CRSS for slip was shown to be many times greater than the experimentally observed stress. The low experimental value can be accounted for by the movement of dislocations [191].

In polycrystalline hexagonal metals, both slip and twinning are observed as there is a lack of sufficient slip systems for the typical imposed strains for slip to be the only deformation mode.

Microstructural inhomogeneity is developed from deformation processes being different in various parts of any grain in polycrystalline materials. The slip and twinning planes correspond to the system with the greatest resolved shear stress and have various orientations from grain to grain and can also be distinguished from grain to grain. This means that within each grain, different levels and deformation processes can take place, meanwhile are subjected to the constraints of each of the neighbouring grains, all of which are deforming uniquely. Due to this, and the fact that the grains must be contiguous for deformation to continue, that microstructural inhomogeneity occurs [189]. Slip processes and their variation within and between grains, largely determine the deformation microstructures, whereas changes in orientation are a consequence of the crystal plasticity, determine the deformation textures.

Aluminium, nickel, and copper alloys or any other metal of high or moderate γ_{SFE} deform by slip. With these metals, the deformation is typically heterogenous. Furthermore, as crystals transition through different orientations during deformation, areas of varying orientations develop within the original grains. This is known as grain subdivision or fragmentation. It is widely known in the literature that this subdivision can span from millimetres to nanometres in scale when deforming. Humphreys and Hatherly [189] also highlight from this point the scale of the microstructural hierarchy. The main features observed in medium and high γ_{SFE} deformed microstructures are highlighted:

1. **Dislocations** - typically exist as random structures or tangles seen in Figure 2.30(a), especially after low imposed strains. In the case of metals that do not form cells, dislocations can be observed even after large strains.

2. **Cells and Subgrains** - Commonly, the dislocations formed from deformation for the boundaries of cells or subgrains, seen in 2.30(b).

3. **Deformation and Transition bands** - Often subdivision of grains can occur on a large

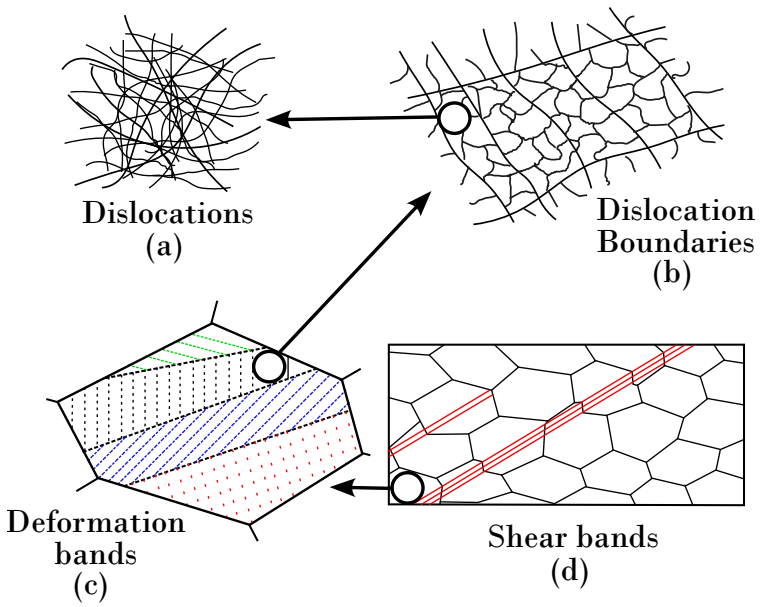

Figure 2.30: The hierarchy of microstructure in a polycrystalline metal deforming by slip. The various features are shown at increasing scale: (a) Dislocations, (b) Dislocation boundaries, (c) Deformation and transition bands within a grain, (d) Specimen and grain-scale shear bands. Adapted from Humphreys and Hatherly [189].

scale during deformation into discrete regions of different orientations, which is a result of inhomogeneous stresses from neighbouring grains or the instability of the grain throughout plastic deformation. These are known as deformation bands, seen in Figure 2.30(c), deform on different slip systems. The narrow regions between the bands, which are either diffuse or sharp, are known as transition bands.

4. **Shear bands** - are a phenomena that occurs due to plastic instability, or more accurately intense shear that occurs in planes inclined to the rolling plane during deformation. They can pass through many grains, seen in Figure 2.30(d), and outward through the specimen.

For this work, it is important to highlight the effects of not only materials that deform by slip alone, but also discuss metals that deform through both slip and twinning.

In materials with low γ_{SFE}, (*e.g.,* copper alloys), the dislocations dissociate to form planar arrays of stacking faults on the slip planes. As a result at an early stage of deformation, thin bands of deformation twins occur [189]. Twinning is a major deformation mode in FCC metals with γ_{SFE} $< 25\ mJm^{-2}$ and in all close-packed hexagonal (HCP) metals. It can occur in FCC metals with high γ_{SFE} values and in BCC metals if the deformation occurs at low enough temperatures or high enough strain rates, although it must also be understood that twinning is always dependent on orientation.

Twinning can be clearly seen on polished and etched specimens using electron microscopy, shown in the schematic in Figure 2.31. Strain markings seen under the microscope consist of fine deformation twins. These features develop freely on the {111} planes of many FCC copper alloys. The marking width is decided primarily by the γ_{SFE} and the deformation temperature, and the twins only become wider as these variables increase. Twinning is a primary feature of the microstructure of cold worked or low temperature deformed copper due to these variables.

Close-packed hexagonal (HCP) metals also initally deform by slip, however, lattice symmetry and the availability of slip systems are less than with cubic metals. Meaning that in the early deformation stages, or at low strains ($\varepsilon < 0.2$), twinning becomes a significant deformation mode. The key feature to be highlighted in the deformation microstructure of HCP metals is the rapid development of an array of large, broad, lenticular deformation twins. The twins typically start as long, thin lamellae at low strain, but quickly widen. Deformation twins are wider in HCP metals compared to cubic metals due to the smaller value of twinning shear [189]. Moreover, due to the limited magnitude of twinning shear, twinning contributes little to the overall deformation at

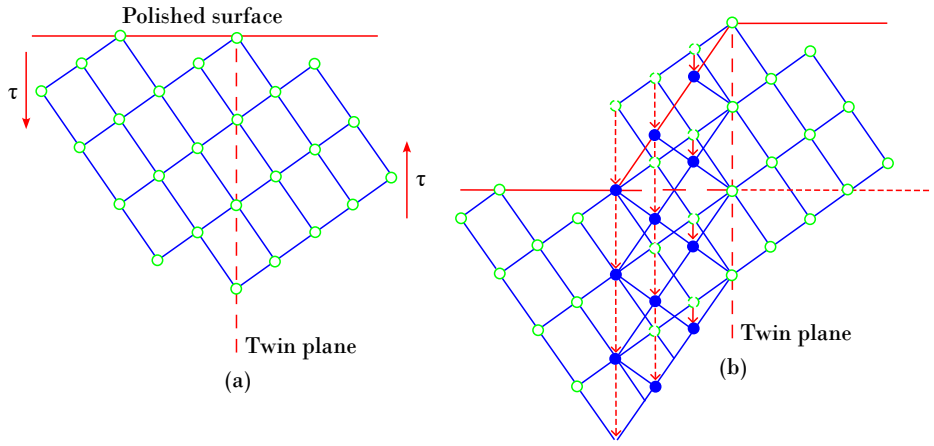

Figure 2.31: Schematic showing how twinning occurs from an applied shear stress τ. In (b), open circles represent atoms that did not change position; dashed and solid circles represent original and final atom positions, respectively. Adapted from Dieter [13].

medium to high levels of strain. Once twinning stops, deformation by slip occurs in the new twins and the entire process repeats.

The amount of bulk plastic deformation from twinning is normally small relative to that resulting from slip. However, the real importance of twinning lies with the accompanying crystallographic reorientations; twinning may place new slip systems in orientations that are favourable relative to the stress axis such that the slip process can now take place [192].

A final area in relation to this work that is vital to discuss and understand before moving forward into recovery, recrystallisation, and regrowth are the fundamentals of grain boundary structures and migrations, and their importance in deformed metals.

Overview of Grain Boundary Structure and Migration

The fundamentals of grain boundary structures are important to highlight in this section as they play a significant role in this work. Recrystallisation is a major feature within thermomechanical processing, and to fully understand the dynamics happening within any forged metal, the grain boundaries and their migrations are discussed.

First, consider the grain boundary seen in Figure 2.32. The geometry of the boundary is

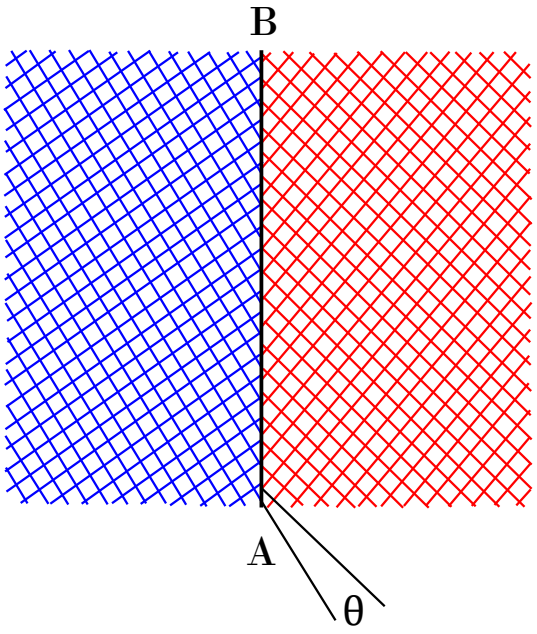

Figure 2.32: A grain boundary between two crystals misoriented by an angle θ about an axis normal to the page. Adapted from Humphreys and Hatherly [189].

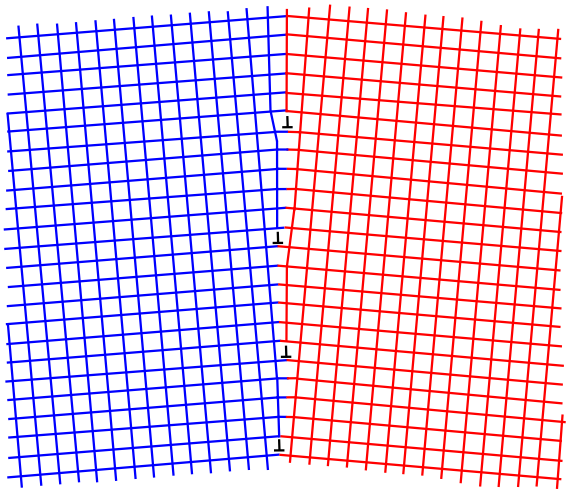

Figure 2.33: A symmetrical tilt boundary. Adapted from Humphreys and Hatherly [189].

defined by the boundary plane AB's orientation with respect to one of the two crystals (two degrees of freedom) and by the smallest rotation (θ) required to make the two crystals coincident (three degrees of freedom). Therefore, there are five separate macroscopic degrees of freedom which define the geometry of the boundary. Moreover, the boundary structure itself depends on three microscopic degrees of freedom, which are the rigid body translations parallel and perpendicular to the boundary.

The structure of the boundary depends also on the local displacements at the atomic level and is influenced by external variables such as temperature and pressure, and internal parameters such as bonding, composition, and defect structure [189].

Misorientations between grain boundaries can be described as low-angle (LAGB), or high-angle (HAGB) boundaries. A low-angle boundary or sub-boundary can be represented by an array of dislocations. One example of a low-angle grain boundary is a symmetrical tilt boundary, seen in Figure 2.33. This tilt boundary consists of a wall of parallel edge dislocation aligned perpendicular to the slip plane and the lattices are related by a misorientation about the plane of the boundary [189].

If the spacing of the dislocations of Burgers vector $\boldsymbol{b}$ in the boundary is h, then the crystals on either side of the boundary are misoriented by a small angle θ, where:

$$\theta \approx \frac{b}{h} \tag{2.37}$$

The energy of such a boundary γ_s, is given as:

$$\gamma_s = \gamma_0 \theta \left(A - ln\theta\right) \tag{2.38}$$

where $\gamma_0 = Gb/4\pi\left(1-v\right), A = 1 + ln\left(b/2\pi r_0\right)$ and r_0 is the radius of the dislocation core, usually taken as between b and 5b.

High angle grain boundaries consist of regions of good and bad matching between grains [189]. Kronberg and Wilson [194] presented the concept of coincidence site lattices (CSL), where two interpenetrating crystal lattices are translated to bring a lattice point of each together in coincidence. Where other points meet in the two lattices, these sites form the coincident site lattice. Grain boundary engineering through processing is centred around increasing the number of CSL or 'special' boundaries to improve the material properties.

Although there is importance in understanding the fundamental background of individual grain boundaries, for this work grain boundary arrangements and migrations within metals remains of higher importance. In both 2-D and 3-D, the microstructure consists of vertices which are joined by edges which surround faces, shown schematically in Figure 2.34. In the 3-D case, the faces surround cells or grains. Cells, faces, edges, and vertices of cellular structures all obey the conservation law

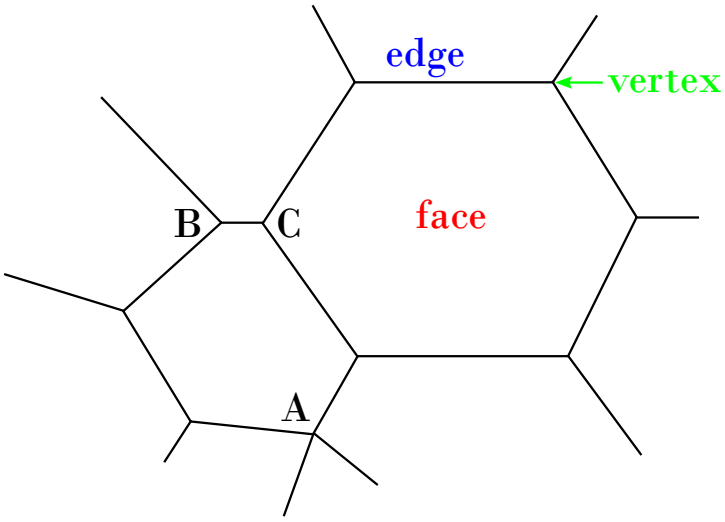

Figure 2.34: A 2-D section of a grain structure. The 4-rayed vertex at A will tend to decompose into two 3-rayed vertices such as B and C. Adapted from Humphreys and Hatherly [189].

of Euler's equation (equation 2.39), when the face or cell at infinity is not counted [195].

$$\begin{aligned} F - E + V &= 1 \,(2 - D \; plane) \\ -C + F - E + V &= 1 \,(3 - D \; Euclidean \; space) \end{aligned} \tag{2.39}$$

where C is the number of cells, E edges, F faces, and V vertices.

The number of edges connected to a vertex is its coordination number z. For topologically stable structures, $z = 3$ in 2-D, and $z = 4$ in 3-D. Therefore in 2-D, a 4-rayed vertex such as that shown at A in Figure 2.34 will be unstable and will decompose to two 3-rayed vertices such as B and C [189].

The mobility and migration of these boundaries and their phenomena is a widely studied subject in the literature [196–201]. The migration of both LAGB and HAGB is central in the annealing of cold-worked metals. LAGB migration occurs during both recovery and the nucleation stage of recrystallisation, whereas HAGB migration happens during and after primary recrystallisation [189].

Grain boundary migration involves atomistic rapidly occurring processes, at high temperatures, and under conditions far from equilibrium [189]. Thus, there is great difficulty in experimental and even theoretical studies of boundary migration. On the contrary, there has been a great deal of experimental data captured, from which clear trends can be seen, but also results that are directly contradictory. It is known that even small amounts of solute can impact the boundary mobility, meaning it is also difficult to conclude the intrinsic mobility of a boundary. Models are used in conjunction with the wealth of knowledge on grain structures and boundaries to understand these migration processes. However, there are still many alignments to be seen between the models and experimental data.

Basic boundary migration mechanisms are subject to several influencing parameters: firstly, the boundary structure, which is constituted by misorientation and boundary plane; secondly, the experimental conditions, *i.e.,* temperature and forces on the boundary; and lastly, the point defects in the material, made up of solutes and vacancies.

LAGB migrate through climb and glide of the dislocations at the boundary, thus mostly can be interpreted by the theory of dislocations discussed previously. However, HAGB migrate through the transfer of atoms between adjacent grains to the boundary, which are known as thermally activated atomic jumps. There is also evidence that suggests HAGB can migrate through intrinsic boundary defects such as ledges, steps, or grain boundary dislocations. Even diffusion-less shuffles, (cooperative movement of groups of atoms) may be involved in some grain boundary migrations [189].

Grain boundaries move with a velocity (v) in response to the net pressure ($P = \Sigma P_i$) on the

boundary. Generally, it is assumed that the velocity is directly proportional to the pressure, the constant of proportionality being the mobility (M) of the boundary, and therefore:

$$v = MP \tag{2.40}$$

This type of relationship is predicted by reaction rate theory if the mobility is independent of the driving force and if $P \ll kT$. Grain boundary mobility is also temperature dependent and generally follows an Arrhenius relationship of the form:

$$M = M_0 \exp\left(-\frac{Q}{RT}\right) \tag{2.41}$$

If plotted, the slope of $ln(M)$, or $ln(v)$ (under a constant pressure), against $1/T$ yields a value of Q (the apparent activation energy), which may be related to the atom-scale thermally activated jump processes which determine boundary migration.

There are large amounts of information and literature pertaining to boundary migration beyond the scope of this work, the most crucial points of understanding in this section are that of recovery, recrystallisation, and regrowth.

2.2.3 Recovery after Deformation

Recovery refers to any changes in a deformed material which occur prior to recrystallisation due to changes in dislocation structure, and usually partly returning material properties to their initial state [189]. It is also a relatively homogeneous process, as similar changes are happening simultaneously across the sample. Recovery progresses gradually over time, with no easily distinguishable beginning or end of the process.

Dislocation recovery is a series of events rather than a single process, as shown schematically in Figure 2.35, and although recovery tends to occur in this sequence, they typically overlap. Material, strain, purity, deformation and annealing temperature all influence whether these stages of the recovery process will occur during annealing. In most cases, some of these stages will have already occurred during deformation, which is known as dynamic recovery.

Recovery and recrystallisation processes are both driven from the stored energy of the deformed

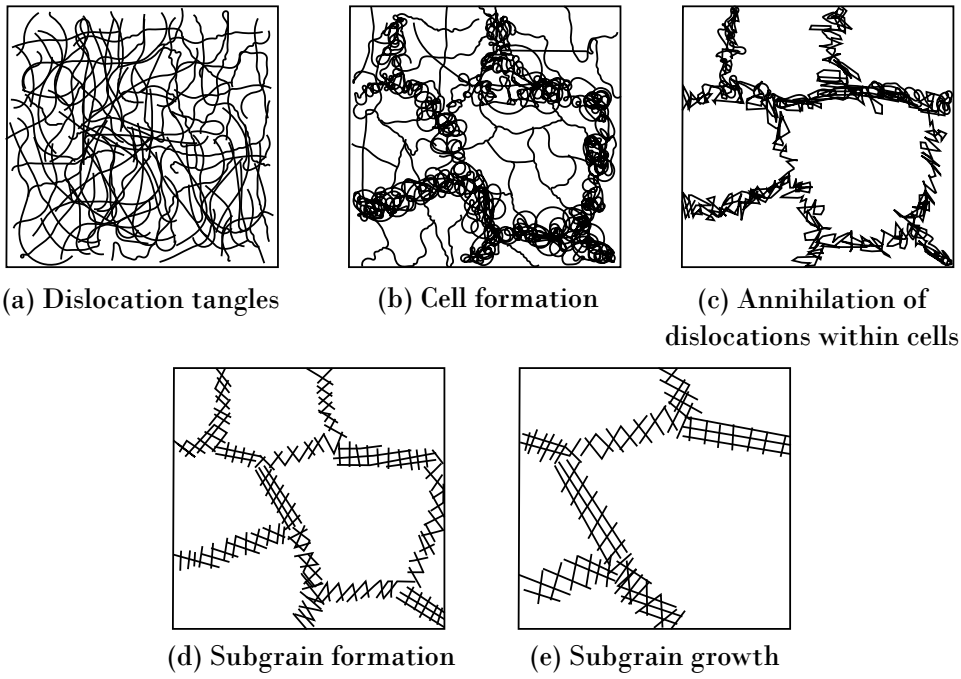

(a) Dislocation tangles **(b) Cell formation** **(c) Annihilation of dislocations within cells**

(d) Subgrain formation **(e) Subgrain growth**

Figure 2.35: Various stages in the recovery of a plastically deformed material. Adapted from Humphreys and Hatherly [189].

state, and as this stored energy is limited, they are considered to be competing processes. Recovery is therefore limited by the ease of recrystallisation and vice versa, as recovery ceases once recrystallisation has occurred to where all of the substructure is consumed. The division between recovery and recrystallisation is not clear as some recovery mechanisms are important in the nucleation stage of recrystallisation [189].

Throughout recovery microstructural changes are not obvious through microscopy, therefore recovery is measured indirectly through measuring changes in physical or mechanical properties. Calorimetry is the most direct method after recovery, as the stored energy is tied to the number and configuration of the dislocations [189]. Density and electrical resistivity are also affected by recovery, however are difficult to measure quantitively as they have such small values. More commonly, recovery is measured through changes in yield stress or hardness of the material, yet these changes are also small. The mechanical properties of a recovered material are of great practical importance, because they become more ductile and formable for further processing.

The degree of recovery in a deformed material, as mentioned before, depends on several parameters. Complete recovery can occur under several circumstances of varying strains, examples of this can be seen in lightly deformed polycrystalline materials or large strains on single slip systems of single crystal HCP metals which can fully recover their original microstructure and properties on annealing. Leslie *et al.* [202] found that the fraction of the property change which may be recovered on annealing at a constant temperature is usually found to increase with strain. However, this can be seen to be the opposite in highly strained materials due to earlier recrystallisation.

On top of strain, more complete recovery tends to be seen at higher annealing temperatures in general. Of course, a key factor in the extent of recovery is the nature of the material itself, and more particularly the stacking fault energy γ_{SFE}. The γ_{SFE} determines the rate of dislocation climb and cross slip, both of which are mechanisms which typically control the rate of recovery [189]. In metals of low γ_{SFE}, climb is hindered, resulting in little recovery before recrystallisation. Conversely, in high γ_{SFE} metals, climb is easier, resulting in faster and often increased recovery.

Solutes are also known to affect recovery by pinning dislocations, or by affecting the concentration and mobility of vacancies. Solute pinning results in a higher stored energy than solute-free materials as it both static and dynamic recovery [189]. Dislocation movement lowers the stored energy in metals during recovery. There are two key processes that have this effect, including the rearrangement and the annihilation of dislocations into lower energy setups. Both processes are a result of glide, climb, and cross-slip of dislocations. These phenomena, although briefly mentioned, in depth discussion is outside the scope for this work.

Subgrain formation during recovery is of note, where in an alloy of medium or high stacking fault energy, the dislocations are typically arranged after deformation in the form of a three-dimensional cell structure [189]. The cell walls at this stage are made up of complex dislocation tangles seen in Figure 2.35(b), the size of the cells depends on the material and strain. Through annealing the tangled cell walls are rearranged and annihilated into finally forming subgrains, seen in Figure 2.35(d). Subgrain structures can often already be formed from dynamic recovery, so that all post deformation occurring involved the coarsening of the subgrain structure (Figure 2.35(e)).

High γ_{SFE}, low solute content, large strain, and high deformation temperatures all promote dynamic recovery to form subgrain structures over cell structures, as these all act as catalysts to the recovery process. The stored energy at this subgrain stage is still far higher than that of a fully recrystallised material. Subgrain coarsening lowers the stored energy and also leads to a reduction in the total area of LAGB in the metal.

The kinetics of subgrain growth discussed at this small scale leads into the discussion on recrystallisation and microstructural changes undergone by alloys throughout thermomechanical processing. If the microstructure can be approximated to an array of subgrains of radius R and subgrain boundary energy γ_s, then the stored energy per unit volume E_d is $\alpha\gamma_s/R$, where α is a shape factor of ~ 1.5. As the stored energy is reduced as the subgrain grows, this provides the driving force F

for subgrain growth, which can be found by:

$$F = -\frac{dE_D}{dR} = -\alpha \frac{d}{dR}\left(\frac{\gamma_s}{R}\right) \tag{2.42}$$

If the stored energy is assumed to be uniform and that the force is evenly distributed, the driving pressure P is given by:

$$P = \frac{F}{A} = -\alpha R \frac{d}{dR}\left(\frac{\gamma_s}{R}\right) \tag{2.43}$$

If γ_s is constant during subgrain growth then:

$$P = \frac{\alpha \gamma_s}{R} \tag{2.44}$$

However, as γ_s is a function of the misorientation of the adjacent subgrains, the driving pressure P may not remain constant during subgrain growth.

One aspect important to this work in relation to recovery is the relationship between subgrain size and mechanical properties. As mechanical properties are used to measure recovery and strength of materials comes inherently from their substructures, the importance of flow stress and subgrain structure is vital to understand. Substructure strengthening was reviewed broadly in the literature, [203–207].

There are three approaches highlighted by Humphreys and Hatherly [189] for determining the flow stress based on the substructure:

1. The Hall-Petch relationship is used to determine the yield stress, when it is assumed that subgrains behave like grains, where c represents a temperature-dependent rate constant, and D is the change in subgrain size:
$$\sigma = \sigma_0 + c_1 D^{-\frac{1}{2}} \tag{2.45}$$

2. It is assumed that the flow stress is calculated by the operation of dislocation sources [206]:
$$\sigma = \sigma_0 + c_2 D^{-1} \tag{2.46}$$
Equations 2.45 and 2.46 may both be written as:
$$\sigma = \sigma_0 + c_3 D^{-m} \tag{2.47}$$

3. The last approach assumes that the dislocations which comprise subgrain boundaries can be averaged over the microstructure. The area of subgrain per unit volume (A) is $\sim 3/\mathrm{D}$. For small misorientations $\theta = b/h$, and the length of dislocation per unit area of boundary (L) is $1/h$. Thus:
$$\rho = AL = \frac{3}{Dh} = \frac{3b\theta}{D} \tag{2.48}$$
Then when taking the relationship between flow stress and dislocation density into account, the flow stress can be determined with:
$$\sigma = \sigma_0 + c_4 \left(\frac{\theta}{D}\right)^{\frac{1}{2}} \tag{2.49}$$
which is of the same form as Equation 2.47.

These equations have been used to analyse substructure strengthening, however there is little agreement on their application. In Thompson's review [203] there is support for all three approaches being utilised. However, Humphreys and Hatherly concluded that more research would be required for the application of these.

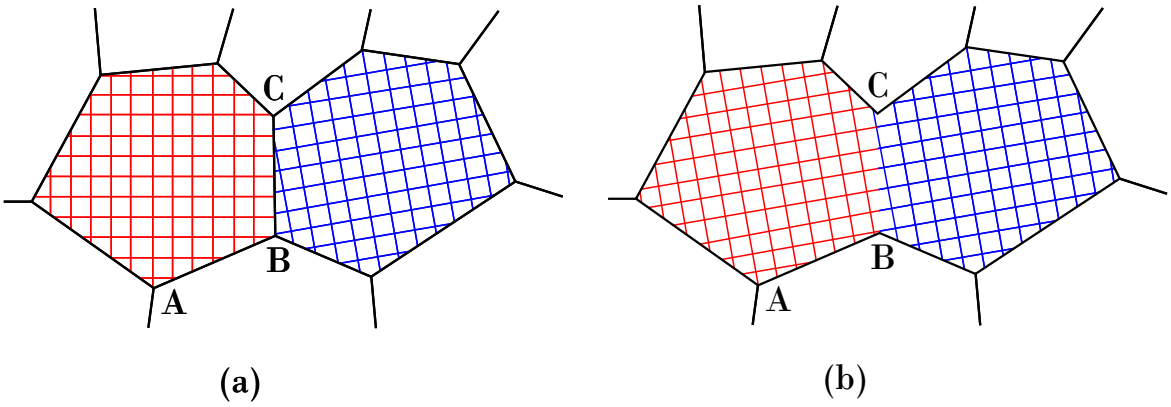

Figure 2.36: Proposed mechanism for the rotation and coalescence of subgrains during recovery. (a) Two subgrains with highlighted low angle grain boundaries AB and BC, and (b) coalescence of the subgrains at LAGB BC. Adapted from Humphreys and Hatherly [189].

Subgrain growth is another important parameter in recovery. Subgrain growth can occur through two primary mechanisms, subgrain boundary migration, and subgrain rotation and coalescence. In both deformed and recovered polycrystals, the subgrain structure may be topologically like the grain structure seen in recrystallised material. Subgrain coarsening through migration of LAGB (the first mechanism) is considered to be a similar process to that seen in the grain growth following recrystallisation, however there are significant differences [189].

These differences are primarily between the energies and angles of boundaries between subgrain and grain boundary migration. Where grain boundaries are mainly high angle and have similar energies, as well as the equilibrium angle being typically 120°. Whereas, subgrain growth is typically through LAGB migration, and depends strongly on misorientation and the boundary place, with equilibrium angles unlikely to be 120° [189].

The second mechanism, subgrain rotation and coalescence, was proposed by Hu *et al.* [208]. The authors discovered through in-situ TEM annealing experiments, that subgrains might rotate by boundary diffusional processes until adjacent subgrains were of similar orientation. Li *et al.* [209] in the same year, discussed that the two subgrains once orientated would then form, or coalesce, into one larger subgrain. This process would have little boundary migration, where the driving force would arise from the reduction in boundary energies.

The process for subgrain rotation can be seen schematically in Figure 2.36. It shows two adjacent low angle boundaries AB and BC in Figure 2.36(a) before coalescence, where the misorientation of the low angle boundary (BC) is then reduced. As the two boundaries have similar areas, the increase in energy of boundary AB is less than the energy decrease of boundary BC, as Equation 2.38 shows that the change in boundary energy, $d\gamma/d\theta$ is greater the lower the angle of the boundary. Therefore, there is an overall decrease in energy if rotation occurs in this way, eventually leading to coalescence as seen in Figure 2.36(b). Many experimental TEM observations, as well as computer simulation studies on the kinetics of subgrain coalescence [209, 210], corroborate the alternative subgrain growth mechanism presented in Chan *et al.*'s work [211].

A final consideration for the mechanism of recovery, is the role played by second-phase particles, as these can be present during deformation and distributed equally throughout the microstructure. Similarly, they can precipitate during annealing, where their distribution is linked to the dislocation distribution. Second-phase particles can impact recovery mechanisms in several ways. For example, through the annihilation and rearrangement of dislocations to form LAGB, the particles can pin the individual dislocations and slow this stage of recovery.

Following recovery is the key focus of many studies in materials for the last century and is of key importance due to the role it plays in the resultant material physical and mechanical properties. Recrystallisation is a highly explored subject for many materials and is still widely studied today.

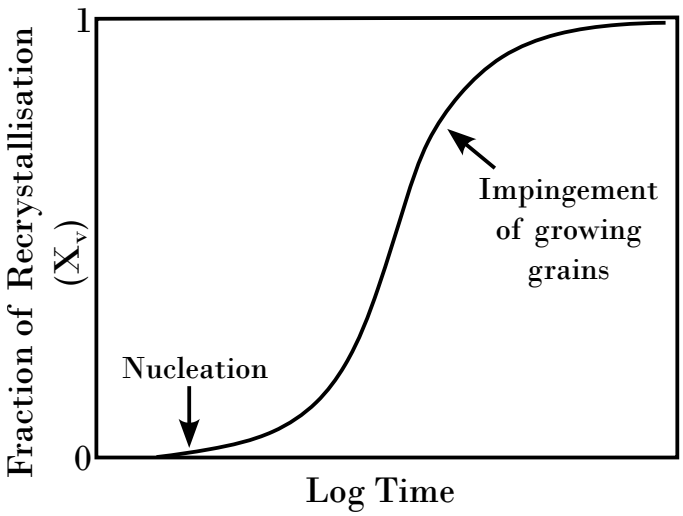

Figure 2.37: Typical recrystallisation kinetics during isothermal annealing. Adapted from Humphreys and Hatherly [189].

2.2.4 Recrystallisation

Recrystallisation is the initiation of new strain-free grains in areas of a material which then subsequently grow and evolve by consuming the deformed or recovered microstructure [189]. The microstructure is divided into recrystallised and non-recrystallised regions, and the fraction of recrystallised material climbs from 0 to 1 over the transformation period. Recrystallisation over time during isothermal annealing is often displayed by a plot of the volume fraction of material recrystallised (X_v) as a function of $log\,(time)$, shown in Figure 2.37.

There is a distinction of terms between primary and secondary recrystallisation, where the former refers to the recrystallisation of the deformed microstructure and the latter is more well known to be the following process of abnormal grain growth that occurs in a fully recrystallised material. In this section, the aim is to highlight the underpinning key points of understanding regarding recrystallisation and lay the groundwork for discussion on ingot-to-billet conversion of both single and dual-phase alloys. This is crucial to be able to determine the fundamental microstructural kinetics and changes occurring throughout the cogging process, as well as discuss important aspects of recrystallisation theory for computer simulation work.

Nucleation and Growth

Primary recrystallisation is divided into two stages: nucleation and growth. These steps can occur in parallel in different areas of a metal during recrystallisation, but always consecutively for any single grain. Nucleation refers to the generation of new grains within the microstructure, whereas growth is when these new grains 'grow' over or replace the deformed microstructure.

The working definition given by Humphreys and Hatherly [189] for a recrystallisation nucleus is, "a crystallite of low internal energy growing into deformed or recovered material from which it is separated by a high angle grain boundary." Models for recrystallisation kinetics refer to the nucleation rate ($\dot{N}$) which is known to be a difficult to measure parameter using microscopy techniques.

Grain growth during recrystallisation is more commonly analysed over their nucleation. It is generally accepted that the velocity (v) of a HAGB, which is also known as the growth rate ($\dot{G}$) is given by:

$$v = \dot{G} = MP \tag{2.50}$$

where P is the net pressure on the boundary, and M is the boundary mobility.

The driving pressure (P_d) for primary recrystallisation comes from the dislocation density (ρ), which is equal to the stored energy, given by Equation 2.32. So, the driving force can be expressed

in the same form as:

$$P_d = E_D = \alpha \rho G b^2 \tag{2.51}$$

where α is a constant of the order 0.5.

In the early growth stages of a new grain, the Gibbs-Thomson relationship is also important to consider. For a new grain of radius R, as it grows into the deformed structure, the curvature of a HAGB exerts an opposing force that slows growth and is of specific energy γ_b. The Gibbs-Thomson relationship is known as:

$$P_c = \frac{2\gamma_b}{R} \tag{2.52}$$

This relationship is only significant at the beginning of nucleation and growth when the new grains are small. P_c is found to be equal to P_d when R is $\sim$1µm. Therefore, for grain sizes lower than this, there would be no resultant driving force for recrystallisation. The growth rate ($\dot{G}$) is a complex parameter that does not remain constant throughout recrystallisation due to the driving force and boundary mobility varying throughout the metal due to variations in deformation and annealing conditions [189].

Laws of Recrystallisation

Based on the earliest experimental work of the first half of the twentieth century, there were a set of "laws" created for recrystallisation. This set of rules predicts the effects of initial microstructure (grain size), and processing parameters (deformation strain and annealing temperature), on the time of recrystallisation and on the grain size after recrystallisation. In most cases, the ruleset is adhered to for most metals undergoing recrystallisation when considered to be a nucleation and growth phenomenon, reliant on thermally activated processes, and which stored energy from deformation is the driving force. The laws of recrystallisation proposed by Mehl, and Burke and Turnbull [212, 213] are as follows:

1. **A minimum deformation is needed to initiate recrystallisation.** - The level of deformation needs to be sufficient to provide a nucleus for the recrystallisation, and to have sufficient driving force for growth to continue.

2. **The temperature at which recrystallisation occurs decreases as the annealing time increases.** - Mechanisms controlling recrystallisation are thermally activated and the relationship between temperature and recrystallisation rate can be seen in the Arrhenius equation (Equation 2.53).

   The Arrhenius equation is the general equation used for interpreting the influence of temperature on the rates of chemical reactions [214]. According to this relationship, a rate constant k is the product of a pre-exponential (frequency) factor A and an exponential term of the form:

   $$k = Ae^{-E/RT} \tag{2.53}$$

   where R is the gas constant and E is the activation energy. Laidler [214], discusses the many developments of the Arrhenius-type equation since it origination in the late 19th century. However, nowadays there is a more common usage of the equation of the form:

   $$k = A \exp\left[-\left(\frac{E_a}{RT}\right)^{\beta}\right] \tag{2.54}$$

   where β is an order of 1 dimensionless number, that is mostly used as a fudge factor or empirical correction to enable the models to better fit captured experimental data.

3. **The temperature at which recrystallisation occurs decreases as strain increases.** - Increased material strain results in higher stored energy, meaning higher driving force for

recrystallisation. Thus, in a highly deformed material both nucleation and growth with occur faster and at a lower temperature.

4. **The recrystallised grain size depends primarily on the amount of deformation, being smaller for large amounts of deformation.** - A higher strain will provide more nucleation sites per unit volume, resulting in a smaller grain size as $\dot{N}$ is more affected by strain than growth rate.

5. **For a given amount of deformation the recrystallisation temperature will be increased by:**

   A larger starting grain size. - As grain boundaries are favoured sites for nucleation, a large initial grain size provides less sites for new grain to grow. This results in a lower $\dot{N}$ or requiring higher temperatures.

   A higher deformation temperature. - In this case, more dynamic recovery will occur, lowering the stored energy compared to that of a lower deformation temperature of the same strain.

Rate of Recrystallisation

Although the laws of recrystallisation offer a useful guide to the overall recrystallisation behaviour, it is now recognised to be more nuanced and complex with many more material and processing parameters that need to be considered for the microscale. This section will aim to highlight the parameters that affect the recrystallisation rate.

Firstly, as many of the laws indicated the level of strain in the deformed microstructure plays a crucial role in the recrystallisation kinetics, including the recrystallisation rate. The effect of tensile strain on the recrystallisation kinetics of aluminium is visualised in Figure 2.38, where it can be seen that, for higher values of strain, the overall time for recrystallisation is greatly reduced.

The deformation mode is another major and complex factor that affects the recrystallisation rate. One example of this complexity, found by Haase and Schmid [216], after crystals of zinc were subjected to high plastic strain, they would fully recover their initial properties with no recrystallisation. Whereas other metals after deformation with levels close to no strain, can readily

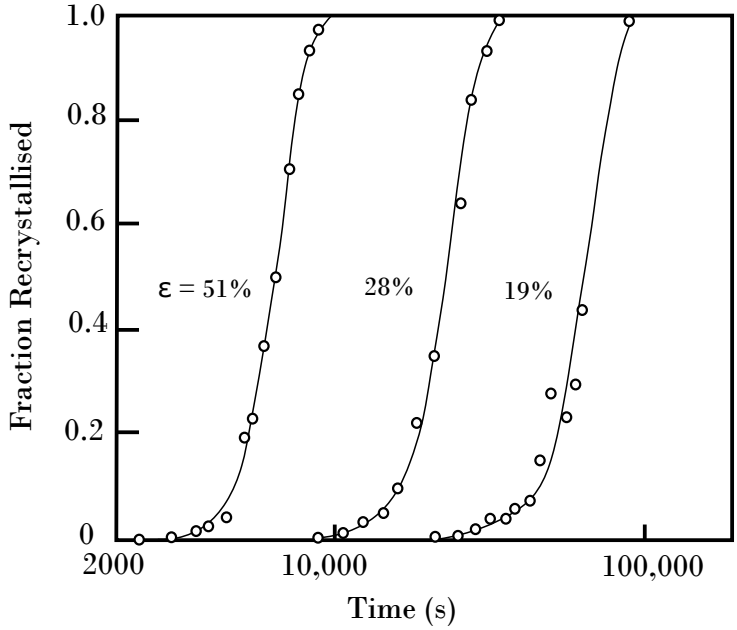

Figure 2.38: Effect of tensile strain on the rate of recrystallisation of aluminium annealed at 350°C. Adapted from Anderson and Mehl [215].

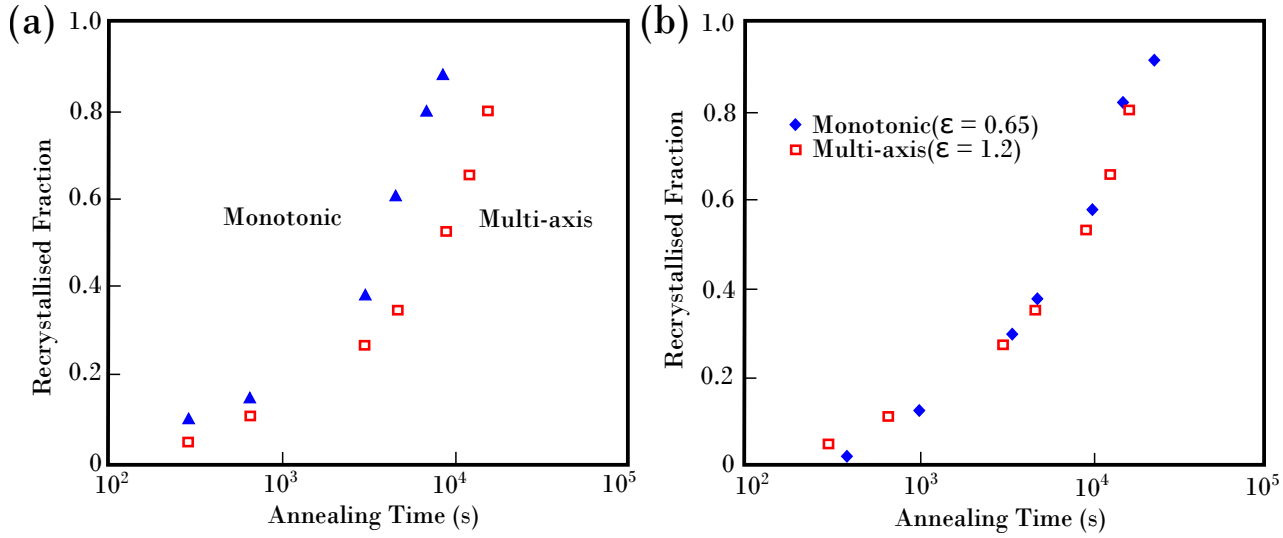

Figure 2.39: Effect of redundant deformation on the recrystallisation of pure aluminium. The recrystallisation kinetics between monotonic and multi-axial compressions. (a) Specimens deformed to the same equivalent strain (0.7), (b) speciments deformed to the same equivalent stress. Adapted from Embury *et al.* [217].

recrystallise. Similarly, changes in strain path are of interest on how this affects the recrystallisation behaviour.

In many industrial metal forming processes, the strain path is not constant, and is often reversed. As an example, in cogging, the strain direction is consistently being changed and rotated. This parameter is of vital importance to this work in terms of understanding the recrystallisation effects seen in open-die forging cogging operations.

Studies on strain path effects typically investigate formability, however, also have been interested in the effect on recrystallisation behaviour. Lindh *et al.* [218] studied the impact of different strain paths on recrystallisation temperature of high purity copper. Recrystallisation temperature decreased for specimens with increasing tensile strain. Whereas, for the same total permanent strain (ε_{perm}), the recrystallisation temperature increased for samples that underwent both tensile and compressive strain. From this study, Lindh *et al.* determined an equivalent strain (ε^R_{equ}) for the samples that was given by:

$$\varepsilon^R_{equ} = \varepsilon_{perm} + \eta\varepsilon_{red} \tag{2.55}$$

where ε_{red} is the redundant strain and η is a constant found to be 0.65 from the study. Which revealed that the redundant strain is 0.35 times less effective in promoting recrystallisation than permanent strain.

Another study by Embury *et al.* [217], compared the recrystallisation behaviour of cubes of pure aluminium under uniaxial compression against samples deformed incrementally in different directions to produce no overall shape change. The results show, for the same equivalent strain, the samples deformed under multi-axial compression recrystallised slower than the specimens deformed uniaxially. However, it was found that if the specimens were deformed to the same level of stress, the recrystallisation behaviour was similar.

Following the results of many investigations, Humphreys and Hatherly [189] suggest that there is a reduction in dislocation density and therefore the flow stress on strain reversal. Lower recrystallisation driving pressure results in slower recrystallisation and larger recrystallised grains.

The growth rate during recrystallisation may also be affected by the orientation between deformed and recrystallising grains. High mobility grain boundaries can also greatly influence the recrystallisation texture, on top of causing more rapid recrystallisation. This is known as orientated growth. Juul Jensen [219], found that this can also occur for LAGB when the recrystallisation grains encounter deformed regions of a similar orientation.

Kinetics of Primary Recrystallisation for Simulation

Many recrystallisation models and simulation works stem from the typical transformation reaction seen in the curve of Figure 2.37, which is often described through the constituent nucleation and growth processes that were determined through the early work of Kolmogorov [220], Johnson and Mehl [221], and Avrami [222] which is commonly known as the JMAK model. A review of the JMAK model and its application was completed by Fanfoni [223] in 1998.

In recrystallisation theory, it can be assumed that nuclei are created at a rate $\dot{N}$ and that grains growth occurs in the deformed material at a linear rate $\dot{G}$. If the grains are spherical, their volume varies as the cube of their diameter, and the recrystallised material fraction (X_v) rapidly increases with time. Eventually, new grains will impinge each other and the recrystallisation rate will decrease, tending towards zero as X_v approaches 1 [189].

In nucleation theory, the standard from of the equation for determining the total number of nuclei dN' can be expressed as:

$$dN' = \dot{N}dt = dN + \dot{N}X_v dt \tag{2.56}$$

where dN is the number of nuclei and $\dot{N}dt$ is the rate of nuclei forming over the time interval dt. Due to nucleation being unable to occur in the areas which have already been recrystallised, dN is lower than $\dot{N}dt$. Nuclei which would have formed in the recrystallised volume is given by $\dot{N}X_v dt$, which gives rise to the equation for the total number of nuclei (including the 'phantom' nuclei) dN'.

This idea of phantom nuclei is carried forward in the theory, where what is known as the extended volume, the fraction of material which would have recrystallised if the phantom nuclei were real (X_{VEX}), is given by:

$$X_{VEX} = \int_0^t V dN' \tag{2.57}$$

where the V is the volume of a recrystallising grain at time t. If the incubation time is significantly less than t, then:

$$V = f\dot{G}^3 t^3 \tag{2.58}$$

where f is a shape factor ($4\pi/3$ for spheres). Thus:

$$X_{VEX} = fG^3 \int_0^t t^3 \dot{N} dt \tag{2.59}$$

If $\dot{N}$ is constant, then:

$$X_{VEX} = \frac{f\dot{N}\dot{G}^3 t^4}{4} \tag{2.60}$$

The extended volume increases during a time interval dt, by an amount dX_{VEX}. As the fraction of unrecrystallised material is known to be $1 - X_v$, it means that $dX_{VEX} = (1 - X_v)dX_{VEX}$, or:

$$dX_{VEX} = \frac{dX_v}{1 - X_v} \tag{2.61}$$

$$X = \int_0^{X_v} dX_{VEX} = \int 0^{X_v} \frac{dX_v}{1 - X_v} = ln\frac{1}{1 - X_v} \tag{2.62}$$

$$X_v = 1 - \exp\left(-X_{VEX}\right) \tag{2.63}$$

Then, combining equations 2.60 and 2.63 gives:

$$X_v = 1 - \exp\left(\frac{-f\dot{N}\dot{G}^3 t^4}{4}\right) \tag{2.64}$$

This is generally written as:

$$X_v = 1 - \exp\left(-Bt^n\right) \tag{2.65}$$

where $B = f\dot{N}\dot{G}^3/4$, and this is the general form of the well-known Avrami, Johnson-Mehl, or JMAK equation that is widely used throughout research. It is also known that nucleation sites are assumed to be distributed randomly when using the JMAK method.

Kinetics of Primary Recrystallisation in Real Materials

It is well known that nucleation sites in recrystallisation are non-randomly distributed. Evidence of the non-random distribution is found in all materials, more evidently in those materials with a large initial grain size. Examples can be seen in both copper and aluminium [224–226].

As nucleation occurs at preferred sites such as prior grain boundaries, at transition and shear bands. Low strain materials form less of these preferable sites, therefore there are less to act as nucleation sites. These small-scale inhomogeneous preferred sites may cause overall inhomogeneous distribution of nuclei. This depends on the number of nuclei relative to the number of sites, shown schematically in Figure 2.40. In the case of nucleation only occurring at grain boundaries for the same number of nuclei, Figure 2.40(a) shows the more homogeneous outcome in a fine grained material in comparison to a coarse grained material seen in Figure 2.40(b).

Typically, it is also seen that not all grains in a material recrystallise at a similar rate, and at a larger scale this is one main factor for inhomogeneous recrystallisation. The difference in recrystallisation rate arises from the difference in adjacent grain orientation. Therefore, grain orientation has become an increasingly important parameter for consideration and measurement. Evidence of growth rate ($\dot{G}$) not being constant is abundant, so a more realistic consideration of recrystallisation kinetics should allow for variation of $\dot{G}$. The variation in $\dot{G}$ change is mainly due to differences in driving pressure, which itself can both increase from microstructural inhomogeneity, or decrease with time due to recovery happening simultaneously with recrystallisation. Due to this combination, the simulation and calculation of growth rates has proved to be challenging [189].

Various equations have been used to express the variation of $\dot{G}$ with time such as:

$$\dot{G} = \frac{A}{1 + Bt^r} \tag{2.66}$$

which reduces to:

$$\dot{G} = Ct^{-r} \tag{2.67}$$

In several cases r is found to be ~ 1, whereas Vandermeer and Rath [227] found r = 0.38 in their investigation of the recrystallisation kinetics of iron.

The basic JMAK model assumes a constant growth rate, which is known to be unrealistic in

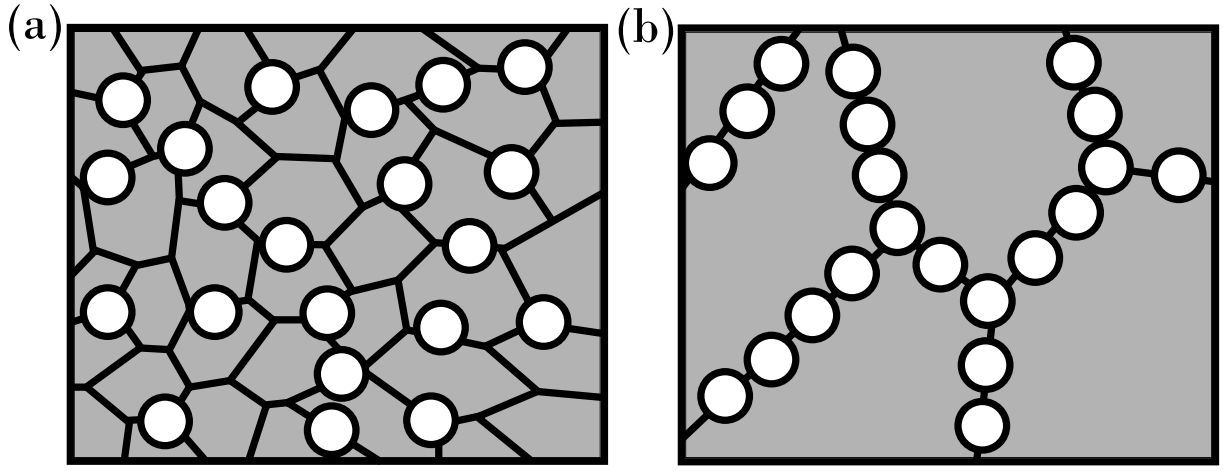

Figure 2.40: Schematic representation of the effect of the initial grain size on the heterogeneity of nucleation. (a) Small initial grain size, (b) large initial grain size Adapted from Humphreys and Hatherly [189].

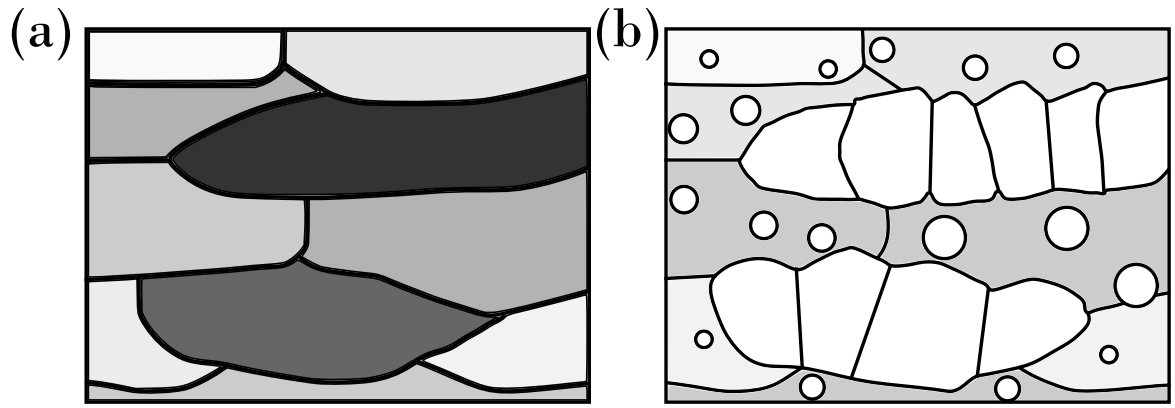

Figure 2.41: Variation in grain to grain stored energy, (a) initial state with higher stored energy regions shaded darker (b) resultant inhomogeneous grain growth during recrystallisation. Adapted from Humphreys and Hatherly [189].

real material recrystallisation. If we allow for $\dot{G}$ to vary, then Equation 2.64 becomes:

$$X_v = 1 - \exp\left[-fN\left(\int_0^t \dot{G}dt\right)^3\right] \tag{2.68}$$

And if the variation of growth rate against time is given by Equation 2.67, then combining Equations 2.67 and 2.68 results in the final equation:

$$X_v = 1 - \exp\left[-fN\left(C\frac{t^{(1-r)}}{(1-r)}\right)^3\right] \tag{2.69}$$

In addition to the inhomogeneous distribution of recrystallisation nuclei, the deformation microstructure results in variations in stored energy which in turn cause inhomogeneous growth rates throughout the deformed material [189]. This is best shown in Figure 2.41.

It can be concluded that deviation from the ideal linear JMAK models and plots are mostly caused by the inhomogeneity of the microstructure. This then leads to the non-random distribution of nucleation sites and stored energy, and finally to a growth rate which decreases with time [189].

The Recrystallised Microstructure

Understanding and interpretation of the recrystallised microstructure of processed alloys is crucial for engineers and metallurgists in determining the material properties, alongside post-process testing. Key points of knowledge for the recrystallised microstructure have been summarised.

Typically, the recrystallised grains have a preferred orientation or texture. The final grain size can be affected by many different earlier processing parameters as well as throughout nucleation and growth. Factors such as strain, initial grain size, and annealing temperatures cause the grains sizes to vary throughout the material. This is alike to different texture components within a material recrystallising at different rates, so the final grain size and shape within each texture component may be different.

If the grains are uniformly distributed in a single-phase alloy, and growth is isotropic then the recrystallised structure will consist of equiaxed polyhedra. In some cases, however, anisotropic growth leads to plate-shaped grains. This type of growth is of particular importance for grains of FCC metals orientated by $\sim 40°$ about a $\langle 111 \rangle$ axis to the deformed matrix, *i.e.,* the inital deformed state/structure of the metal, of a different crystallographic orientation, that the new growing grain is consuming. In this case, tilt boundaries are formed at the sides of growing grains which grow at a faster rate than the other sides. This is only the case for specific orientation relationships and will not make any significant difference to the microstructure of recrystallised polycrystals.

Annealing Twins

During recrystallisation of some materials, particularly the FCC metals with intermediate or low γ_{SFE}, (*e.g.,* copper and it's alloys), annealing twins are commonly formed. This twinning effect takes the shape of parallel sided lamellae. In FCC metals, these lamellae are bounded by {111} planes, otherwise known as coherent twin boundaries (CT) and at their ends by incoherent twin boundaries (IT) as shown in Figure 2.42. Twins can form throughout processing: during plastic deformation [228], solidification, recovery, primary recrystallisation, or grain growth following recrystallisation. Of course, twinning through plastic deformation and solidification is not considered to be annealing twins, although annealing twins are seen to correlate to the previous deformation structure [229].

Improvement of alloy properties through grain boundary engineering and thermomechanical processing control is typically interested in maximising low Σ boundaries such as $\Sigma 3$ twins (Σ refers to coincidence grain boundaries, where 1/n is the fraction of sites common to both grains). There are various mechanisms for twinning propagation during annealing which are important to highlight here. Gleiter *et al.* [230, 231], introduced that the movement of ledges on CT boundaries caused twinning, otherwise known as growth faulting. As the twin propagates by addition of the close-packed planes in a sequence such as ...ABCABC..., twin lamella only requires the nucleation and propagation of a ledge with low energy growth fault to change the stacking sequence:

$$\textbf{...ABCABC|BACBACBA|BCABC...} \tag{2.70}$$

A second mechanism is twinning through boundary dissociation, which was discovered by Goodhew *et al.* [232], where the authors found evidence of the following dissociations in gold:

$$\begin{aligned} \Sigma 9 &\rightarrow \Sigma 3 + \Sigma 3 \\ \Sigma 11 &\rightarrow \Sigma 3 + \Sigma 33 \\ \Sigma 33 &\rightarrow \Sigma 3 + \Sigma 11 \\ \Sigma 99 &\rightarrow \Sigma 3 + \Sigma 33 \end{aligned} \tag{2.71}$$

It has been noted that this type of boundary dissociation could occur from the emission of grain boundary dislocations [189].

The possibility of the observation of twinning will be important moving forward into the analysis stages of cogging and recrystallisation of FCC sample material, and what effect thermomechanical processing may have throughout the various stages of the alloy's lifetime.

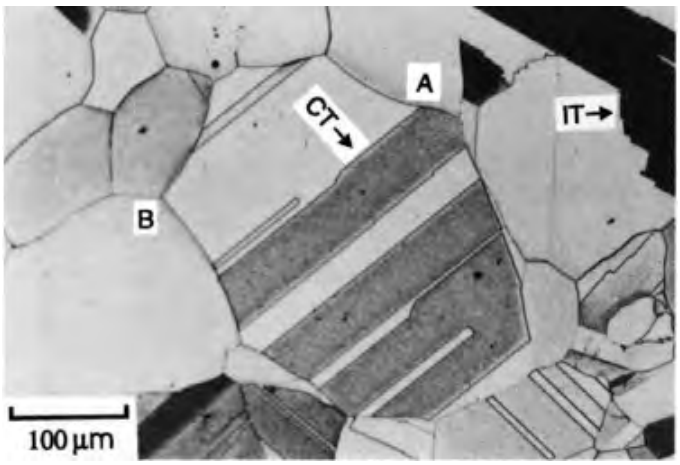

Figure 2.42: Annealing twins in annealed 70:30 brass. Some coherent (CT) and incoherent (IT) twin boundaries are marked. Adapted from Humphreys and Hatherly (courtesy of M. Ferry) [189]

2.2.5 Recrystallisation of Dual-Phase Alloys

Deformed Microstructure of Dual-Phase Alloys

For this work, it is crucial not to only discuss single phase material systems as part of this review, as most industrial alloys contain more than one phase, but it is also imperative to experiment with two-phase materials and must be discussed. These microstructures are constructed with a matrix phase and dispersed second-phase particles [189]. If the second-phase particles are involved with deformation, they will affect the microstructure, and will then influence annealing behaviour. The 3 key aspects of two-phase deformation in alloys are as follows:

1. Particle effect on the overall dislocation density. This may increase the driving pressure for recrystallisation.
2. Particle effect on the inhomogeneity of deformation in the matrix. This can be likely to affect the sites for recrystallisation.
3. The nature of the deformation structure in the vicinity of the particles. This determines whether or not particle-stimulated nucleation of recrystallisation (PSN) will be possible [189].

Throughout deformation of a two-phase alloy that contains second-phase particles, the dislocations will bend around the particles as shown in Figure 2.43. For particles of radius r and spacing λ along the dislocation line, the force (F) exerted on each particle is given by:

$$F = \tau b \lambda \tag{2.72}$$

where τ is the applied stress. If the strength of the particle is less than F, then the particle deforms, otherwise the dislocation reaches the semi-circular configuration of Figure 2.43(b), when the applied stress is given by:

$$\tau_0 = \frac{Gb}{\lambda} \tag{2.73}$$

which is known as the Orowan stress. From the bending, the dislocation then starts to fully encircle the particle, leaving an Orowan loop as shown in Figure 2.43(c). An Orowan loop exerts a shear stress on the particle, due to line tension, which is given approximately by:

$$\tau = \frac{Gb}{2r} \tag{2.74}$$

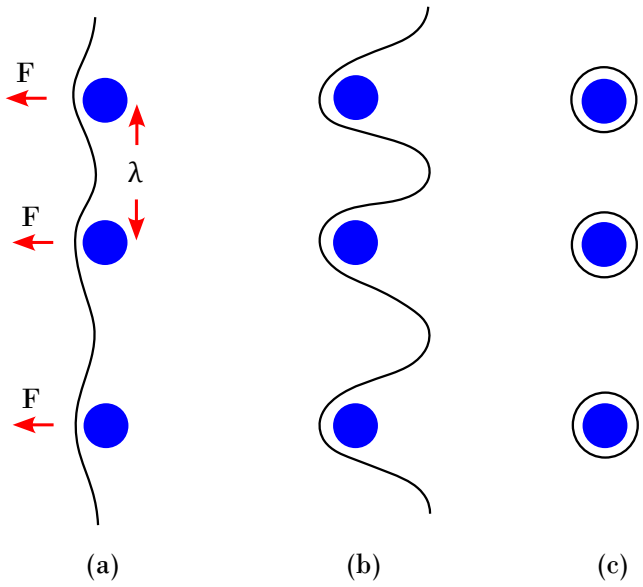

Figure 2.43: The formation of Orowan loops at second-phase particles. Adapted from Humphreys and Hatherly [189].

If the particle is strong enough to withstand this stress, it does not deform and the net result of the passage of a matrix dislocation is the generation of extra dislocation in the form of the Orowan loop, at the particle. If the particle deforms either before or after the Orowan configuration is reached, no extra dislocations are generated at the particle.

2.2.6 Grain Growth following Recrystallisation

Once primary recrystallisation is complete, generally the overall structure of polycrystals remains thermodynamically unstable and the recrystallised grains undergo further growth when at elevated temperature. The driving force for this growth is different to that of the stored energy of primary recrystallisation. It is derived from the total Gibbs free energy of the system. It is conventionally assumed that this energy is contributed from the grain boundaries, where the driving force is significantly less than that for primary recrystallisation. Due to the lower of driving force, boundary velocities subsequently are decreased, so the influence on grain boundary migration is driven more from the pinning effects of solutes and second-phase particles, in addition to any significant grain growth occurring at higher temperatures [189]. Texture is also an important factor that affect grain growth, as a well texture material contains many LAGB, which will further reduce the grain growth driving force. Finally, the specimen size can also impede grain growth as this can limit the grains to grow in a single direction, or through developing texture grooves at the surface further slowing grain growth rate [189].

Understanding of the grain growth kinetics, and stability, as well as the mobilities of grain boundaries is fundamental for the control of microstructures and final properties in metallurgical processing. Therefore, when researching the thermomechanical process of cogging, it is important to capture the key aspects of the current understanding of grain growth following recrystallisation of any sample material, so as that to create a clear picture of the effect of the processing parameters and their effects on the final microstructure.

Grain growth, as highlighted before, can be split into two categories: normal grain growth; and abnormal grain growth, otherwise known as secondary recrystallisation. The former, is known to be a continuous process where the microstructure grows uniformly, whereas the latter, is known to be a discontinuous process due to larger grains growing and cannibalising the smaller grains. Impingement of the large grains in this case allows for normal grain growth to occur afterwards [189]. The process of different grains growing, shrinking, and vanishing takes place under the geometrical and topological constraints of the grain network, attributed by grain boundary faces, triple lines, and quadruple points [233]. For many polycrystalline materials, the grain diameter d varies with time t according to:

$$d^n - d_0^n = Kt \tag{2.75}$$

where d_0 is the initial grain diameter at $t = 0$, and K and n are time-independent constants; the value of n is generally equal to or greater than 2 [192].

For the understanding of grain growth kinetics, it is important to discuss interfacial energies between grains. Excess free energy of interfaces, in almost every circumstance, provides a driving force for the reduction in total surface area, which is indicative of grain growth, but not recrystallisation. When considering interfacial energy, the vector sum of the forces must be zero to satisfy equilibrium:

$$\gamma_1 b_1 + \gamma_2 b_2 + \gamma_3 b_3 = \vec{0} \tag{2.76}$$

where γ is the interfacial excess free energy. This can be rearranged into the formulation of the Young equations (sine law):

$$\frac{\gamma_1}{sin\chi_1} = \frac{\gamma_2}{sin\chi_2} = \frac{\gamma_3}{sin\chi_3} \tag{2.77}$$

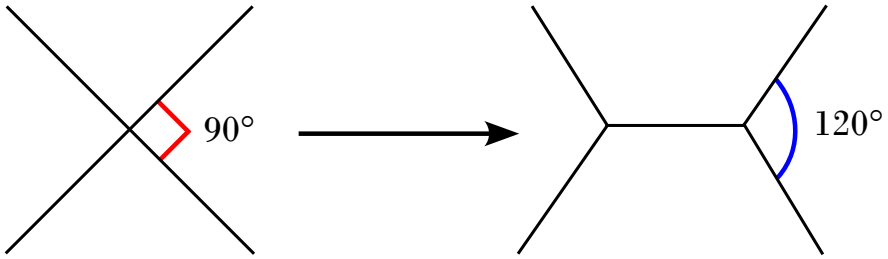

Figure 2.44: Splitting of 4-fold junction into triple junctions. Adapted from Humphreys and Hatherly [189].

If the energies of the 3 boundaries are known, the dihedral angles can then be calculated through:

$$sin\chi_2 = sin\chi_2 \frac{\gamma_3}{\gamma_2} \tag{2.78}$$

$$\begin{aligned} \gamma_1 &= \gamma_3 cos\chi_2 + \gamma_2 cos\chi_3 \\ &= \gamma_3 cos\chi_2 + \gamma_2 \sqrt{1 - sin^2\chi_3} \\ &= \gamma_3 cos\chi_2 + \gamma_2 \sqrt{1 - sin^2\chi_2 \left(\frac{\gamma_3}{\gamma_2}\right)^2} \end{aligned} \tag{2.79}$$

For isotropic Gibbs free energy, 4-fold junctions split into two 3-fold junctions with a reduction in free energy, as seen in Figure 2.44.

The fundamental von Neumann-Mullins law [234] relates the grain area rate of change in a 2D polycrystalline microstructure to the number of neighbouring grains [235], creating the widely known, "N-6," rule [233]. The classical von Neumann-Mullins law is as follows:

$$\dot{A} = -m_{gb}\gamma_{gb}\left(2\pi - \frac{\pi}{3}N\right) = m_{gb}\gamma_{gb}\frac{\pi}{3}(N-6) \tag{2.80}$$

where the area of a polygonal grain is given by $\dot{A}$ and the number of sides or neighbours of that grain and the number of triple points, respectively, is given by N. The grain boundary mobility is described as m_{gb}, and the grain boundary surface tension as γ_{gb}. This "N-6" rule states that for n>6, the grain will grow; and for n<6, the grain will shrink under the condition that the average grain area increases linearly with time, *i.e.,* for normal grain growth. The von Neumann-Mullins law has been validated for 2D grain-growth across various experimental, theoretical, and simulated studies [201, 210, 236]. Streitenberger *et al.* highlights that from this rule, it can also be derived that the rate of grain size change as a function of the number of neighbouring grains for 2D and 3D polycrystals coincides with the N-6 rule and was found to be in good agreement with simulation results [233].

Grain Boundary Engineering

It is known that specific mechanical and physical properties of polycrystals are dependent upon the constituent grain boundaries, making the engineering of these boundaries of industrial importance. The properties of the low energy LAGB are different from those of HAGB, and it is well known that the inclusion of these boundaries may improve the performance of the material. These boundaries may improve the properties of the material with the following: lower rate of grain boundary sliding during creep; high temperature fracture resistance; lower electrical resistivity; increased corrosion resistance; increased stress corrosion resistance; and increased solute segregation, precipitation, and intergranular embrittlement resistance [189].

Watanabe [237] first proposed that grain boundary distributions could be controlled to improve material performance through thermomechanical processing, which gave rise to grain boundary engineering (GBE). GBE has been and still is a very active field of study, especially for metals of

medium and low γ_{SFE} [238]. This branch of materials engineering is closely tied to this work, as the focus of thermomechanical control is for the purpose of improving material properties, and thus greater control over the grain boundary distributions.

Xuanyuan *et al.*'s recent work [239], on the tuning of microstructure and mechanical properties of a TiAl-based alloy through GBE proves the validity and ongoing interest of research in this area. It is also interesting that the methodology used in forging for specific grain boundaries is akin to that of the cogging process. There have been countless studies throughout the past 40 years on the subject of material improvement through GBE [240–243].

Thermomechanical processing of alloys to increase the fraction of low Σ boundaries encompasses both recrystallisation and grain growth, and often utilises many stages of deformation and annealing to produce the final improved result. In many cases, in addition to the fraction of low Σ boundaries, their spatial distribution is also important for property improvement [189]. The example of this given by Humphreys and Hatherly, is that if failure was to occur along the grain boundaries, it is important that the low Σ boundaries are space appropriately to break up the network of the failing boundaries [189]. Therefore, the 3D relationships and connections between boundaries is also crucial to GBE [244–246].

It has been highlighted that the underpinning science behind thermomechanical processing schedules used in grain boundary engineering is "poorly understood" [189]. Specifically controlling boundary character distributions through recrystallisation is less predictable than grain growth effects on the boundaries.

This is another corroborating example emphasising the gap in knowledge surrounding thermomechanical processing of metals and alloys. Cogging is one such thermomechanical process that is poorly understood in terms of control of the deformation effect on the microstructure, as well as tailoring the recrystallisation and grain growth effects to achieve the desired properties.

2.2.7 Dynamic Recrystallisation

Dynamic recovery and recrystallisation (DRX), also known as softening or restoration processes, may occur throughout hot deformation. DRX refers to the formation of new, strain-free grains in a material during deformation and their subsequent growth until the material is completely recrystallised. During deformation, these phenomena are named dynamic recovery and dynamic recrystallisation to separate them from the similar post-deformation static annealing processes which have been discussed previously. Although there are many similarities between static and dynamic processes, simultaneous deformation and softening mechanisms lead to some vital differences. Despite being of great industrial interest, experimental studies and theoretical models have found difficulty in studying dynamic processes [189]. This section will focus on DRX as dynamic recovery has been previously discussed.

The importance of restoration processes lies in the flow stress of the material being lower throughout deformation, meaning the material is easier to deform as well as influencing the texture and grain size. DRX can also occur during creep deformation, with the key distinction between hot working and creep being the strain rate [189]. Typically, hot working is done in the strain rate range of $1 - 100s^{-1}$. While creep strain rates are usually below $10^{-5}s^{-1}$, it is found that there are still many similarities in the recrystallisation mechanisms.

Discontinuous dynamic recrystallisation occurs when new grains originate at the old grain boundaries. However, as the material deforms, the dislocation density of the new grains increases, in turn reducing the driving force for further growth, and the recrystallising grains stop growing [189]. Meanwhile, nucleation of more grains at the migrating boundaries can also inhibit growth. This nature of DRX can be named a discontinuous process as there are distinctive nucleation and growth steps.

Humphreys and Hatherly [189] cover the main characteristics of DRX in their book and are as follows:

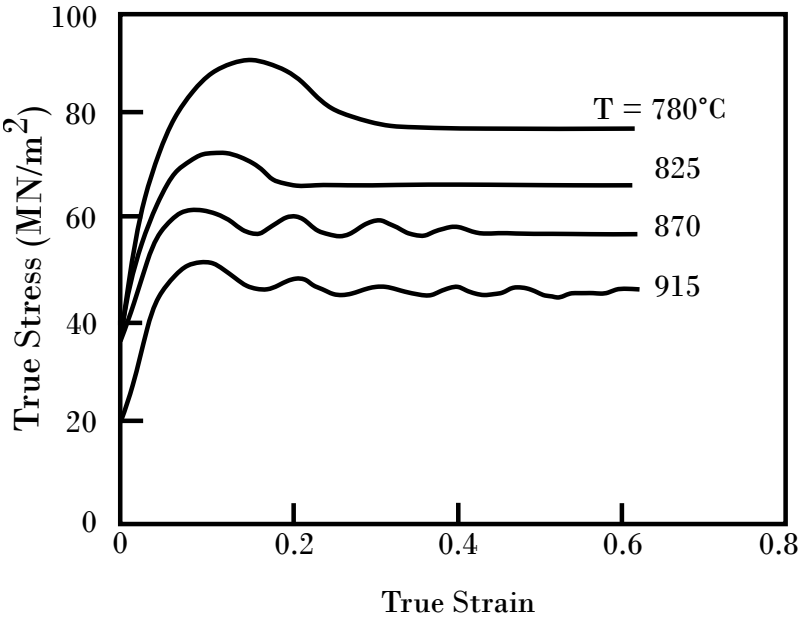

Figure 2.45: The effect of temperature on the stress-strain curves for 0.68wt.%C steel, deformed in axisymmetric compression, $\dot{\varepsilon} = 1.3 \times 10^{-3} s^{-1}$, [248]

1. The stress-strain curve for a material which undergoes dynamic recrystallisation generally exhibits a broad peak that is different to the plateau, characteristic of a material which undergoes only dynamic recovery.

2. A critical deformation (ε_c) is necessary to initiate dynamic recrystallisation. This occurs before the peak (σ_{max}) of the stress strain curve.

3. σ_c decreases steadily with decreasing stress, whereas at creep strain rates the ε_c may increase again [247].

4. The size of dynamically recrystallised grains (D_R) increases monotonically with decreasing stress.

5. The flow stress (σ) and D_R are almost independent of the initial grain size (D_0), but in material with smaller starting grain sizes, the kinetics of dynamic recrystallisation are accelerated.

6. DRX typically originates at grain boundaries, but for very low strain rates and large starting grain sizes, intragranular nucleation becomes important [189].

The overall microstructural evolution that is important to understand and capture when discussing is the general characteristic that nucleation typically happens at existing HAGB, as shown in Figure 2.46. New grains are then formed at the boundaries of these new grains, (Figure 2.46(b)), and this forms a thick band of recrystallised grains. If a large discrepancy in D_0 and D_R is present, then a resultant 'necklace' structure of grains may be created (Figure 2.46(c)), leading to the all of the grains being eventually recrystallised (Figure 2.46d). The average size of the DRX grains does not change as recrystallisation proceeds, which differs from static recrystallisation processes.

Continuous Dynamic Recrystallisation

Continuous dynamic recrystallisation (CDRX) is the general term given to a group of mechanisms that differ from the traditional nucleation and growth at prior boundaries where, under certain conditions, a microstructure of HAGB may develop under hot deformation [189].

One form of CDRX is known as rotation recrystallisation, or progressive lattice rotation, that is seen in material where the dislocation migration is slow either due to a lack of slip systems, or solute drag. It should be noted that this form of CDRX is strain-induced and is unrelated to sub-grain rotation occurring during static annealing. Geometric dynamic recrystallisation is another form of CDRX that occurs during annealing alloys that have underwent large strain deformation.

Throughout dynamic recovery, grain boundaries form serrations which have a similar form to the sub-grain size. If the material undergoes a large reduction in cross section, *e.g.,* hot compression, then the original grains become flattened or elongated as shown schematically in Figure 2.47. Due to the sub-grain size during high temperature deformation being almost independent of strain [189], the ratio of HAGB increases with strain, and eventually the boundary serrations will be comparable with the grain thickness seen in Figure 2.47(b). Eventually, as Figure 2.47(c) shows, interpenetration of the boundaries will occur, leaving a microstructure of small equiaxed grains which are comparable to the sub-grain size.

This phenomenon differs from discontinuous dynamic recrystallisation as an equiaxed microstructure constituted of HAGBs is formed without any new microscopic recrystallisation mechanisms. Crystallographic texture is one element often used to determine the occurrence of geometric dy-

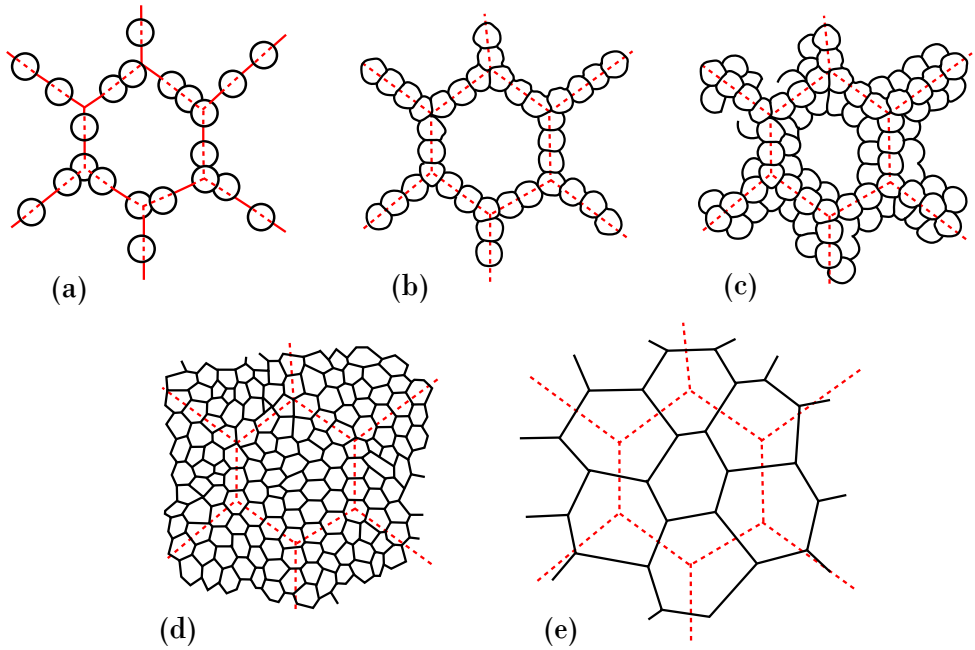

Figure 2.46: The evolution of microstructure during DRX (a)-(d) Large initial grain size, (e) small initial grain size. The dotted lines show prior grain boundaries. Adapted from Humphreys and Hatherly [189].

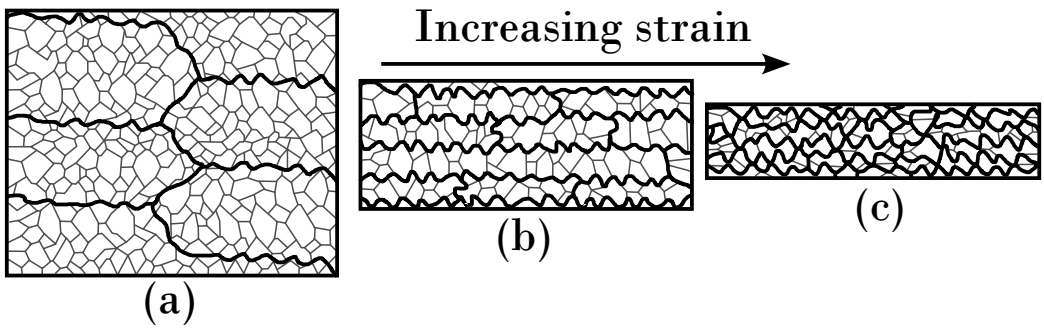

Figure 2.47: Geometric dynamic recrystallisation. During deformation, the serrated HAGBs (thick lines) become closer, while the sub-grain size remains about the same. Impingement of the HAGBs occurs later, resulting in a microstructure of primarily HAGB. Adapted from Humphreys and Hatherly [189].

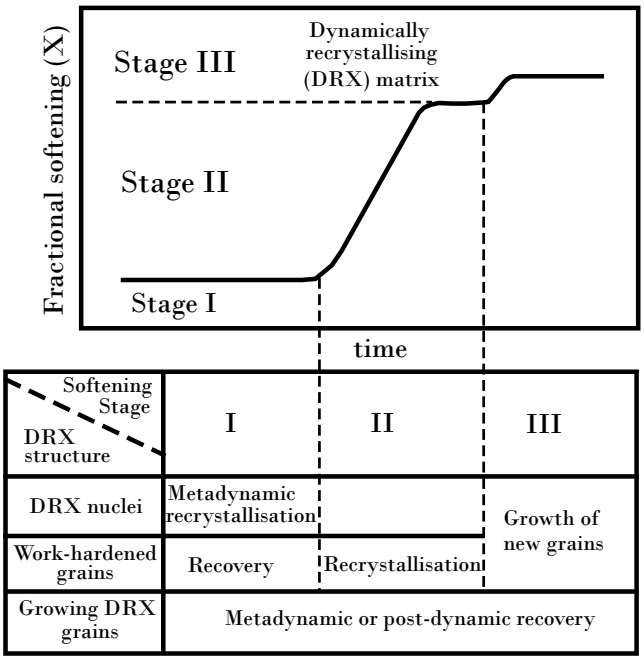

Figure 2.48: Schematic relationship between softening and key restoration processes. Adapted from Xu *et al.* [250].

namic recrystallisation as opposed to conventional discontinuous recrystallisation. Discontinuous recrystallisation textures typically differ from the deformation texture, whereas, as there is little HAGB migration during geometric dynamic recrystallisation, the texture remains almost the same.

Metadynamic Recrystallisation

Recrystallisation nuclei will form if a material experiences a strain greater than the critical strain for DRX (ε_c). If annealing continues once straining has halted, these nuclei will grow immediately into a heterogeneous and partially dynamically recrystallised matrix; this is known as metadynamic recrystallisation [249]. The resultant microstructure at this stage of DRX will be heterogeneous and formed of:

1. **Region A** - Small dynamically recrystallised grains (nuclei) which are mostly free of dislocations.
2. **Region B** - Larger dynamically growing grains of intermediate dislocation density (ρ_m).
3. **Region C** - High dislocation density ρ_m material that is unrecrystallised.

These different regions will have respectively unique behaviour when annealing, where the wider annealing kinetics and grain size distributions could be extremely complex. For example, Sakai *et al.* [251, 252] have found and categorised different annealing stages in hot-forged copper, nickel, steels where:

1. **Region A** - these small grains may continue growing during the first stages of post-forging annealing through metadynamic recrystallisation.
2. **Region B** - these grains will recover, if their dislocation density (ρ) is below a critical value (ρ_{RX}) which is known as metadynamic recovery. If $\rho > \rho_{RX}$, then these areas will undergo static recrystallisation.

3. **Region C** - will undergo static recovery and then static recrystallisation. It may additionally go through further grain growth once fully recrystallised, this can be seen in Figure 2.47.

Control of these recrystallisation phenomena and mechanisms is of great industrial and research interest. Continuous research efforts are made therefore into the thermomechanical processing, grain boundary engineering, and recrystallisation of materials. This leads into a review of the state-of-the-art thermomechanical processing used for ingot-to-billet conversion. This point of the alloy's lifecycle is crucial for any subsequent processing, as the microstructure and strain effects can carry through to the final part.

2.3 Review of Ingot to Billet Conversion

2.3.1 Introduction

After discussing both the background of alloy processing and the groundwork of recovery, recrystallisation, and grain growth pertinent to the current work, it is crucial to refocus on thermomechanical processing (TMP) and billet manufacture. Hot open-die forging, specifically the cogging process, will be the key focus of this section of review. Aiming to realign attention into the literature on the state-of-the-art of the lesser researched ingot-to-billet conversion stage.

The ingots generated through remelting are not suitable for mechanical purposes in their original state. They need to undergo TMP to break up the as-cast structure and decrease the grain size to a suitable level, typically from a few tens of millimeters to a few tens of microns [1]. This transformation process, referred to as ingot-to-billet conversion, is commonly accomplished through the cogging technique. During cogging, the diameter, or cross-section, of the ingot is reduced by a factor of approximately 2, in turn increasing its length. An example of one of these industrial ingot-to-billet conversion, *i.e.,* cogging, processes during forging can be seen in Figure 2.49(a).

The ingot-to-billet transformation occurs through a series of forging stages, otherwise known as heats or passes. Initially, the ingot is placed inside a furnace and heated to the appropriate elevated forging temperature. Once removed from the furnace, it is subjected to a compressive force between two flat dies. These dies compress the material, inducing deformation both within

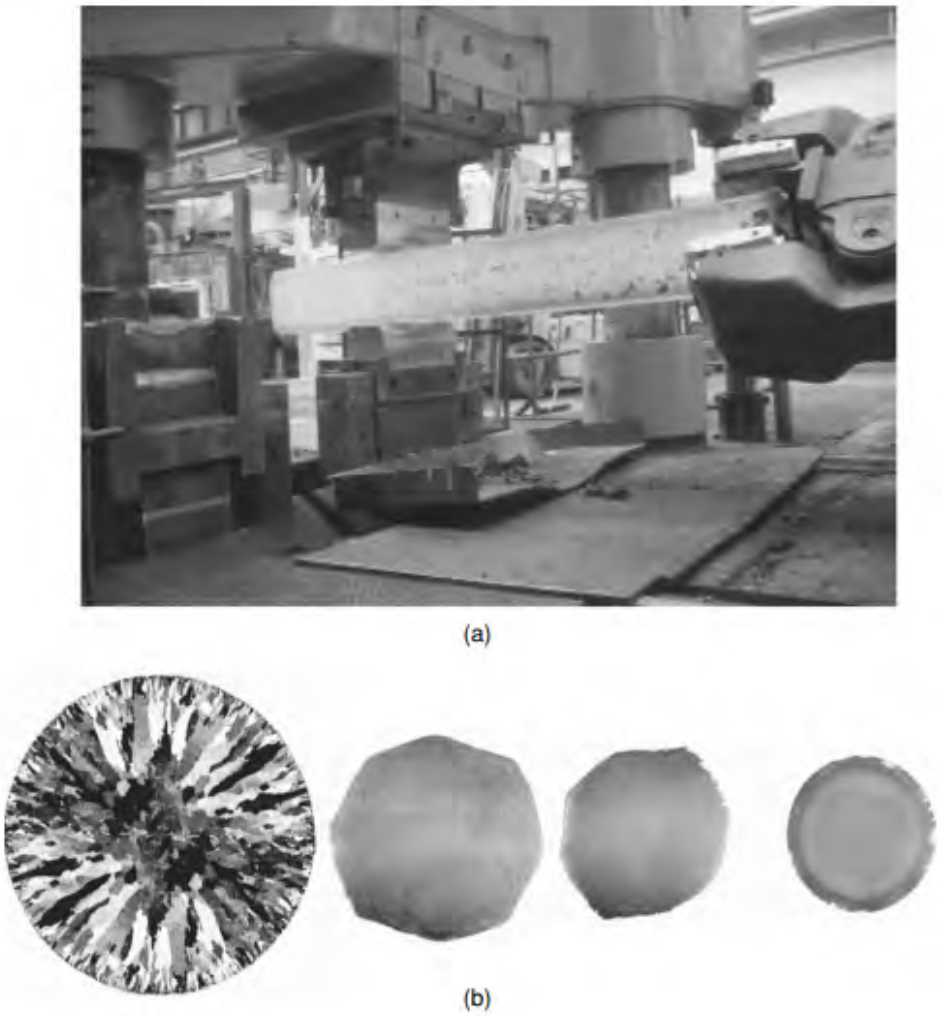

Figure 2.49: (a) Cogging operation for the TMP of a superalloy billet. (b) Cross-sections of the billet throughout various stages of processing, with the initial unworked billet on the left. Adopted from Reed - Courtesy of Mark Roberts [1]

and outside the plane of the dies. Typically, this pattern is repeated as the ingot is rotated through 90°, 45°, and one final 90° turn, presented progressively in Figure 2.49(b). At the end of this sequence, the ingot assumes an octagonal, or square cross-section. The deformation process leads to significant recrystallisation, resulting in a finer grain structure. After reheating, the entire process is repeated [1].

Approximately, up to seven passes may be required to reduce a 60 cm diameter ingot to a final 30 cm billet. In later passes, a temperature below the relevant superalloy solvus, or transus in titanium alloys, is used to prevent excessive grain growth after deformation, *e.g.,* 1010 °C for the δ phase in IN718 Ni-based superalloy. Typically, a final rounding operation is carried out before slicing the billet for subsequent forging processes. Using IN718 Ni-based superalloy as an example, initially the grain size is approximately ASTM000 (1 mm+), but by the beginning of the third pass, it has been reduced to around ASTM0 (0.35 mm). A grain size of ASTM5 or 6 (40–60 µm), is achieved by the end of the process.

2.3.2 Thermomechanical Processing of Single and Dual-Phase Alloys

For this work, it is key to have a clear general understanding material processing routes when discussing ingot-to-billet conversion. More specifically, a greater level of understanding should be reached for processing the alloys used for experimental study.

Recently, studies of emerging routes, such as precision investment casting and additive manufacturing (AM) of titanium alloys, have increased as they have advantages over forging in terms of material, energy usage, and speed of manufacture [253–255]. However, they still cannot produce the required properties for many structure-critical applications. Therefore, conventional thermomechanical processing routes with data informed digital twins, combining constitutive models and forging data with material characterisation, are at the forefront of current research [256].

These processes involve subjecting material to various deformation and heating processes, leading to an improvement in the mechanical properties of the material. TMP is ultimately used to increase strength, toughness, and ductility properties in metal alloys. The effectiveness of TMP can be limited by the initial microstructure of the material, as well as its composition and thermal history. Therefore, it is important to conduct a detailed analysis of the material prior to TMP to determine its suitability for processing.

The processing of the single-phase alloy copper C101 and aluminium Al6060 alloys, used in this study as starting material for proof of concept analysis, typically involves extrusion, or sheet metal forming processes (*e.g.,* rolling), since these alloys are used for their higher ductility properties. Full TMP of these alloys in the form of ingot-to-billet conversion is usually not carried out, except in some wrought Al alloys where it is usually done by the forming process itself. However, there are also studies that explore general TMP of copper [257, 258], copper powders [259] and aluminium 6000 series alloys [260].

While the literature favours the processing of dual-phase steels and titanium alloys, pertinent to this work is the discussion of $\alpha + \beta$ Ti-6Al-4V alloys. As this is one of the primary alloys used to simulate the ingot-to-billet conversion process in this study, it is fundamental to have an understanding and explore the processing routes, and any factors that may affect the material properties.

Titanium alloy components play a critical role in the future of aerospace, energy, and electric vehicle industries due to their high strength-to-weight ratio [261], outstanding fracture resistance and fatigue properties, and compatibility with carbon fibre composites [262, 263]. Ti-6Al-4V, also known as Ti-64, is an $\alpha + \beta$ titanium alloy that is most widely used and accounts for around half of the market share in titanium products used worldwide. Conventional manufacture of Ti-6Al-4V products requires a series of casting, open and closed-die forging, and rolling of bulk feedstock materials [67]. Unfortunately, these processes result in non-uniform microstructures and properties across different regions of the billets. As a consequence, approximately 70% of the processed material is subsequently machined away to achieve the desired microstructure and properties throughout the

final part, which is both costly and wasteful. Consequently, there is a widespread industry push to produce components with more homogeneous microstructures and evenly distributed properties using less material. The high-value manufacturing sector now needs the tools to objectively inform which processing route is optimum, be it state-of-the-art or emerging routes, *e.g.,* FAST-forge [264], based on key drivers such as cost, volume, energy consumption, resource use, and in-service properties.

Controlling grain size through TMP is an effective approach for achieving desired mechanical properties. The alteration in grain size is closely associated with dynamic, metadynamic, and static recrystallisation phenomena that occur during hot deformation discussed previously. The kinetics of recrystallisation are intricate and strongly influenced by process variables, including forging temperature, strain rate, initial grain size, and the extent of plastic deformation [265–267]. In recent years, there has been significant attention given to the development of microstructure evolution models in order to predict the distribution of grain sizes in finished components [268–272].

Finite element (FE) and combined crystal plasticity finite element (CPFE) modelling [273] has emerged as a primary focus of research in engineering materials research, primarily due to the costly, resource-intensive, and complex nature of conventional ingot-to-billet conversion processes [274,275]. Titanium alloys are one branch of metallic material that undergoes an numerous different TMP routes, with cogging being one key stage of this processing. For this work it is important to understand how these alloys are processed, and develop an understanding of how processing parameters can effect the end result, *e.g.,* the effect of strain path.

2.3.3 Review of $\alpha + \beta$ Titanium Alloys

Titanium alloys can be categorised into five distinct groups based on their microstructure characteristics: (i) α, (ii) near-α, (iii) $\alpha + \beta$, (iv) metastable β, and (v) β alloys. A pseudo phase diagram illustrates the stability regions of these phases, delineating the initiation and conclusion points of martensite formation, denoted as the M_s/M_f line in Figure 2.50.

When cooling from elevated temperatures, the transition through the β-transus phase triggers the $\beta \rightarrow \alpha$ transformation. The nature of this transformation depends on the cooling rate. A fast cooling rate surpassing the M_s/M_f threshold can result in either the nucleation and growth of α phase or a diffusionless martensitic transformation. Consequently, retaining a certain amount of β phase at room temperature becomes feasible. However, if cooling extends beyond the M_s/M_f line,

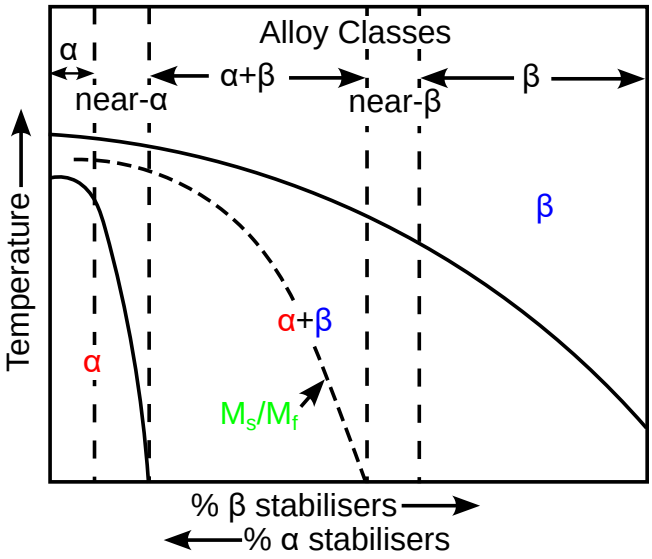

Figure 2.50: Schematic representation of titanium phase diagram as function of chemical composition (*i.e.,* α and β stabilising elements) and temperature, with the domain of stability of five different classes of titanium alloys highlighted [276].

complete retention of the β phase occurs.

$\alpha + \beta$ alloys contain a certain proportion of both α and β stabilisers, typically ranging from 4 to 6 wt.% [277]. This composition expands the $\alpha + \beta$ phase field, enabling the retention of a certain portion of the β phase at room temperature. Consequently, depending on the specific thermomechanical processing employed, a diverse array of microstructures can be achieved within this alloy category, resulting in a wide spectrum of desired mechanical properties. α+β alloys exhibit favourable combinations of mechanical characteristics and resistance to degradation. Notably, they offer medium to high strength, good toughness, and a high level of resistance to fatigue and creep fracture [22]. One of the most commonly used $\alpha + \beta$ alloys is Ti-6Al-4V, which finds extensive applications in components like fan discs, low-pressure compressor discs, and compressor blades in jet engines [278]. Ti-6Al-4V alloys are also used across the medical field, including orthodontic appliances and joint replacements [279].

Mechanical properties (*e.g.,* yield stress, ductility, fracture toughness, *etc.*) and resistance to degradation in $\alpha + \beta$ titanium alloys are very sensitive to the microstructure (distribution and geometrical arrangement of the two phases), as well as the crystallographic texture of the α phase [280]. Titanium alloy microstructure is mostly influenced by the chemical composition and the thermomechanical processing history of the material, (*i.e.,* the material fingerprint or digital-passport), *e.g.,* the strain path history. The microstructure constituents are distinguished based upon their crystallographic structure, grain size and morphology. The $\beta \rightarrow \alpha$ transformation can occur through a diffusion controlled mechanism or a diffusionless shear process, each resulting in different forms of α phase.

Primary α does not form by nucleation and growth from the β phase during cooling. Instead, it arises as the unaltered α phase when the alloy is heated into the $\alpha + \beta$ temperature range. The proportion of primary α diminishes as the temperature rises towards the β-transus. Extended exposure to temperatures within the dual-phase $\alpha + \beta$ region leads to an equilibrium between the fractions of α and β phases, driven by diffusion-controlled $\beta \leftrightarrow \alpha$ transformations [281]. The remaining untransformed α phase is referred to as primary α. The morphology of primary α grains is influenced by whether the material has undergone thermomechanical processing. In non-deformed materials, primary α grains adopt a plate or lath structure, while deformed materials exhibit curved, or kinked, laths with varying degrees of spheroidisation [282]. In recrystallised materials, a fully globular structure can be achieved [22].

Secondary α, also known as transformed β, emerges during the cooling of the β phase as it passes through the β-transus. The α phase rapidly nucleates and grows along the boundaries and triple junctions of the β grains. Within the β grains, a slower diffusion-driven transformation occurs, giving rise to α lamellae interspersed with the β phase, which is retained due to the partitioning of the β-stabilising elements. Aggregates of α and retained β lamellae can come together to form what is known as a colony, serving as a larger structural unit within the microstructure. The rate at which the material cools from elevated temperatures is a crucial factor in determining the resulting lamellar structure. Slower cooling rates promote the growth of laths, yielding a coarser structure, whereas faster cooling rates encourage the nucleation of thinner laths, resulting in a finer structure [281]. With faster cooling rates, colonies can nucleate not only near the boundaries of β grains but also within the β grains themselves, leading to the formation of a Widmanstätten structure, *i.e.,* "basketweave structure" [283].

The α' (alpha prime) phase is a product of the martensitic transformation, which involves rapid cooling and occurs without diffusion, from the β phase. To initiate this transformation, a swift cooling process, such as water or oil quenching, is essential, and it is more effective when the concentration of β stabilisers is relatively low [22]. The α' phase shares the same HCP (*i.e.,* hexagonal close-packed) structure as the α phase. However, it takes on a fine acicular form, resembling needle-like structures, and possesses a high density of dislocations and stacking faults [261].

The α'' (alpha double prime) phase represents an alternative martensitic structure that can be produced when quenching titanium alloys with elevated levels of β stabilisers, starting from lower

temperatures. During the rapid cooling of a titanium alloy from lower temperatures, a larger proportion of β stabilisers remains within the alloy, consequently lowering the M_s/M_f temperature and facilitating the creation of α'' martensite. This phase possesses an orthorhombic crystal structure and exhibits a lower level of hardness compared to α' martensite [261].

Dual-phase α/β alloys typically exhibit three primary microstructures: lamellar, equiaxed, and bimodal. The fully lamellar structure, also known as the β-annealed structure, can be achieved during the final stage of processing through annealing at temperatures above the β-transus. This structure consists of colonies comprising α and β plates within the original β grains, with α phase also present at the boundaries of these prior β grains.

The critical factor influencing the formation of such a microstructure is the rate at which the material cools from temperatures above the β-transus, which is within the β phase field. Indeed, as the cooling rate increases from these elevated β-transus temperatures, the size of the plates, the dimensions of the colonies, and the thickness of the α layer at the β grain boundaries all decrease [22].

Processing of $\alpha + \beta$ Titanium Alloys

Extraction of titanium from its oxide forms (*i.e.,* ilmenite or rutile) is carried out over a series of chemical processes. Firstly elements such as oxygen and iron are removed through carbochlorination into a vapour of $TiCl_4$ [284], which is then reduced at high temperature by a molten magnesium vapour to create metallic titanium sponge. Impurities are then removed by leaching or vacuum distillation [285].

Titanium alloys are then produced through crushing of the titanium sponge and incorporating alloying elements. To ensure a satisfactory level of homogeneity in the resulting ingot, a minimum of two melting steps is typically required. Precise control of these operations is imperative to yield a high-quality ingot while preventing the segregation of alloying elements and the occurrence of defects, including high-density inclusions, beta flecks, and voids [262].

Thermomechanical processing of titanium alloys comprises two main stages:

1. Primary working (*i.e.,* ingot-to-billet conversion), which converts the ingots into mill products like billets, flat rolled items, or bars [22].

2. Secondary working, encompassing forging and heat treatments to achieve the desired final product shape.

Schematic diagrams of the primary working process routes for different titanium alloy microstructures are presented in Figure 2.51. The initial process of breaking down the ingot involves preheating followed by cogging at temperatures approximately 100-150 °C above the β-transus. These elevated temperatures facilitate substantial plastic deformation without the need for excessive force. The primary objective of this operation is to homogenise the microstructure and decrease the size of the as-cast β grains.

Next, forging is carried out within the $\alpha+\beta$ temperature range, followed by annealing above the β-transus. This is followed by a controlled cooling process to reach room temperature. The objective here is to achieve a microstructure characterised by lamellar α phases within the recrystallised β structure. This operation has undergone extensive research to build a comprehensive understanding of static recrystallisation, texture development in the β phase, and the evolution of the transformed microstructure during cooling. This includes aspects like α variant selection and platelet thickness [263].

Lastly, a series of hot working and annealing steps are conducted within the dual-phase $\alpha + \beta$ temperature range to transform the lamellar structure into equiaxed grains, which possess increased ductility and are more suitable for subsequent forming operations [263]. Extensive research efforts

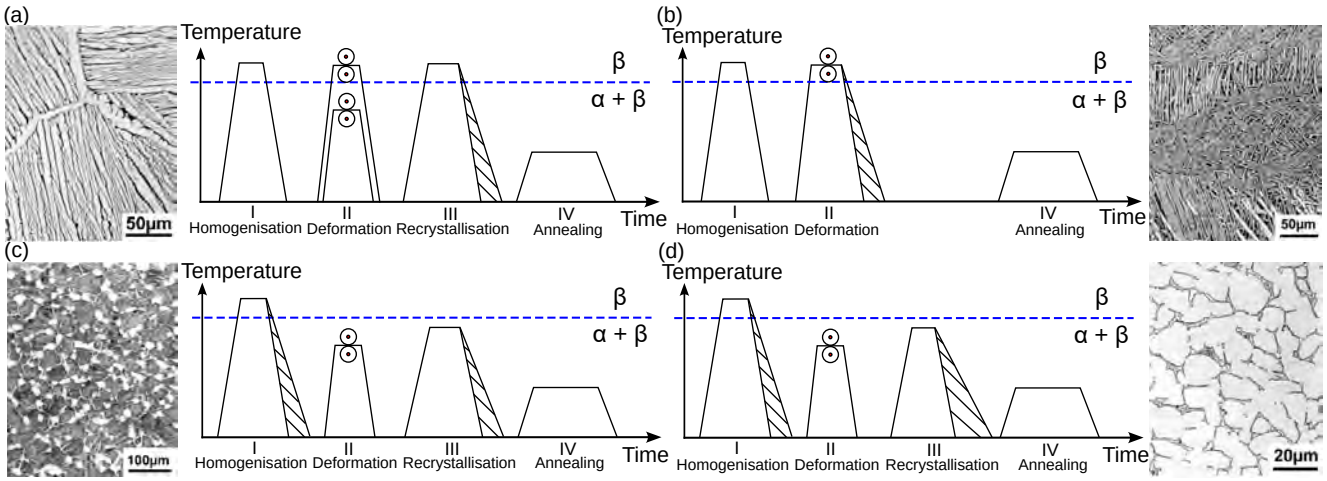

Figure 2.51: Schematic representation of processing route for (a) lamellar microstructures, (b) β processed microstructures, (c) bi-modal microstructures, and (d) fully equiaxed microstructures (slow cooling from bi-modal recrystallisation annealing temperature), of $\alpha + \beta$ titanium alloys. Adapted from Lütjering and Williams [22]

have been dedicated to uncovering the fundamental mechanisms governing plastic flow and deformation during this forging stage. This research has also aimed to characterise the kinetics of α phase globularisation and the evolution of microstructure and crystallographic texture in the material.

Subsequently, the mill products are shaped into final parts using processes such as ring rolling, extrusion, or closed-die forging. After the forging process, forged components typically undergo heat treatment. Different heat treatments have been developed to suit various applications, with each treatment capable of producing specific microstructures to achieve desired mechanical properties. Additionally, heat treatment can be employed to alleviate residual stresses within the material. Under certain conditions, aging may also take place, enhancing the strength of the alloy through the precipitation of particles, such as secondary α or Ti_3Al.

Effect of Strain Path

The alteration of the strain path during material processing introduces an extra variable that can modify both the microstructure and crystallographic texture, consequently influencing the mechanical characteristics of the final product [286]. The effects of a changing strain path have been explored through different materials processing techniques, *e.g.,* rolling and cross rolling in the works of Suwas and Gurao [286], extrusion by Yang *et al.* [287] and Tang *et al.* [288]. Davenport and Higginson [289] concluded from their review that the strain path throughout processing can influence the microstructural evolution of a material at room temperature, *e.g.,* deformation textures and dislocation sub-structures. For hot working conditions, the challenge in strain path research lies in quantitatively identifying the crucial parameters among the multitude of possibilities. Additionally, it involves determining at which specific industrial conditions strain path effects start to exert a significant influence. A further consideration that presents a challenge for metallurgists and researchers are the effects of the strain path history on the final microstructure and properties of a component.

The effect of thermo-mechanical history on hot compression behaviour and the result microstructures of a nickel-based superalloy was investigated by Gardner *et al.* [290] where single- and multi-pass specimens were compared. From the results of this study, it was established that a higher grain size was observed in the multi-pass specimens due to grain growth occuring during the inter-pass anneal. Additionally, Gardner *et al.* concluded that when reproducing forging processes in a laboratory setting, the previous forging history can generally be disregarded, as long as the material undergoes adequate DRX during the final pass [290]. This assessment from Gardner *et al.* could be an avenue of further investigation through the use of the apparatus designed as part of this work.

In the case of the processing of titanium alloys, the effect of strain path, and the thermomechanical history, have been reviewed. Reports indicate that strain levels ranging from 2 to 3 are necessary to achieve a fully globular microstructure [291]. However, employing methods like uniaxial compression or extrusion to attain such high levels of deformation results in considerable alterations in the shape and dimensions of the material. Moreover, these processes typically induce significant texture development, which is often undesirable. Additionally, extensive strains can trigger the initiation of defects such as cracks and cavities within the material. Therefore, non-monotonic deformation processes like cogging are preferred for the production of industrial products. In commercially pure titanium (CP titanium), altering the rolling direction triggers the activation of a greater number of slip systems. This, in turn, creates increased interactions among dislocations, resulting in reduced intragranular misorientation and consequently, a greater abundance of high-angle grain boundaries [292].

The process of globularisation in $\alpha + \beta$ titanium alloys is influenced by the strain path and has been investigated in various studies [293–296]. For instance, as depicted in Figure 2.52(a) and (b), there are notable differences in microstructures between torsion and reversed torsion when subjected to similar levels of deformation. It is evident that reversed torsion results in reduced globularisation kinetics. Additionally, Figure 2.52(c) demonstrates the impact of strain path on globularisation kinetics in other processes.

Salishchev *et al.* [291] and Zherebtsov *et al.* [298] studied multiaxial forging along three orthogonal directions as a means to induce a globular sub-micron crystalline structure in titanium alloys. Experiments were conducted at lower temperatures ranging from 450 to 800 °C, with a strain increment of 0.4. Between each forging cycle, the samples underwent quenching and machining to

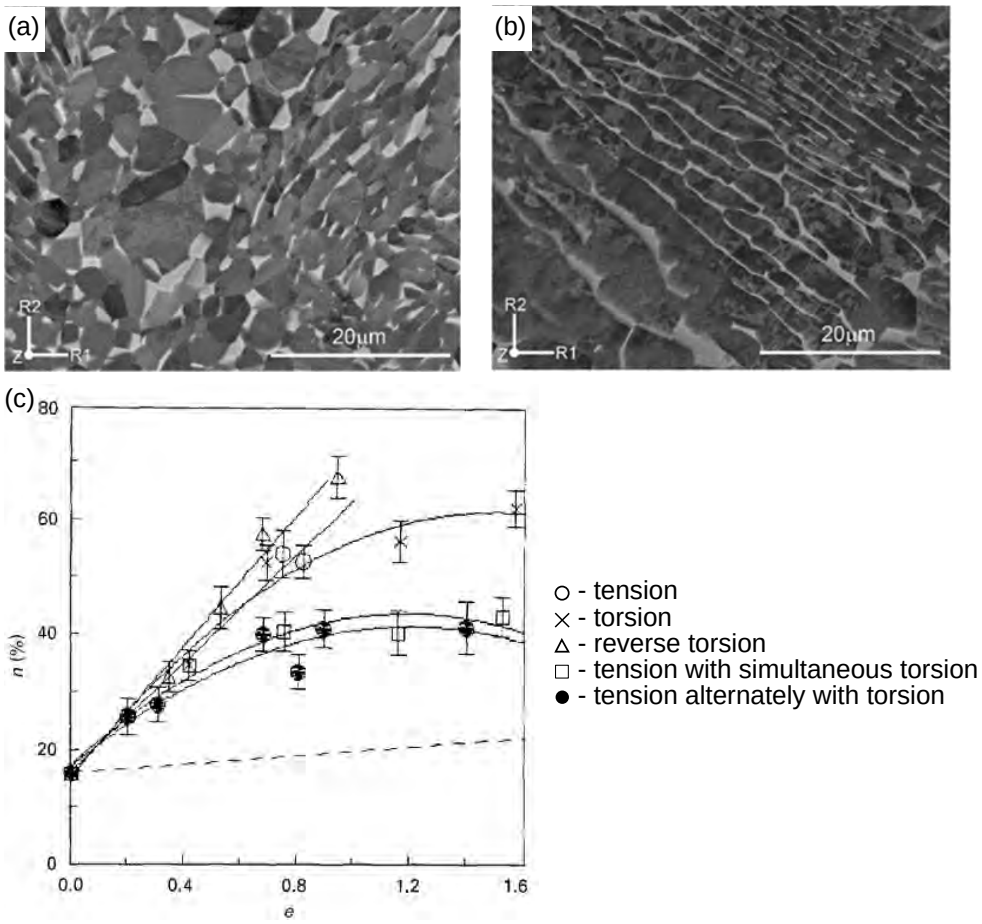

Figure 2.52: Resultant microstructures of $\alpha + \beta$ titanium alloy after applying a strain of (a) 0.5 in torsion and (b) 0.5 in reversed torsion [297]. (c) Fractions of equiaxed particles vs accumulated strain for various strain paths [294].

maintain straight edges consistently.

Globularisation was observed to occur after reaching a strain of approximately 3 in materials initially possessing a martensitic structure. Conversely, in materials characterised by a coarse lamellar structure, heterogeneous transformation occurred, leaving around 30% of laths intact by the end of the process. The evolution of the microstructure was closely associated with the formation of high-angle boundaries and incoherent inter-phase boundaries, whose prevalence increased notably with higher strain magnitudes, particularly when a change in strain path was introduced.

This alteration in strain path proved advantageous in activating a greater number of slip systems, aligning with previous findings by Bieler and Semiatin [299], as well as Mironov *et al.* [300] Their studies concluded that due to the presence of laths exhibiting a "stable orientation" concerning the loading direction, a change in strain path could indeed enhance the globularisation process.

Kim *et al.* [293] investigated the multi-axial forging of Ti-6Al-4V alloy and noted a strong dependency of the globularisation rate on the instantaneous microstructural changes - specifically, the thickness of laths and the fraction of phase - occurring during each compression step. These changes were attributed to the non-isothermal conditions, deformation cycles, and reheating cycles. Both forging temperature and initial lath thickness were identified as influential factors affecting the kinetics of globularisation. Notably, complete globularisation was only achieved in thin structures at elevated forging temperatures.

Throughout the forging process, a dual-phase titanium alloy experienced an effective strain of approximately 2.4. However, the localised strain at the microstructural level varied due to non-isothermal conditions and changes in strain path. Quantitatively comparing the kinetics of globularisation between forged materials and those resulting from other processes, such as uniaxial compression, proved challenging. Nevertheless, it is evident that when deformation occurs at lower temperatures (*e.g.,* 900 °C), the kinetics of spheroidisation are significantly slower compared to monotonic deformation processes (*e.g.,* compression testing).

In their study, Sheed *et al.* [301] did not observe any globularisation even after applying a strain of 1.5 through multi-directional forging. Instead, the material's microstructure predominantly consisted of non-deformed, kinked, and fragmented lamellae. These observed microstructural characteristics were interpreted as indicative of a significant amount of strain energy stored within the material due to the deformation process. This assumption was supported by the subsequent occurrence of globularisation following a 2-hour post-deformation annealing at elevated temperatures.

Reviewing the literature, it becomes apparent that achieving globularisation through multi-axial cogging is feasible, although there are noted differences in kinetics compared to monotonic deformations. Furthermore, limitations exist concerning the initial structure, which should ideally be fine lamellar or martensitic. However, these studies have primarily focused on the overall cogging process rather than delving into the specifics of individual steps involved, thus providing limited insight into the microstructural evolution throughout the process. Factors such as reheating frequency and duration, as well as the strain applied at each increment, have not been thoroughly investigated.

Moreover, the existing literature predominantly discusses the kinetics of globularisation, with less emphasis placed on understanding the mechanisms underlying variations in kinetics. Therefore, there remains a need for more comprehensive studies that explore the detailed mechanisms driving the evolution of microstructure during cogging operations. One of the published works from this study, aims to capture how future studies could utilise the designed experimental cogging apparatus to perform microstructure evolution studies to Ti-6Al-4V and other alloys of interest [302]. This work could act as a fundamental processing investigation element to aid understanding of the kinetics and effect of strain path in the cogging of engineering alloys in the future.

2.3.4 State-of-the-Art Review of Cogging

Process modelling, and the optimisation of cogging pass-scheduling, remains at the forefront of research in this area and is of interest to this work. In industrial open-die forging, pass-schedule

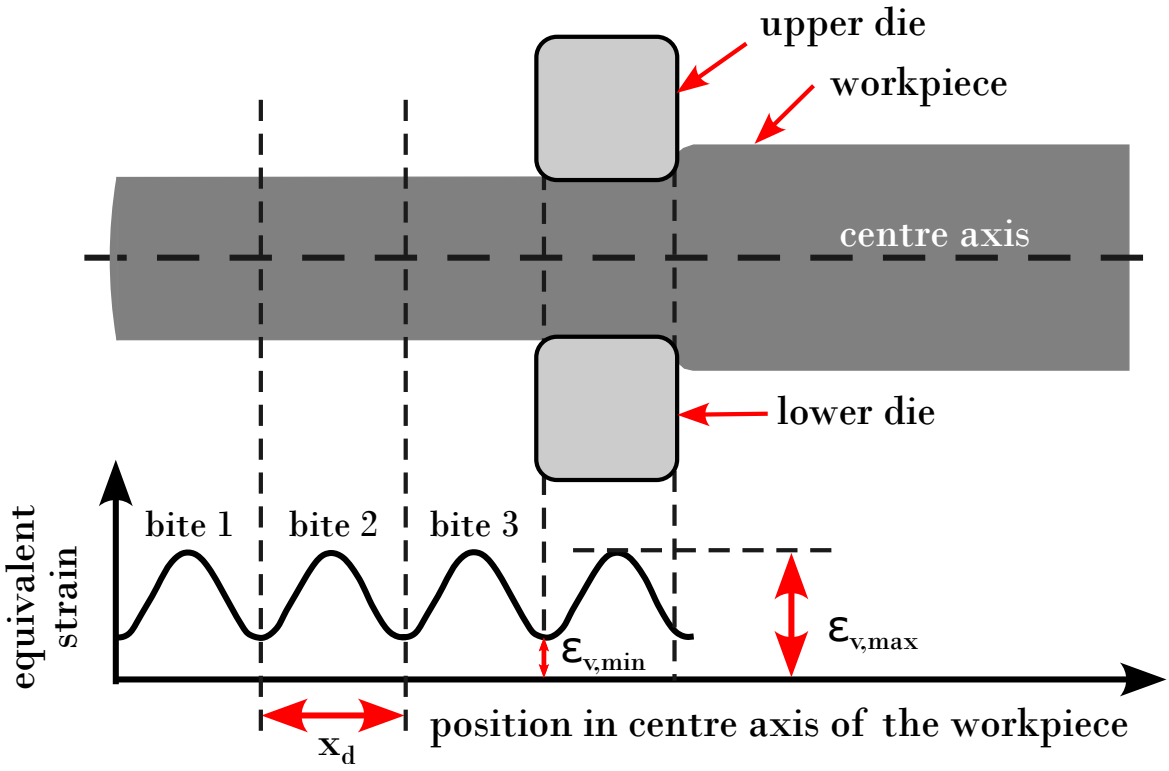

Figure 2.53: Calculation of the equivalent strain along the centre axis. Adapted from Wolfgarten *et al.* [308].

algorithms calculate forging schemes by defining the forging parameters as height reduction and bite ratio. Typically, the pass-schedule algorithms take into account the geometric changes occurring within the ingot. These changes are primarily described by fundamental principles such as volume constancy and the characterisation of material flow in the lateral direction *e.g.,* proposed by Tomlinson and Stringer [303] or Knap *et al.* [304].

Nieschwitz [305] and Fister [306] introduced early computer pass-schedule calculation software, which were based on fundamental investigations of material flow. These software programs enabled automated realisation of forging sequences. Over the years, these well-known calculation algorithms have been further refined and can now predict the average temperature of the ingot [307] or optimise the forging sequence by estimating void closure [132]. However, a common limitation of all these algorithms is that their application range and calculation results have limited relevance to the final properties of the workpiece. Typically, the calculations only provide information about the expected geometric changes of the ingot during the forging sequence, making it challenging to establish a clear relationship between the calculated forging sequence and the resulting properties.

To overcome the limitations of conventional pass-schedule calculations and the lengthy calculation times associated with FE analysis, rapid calculation models were developed. These models employ semi-empirical formulas to enable quick predictions of critical process parameters in open-die forging. Recognising that defects like voids primarily occur in the central region of the initial ingots, these models specifically concentrate on the centre axis of the workpiece when considering equivalent strain and microstructure. This approach facilitates faster calculation times while still addressing the crucial aspects of the forging process.

Wolfgarten *et al.* reported a new approach for the optimisation of pass-schedules using fast models [308], that were found to be able to predict equivalent strain and temperature accurately when compared to FE simulations. Wolfgarten also suggested that the optimisation through equivalent strain distribution is only useful to a degree, as further process parameters should be considered as impacts on the microstructure. This work concludes with a future idea of digital twin working alongside vision systems to update the press and manipulator in order to deal with any disturbances,

but this will require future optimisation and speeding up of predicting algorithms.

The principle of modelling equivalent strain first proposed by Siemer [310] is described as the equivalent strain distribution along the central axis of a workpiece using a $\sin^2$-function. Subsequently adapted by Recker and Franzke [311] and further developed by Recker and Rosenstock [131, 312], Figure 2.53 presents the principle where each forging bite imposes its own $\sin^2$-function and it can be observed that the maximum equivalent strain can be found in the centre of each bite in the deformed material. Rosenstock optimised the model again accommodating shapes with a high width to height ratio, bite ratios greater than 1 and accounting for flow stress variations between the surface and core when dealing with inhomogeneous temperature distributions [308].

Current modelling capability has improved greatly in recent years, with FE models and CPFE models (*e.g.,* Agius *et al.*'s work on fatigue-dwells [313]) beginning to pick up even more traction with the implementation of machine learning neural networks alongside data driven multi-scale modelling [314, 315].

Presently, the difficulty with the relatively high quantity and cost of material for the investigation of open-die forging has limited research primarily to FE simulations. For example, Huang *et al.* created a model for the prediction of grain size evolution during cogging of Waspaloy and IN718 superalloys, presented in Figure 2.54. However there are also some microstructural studies of large upset cylindrical billets, truncated cones, and standard compression tests [8] that can be related to cogging. Reproducing industry strain levels in billets has been achieved using double-truncated cone ingot specimens as they can achieve higher localised strain due to their geometry. These of course are only upset, so only capture one strain path which is the same as standard laboratory compression testing. Therefore, these studies do not capture the kinetics of multi-directional loading seen in cogging operations.

In the production of superalloy turbine discs, after achieving a fine grain structure through ingot-to-billet conversion, the objective becomes shaping the metal into the approximate size and geometry of a turbine disc. The key concern at this stage is not to cause any excessive grain growth, and follow the three-stage forging process to finalise the disc components, consisting of:

1. Open-die upsetting, to create an axisymmetric billet of the desired thickness and cross-sectional area
2. Blocking by closed-die forging, to concentrate material into the desired locations across the billet
3. Final finishing via closed-die forging, producing the required disc shape.

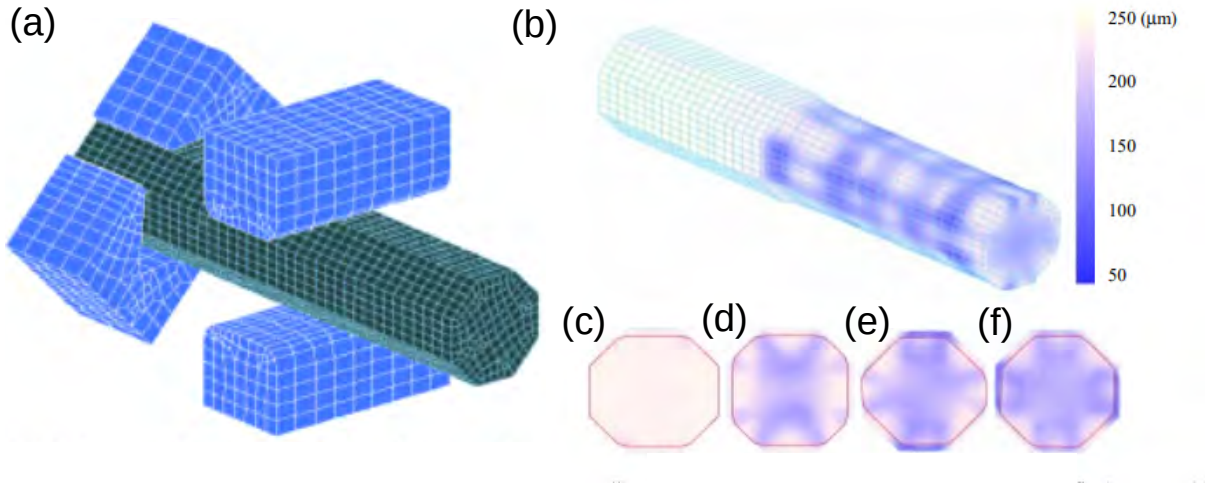

Figure 2.54: (a) Meshes used for FE simulation of the cogging process. FE predicted average grain size: (b) On the free surface after the final pass or within the workpiece after pass number (c) 1, (d) 2, (e) 3, or (f) 4. Captured from Huang *et al.* [309].

Throughout, the temperature is closely maintained near the alloy's relevant solvus point during forging. This meticulous temperature control ensures that any recrystallisation that takes place leads to a finer grain structure than what is attained during the conversion stage. After processing, the forged discs are either quenched in an oil, or water bath, or allowed to air cool.

One example of a recent open-die forging microstructural study on AD730 Ni-based superalloy by Coyne-Grell *et al.* used cylindrical billets at an intermediate stage of the ingot-to-billet conversion process to study recrystallisation mechanisms [266]. The billet specimen was subjected to a uni-axial upsetting at 1080 °C (sub-solvus for AD730) to a reduction of 50% and subsequently analysed. The authors found that within a single sample, under a single set of external TMP parameters, different local microstructures, particularly in different precipitation states, resulted in different recrystallisation mechanisms occuring [266]. In a second study by Coyne-Grell *et al.* the recrystallisation behaviour that occurs during slow cooling rate undergone by billets between super-solvus and sub-solvus open-die forging was investigated [267]. This is interesting because it is focused on an intermediate stage of ingot-to-billet conversion, rather than the more common studies on recrystallisation behaviour typically investigating the effect of heat treatments. Furthermore, these heat treatments are carried out following the oil, or water quenching, of closed-die forged components, which happens at a later stage in turbine disc manufacture [1]. This study is an example of how FE modelling can be used in conjuction with experimental compression testing to study ingot conversion, with the focus on the relationship between microstructural mechanisms, recrystallisation, and strain, as presented in Figures 2.55 and 2.56.

Another recent study by Schulz *et al.* [316] demonstrated significant improvements in the hot formability of Ni-based superalloy Udimet-720 by control of recrystallisation behaviour during ingot-to-billet conversion by varying heating and cooling. The introduction of slow cooling, over the typical solutionising and ageing processes, to promote discontinuous γ' over globular γ' has resulted in significant forging improvements, as can be seen in Figure 2.57. The generation of these discontinuous γ' grains seen in Figure 2.57(b) in this study has removed the defects previously seen in globular γ' forgings. The authors present a good example of the benefits of grain boundary engineering, as integrating discontinuous γ' precipitation into advanced manufacturing routes will allow for crack-free forging of complex components for turbine components at lower temperatures and forces, adding value economically and environmentally.

In industrial open-die forging, multi-tonne ingots are heated to a forging temperature before being placed inside heated dies (usually 450 °C) and deformed. Due to their large mass much of the heat throughout the ingot is retained. The edges that become colder throughout forging are machined away, keeping the refined centre of the billet for use in the final component. Although, there is still difficulty in achieving full microstructural control, homogeneity, and specific textures.

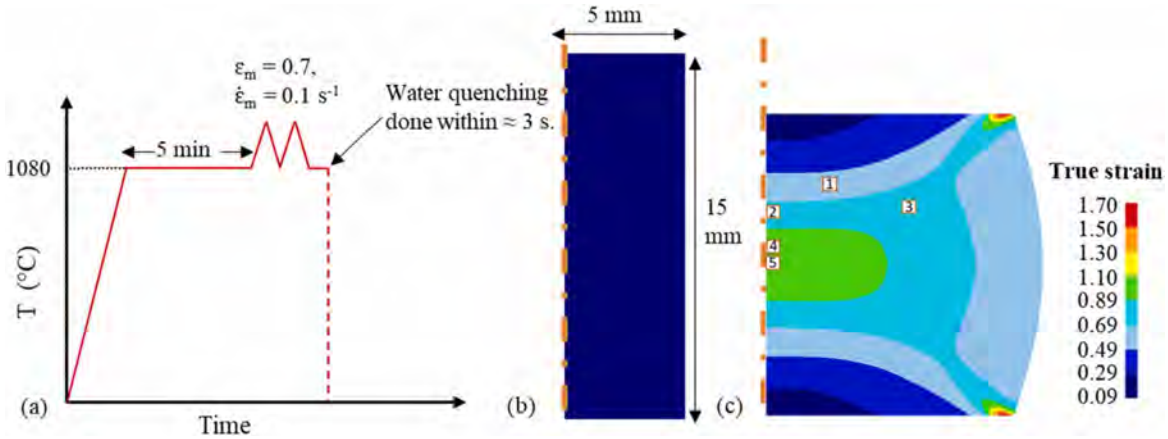

Figure 2.55: (a) Schematic overview of the compression trial for Ni-based superalloy AD730, (b) a sketch of the sample geometry prior to compression with all dimensions, and (c) the strain distribution after compression predicted by the FE simulation, with the regions from which the EBSD data were collected highlighted and numbered. Captured from Coyne-Grell *et al.* [266]

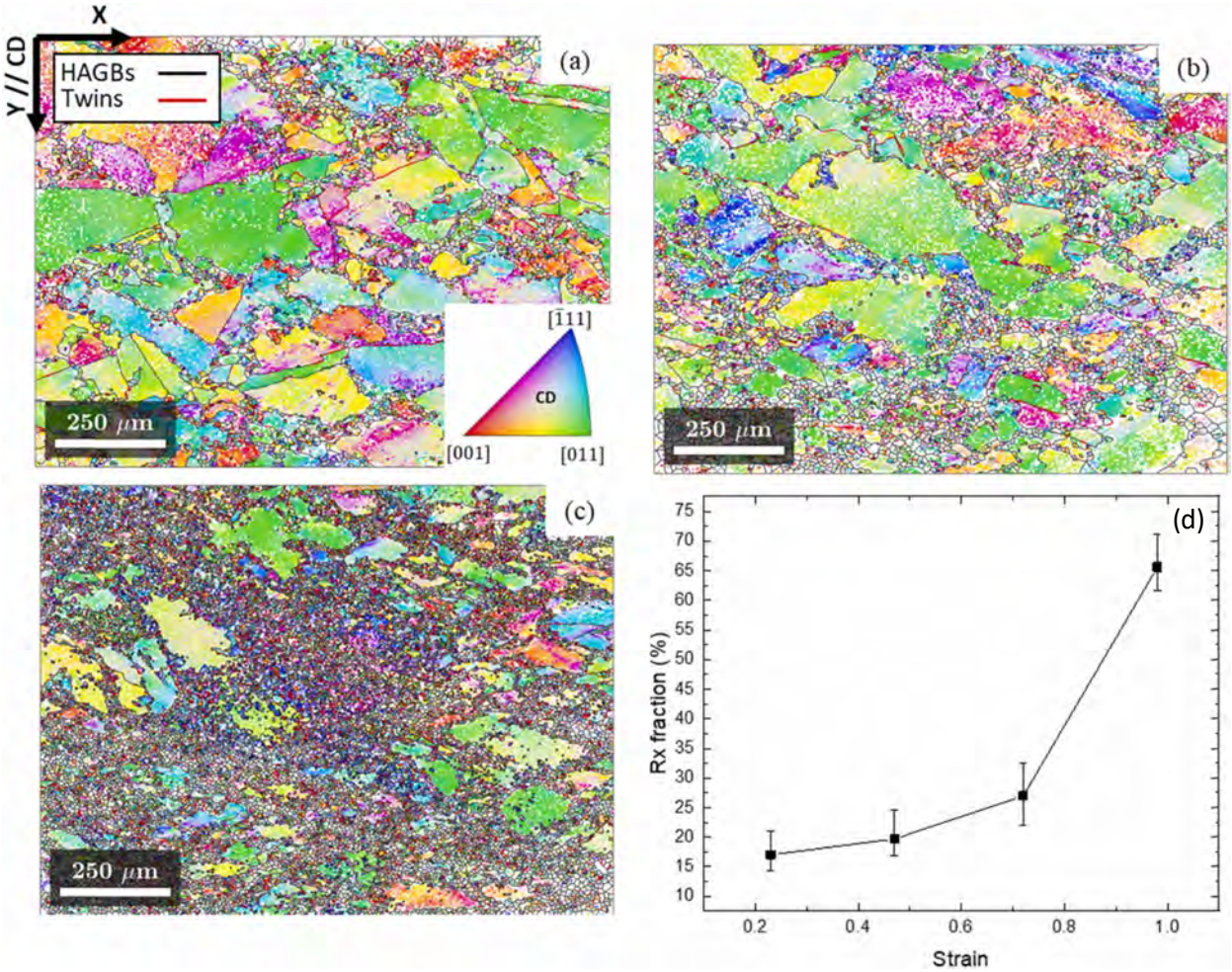

Figure 2.56: Effect of local strain on microstructure evolution on partially recrystallised Ni-based superalloy AD730, (a) $\varepsilon \approx 0.23$, (b) $\varepsilon \approx 0.72$, and (c) $\varepsilon \approx 0.98$. The step size for the EBSD maps in (a) through (c) were 4 µm, 4 µm, and 2.5 µm, respectively. (d) A plot of the area fraction of recrystallised grains as a function of strain. The compression direction (CD) is vertical, as indicated. Captured from Coyne-Grell *et al.* [266]

Interdisciplinary non-destructive testing (NDT) quality control methods are often applied to forging and forming of metals [317]. NDT methods, such as ultrasonics, are often applied for the inspection of welds and AM parts [318–320]. However, for defects and heterogeneities found in the centre of large billets (*e.g.,* those seen in Perez *et al.*'s work on AD730 [8] and Huang *et al.*'s work on Ti-6242 [321], shown in Figure 2.58), NDT methods are still limited and in development. These methods are now being explored to inspect new and in-service aerospace parts alongside machine learning to predict where faults may propagate [322].

Due to the difference in geometry scale, heat is lost at a higher rate in research forgings. Therefore, any research-scale open-die forging has the aspects of temperature distribution, billet size, and strain path to take into consideration when performing detailed analysis. For these reasons, replication of industry conditions has been a long term obstacle for researchers, on top of the material and overhead costs. With large investment in experimentation at "close-to-industry scale" such as the ATI** funded Future Forge project [323–325], it is crucial to ensure the equivalence and relevance/applicability to the industrially manufactured material. If found to be equivalent in nature, there is merit in creating even smaller scale experiments in order to study the material mechanisms and the effect that process parameter changes have on the microstructure. Identifying the bounds of experimentation before size effects impact the quality and relevance of the results to industry is crucial. The success of achieving relevance in laboratory-scale standard testing could have a great operational impact as it can be scaled to materials testing laboratories across the globe for many matrix material studies. Allowing these studies to inform multi-scale models so

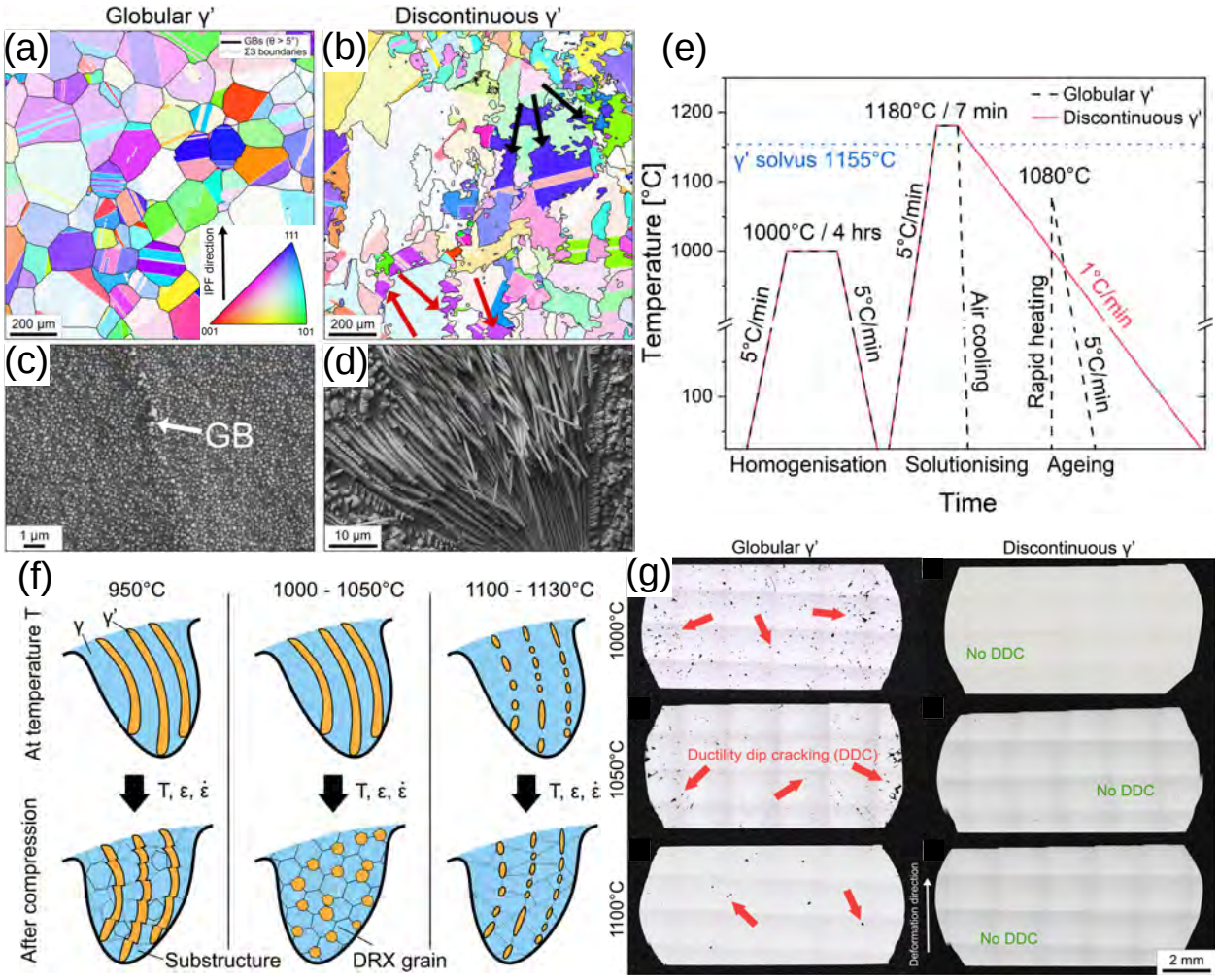

Figure 2.57: The initial microstructures with (a) & (c) globular γ' and (b) & (d) discontinuous γ'. (a) & (b) show EBSD IPF maps of the γ matrix. The black and red arrows respectively indicate grains that are entangled with neighbouring grains (the grains appear separate because we can only see the boundary traces within the observable plane). (c) & (d) are SE micrographs of the samples that were electro-etched to reveal the γ' morphology. The white arrow indicates a grain boundary (GB). (e) Schematic of the heat treatments to achieve the microstructure with globular γ' (shown in dashed black lines) and the microstructure with discontinuous γ' (shown in solid red lines). The rapid heating indicates that the sample was put into an already pre-heated furnace. (f) A schematic that summarises the observed evolution of discontinuous γ' at different compression temperatures T with a strain rate of $0.1\,s^{-1}$ to strain $\varepsilon = 0.6$. (g) Overview light optical micrographs of the samples with globular γ' and discontinuous γ' after hot compression with $0.1\,s^{-1}$ to strain $\varepsilon = 0.6$. The red arrows highlight ductility dip cracking. Adapted from Schulz *et al.* [316]

that pass-scheduling can be driven with live database models, allowing for manipulators, presses, and operators to achieve the desired final properties for the ingot-to-billet conversion stage.

2.4 Summary

The gap in knowledge that this work addresses is surrounding the experimental knowledge of ingot-to-billet conversion (*i.e.,* open-die/multi-axial forging) as all previous experimental work in this area predominantly captures uni-axial or upsetting operations. In this literature review, it has been important to discuss the full process stream and ingot history prior to the ingot-to-billet conversion stage, to understand the stages involved in achieving the inital state (*i.e.,* purity and composition) of the ingot for subsequent ingot-to-billet hot working. Understanding the influence of these stages on the microstructure and the potential defects, as well as the critical mechanisms throughout the entirety of the thermomechanical processing history of advanced alloys is crucial for

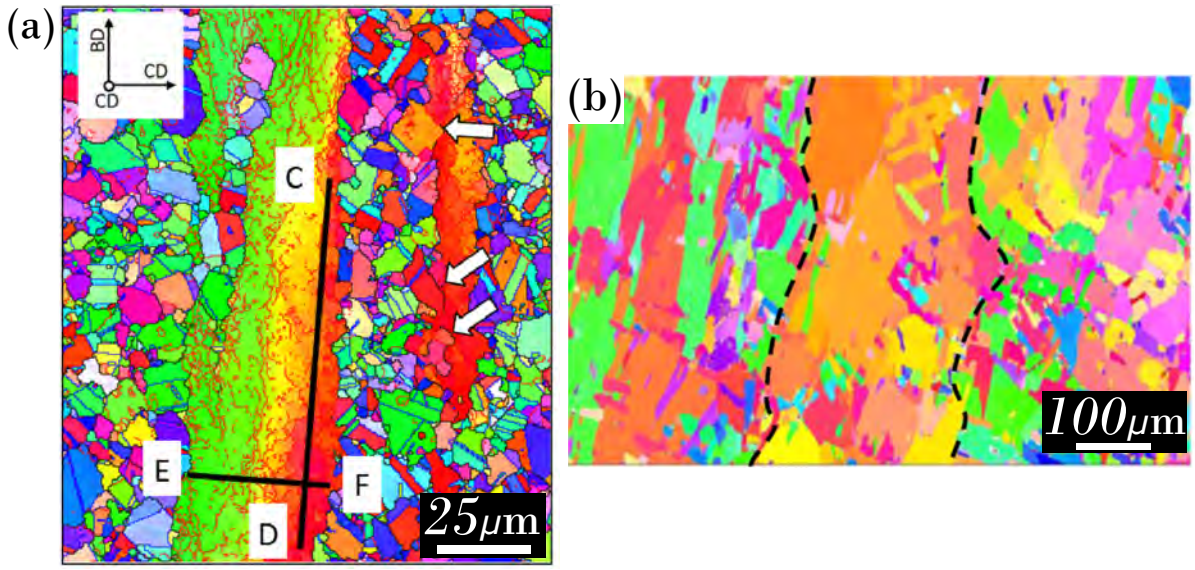

Figure 2.58: (a) EBSD analysis of AD730 material in the as-received condition, showing zoom on unrecrystallised grains. Captured from Perez *et al.* [8]. (b) EBSD IPF map of Ti-6242S after heat treatment at 1000 °C/30 mins, highlighting macrozone structure. Captured from Huang *et al.* [321].

any metallurgist. The review of theory surrounding the thermomechanical processing of advanced alloys puts into perspective the importance of each separate stage of the process and the mechanisms involved.

A significant body of current research on ingot-to-billet conversion focuses on computer modelling of these processes which may not adequately represent the reality of industrial forgings without experimental input verification, and therefore cannot be solely relied upon. Linking experimentally informed models in the future may hold a great deal of value for researchers and metallurgists. This work aims to bridge this gap through creating a new laboratory based method for ingot-to-billet conversion study. It aims to create a platform for a number of future material investigations, while suggesting improvements that may allow for a wider range of materials testing. The advantages and opportunities that this novel equipment may provide are also discussed. From the presented gap in knowledge the research questions for this work are as follows:

1. How to build an experimental test-rig to simulate large-scale industrial processes?
2. How do you attain optimal microstructural control in industrial processes?

Furthermore, it is also important to draw objectives from the presented gap in knowledge. These are as follows:

1. Can an experimental apparatus achieve grain refinement through experimental multi-directional cogging?
2. Is it possible to achieve different grain morphologies and temperature ranges through the use of high temperature tooling?
3. Can experimental cogging be used to achieve globularisation of α in Ti-6Al-4V titanium alloy?

Investigating the relevance of a novel experimental-scale method requires a pilot study to assess capability of the designed equipment in replicating open-die forging to any extent. This work aims to do this through initially applying a new method to single-phase materials as models at lower elevated temperatures, this results of these trials are presented in Chapter 5. After these proof of concept trials, the method will finally be applied to a commercial dual-phase alloy that is of high

interest to industry and that normally undergoes the same forging operation, results of these tests are shown in Chapter 6.

Lastly, it is important to understand how to characterise, and analyse the specimens from these experiments to find the structure-property relations. Characterisation techniques are constantly in development, *e.g.,* Georgios Fotos, a fellow PhD student is developing an algorithm using machine learning to automatically detect grain boundaries from microscope images, which can then be used to output grain distributions and volume fractions. This work explores the grain refinement and microstructural evolution of the selected material specimens through multiple conventional and advanced techniques which are detailed in the Materials and Methods section.

3 Experimental Equipment Design

3.1 Introduction

A fundamental prerequisite, and outcome, for this research has been the design and development of automated experimental apparatus to cost-effectively simulate cogging on a laboratory scale. Strong emphasis must be placed on the design work and implementation for the novelty of this research. As this is a brand new design and method of testing, it should be taken that this is the major key output, with other chapters supporting the design as, not only standalone materials research examples, but as proof of concept for the generated design. Whereby test specimens will be rotated in synchronous rotation with compressive deformation at a range of temperatures. Given the significant costs of large multi-tonne workpiece ingots, and the difficulties with their non-destructive evaluation, it has been crucial to develop for a laboratory-scale evaluation so that scrapping and re-processing can be avoided. Design iteration and development of this apparatus, from conceptual to detailed design, is discussed.

A new apparatus for studying the thermomechanical cogging process has been created. This equipment will be used with a variety of alloys to help gain an improved understanding of plastic deformation during cogging and optimise the processing conditions. This study reviews the experimental setup that has been used for the effects of cogging on localised deformation in alloys. It is not the intention only to review the laboratory setup, but also discuss the shortcomings and limitations, as well as the benefits that a laboratory design of this nature can bring to the fore.

3.2 Equipment Design

The experimental apparatus design relies on the use of the extensometer slot in laboratory-scale furnaces typically used for thermomechanical testing on uni-axial load frames. For furnaces, where such a slot is not available, the apparatus may still be used, *e.g.,* by using a partly open split-tube furnace with clamps loosened and gaps filled with ceramic wool. This section will detail the main

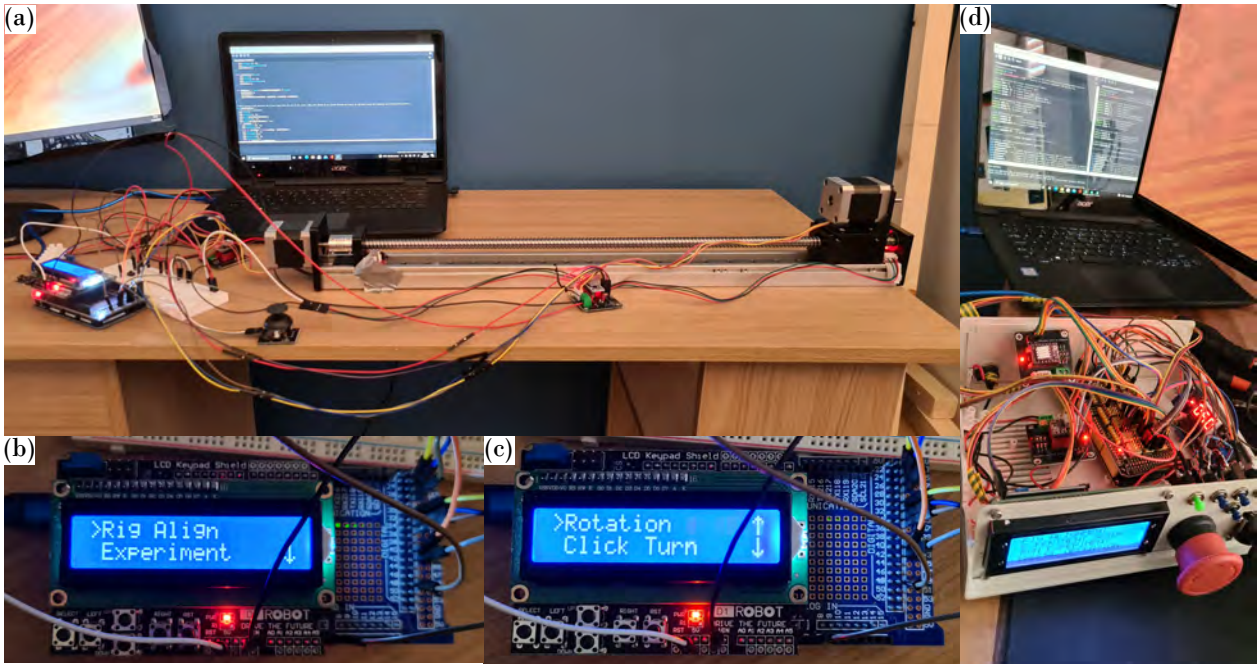

Figure 3.1: (a) Photograph showing first iterative connectivity set-up between actuator sub-assembly and microcontroller, (b) Photograph showing LCD screen, indicating different menu selection options, (c) Photograph showing LCD screen with more menu selection options, and (d) Photograph showing first integration of circuitry into control box.

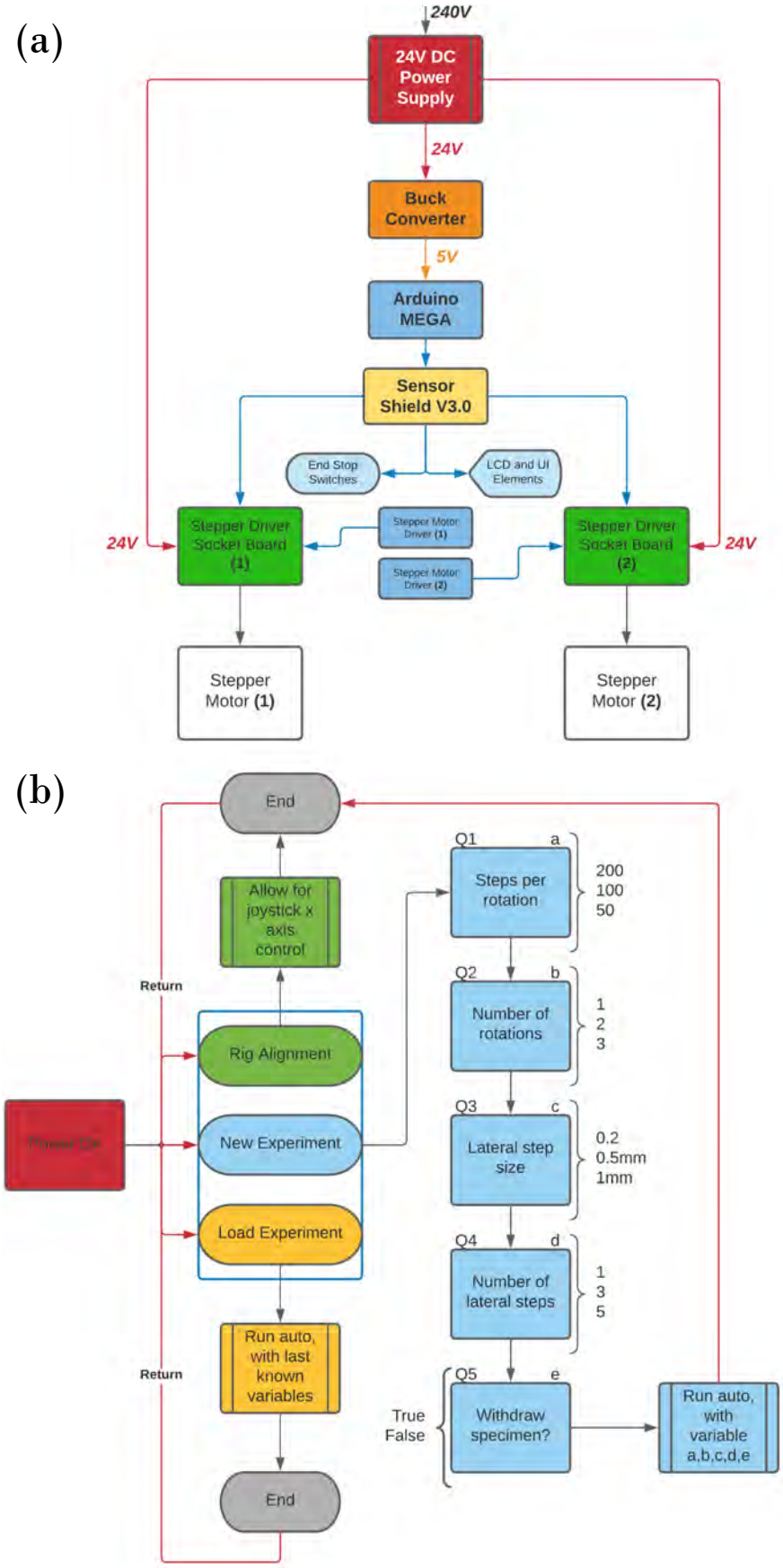

Figure 3.2: (a) Initial concept of how the hardware would be connected and the flow of electricity through the circuit, and (b) Initial concept of how the firmware would allow the operate to control the manipulator arm within the experimental set-up.

elements of the equipment design and discuss some of the key design considerations of each. The overall apparatus design employs an assembly of commercially available components and a limited number of custom-manufactured parts.

3.2.1 Early Design Iteration

It is important in this work to capture some of the early work that went onto generate the final successful design. Conceptual design of how the integrated controller would operate the manipulator arm was first mapped out using the online tool LucidChart™. A conceptual flow diagram detailing the electrical connections of components is presented in Figure 3.2(a), and a conceptual flow diagram of how the software program would operate can be seen in Figure 3.2(b).

These early concepts were then carried forward and iterated on using iterative programming and testing. Some early programming work on GUI design and operation of the manipulator is shown in Figure 3.1. Automation of the test-rig included at this point creating a set of questions that the operator could follow in order to create a full program, including insertion and removal of the sample laterally from its forging place inside the furnace. This was tested using the smaller LCD screen seen in Figure 3.1(b) and (c) that had built in control buttons that could be used to create the user menus. As an example, following the typical procedure of an operator, the early design considered alignment of the specimen with the furnace extensometer slot. Then, once aligned could be inserted using the GUI, allowing for both coarse and fine movement for adjustment inside the furnace. When aligned it could then be set to carry out a cogging procedure that could be programmed directly from the GUI, with wait functions added to communicate with the press. Otherwise, manual control could be taken, so that it could be rotated by the operator. These considerations of automation and manual control drove the logic of the implementation of different control methods in the early coding design.

In practice, this level of automation inside the furnace was not warranted due to the amount of internal space and collision issues that this could cause, without neccessary checks between. Furthermore, further safety points had to be ensured through, firstly a fuse before reaching the circuitry, an emergency stop to kill power to the system if required by the user, and then also endstops that would also stop any movement in the rig to ensure user and accompanying safety.

3.2.2 Motion Actuator Sub-assembly

The motion actuator sub-assembly (seen in Figures 3.4, 3.6, and 3.7) is designed around an off-the-shelf pre-assembled linear motion mechanism. The mechanism uses a profiled aluminium extrusion as its frame, which supports a 12 mm wide linear guide-way along its length. A CNC-machined aluminium platform is mounted to the guide-way carriage and is able to slide from one end of the guide-way to the other. A 500 mm long 12 mm diameter lead screw runs through a matched

Figure 3.3: Photograph showing the subassembly of the Manfrotto™ tripod mount adaptor for the motion-actuator subassembly.

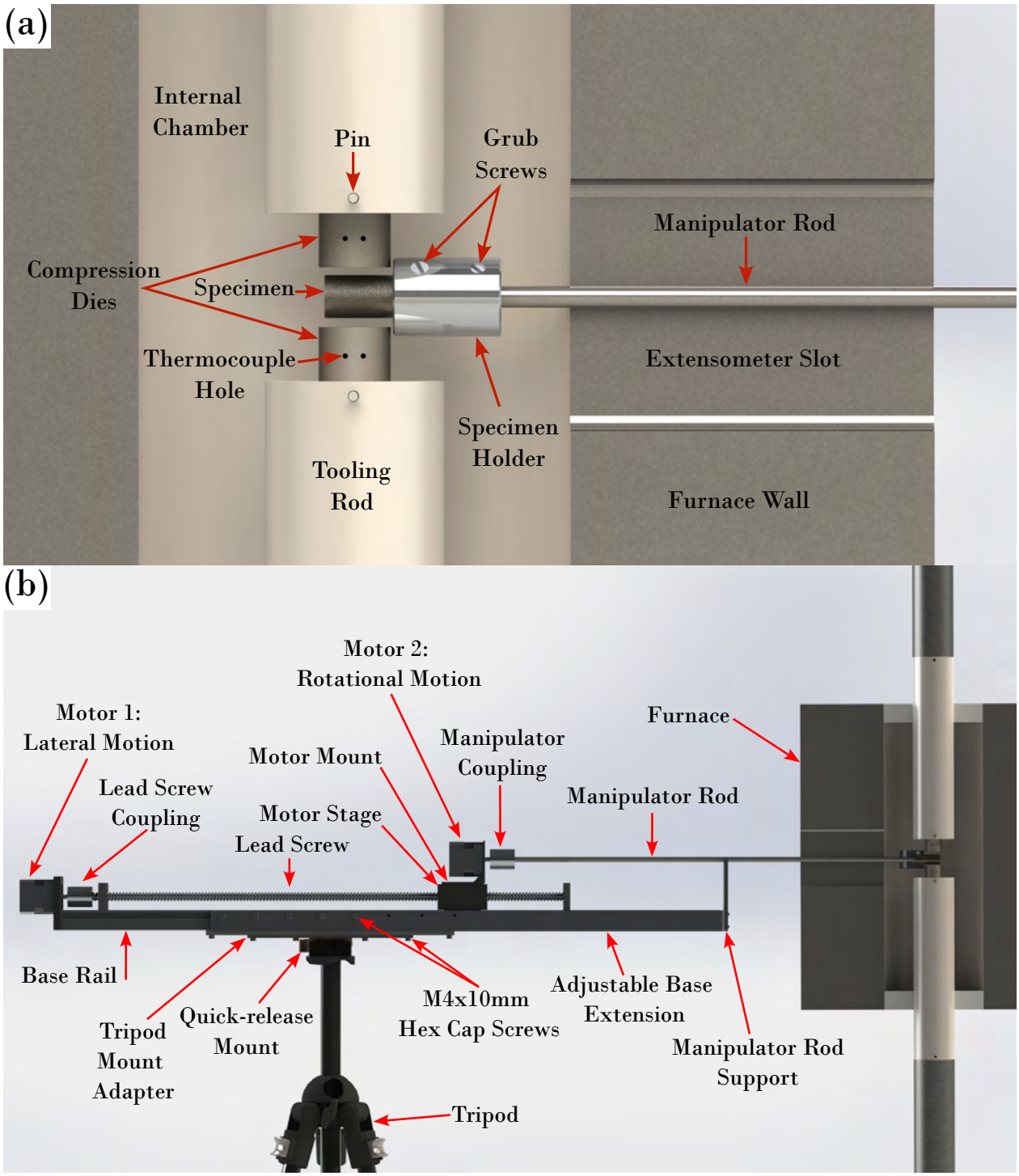

Figure 3.4: (a) CAD rendering of the internal furnace chamber during test set-up, showing the arrangement of the workpiece, dies, and manipulator, (b) CAD rendering showing a side profile of the component arrangement in the experimental set-up. Both were generated using Dassault Systémes SOLIDWORKS®, rendered with Photoview 360.

nut in the platform and spans the entire length of the frame. This length was chosen to ensure the workpiece could be fully extended into the furnace allowing for a safe distance between the furnace door and the electronic components. Two Nanotec® ST4118L NEMA17 stepper motors (with 200 steps per revolution) actuate the motions of the apparatus during specimen testing and positioning. One of the motors is mechanically coupled with the lead screw and is used for lateral translation of the aluminium platform. This lateral movement allows both the entry and removal of the test specimens from the furnace, as well as adjustment of their position within the mechanical

working zone (*i.e.,* their location relative to the compression dies). The second motor is mounted using a standard L-bracket to the lead screw platform. This motor is used for the axial rotation of the specimen manipulator assembly via a cylindrical coupling. In addition to providing controlled rotation of the workpiece between compression bites, the motor additionally applies a holding torque during compression to aid against workpiece slippage.

Two custom components have been added to the actuator assembly. Firstly, a mount, consisting of stacked ABS plates connected to a Manfrotto™ quick-release camera tripod mount, is attached with screws to the base extrusion of the linear motion mechanism. Engineering drawings of these custom components are presented in Appendix A, and an image of this mount is additionally presented in Figure 3.3. This allows the attachment of the motion actuator assembly to a heavy-duty adjustable camera tripod, allowing for height, pitch, yaw, and roll adjustments into the relevant positioning for the furnace and load frame. Adapting the actuator for mounting to a tripod allowed for considerable portability and freedom of adjustment without requiring any modifications to be made to the load frame. However, improvements to this design will be explored in the discussion.

The second component is an extendable specimen manipulator support, machined from 316 stainless steel sheets, engineering drawings of these components are presented in Appendix A. It is connected with screws to the sides of the motion actuator frame via square nuts in the guide slots in the extrusion. The main function of this extendable support is the horizontal support of the specimen manipulator rod in the vicinity of the furnace door. This addition aids against excessive vertical and horizontal deflection of the manipulator rod during testing. Figure 3.4 shows a detailed representation of the experimental arrangement of components and specimen placement within the tube furnace interior.

3.2.3 Electronic Controller

Initially, National Instruments™ LabVIEW software was planned for motor operation, but ultimately it was decided to employ the more flexible Arduino microcontroller setup. The rationale for this choice was that the arduino setup was found to be more easily accessible and cost effective. The electronic controller unit was constructed around an Arduino® MEGA 2560 R3 microcontroller development board coupled with a KEYESTUDIO™ MEGA sensor shield V1 to facilitate the connection of the required module boards. The controller firmware was programmed and compiled using the popular free-and-open-source Arduino® IDE software which uses the C++ language. The firmware code is presented in Appendix B. A 24 V 6.25 A AC-DC switching mode power supply was used to power stepper motors of the motion actuator assembly, while an LM2596 DC-DC buck converter module was used to step-down the voltage to 5 V to safely power to the microcontroller board connected associated modules. Two motor driver modules based on the DRV8825 chip were used to control the primary and secondary stepper motors. Two 4N25 optocouplers were used for isolation of input and output electrical signals between the controller of the Zwick/Roell™ load frame, with standard BNC male connectors provided for the use of shielded coaxial cables. A standard ABS instrument enclosure was used to house the electronic components, with the front and rear panels laser-cut to allow the mounting of an LCD screen, user interface buttons, and other switches and connectors. The operator controls and interface are shown in Figure 3.6(a), while a schematic of the electrical connections used in the electronic controller assembly can be seen in Figure 3.5.

3.2.4 Tooling

Two pairs of custom-manufactured platens were used as compression die sets: one used for ambient temperature and the other for elevated temperature testing. The cylindrical platens, 20 mm in diameter, 15 mm in height, were manufactured by wire electric discharge machining (EDM) from IN718 and Nimonic®-90 nickel-base superalloys, respectively. The platen size was determined by the internal volume available within the vertical split-tube furnace used for the highest temperature

experiments. The inner diameter of the furnace was 80 mm, and the platens needed to allow enough room for the specimen grip at the end of the manipulator rod. This also permitted placement of the specimens over the entire span of the dies to avoid equipment damage due to uneven loading.

Sets of manipulator rods 8 mm in diameter were manufactured to allow testing over a range of temperatures. Accompanying sets of standard cylindrical couplings with a range of internal diameters were also procured for the purpose of motion transmission from the rotation-axis stepper-motor to the manipulator rods and, hence, the specimens. The manipulator rods were manufactured from type 316 stainless steel and Nimonic®-90 superalloy.

Sets of cylindrical couplings were manufactured and mounted on the opposing ends of the manipulator rods for gripping of the test specimens during the positioning and forging operations. These 8 mm to 12 mm diameter cylinders were cut from type 316 stainless steel and Nimonic®-90 superalloy using wire EDM. All couplings were manufactured with threaded side holes to allow the use of fixating grub screws for both the manipulator rods and the test specimens. Grub screws for high temperature testing were machined from Nimonic®-90. All grub screws for the type 316 stainless steel have 2mm allen key holes for adjustment, whereas the Nimonic®-90 alloy grub screws were designed with 1.2 mm wide x 2 mm deep channels for adjustment with a flat head screwdriver, drawings of these are presented in Appendix A.

The elevated temperature testing in this study was carried out at 450, 600, and 950 °C for

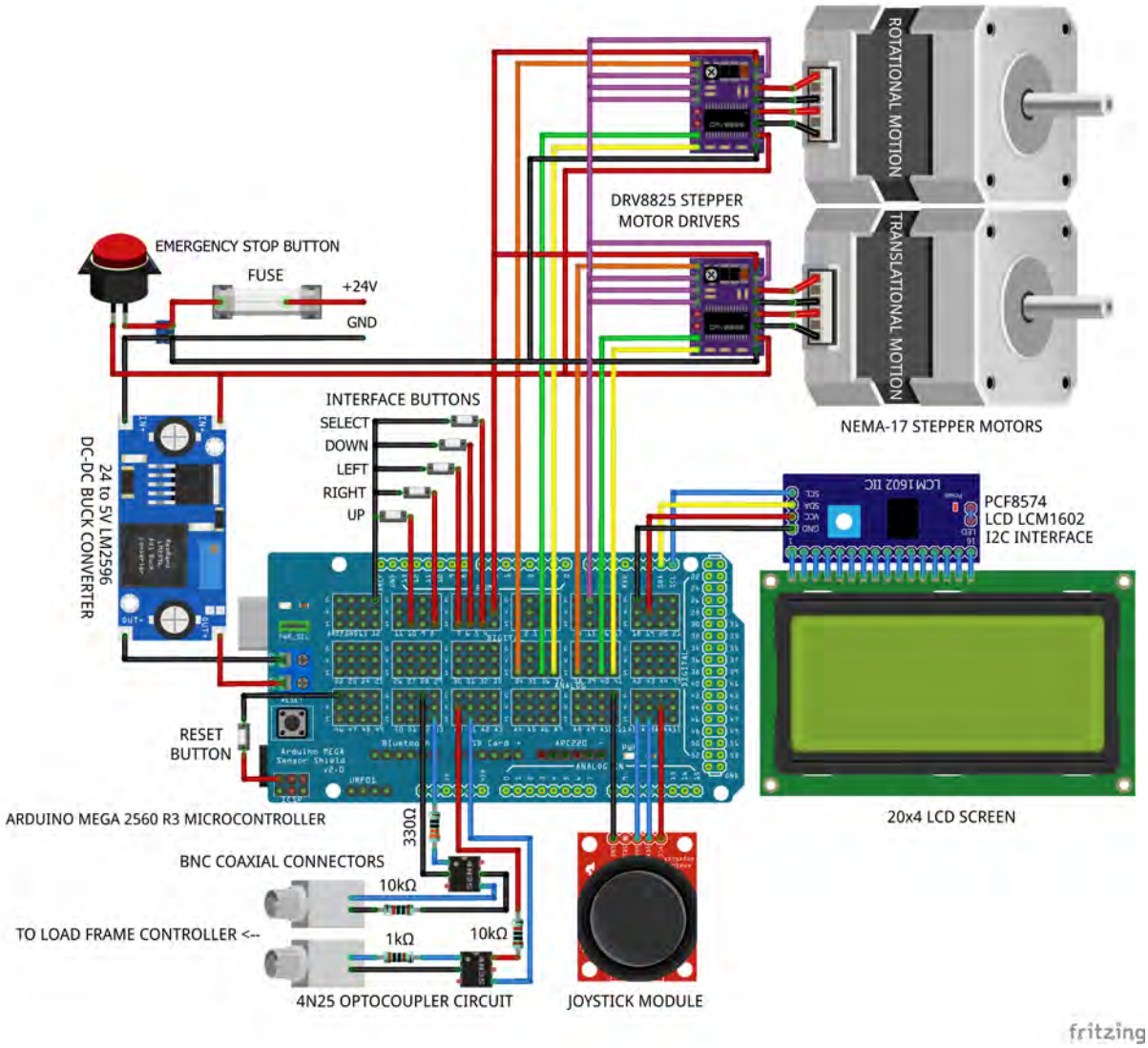

Figure 3.5: Diagram showing hardware set-up and connections within the electronic controller. Generated using Fritzing, open-source software.

Al6060, C101, and Ti-6Al-4V alloys respectively. These temperatures were selected as they were in an acceptable range below the melting point of each alloy, or otherwise in the case of Ti-6Al-4V, an industry known sub-transus forging temperature. Therefore, to extend the longevity of the IN718 platens, boron nitride suspension was used as a lubricant and anti-stick agent. Additionally, Loctite® LB 8009 heavy-duty anti-seize lubricant was applied to the grub screws of the couplings for all high temperature testing. An image showing the full tooling set is shown in Figure 3.6(c).

Tooling Materials

It is important to detail the rationale of the material choice, and preparation of the tooling for the experimental setup. As these choices were crucial to the success of the design. Tables 3.1, 3.2, and 3.3 present the nominal compositions of the tooling materials. The material properties derived from these compositions will be briefly discussed.

Table 3.1: Nominal chemical composition of the IN718 nickel superalloy. "mx" represents maximum % value. *Reference to the 'balance' of a composition does not guarantee this is exclusively of the element mentioned but that it predominates and others are present only in minimal quantities.

Element	Ni	Cr	Fe	Nb	Mo	Ti	Al	Co	C	Mn	Si
Weight %	50.0-55.0	17.0-21.0	Bal*	4.7-5.5	2.8-3.3	0.6-1.1	0.2-0.8	1.0mx	0.1mx	0.3mx	0.3mx

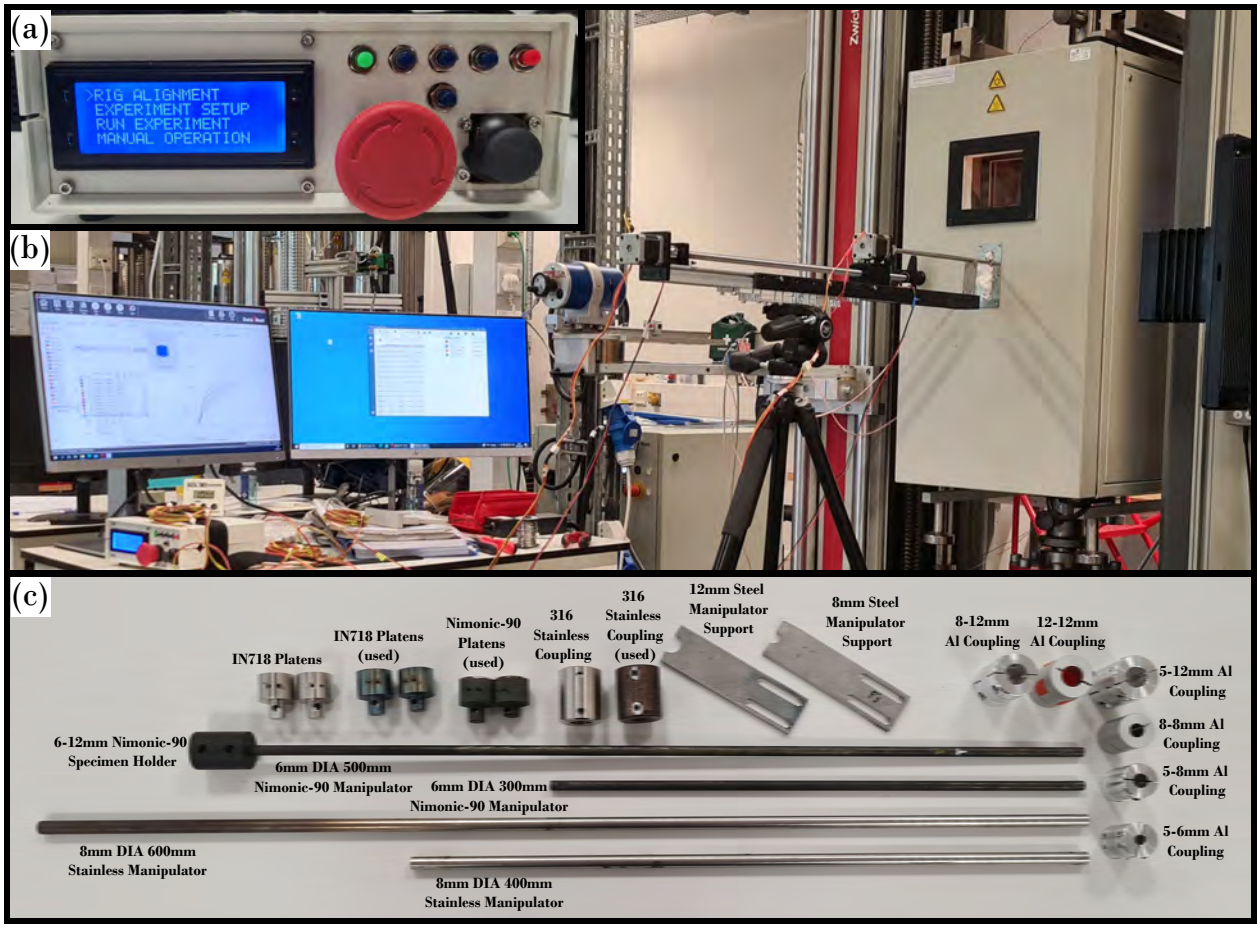

Figure 3.6: Collection of experimental operation, set-up and tooling showing: (a) an image of the front operator interface of the control box, (b) an image of full laboratory set-up during testing, showing arrangement of design methodology within Zwick/Roell™ load frame and utilisation of the Severn Thermal Solutions EC2112 environmental chamber and use of ceramic wool for thermal insulation. Also showing the use of the Electronic Controller, in conjunction with the Zwick™ testXpert III software, (c) an image showing the collection of experimental tooling, including experimental platens, manipulator rods, manipulator rod supports, motor and specimen couplings.

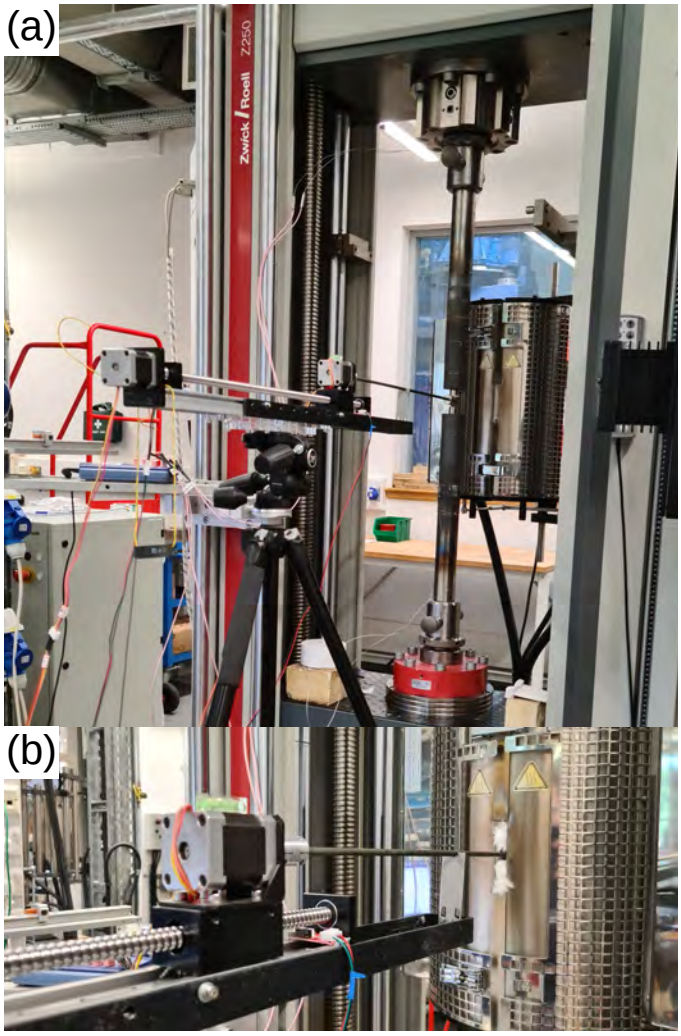

Figure 3.7: (a) Photograph showing apparatus during alignment within Zwick/Roell™ Z250 load frame prior to testing, (b) Photograph showing close-up of apparatus during high temperature testing.

INCONEL® alloy 718 is a high-strength, corrosion-resistant nickel chromium alloy typically employed between -252 to 705 °C [327]. The age-hardenable alloy can be readily fabricated into complex parts, which made a good choice for die material for machining and use in lower temperature compression tests. Stress-strain curves with influences of temperature are shown in Figure 3.8. The material was procured from the AFRC stores under free-issue material, from there was machined using EDM. Due to the forging temperature conditions (450 & 600 °C), and the expected ease of formability of the test materials, an additional heat treatment of the IN718 alloy die material was unnecessary.

Table 3.2: Nominal chemical composition of the Nimonic®-90 nickel superalloy. "mx" represents maximum % value.

Element	Ni	Cr	Fe	Cu	Mn	Ti	Al	Co	C	Mn	Si
Weight %	Bal.	18.0-21.0	1.5mx	0.2mx	1.0mx	2.0-3.0	1.0-2.0	15.0-21.0	0.1mx	1.0mx	1.0mx

Nimonic®-90 alloy is a wrought nickel-chromium-cobalt base alloy strengthened by additions of titanium and aluminium. It has been developed as an age-hardenable creep-resisting alloy for service at temperatures up to 920 °C [328]. It is typically used for turbine blades, discs, forgings, ring sections, and hot-working tools. The recommended heat treatments for Nimonic®-90 alloy bar are as follows: 8h/1080 °C/AC + 16h/700 °C/AC. After machining and prior to testing, the second stage heat treatment was carried out on the Nimonic®-90 alloy material in the AFRC using a VFE

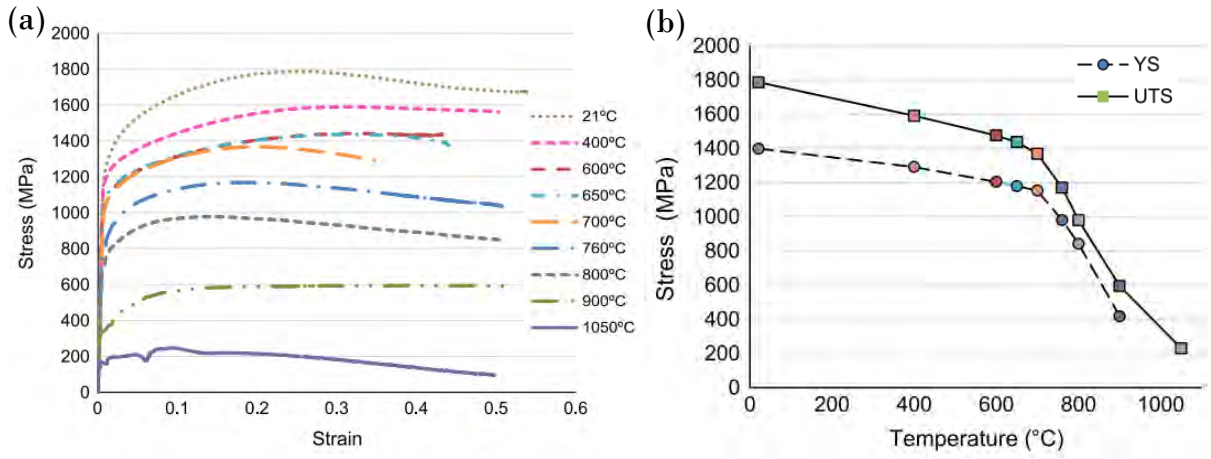

Figure 3.8: (a) Influence of temperature on the flow behaviour of IN718 when compressed at a strain rate of $1\,s^{-1}$ and, (b) Influence of temperature on the Yield Strength (YS) and Ultimate Tensile Strength (UTS) of IN718 when compressed at a strain rate of $1\,s^{-1}$. Captured from Iturbe *et al.* [326].

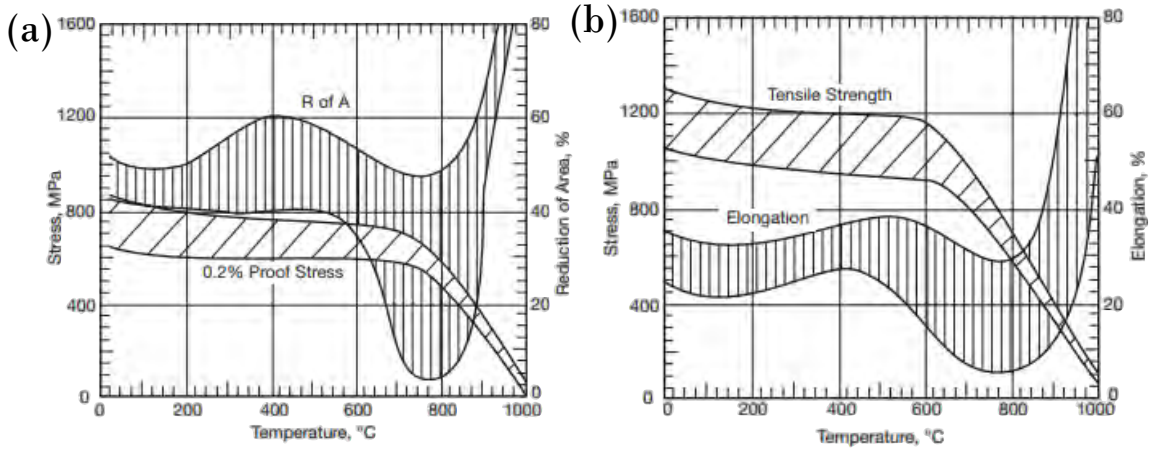

Figure 3.9: Tensile properties of hot-rolled bar. After heat treatment of 8h/1080 °C/AC + 16h/700 °C/AC (a) showing 0.2% Proof Stress and Reduction of Area, and (b) showing Tensile Strength and Elongation. Captured from Special Metals Nimonic®90 alloy datasheet [328].

TAV TPHF horizontal vacuum furnace.

Table 3.3: Nominal chemical composition of the type 316 stainless steel. "mx" represents maximum % value.

Element	Fe	Ni	Cr	Mo	C	Si	P	S	Mn	N
Weight %	Bal.	10.0-13.0	16.5-18.5	2.0-2.5	0.07mx	1.0mx	0.05mx	0.03mx	0.0-2.0	0.1mx

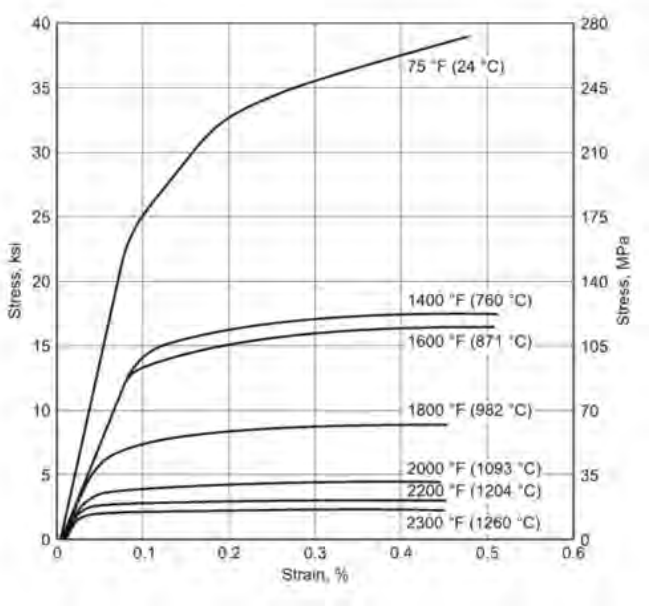

Figure 3.10: 316 annealed stainless steel bar, stress-strain curves at room and elevated temperatures. Captured from Gibbs *et al.* [329].

Stainless steel types 316 also known as 1.4401, is an austenitic grade steel, second only to 304 in commercial importance. Type 316 stainless steel contains an addition of molybdenum, which improves the corrosion resistance. It is supplied in many forms from sheet, tube, bar *etc.* and used in many applications across multiple sectors. It proved a good choice for use as manipulator rod and coupling material, as the maximum operating temperature would be 800 °C less than the melting point of 1400 °C, ensuring acceptable strength for the lower temperature testing applications. Stress-strain curves are given for type 316 stainless steel annealed bar at a range of temperatures in Figure 3.10 [329].

Assessment of the relevant literature and datasheets surround these materials provided sufficient data to validate the choices of tooling material for their various purposes. For added validation for material choice for the custom dies, 3D GOM scans and surface roughness profiles/areas were captured after experimentation. These allow for insights into the expected tool/die life for the custom miniature dies for the various materials, when comparing resultant dimensions against original dimensions over the number of tests. Surface profiles both parallel and perpendicular to the thermocouple hole directions were captured. Figure 3.11 presents the surface roughness data comparison perpendicular to the thermocouple hole direction between an unused IN718 die and a used IN718, after both copper and aluminium cogging tests. All surface roughness measurements captured using an Alicona™ Infinite Focus IFM G4 microscope.

Clear manufacturing marks or lines are observed in Figure 3.11(a) in the unused 718 die which seems to carry forward into the used IN718 die seen in Figure 3.11(d). This indicates that minimal amount of wear has occured throughout the single-phase tests with these dies as marks from the lathe are still visibile after forging, and even sandpaper removal/grinding of lubricant between tests. However, due to repeated forging and use of sandpaper the overall surface roughness has actually become smoother going from -7.3 and $12.3\,\mu m$ to -2.5 and $2.9\,\mu m$ as minimum and maximum measurements of surface heights respectively, which is a resultant 71.6% decrease in maximum and minimum.

Due to material and labor costs as well as time limitations, manufacturing spare Nimonic®-90 alloy dies was not possible for the current study, therefore analysis of these dies is only presented post high temperature testing. However, it is observed that the overall surface roughness results are similar to the IN718, the key difference seen in Figure 3.12(a) is the absence of any machining lines. This is likely due to the cylic heating and forging at hot forging temperatures, as well

as the increased grinding requirement to remove lubricant. Also observed from Figure 3.12 the Nimonic®-90 dies also show small damage marks which may just be a result of storage.

Overall, the results shown across Figures 3.11 and 3.12, proves that at the forging temperatures and loads involved with cogging the materials presented in the following chapters that minimal die wear can be expected. This data reinforces the validation of choice of die material for the micro-cogging apparatus.

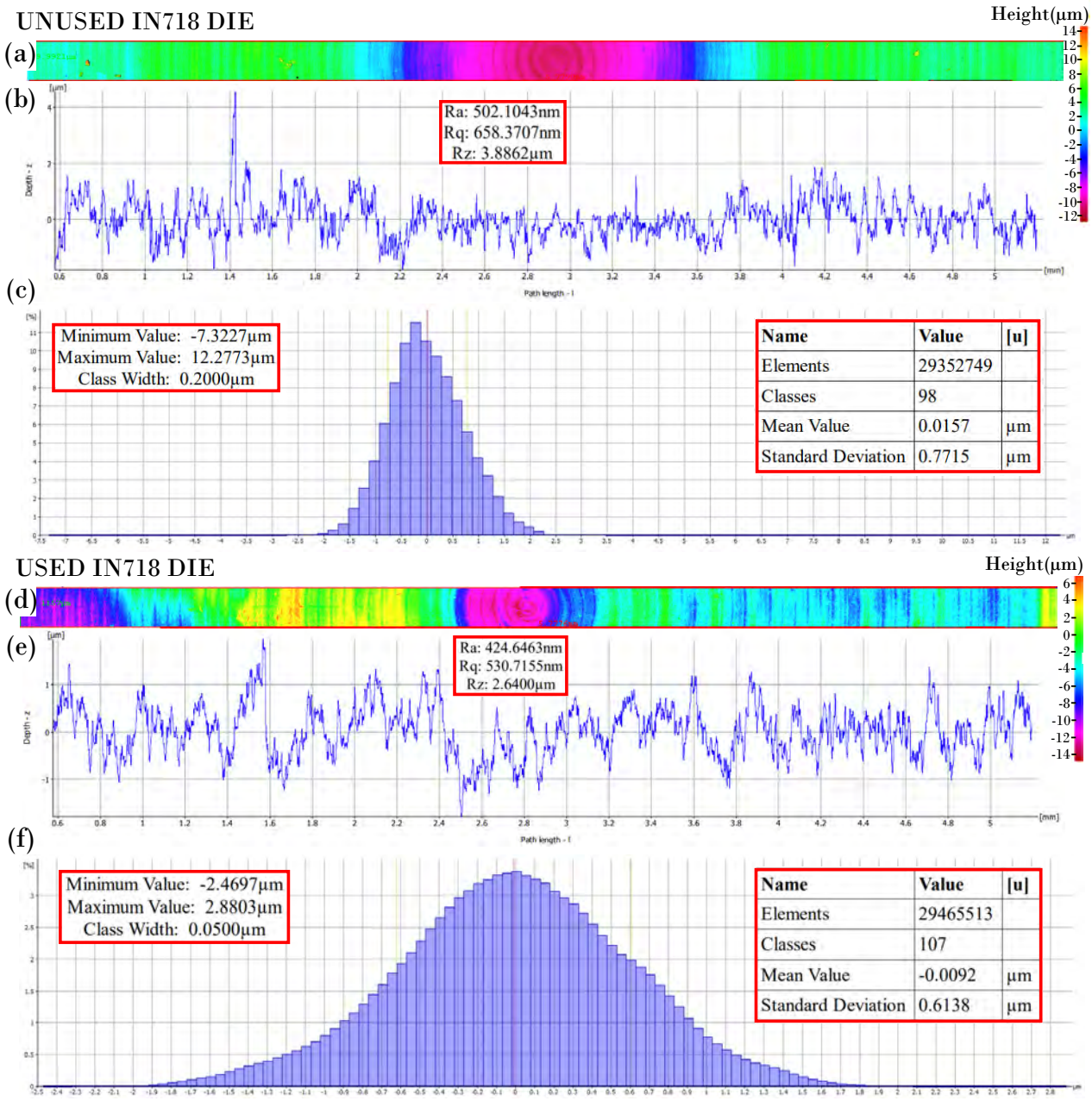

Figure 3.11: Surface data captured for unused and used IN718 dies, captured perpendicular to thermocouple hole directions, (a) Coloured micrograph of unused surface profile, (b) Unused surface profile measurement, (c) Unused surface texture measurement histogram, (d) Coloured micrograph of used surface profile, (e) Used surface profile measurement, and (f) Used surface texture measurement histogram.

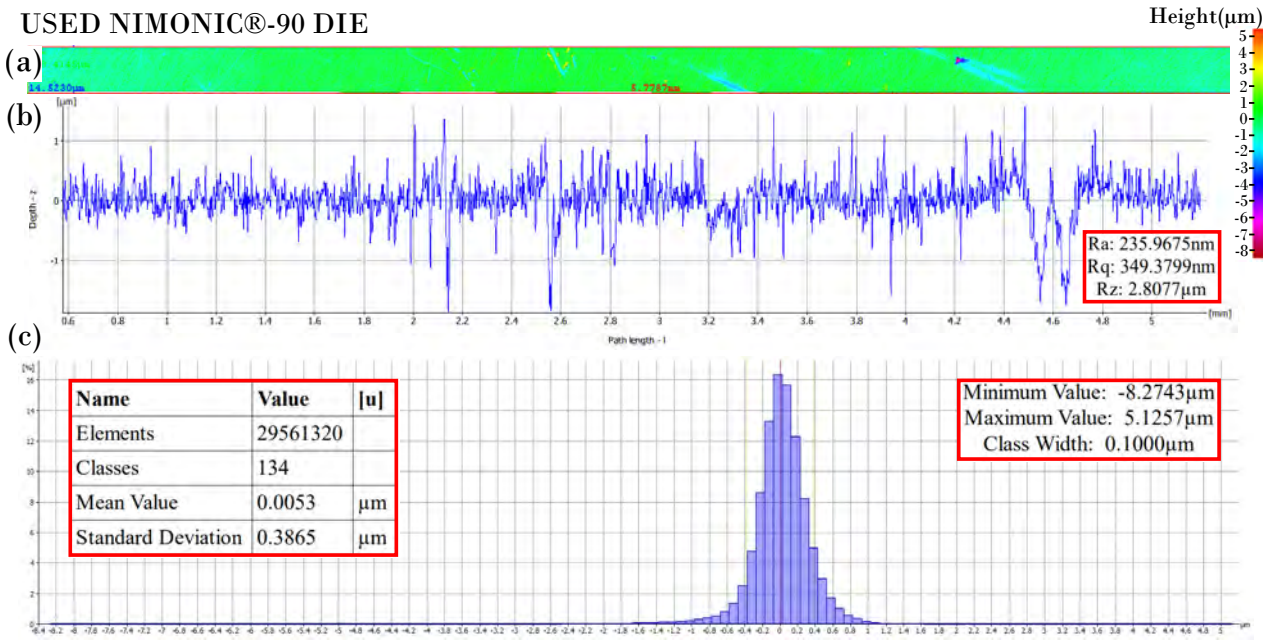

Figure 3.12: Surface data captured for used Nimonic®-90 dies, captured perpendicular to thermocouple hole directions, (a) Coloured micrograph of surface profile, (b) Surface profile measurement, (c) Surface texture measurement histogram.

3.3 Method Design

As an apparatus pre-check, before beginning matrix cogging tests, a room temperature experiment was done on an Aluminium 6060 sample that was cut to 60 mm (presented in Figure 3.13(a)), so that it could be deformed in the conventional 50 mm DIA dies, shown in Figure 3.13(b) and previously in Figure 3.7(a).

This test was carried out in order to establish the running of the rig in the lab environment. Ensuring that rotation of the sample within the load frame could be completed with enough clearance. Additionally, it allowed for the operator to see the extent of the bending of the manipulator rod from the loading within the load frame, and allowed for the assessment of alignment prior to testing starting.

Over the course of the inital test specimens, the experimental procedure evolved from the originally planned method. Initially, the conditions were planned to make use of positional control of the Zwick™ 150 kN press alongside the signal control box. This signal control interface seen in Figure 3.14, can be used to send and receive trigger voltages that can allow the press to communicate

Figure 3.13: (a) Photograph of aluminium sample after pre-test, prior to design and manufacture of custom die tooling and, (b) Photograph of tooling rods/dies used in conventional compression testing on Zwick/Roell™ load frame.

with external equipment through a BNC connection. Through the inclusion of a BNC connection onto the microcontroller in the rig design, this allowed for the set up of a simple program to automate the cogging procedure. Allowing the Zwick™ machine to compress the sample once a 5 V trigger signal had been received, and vice versa, the machine would send a signal out once it had completed the operation, allowing the sample to then be rotated.

However, due to external circumstances and necessary repairs, availability to carry out the first experiments was only possible on the Zwick™ 250 kN machine, which did not have the compatibility for automation. This meant that for the first set of experiments it allowed for a lot more manual control and checks between compressions, which in turn was very successful in ensuring the method was adapted for better geometric control. Further exploration of this integration is open for future testing.

With the first data captures, the specimens were deformed using more traditional Zwick™ control methods. This was through the use of the strain control. The strain control method uses the Zwick™ machines internal calculations of strain, with the input of the initial height of the specimen and the forces involved in compressing the sample. Typically, this is used in traditional compression testing, which did not fully translate to the new open-die forging set up for the lab test environment. In most cases, as the strains increased in the samples this method led to over or under straining the samples. This issue then in turn led to further problems, with increased chance of slippage and shearing. Due to machine experience, all starting room temperature experiments and the first four experiments at an elevated temperature were carried out under this strain control method, before the initially planned and primary method was explored.

The second method, which will be discussed more in the following chapter, was through the use of both step and positional control methods. These methods allowed for improved geometric control by reducing shear strain, and improved reduction symmetry. This improvement, further reduced the potential for specimen shearing as it had increased accuracy at this scale, meaning that the deformation result on each rotational axis was more similar. Moreover, this improved accuracy allowed for higher reductions to be reached as the reductions remained to a closer tolerance after each set of compressive strikes, meaning the first methods over or under compression was, on the most part, eliminated.

Figure 3.14: Zwick™ signal control box with BNC trigger connections.

3.4 Design Discussion

The proposed experimental set-up and pilot experiments have successfully demonstrated the capability of performing rotary open die forging or cogging at the laboratory scale, with clear evidence of microstructural control being achieved during the thermomechanical processing. However, when considering such a reduced scale approach for studying large scale industrial manufacture, one has to be mindful of a number of limitations.

First, there are the limitations of the laboratory test environment vs. industrial facilities. For example, the present apparatus used has both the workpiece material and forging dies under isothermal conditions, whereas industrial ingot-to-billet conversion processes are non-isothermal. This means industrially, the material is losing thermal energy because it is exposed to air at the ambient temperature and because the dies are not heated to the same temperature level as the billet. This is done to prolong tool life, as die material is costly. One could assume a quasi-isothermal state due to the large thermal mass of the industrial-scale workpieces, especially within the interior. However, there is, in most cases, a discrepancy in the resulting core and surface microstructure which cannot be overlooked.

Isothermal testing presents the advantage of allowing for controlled conditions, and precise knowledge of the material temperature. But also places additional strength requirements on the tooling material which is also subject to high compressive loads. Nickel-based superalloys were used in the manufacture of the dies to minimise the problem of tool wear. However, the high temperature strength of superalloys relies on the presence of a sufficient volume fraction of the γ' $L1_2$-ordered intermetallic phase which precipitates from a disordered solid solution with a face-centred cubic structure. Increasing the forging temperature closer to the γ' solvus, reduces the overall volume fraction available for precipitation strengthening, effectively weakening the die material. This, therefore, places a limit on the maximum isothermal forging temperature with the present configuration of the experimental apparatus. For example, this would present a challenge for cogging experiments on superalloys which would require temperatures in excess of 1100 °C. This could be overcome with dies made from highly-sintered oxide ceramics in air, or molybdenum alloy dies under vacuum. In contrast, the cogging dies used in industry do not reach such high temperatures and hence can be manufactured from more cost-effective materials.

The present method also requires specimen alignment to be completed prior to heating, with pre-loads being introduced when the sample is close to forging temperature. The apparatus, in its current form, also does not allow re-coating of the dies with boron nitride lubricant. As a result, the friction coefficient increases with progressive forging bites as the initial coating (applied prior to heating) is depleted. This loss of lubricant from the surface of the dies can also lead to the sticking of the workpiece to the compression dies. While this was not found to be problematic with specimens with a round initial cross section, samples with initially rectilinear cross sections were found to be more prone to sticking due to increased surface area contact with die surfaces. The risk of sticking was also found to increase when a higher-strain/displacement per bite was used, *i.e.,* higher load, and reduced number of passes. The higher friction can also lead to more pronounced barreling of the specimen, which may subsequently complicate specimen rotation due to convex surfaces and protruding corners catching on the compression platens.

The geometry of the sample is also important to consider. Extruded cylindrical bars were used for this study, leading to increased risk of sideways slippage of the samples during initial bites. Once these first chamfers/flats were generated, the risk of slipping greatly decreased. For copper C101 alloy specimen SP8 (see Tables 4.4, 4.5, and 4.6 in the next chapter for all of the samples used in the proof of concept studies), which was an exploratory sample in octagonal cogging, it was found that due to the size effects of the sample geometry it was of even higher risk of slipping into one of the already created flat faces. Furthermore, as it was repeatedly deformed, it became apparent that this slippage increased with passes as the bite surface area was progressively decreased.

The compensation of tooling loss was approximated from the benchmark sample through in-

Figure 3.15: Photograph of Zwick/Roell™ load frame, with arrow indicating extensometer arm fixture. Captured from Zwick/Roell™ product website.

creased input loads to achieve cross-section reductions closer to the target height reduction. Further exploration and consolidation of this method would benefit from further study. Despite having isothermal conditions, small fluctuations of 3-4 °C were observed when the specimen was rotated, possibly caused by small air vortices introduced by the motion and affecting thermocouple readings. Another possible cause is leakage of hot air through the extensometer slot.

Specimen alignment is also complicated by the restricted or null visibility of the specimen when a split tube furnace or EC is used for isothermal experiments. Fine adjustment of the specimen position had to be done prior to heating. Moreover, thermal expansion of the specimens, sample holder, and tooling is important to consider during the temperature ramp-up. During pre-deformation alignment, and checks between bites, a small viewing window in the EC chamber proved highly valuable. The visibility decreases with increasing test temperature (above 600 °C), as, without special modifications, tube furnaces do not provide any way of observing the furnace interior during operation.

In addition to the limitations of using laboratory equipment, some material-specific limitations need to be determined individually for the types of test being carried out. Size effects in materials, can be pronounced and very influential to the overall method and component design. Such effects can be of crucial importance when performing material studies, as phenomena that occur at large scale may not be observable at small scale and vice versa. The specimen size was chosen primarily based on the internal chamber volume of the furnace, as well as initial strength properties with respect to load frame capability.

3.4.1 Future Design Considerations

Greater investment in robust components and more focused adaptation of pre-existing equipment fixtures and features, could further improve the efficacy and robustness of the apparatus design.

Firstly, designing for portability was one major benefit of this method as it could be used

with any load frame system using the current tripod-mounted configuration. However, some load frames provide existing external mounts, allowing for rig mounting to the pre-existing extensiveness fixtures, *e.g.,* mounting arms available on some Zwick/Roell™ load frames, typically used for extensometers, as indicated in Figure 3.15. This would allow for more consistent specimen alignment and also reduce the alignment time, allowing a faster specimen turnover. In addition, increasing the holding torque on the sample via the use of more powerful stepper motors (*e.g.,* NEMA23) would further increase the resistance to slippage. The addition of a third motor system would aid to compensate for the vertical displacement of the specimen during compression, rather than relying on deflection of the long manipulator rod to accommodate this displacement. It would also help fine position adjustments.

Another consideration would be the "flying-blind" nature of the method at higher forging temperatures (greater than 600 °C) using tube furnaces, *i.e.,* not being able to use environmental chamber viewing windows. A small form factor optical fibre-optic camera solution could provide an invaluable additional degree of workpiece position control during operation. It would allow the state of the specimen after each bite to be evaluated and adjustments to be made accordingly. Alongside this system, an in-situ lubrication injection system could prove highly beneficial, if not a necessity, when studying greater levels of strain during hot forging at temperatures exceeding 900 °C. Exploration of the use of graphite films may also provide useful as future work. As the isothermal conditions and repeat passes remove lubricant from the sample, the risk of sticking increases the longer the test runs. In-situ lubrication is used in many larger scale research and industry to not only ensure die/workpiece separation and lower friction, but preferably to also act as a thermal insulator.

Routine programs can be created alongside the load frame control software (*e.g.,* Zwick™ testXpert III) to fully automate each process. Addition of the BNC connections was primarily done to automate this process, however was never tested due to external circumstances and early-stage nature of this work. This change could increase positional accuracy, and throughput of testing.

A final consideration is in the design of the coupling tooling. Currently, grub screws are used to hold the sample and manipulator rod in place. This works well for the manipulator rod, however, as specimens need to be repeatedly inserted and removed from this coupling, this design may not be optimal for high temperature applications due to the reduced longevity of the grub screws. The thermal expansion and oxidation that may occur, can lead to seizure of the workpiece inside the barrel of the specimen holder. Inclusion of a capped pin/pin system, or lock-and-key design, could eliminate this issue, at the expense of more complex sample and holder machining that would be required.

3.5 Summary

First and foremost, the main research output from this work is the novel design of miniaturised experimental simulation of open-die forging, *i.e.,* cogging. After creating and discussing the early design, design methodology, and what can be considered for future development of the design, it is also a key outcome of this research to capture proof of concept studies. These studies are imperative for understanding of how more material studies can be carried forward into the future research projects that can make use of this new apparatus. Thus, it was important for this proof of concept to select materials that are easily deformed, and at a lower temperature as an initial benchmark. Moreover, as these are the first tests carried out on the design, it is less important to get linearity in the samples themselves from the materials standpoint. It is more crucial for understanding to use these samples to better develop the design and method of use itself.

SOLIDWORKS® modelling proved to be instrumental throughout all of the design stages to create a functional design, that could be iterated and improved for manufacture. It was essential in generating the drawings for the manufacturing of the various custom parts, and validating they integrated well with any purchased components. FE modelling was also a useful tool prior to testing

to estimate approximate loads and deformation of the material during testing. Finite element became a vital tool for validating the experiment, demonstrating similar trends in expected loads, and allowing for strain distribution calculation and visualisation.

The materials and methods selected for the proof of concept studies are detailed in Chapter 4, including rationale on any differences in the examination of each material.

4 Materials & Methods

4.1 Introduction

This section details the materials used for the proof of concept cogging studies that are a core outcome from this work. Additionally, it details and discusses the techniques used to characterise and quantify the success of the new apparatus, including FEM and advanced techniques.

4.2 Material and Open-die Forging

C101 copper alloy and Al6060 aluminium were used as the single-phase test specimen material for the pilot forging trials on the designed apparatus. $\alpha + \beta$ Ti-6Al-4V alloy (also known as Ti-64) was selected as the commercial specimen material for the high temperature forging trials. These were the selected alloy choices, to allow for proof of concept of the method and the development process to be carried out through different materials and slowly raising the temperature so as to evaluate the tool-life. This also allowed for improvement of the software and operation of the new apparatus with the operation of the load-frame with the technicians. As an $\alpha+\beta$ alloy, Ti-64 can have differing volume fractions of alpha and beta phases, depending on heat treatment and interstitial (primarily oxygen) content. The nominal chemical composition of the copper, aluminium, and titanium alloys are provided in Tables 4.1, 4.2, and 4.3 respectively.

Table 4.1: Nominal chemical composition of the C101 copper alloy, from the EN1652-EN13601 standard. [330]

Element	Cu	Pb	Zn	Fe	P	Ag	As	O	Sb	Te
Weight %	Bal.	0.0005	0.0001	0.0010	0.0003	0.0025	0.0005	0.0005	0.0004	0.0002

Table 4.2: Nominal chemical composition of the Al6060 aluminium alloy, from the EN 573-3 standard. [331]

Element	Al	Mn	Fe	Mg	Si	Cu	Zn	Ti	Cr	Others
Weight %	Bal.	0.0-0.1	0.1-0.3	0.35-0.6	0.3-0.6	0.0-0.1	0.0-0.15	0.0-0.1	0.0-0.05	0.0-0.15

Table 4.3: Nominal chemical composition of the Ti-6Al-4V titanium alloy, from the Materials Properties Handbook [261]

Element	Ti	Al	V	C	Fe	O	N	H
Weight %	Bal.	5.80	4.00	0.08	0.30	0.20	0.05	0.01

All alloy material was procured as 12 mm diameter hot-rolled round bar. Anti-oxidising glass coatings were applied to the Ti-64 bar prior to heat treatment. Sections of the alloy bars were then subjected to an abnormal grain growth heat treatment in a VFE TAV TPHF horizontal vacuum furnace for 2 hours at 580, 800, and 1100 °C for Al6060, C101, and Ti-6Al-4V alloys respectively before being air-cooled. This material will henceforth be referred to as "as-heat-treated" (AHT) Al6060, C101, and Ti-64. The AHT Al6060, C101, and Ti64 bar sections were subsequently cut into shorter test specimens 28-35 mm long, examples of each can be seen in Figure 4.1.

The open-die forging was carried out on a 250 kN Zwick/Roell™ Amsler Z250 load frame using the Zwick™ testXpert III software. The load frame was equipped with a Severn Thermal Solutions EC2112 environmental chamber (EC) for single-phase experimentation. For dual-phase experimentation the load frame was equipped with a Severn Thermal Solutions SF2113 Split Furnace (SF) using a CU2113 Eurotherm™ temperature control system. Initial testing was performed at ambient

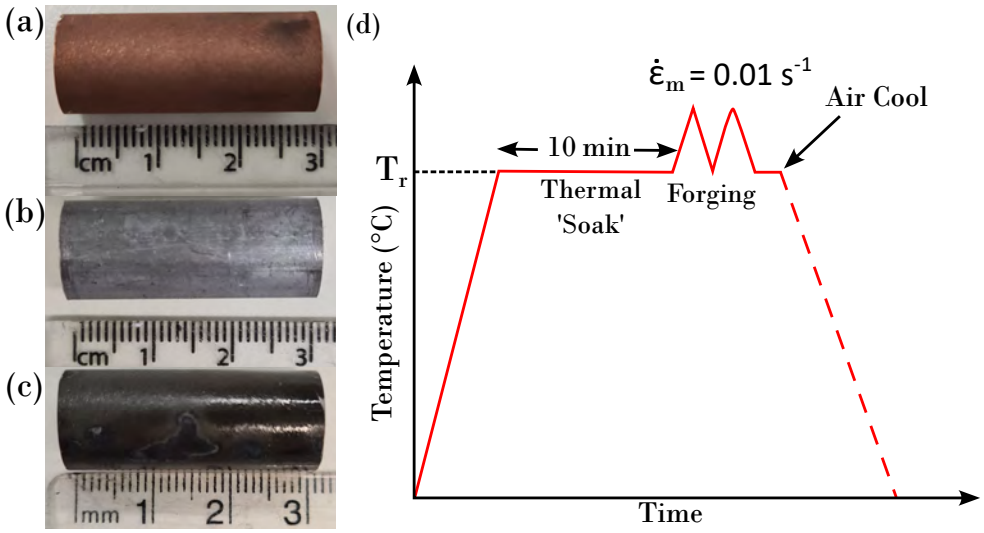

Figure 4.1: (a) C101 alloy, (b) Al6060 alloy, (c) Ti-64 alloy, specimens before testing and, (d) General schematic overview of the elevated temperature compression used in this study, T_r can be used a reference temperature (changes per alloy material).

temperature, and used the standard strain control method. Single-phase specimens for elevated temperature testing were first mounted onto the manipulators and then backed through the EC extensometer slot before attachment to the motor coupling. High temperature dual-phase specimens were first mounted into the manipulator coupling and then aligned through the extensometer slot, with boron nitride suspension being applied as lubricant and anti-stick agent to the specimen and die surfaces. Specimen positioning was then adjusted remotely inside the EC/SF prior to heating and the remaining gaps in the extensometer slot were filled with ceramic wool for thermal insulation. The elevated temperature tests used a step control program method within the textXpert III software.

The Al6060, C101, and Ti-64 specimens were then brought to 450, 600, and 950 °C respectively (T_r in Figure 4.1(d)) and "soaked" for 10 minutes to ensure a homogeneous and stable temperature distribution. A pre-load of 20 N was applied at the end of the soak time, to aid against specimen slipping. The specimens were then repeatedly deformed in 5% cross-section height reduction increments using a controlled step program, with a cross-head displacement of 0.12 mm/s, with the aim for a nominal strain rate of $0.01s^{-1}$ ($\dot{\varepsilon_m}$). Between each deformation, or "bite", the specimen was rotated 90° (except where specified otherwise) to simulate the cogging (*i.e.,* open-die forging) operation. The manipulator rods were marked at 0° in vision of the operator to track specimen rotation between bites. The test matrix for all the cogging operations conducted on the Al6060, C101, and Ti-64 specimens can be seen in Tables 4.4, 4.5, and 4.6 respectively. The specimens were then withdrawn from the EC/SF and allowed to air cool, unless otherwise specified. A schematic diagram of the thermomechanical procedure for the forging tests is presented in Figure 4.1(d).

After forging, 3D GOM scans of the samples were captured using the GOM ATOS TripleScan III rotary table scanner. This 3D data was loaded into the GOM Suite and average strains were measured for each sample using section areas taken every 1 mm along the sample. The average

Table 4.4: Test matrix for Al6060 aluminium alloy, deformed at 450 °C, detailing number of bites, % of deformation (reduction in cross-sectional height), and specimen geometry targets.

Specimen No.	SP1	SP2	SP3	SP4	SP5	SP6	SP7	SP8	SP9
Target Red. in X-section height(%)	10	15	20	25	5	30	40	10	10
Target Geometry	□	□	□	□	□	○	□(2)	○	○(4)
Total No. of Bites	4	6	8	10	2	24	32	12	48
Temperature (°C)	450	450	450	450	450	450	450	450	450

strain reduction was then calculated from the difference in area between sections in the stub zone against the cogged zone.

4.3 Summary of Experimental Cogging Technique

It is crucial to record and highlight the experimental method and preparation stages that are essential to the set-up of this experiment, to ensure that future operators have a reference for rig operation. For test preparation, Loctite™ anti-seize lubricant is applied to the grub screws of couplings that are to be held at elevated temperatures. Additionally, Boron Nitride lubricant is applied onto the dies and sample surfaces for all elevated temperature testing.

Firstly, at room temperature, fix the lead screw and motor assembly onto the assembled tripod using the Manfrotto™ quick release mount ensuring the assembly is locked in at the correct height and orientation. The specimen and rod is then placed into the furnace with the manipulator rod being pulled through the extensometer slot on the front of the furnace/environmental chamber. Close the furnace door, ensuring the specimen and manipulator rod are then placed and fixed to the external coupling using a combination of ⌀3.0 mm and ⌀2.5 mm Allen keys. Place ceramic wool in the remaining extensometer slot space to ensure maximum heat insulation. Set up the cogging rig control box, ensuring it has power and the correct connections have been made. *N.B.* It is worthwhile here also to bring the Zwick™ compression tooling platens closer to the specimen to ensure it is easier to visually align and begin the compression testing.

Once this has been completed, begin heating to temperature. During heating there will be a small amount of thermal expansion, ensure that the load on the machine does not rise too sharply, if at all. Some load drift may be observed. Once the working temperature has been reached, allow for 10 minutes of soaking time to ensure the sample is at a uniform temperature for hot working. This time was calculated with the diameter of sample material based on the ASM International Handbook chapter on the forging of aluminium alloys [332]. Where it is stated, "generally, times at temperature of 10 to 20 min/inch of section thickness are sufficient to ensure that aluminium alloy workpieces are thoroughly soaked and have reached the desired preheat temperature" [332]. This

Table 4.5: Test matrix for C101 copper alloy, deformed at ambient and elevated temperatures, detailing the number of bites, % of deformation (reduction in cross-sectional height), and specimen geometry targets.

Specimen No.	SP1	SP2	SP3	SP4	SP5	SP6	SP7	SP8
Target Red. in X-section height(%)	30(Control)	5	10	15	15	30	40	10
Target Geometry	□	□	□	□	□	□	□(2)	○
Total No. of Bites	12	2	4	6	6	12	16	8
Temperature (°C)	20	20	20	20	600	600	600	600

Figure 4.2: Annotated electronic controller diagram showing current set-up of programmable buttons.

Table 4.6: Test matrix for Ti-64 alloy, deformed at hot temperatures, detailing number the of bites, target % of deformation (reduction in cross-sectional height), and specimen geometry targets.

Specimen No.	SP1	SP2	SP3	SP4	SP5	SP6	SP7	SP8	SP9	SP10	SP11
T. Red. in X-section height(%)	5	10	10	10	15	20	25	5	10	10	15-30
T. Geometry	□	□	□	□	□	□	□	○	○	□	□
Total No. of Bites	2	4	4	6	6	8	10	4	8	4	12
Temperature (°C)	950	950	950	950	950	950	950	950	950	950	950 & 1050

was used as a general rule of thumb for the small ⌀12 mm sample size, ensuring sufficient soaking time.

Once the sample has been soaked for the appropriate time, find the point at which the platens touch the specimen, *i.e.,* the point at which the load cell sees a small yet rapid increase in Z load(N). Set this as the datum zero point. Begin the pre-setup step program for the experiment that is being carried out. This pre-setup program is created graphically with parameters set in the Zwick™ testXpert III software. Between each bite the sample is rotated using the cogging rig control interface. The electronic controller has a set of programmable keys that are currently set-up within the Arduino code to have multiple functions depending on which submenu is selected, *e.g.,* selecting the "Run Experiment" option when an automatic test has not been set-up within the code will result in the rotational motor will be driven. This driving force aids against slipping during the compression tests. The general top level controls are labelled in Figure 4.2.

4.4 Finite Element Analysis

A 3D finite element method (FEM) simulation of the cogging tests, including the initial heating and soaking stages, was performed using the DEFORM™ software to predict the strain distribution at different locations along the samples. Material data for the respective forging temperatures and strain rates was captured in the lab through standard compression testing as part of this work. For validation, the flow stress was calculated using the 0.2% proof stress method and was found to be a close match to the flow stress data available within DEFORM™ and published works [333].

A thermal conductivity of 209 W/mK for Al6060 and 391.1 W/mK for C101 were used for heating operations for the simulated workpieces. A thermal conductivity range of 6.9-18 W/mK for Ti-64 was used as a function of temperature for heating operations of the simulated specimen as suggested by DEFORM™ which are values corroborated in Kim & Lee's work [334]. A convection coefficient of 0.02 N/s/mm/°C was used for all simulations. For the deformation operations, a friction coefficient of 0.3 between the dies and the sample were implemented, as per the software's suggested values for lubricated hot forging. Additionally, the deformation conditions were set up with no heat transfer with the environment, die, and workpiece temperature fixed at 450, 600, and 950/1050 °C for Al6060, C101, and Ti-64 respectively. A Taylor-Quinney factor of 0.9 was used [335, 336], which is a good approximation of the fraction of mechanical work converted into heat during deformation [337–339]. A mesh with 16,000 tetrahedral elements was generated for the workpiece geometry, *e.g.,* specimen C101-SP6 presented in Figure 4.3, with the simulation dies shown in Figure 4.3(d). The movement speed of the lower die during the experimental compression tests was recorded, and the measured value was used as an input for the FEM simulation.

The specimens dimensions predicted by the model were compared with the actual dimensions of the deformed specimens after compression. The model was set up to replicate the same compression levels of the various samples up to a macroscopic true strain(ε_m) of 0.7. The FE models match the geometry of the deformed parts, and using specimen C101-SP6 as an example, predicts a maximum final diameter of 6.37 mm, which was within 2% of the measured diameter of 6.25 mm. This validates the chosen values of heat transfer coefficient and friction coefficient, and suggests that the strain

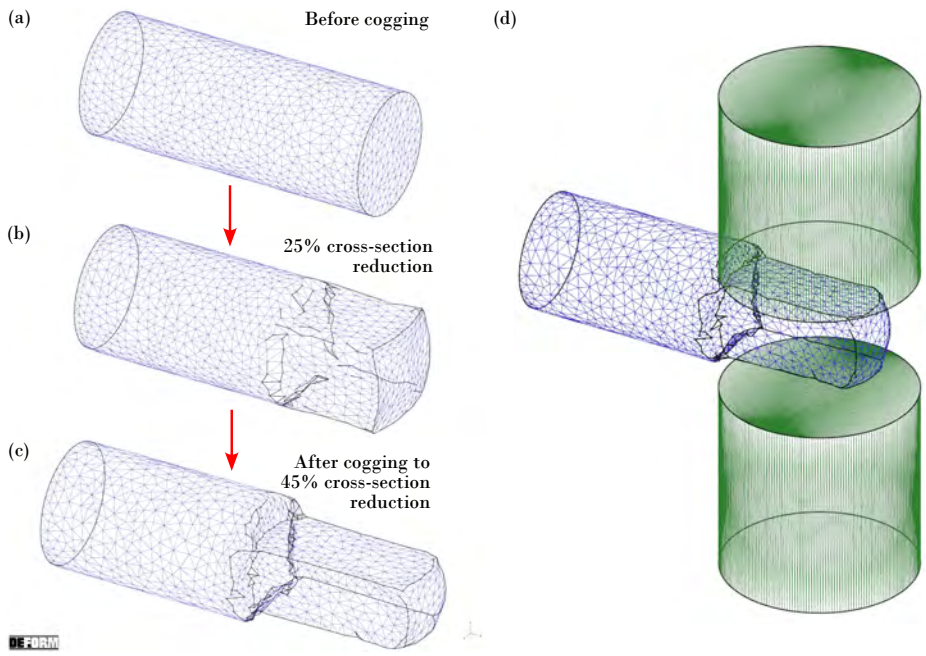

Figure 4.3: (a) The FE generated mesh for specimen C101-SP6 following cogging trial, showing the mesh (a) before cogging, (b) during cogging at 25% cross-section reduction, (c) after cogging to 45% cross-section reduction and, (d) before second cogging bite at 45% cross-section reduction with cogging dies shown.

distribution is reasonably accurate. As another example, specimen Ti-64-SP7 predicts a final cross-section of 8.5 mm in one direction, which was also within 2% of the measured diameter of 8.3 mm. This reinforces the chosen values of heat transfer coefficient, friction coefficient, and suggests that the strain distribution is reasonably accurate for Ti-64.

The model for this study was first set up for nominal cogging conditions, assuming all rotations and compressions are in accurate 5% incremental bites throughout. A second model was set up post experimentation for specimen Ti-64-SP7, which during testing had a sticking complication. This sticking was due to numerous factors, including the large number of bites, which resulted in the final rotation being interrupted. The final compression was repeated in the first compression direction. Therefore, this element was carried forward into the model and the simulation repeated, which resulted in the 2% tolerance previously mentioned.

The Johnson-Cook material model was also briefly explored, this model is a function of von mises tensile flow stress, taken from the DEFORM software package is expressed as:

$$\bar{\sigma} = (A + B\bar{\varepsilon}^{n}) \left(1 + C \ln\left(\frac{\dot{\bar{\varepsilon}}}{\dot{\bar{\varepsilon}}_0}\right)\right) \left(\frac{\dot{\bar{\varepsilon}}}{\dot{\bar{\varepsilon}}_0}\right)^{\alpha} \left(D - ET^{*^m}\right) \tag{4.1}$$

where:

$$T^* = \frac{(T - T_{room})}{(T_{melt} - T_{room})} \tag{4.2}$$

and:

$$D = D_0 \, \mathbf{exp}\left[\, k\,(T - T_b)^{\beta}\right] \tag{4.3}$$

where $\overline{\sigma}, \overline{\varepsilon}, \dot{\overline{\varepsilon}}, \dot{\varepsilon}_0, T_{room}$, and T_{melt} are flow stress, plastic strain, effective strain rate, reference strain rate, room temperature, and melting temperature respectively [340]. At this stage, microstructural modelling was not considered further and should be considered as future work as presently the strain distributions was the critical data to capture using DEFORM™ simulation.

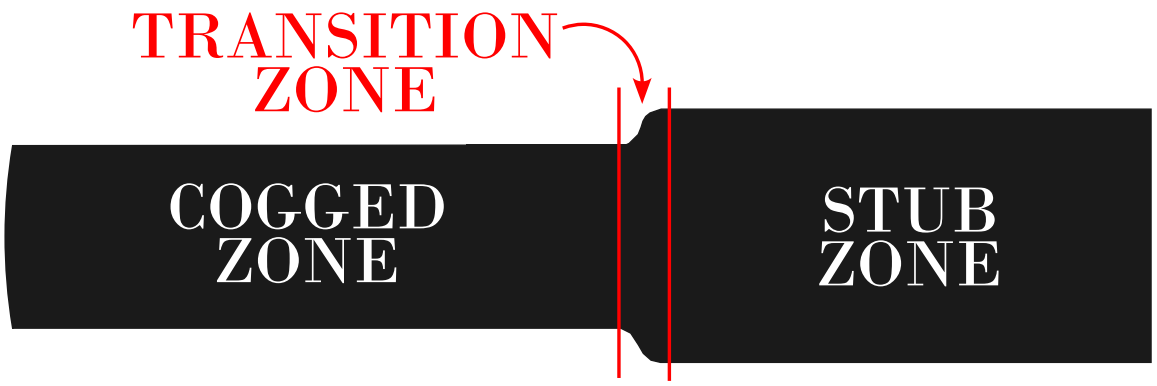

Figure 4.4: Diagram indicating deformed billet zone classifications.

4.5 Microstructure Characterisation

The deformed samples were sectioned along the longitudinal axis using EDM, cold-mounted in non-conductive epoxy resin, ground using silicon carbide abrasive papers and polished with diluted colloidal silica suspension (up to 20% with deionised water) to a mirror finish. The final grinding and polishing recipes for C101 copper, Al6060 aluminium, and Ti-6Al-4V titanium alloys are presented in Table 4.7. The C101 alloy specimens were subjected to a final etching by immersion of approximately 15-25 s per sample. The etching reagent used was a solution of 4-6 ml nitric acid in 9 ml water. This water-to-acid proportion was selected because a 1:1 ratio proved too aggressive. The Al6060 alloy was subjected to a long exposure final etching of a solution of 2.5 ml nitric acid, 1.5 ml hydrochloric acid, 1 ml hydrofluoric acid, and 95 ml distilled water. The Ti-64 specimens were subjected to a final etching by swabbing of Kroll's reagent (*i.e.,* 100 ml water, 1-3 ml hydrofluoric acid, and 2-6 ml nitric acid).

Light micrographs were then acquired using a Leica™ DM12000 microscope with a motorised stage. First, an overall macro image of the entire sample was taken and then higher resolution micrographs were acquired in 3 zones, including stub, transition, and cogged zones; these zones are highlighted in Figure 4.4. The mean linear intercept method was used within ImageJ software to determine average grain size in the stub and cogged zones, which were then used to calculate the reduction in grain size. These lines were drawn perpendicular to the Billet Direction (BD) in all cases, in order to determinethe average grain size, or average grain width for the given area of the sample.

The C101 and Ti-64 specimens were also hot-mounted in conductive bakelite and ground and polished to a mirror finish (Al6060 specimens were just repolished as they could not be hot-mounted due to aging), before subjecting to a final vibratory polishing for 1h C101, 3h for Al6060, and 16h for Ti-6Al-4V using 0.02 µm colloidal silica suspension diluted to 20% with deionised water. EBSD maps were acquired using a Thermo Fisher Scientific™ Quanta 250 field emission gun scanning electron microscope (FEG-SEM), with an Oxford Instruments™ Nordlys EBSD detector and the

Table 4.7: Final grinding and polishing recipes for C101 copper alloy, Al6060 aluminium alloy, and Ti-6Al-4V titanium alloy. Grinding stage values denote abrasive grit level. Polishing step values denote force of specimens into microcloth with diluted colloidal silica suspension. Polishing steps were repeated until specimen reached mirror finished condition. ** where required for level surface.*

Alloy	Grinding (Abrasive Paper)					Polishing (Microcloth)		
C101	400*	800	1200	2500	4000	20N	15N	10N
Al6060	400*	800	1200	2500	/	20N	15N	10N
Ti-6Al-4V	400*	800	1200	2500	/	20N	15N	10N

Oxford Instruments™ AztecHKL 4.1 software. This data was captured to demonstrate the qualitative output capability from the methodology, and visualise the microstructural changes in the C101 material. A series of various area sizes were captured on specimens at locations within the cogged zone, ranging from the smallest area of 49.8 µm×43.8 µm to the largest of 3768 µm×3294 µm, using varying step sizes, that were selected relative to the map size being captured, ranging from 0.1 µm - 6 µm. Generally, minimal variations in map sizes can be seen across materials, but large variation was necessary for Ti-6Al-4V samples to capture both the as-received microstructure with small map areas, and α colonies (prior β grains) using larger map areas. Unless otherwise stated, in general all EBSD data maps were captured from the cogged zones of each sample. In all cases, at least 80% of the points were successfully indexed.

The captured EBSD data was analysed using the MTEX Toolbox [341] developed in the MATLAB® software package. The analyses showed that high angle grain boundaries (HAGBs) were predominantly observed throughout, the settings for these MTEX calculations were as follows: low angle grain boundaries (LAGBs) were defined as those with misorientations between 3° and 5°, and medium angle grain boundaries (MAGBs) were defined as boundaries with misorientation angles between 5° and 10°. HAGBs were defined according to a misorientation angle of at least 10°, and twin boundaries were defined as those with a 60°<111> misorientation, allowing an 8.66° tolerance, following the Brandon criterion [342].

Additionally, Vickers microhardness indentation maps and series measurements were captured using a DuraScan® 70 G5 hardness tester with a load of 1 kg (HV1) for copper and titanium, and 0.1 kg (HV0.1) for aluminium specimens, all with a dwell time of 10 s under the Vickers BS EN ISO 6507 [343] standard for all copper and titanium samples. Example of microhardness indentations for each alloy used in this work is presented in Figure 4.5. These hardness maps were overlaid on the light micrograph images to compare grain structure against hardness. Indentations were made every 1.7 mm for maps and 0.7 mm for line series measurements. These distances were selected in order to get an even and controlled distribution of indentations to best capture the hardness of the specimens.

4.6 Advanced Techniques

4.6.1 3D Grain Mapping using DCT

Grain Mapping

The microstructure of polycrystalline materials like metals, minerals or ceramics is composed of grains with crystallographic orientation, shape and size. The microstructure influences material properties, such as *e.g.,* strength or ductility. Its appearance depends on the processing of the material, and can be manipulated for instance by deformation or annealing. Grain mapping is a common name for a variety of non-destructive tomographic techniques originating from synchrotron X-ray facilities to access the grain-based three-dimensional (3D) polycrystalline microstructure of bulk samples. The volumetric information gained from 3D grain mapping allows to investigate

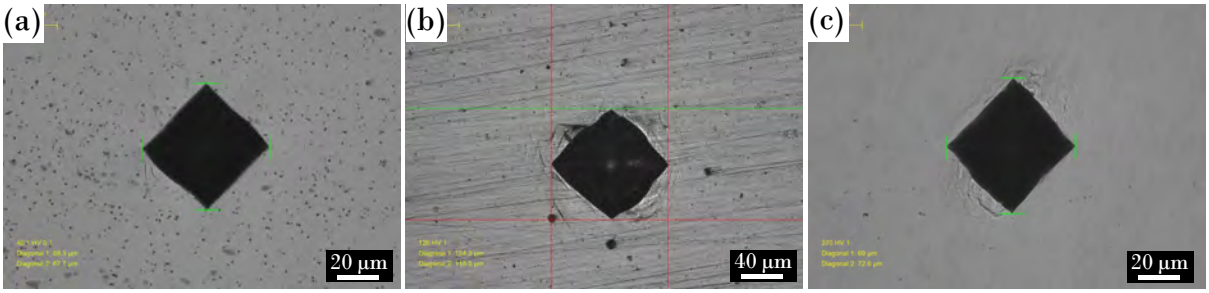

Figure 4.5: Examples of vickers microhardness test indentations for (a) Al6060 alloy, (b) C101 alloy, and (c) Ti-6Al-4V alloy.

relationships between sample processing, polycrystalline microstructure and material properties.

One selected advanced technique chosen for analysis of the mini-billets in this study was use of X-ray computed tomography (XCT) [344]. For this, beam time was accessed at the Photon Science Institute (PSI) at the University of Manchester where the Zeiss Xradia 620 Versa, shown in Figure 4.6 was used to scan selected single phase specimens of aluminium alloy Al6060 of low strain, and a singular dual-phase exploratory Ti-6Al-4V specimen. These materials were selected as the low strained single phase Al6060 alloy was understood to be the simplest to image using this technique, allowing for the advanced technique to be assessed between 2 strain levels of the same material. Titanium alloy Ti-6Al-4V specimen was used as it was more difficult to image, and was interesting to try to characterise a dual-phase material using this technique. Unfortunately, this resulted in a long exposure and capture of the 3D data (over 48 hours), which ultimately resulted in an extremely 'noisy' 3D grain map, which was inconclusive. The specific technique used is known as X-ray diffraction contrast tomography or labDCT, which was developed at PSI. This proved to be an excellent validation technique in terms of grain measurement and mapping. The schematic presenting the experimental set-up of the labDCT technique in the laboratory X-ray microscope is displayed in Figure 4.7.

LabDCT

X-ray microscopes equipped with a Laboratory Diffraction Contrast Tomography (LabDCT) imaging module form images based upon the X-rays diffracted by the individual grains within the sample. The LabDCT imaging module as shown in Figure 4.7 consists of a set of apertures and beam stops and a specialised detector objective optimised for diffraction imaging. The aperture shapes a conic X-ray beam, emitted by a micro-focus X-ray source such that only the sample or part of it is illuminated. Furthermore, the beam stop in front of the X-ray detector blocks the direct beam and the detector records images of the signal diffracted by the sample. Where crystals in the sample diffract X-rays, corresponding bright diffraction spots appear in the images. The diffracted intensities originating from a crystal increase with its volume and electron density and decrease with lattice imperfection and mosaicity, caused by crystallographic defects like plastic strain, or other effects like absorption.

Shannon Nyquist Theorem [345] was used for calculating the number of projections to input

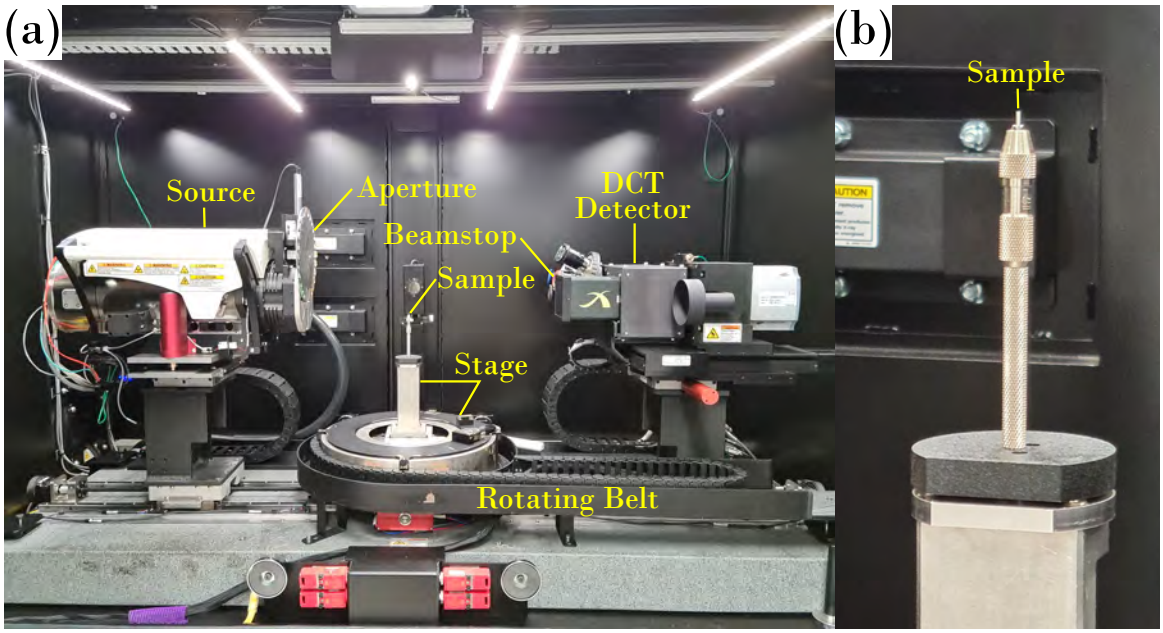

Figure 4.6: (a) Image showing internal chamber and labelled DCT setup of Zeiss Xradia 620 Versa equipment, and (c) Image showing close up of mounted sample, highlighting 1mm scale.

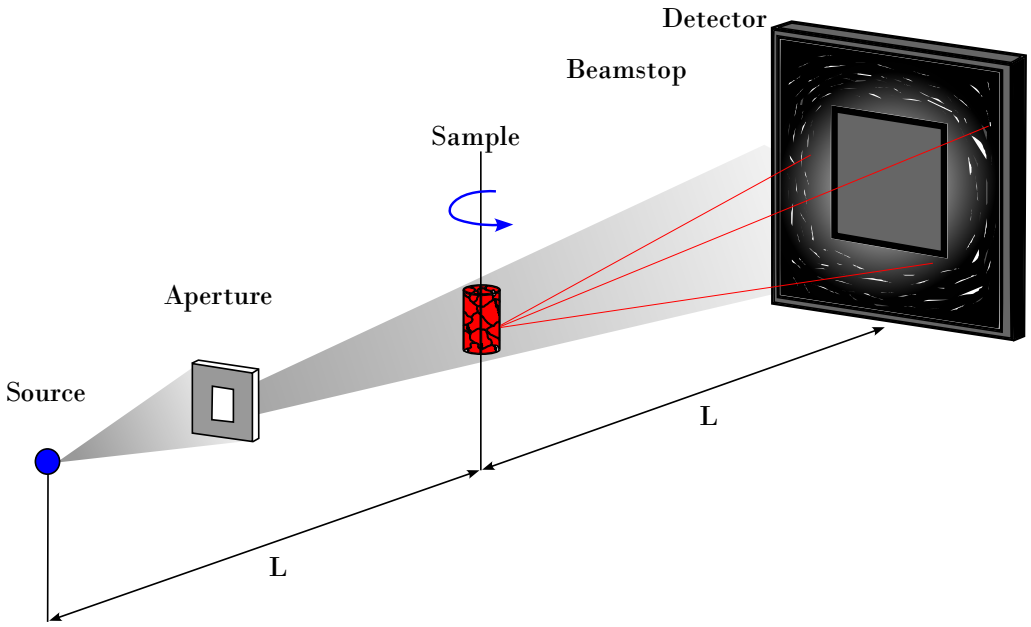

Figure 4.7: Schematic showing the experimental setup of labDCT in the laboratory X-ray microscope.

into the CT machine:

$$p_{min} = \frac{\pi}{2} \cdot pxl_h \tag{4.4}$$

where p_{min} is the minimum number of projections and pxl_h is the number of pixels occupied by the specimen on the horizontal axis.

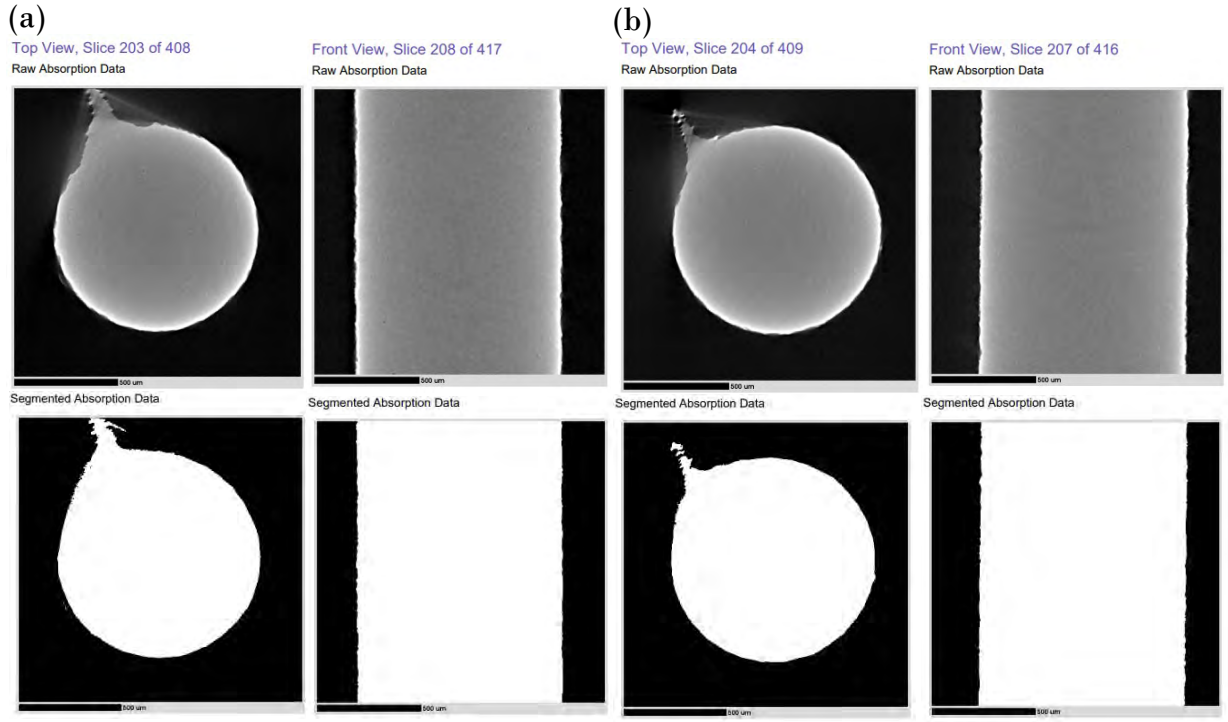

Figure 4.8: Raw and segmented absorption data of DCT specimens, (a) SP1 (2.9%), and (b) SP2 (10.6%).

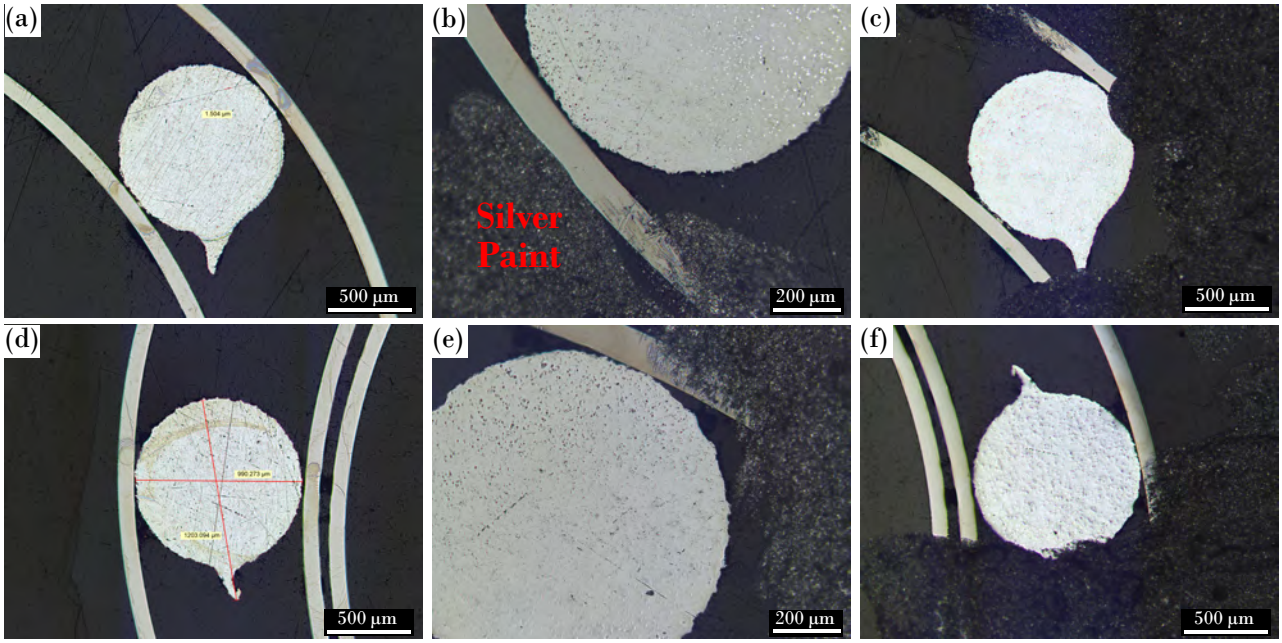

Figure 4.9: Light micrographs showing stages of sample preparation for EBSD, SP1 (a) Pre-final polish, measuring scratch width, (b) silver paint check, (c) final application, and SP2 (d) pre-final polish, measuring specimen dimensions, (e) silver paint check, (f) final application.

LabDCT Reconstruction

In LabDCT, the sample is usually imaged across an angular range of 360°, ideally with a regular stepping of 2° or less. A single image recorded in LabDCT mode is called a diffraction contrast pattern (DCP). The process of separating signal originating from diffraction and background is referred to as segmentation. The segmented signal from a series of diffraction contrast patterns is used by computer algorithms to reconstruct the 3D crystallographic microstructure of a region of interest (ROI) in the sample. Grains and their grain boundary counterpart are then defined by connected regions of similar crystallographic orientation. The raw and segmented absorption data of the two samples are presented in Figure 4.8. After reconstructing all of the 3D data output, the data was then loaded into and analysed using Dragonfly™ software. The next stage was to verify the 3D results using an alternate method, for this EBSD analysis of the specimens was selected.

EBSD Validation Method of DCT Samples

For validation, the specimens were cold mounted in epoxy resin, while being held in a steel clip to ensure the sample remained in the correct position, and then mechanically ground and polished in preparation for EBSD analysis. Before EBSD, the samples were vibropolished using 0.02 µm colloidal silica for 3 hours, and then were painted with silver paint to ensure electrical grounding in the SEM. For these samples in particular, this presented a new challenge. As the samples are ∼1 mm in diameter, the small brush used to apply the silver paint for EBSD analysis was too large. Instead, a single bristle was taken from a regular artist paintbrush and held with tweezers for the application of silver paint near the sample edge. Light micrograph comparisons before final polishing, during silver paint application, and final application is presented in Figure 4.9.

After numerous issues with charging, due to the non-conductive epoxy resin, which caused drifting and no results when indexing in the SEM, the samples were carefully broken out of the epoxy resin and remounted onto a stub and again painted with silver paint. EBSD was then attempted again at this stage, however the indexing was again too poor to continue due to scratches introduced from sample removal from epoxy. Instead, the samples were fully removed from the epoxy resin and finally hot-mounted into bakelite, as the ageing/precipitation hardening was ultimately not a concern for investigating the grain size for validation of the 3D DCT grain mapping. Whereas

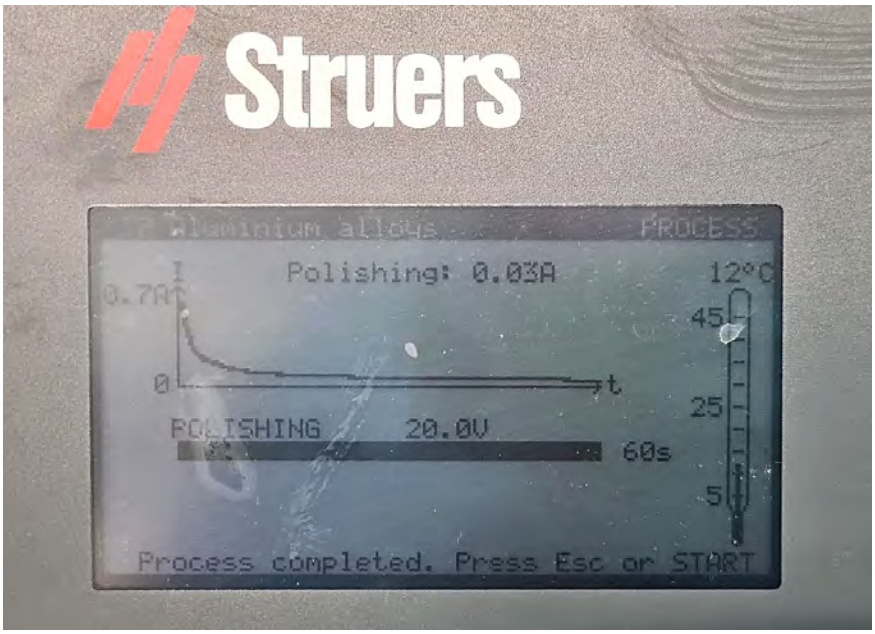

Figure 4.10: Image of LectroPol 5 electronic screen showing electropolishing process for DCT Specimen 1, highlighting current and voltage over time, and temperature.

for the main specimen range, other properties (*i.e.,* hardness) were important to capture from the open-die forging. The hot-mounted specimens were then subjected to a 60 s electropolish with Struers™ A2 solution on a Struers™ LectroPol 5 machine, an image of the LectroPol 5 screen after electropolishing of DCT Specimen 1 (2.9% cross-section reduction) is presented in Figure 4.10. Results gathered from this advanced DCT technique are presented in Chapter 5.

4.7 Summary

The copper C101 and aluminium Al6060 alloys were selected to allow for proof of concept of the method and the development process to be carried out at lower temperatures, to evaluate the inital operations and set-up. This also allowed for improvement of the software and operation of the new apparatus with the operation of the load-frame with the technicians. The Ti-6Al-4V titanium alloy, which is of more commercial and research interest for ingot-to-billet conversion was used for a higher temperature evaluation of the tooling and the technique.

Finite element, and various microstructure characterisation methods were then used to evaluate the impact of the new apparatus and developing techniques on the microstructure morphology and grain size evolution of the different materials. In the case of the aluminium alloy Al6060, EBSD characterisation methods were chosen to be limited due to the results of the initial light micrographs showing the least change in grain size and morphology. It was concluded due to the grain size on these optical macrographs, that it was acceptable for EBSD maps of a selection of strain levels to be captured. However, it was material selected for the advanced characterisation technique LabDCT, as the larger grain size and morphology (*i.e.,* less grains in the specimen volume) would have better resolution in X-ray diffraction, compared to the copper C101 and Ti-6Al-4V titanium alloys.

Chapter 5 presents and discusses the first set of experimental proof of concept material results from the novel design, demonstrating the objective of achieving grain refinement and the aim of replicating the cogging process experimentally.

5 Micro Cogging of Single-Phase Alloys

5.1 Introduction

Cogging of various single-phase metal alloys was completed in the lab environment at a miniaturised scale using the novel equipment design. These initial studies were carried out as a proof of concept study for the new apparatus. It allowed for insights into the capability of the rigs tooling under both ambient and elevated temperature testing. The selected materials for this study were copper C101 alloy, and aluminium Al6060 alloy as they were cost-effective and relatively soft metals which are more easily worked at lower temperatures. Both materials have an FCC crystal structure meaning they are relatively soft and ductile materials. Copper C101 alloy proved to be excellent in showing the effectiveness of the apparatus in achieving measurable grain refinement in the hot-work material. The aluminium alloy Al6060 ultimately showed characteristic traits with high levels of internal strain between sub-grain boundaries however, did not present the same visible level of recrystallisation and grain refinement.

When designing accurate control schedules, an understanding of material behaviour during the hot forming processes is crucial. To achieve desired mechanical properties of the product, understanding of microstructural changes and deformation mechanisms occurring inside the workpiece is required. For hot working processes such as cogging, it is essential to determine an accurate microstructure evolution model which is suitable for various forming conditions depending on strain, strain rate, and temperature. In this chapter, the preparation and testing of single-phase alloys using the novel designed apparatus is presented, analysed, and discussed.

5.2 Heat Treatment Study

In this study, it is necessary to understand the state of the ingot material through all the various stages of its microstructure, from the state of purchase, through heat treatment, and finally after deformation, and any post-processing.

An essential part of this is understanding the process parameters that control the grain growth kinetics of the purchased hot-rolled bar when undergoing heat treatment. From this, it is imperative to investigate which heat treatment, with regard to time and temperature would be best to grow

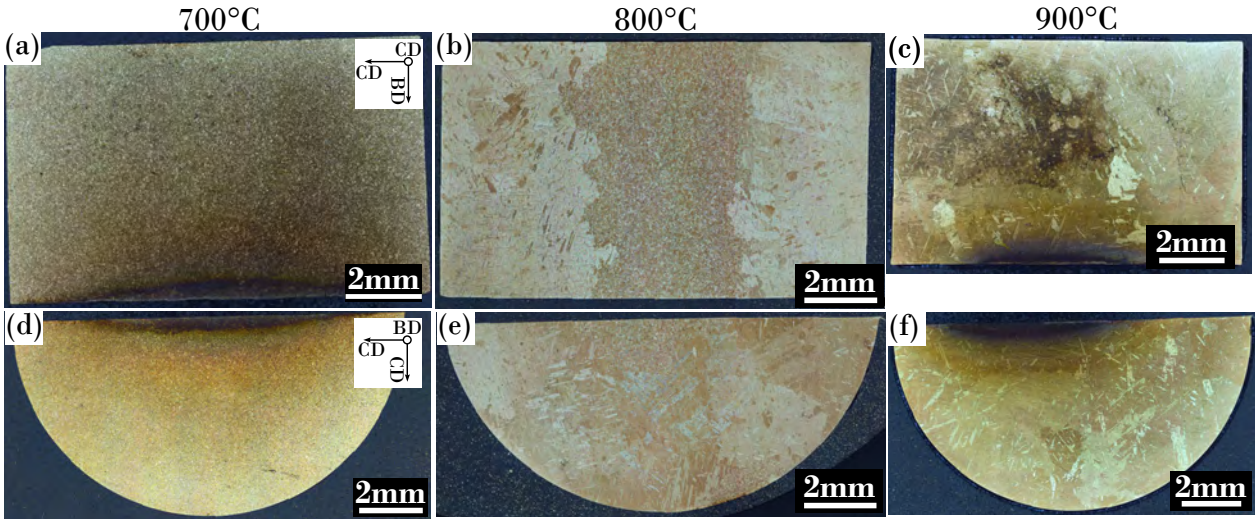

Figure 5.1: Light macrographs of C101 heat treated material sections, (a) 700 °C longitudinal section, (b) 800 °C longitudinal section, (c) 900 °C longitudinal section, (d) 700 °C transverse section, (e) 800 °C transverse section, and (f) 900 °C transverse section.

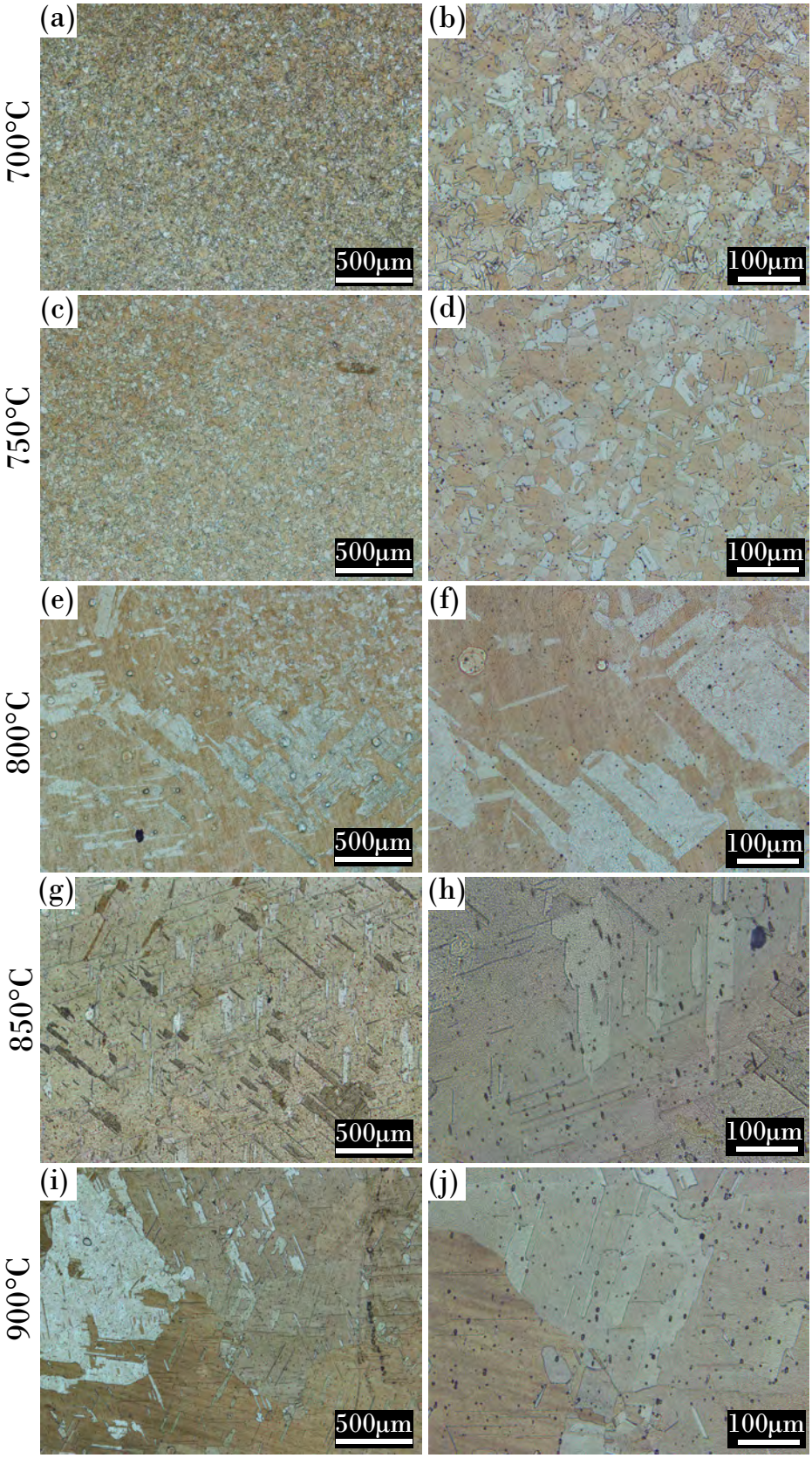

Figure 5.2: Light micrographs of C101 heat treated material sections at different magnifications, (a) - (b) 700 °C, (c) - (d) 750 °C, (e) - (f) 800 °C, (g) - (h) 850 °C, and (i) - (j) 900 °C.

the grains to be of an acceptable size to analyse at a miniaturised scale. Therefore heat treatment trials were undertaken at the Advanced Materials Research Laboratory (AMRL) at the University of Strathclyde in order to better compare temperatures and timings for the grain growth heat treatment. The furnaces used for this heat treatment study were Carbolite™ Furnaces CSF 1200 and CWF 1200.

Figure 5.1 presents macro images of samples heat treated for 1 hour at 700, 800, and 900 °C, these temperatures and times were chosen to investigate the grain size differences as the alloy approached melting point. Grain growth evolution can be seen through these images, where (a) and (d) show a fine structure at 700 °C demonstrating this temperature and time is insufficient in growing the grains to a desired level of coarseness for visualing any grain refinement at this scale. Figure 5.1(b) and (e) show 2 regions, a coarse grained area along the external edges of the sample and the initial fine grain structure in the centre of the sample. This indicates that 800 °C is sufficient in achieving the desired grain growth, but would require more time in order to fully homogenise to the desired coarse structure for this sample size. 5.1(c) and (f) show a fully coarse structure, demonstrating 900 °C for 1 hour is sufficient, albeit more aggressive method of growing the grains as it is far closer to the materials melting temperature of 1083 °C.

Figure 5.2 presents micrographs of samples heat treated for 1 hour at 700, 750, 800, 850, and 900 °C. These images were captured in order to capture the grain size and morphology difference between the different heat treatment parameters. These images confirm that 800 °C is a sufficient grain growth temperature, with 750 °C being similar to the 700 °C sample.

From this study, for copper C101 alloy, a temperature of 800 °C for 2 hours was selected to grow the grains in this sample size of material to an acceptable size for subsequent experimentation, an extra hour was added to achieve a more uniform grain distribution, *i.e,* homogenous morphology. Secondly, for aluminium Al6060 alloy, a temperature of 580 °C for 2 hours was chosen to grow the grains for this sample size for testing, both as it is to the melting interval of 600 to 655 °C [346], and follows the EN 573-3 standard where it is stated for a homogenisation procedure a temperature of 580 °C is employed for at least 2 hours [331].

These findings were taken forward to the final heat treatments that were then carried out in an VFE/TAV Vacuum furnace at the AFRC. The reason behind carrying out these heat treatments in the vacuum furnace is that, in addition to investigating the grain growth, this short study allowed

Table 5.1: Mass measurements of heat treatment trials, before and after heat treatment with Carbolite™ Furnaces CSF 1200 and CWF 1200 at the AMRL. All measurements made with Internal Calibration high precision electronic balance, measurement standard deviation is equal to ± 0.001.

Material	Temperature (°C)	Temperature (K)	Mass Before (g)	Mass After (g)
Ti-6Al-4V	900	1173	3.173	3.157
	950	1223	3.541	3.565
	1000	1273	3.061	3.089
	1050	1323	3.321	3.364
	1100	1373	3.085	3.143
Al6060	500	773	2.122	2.121
	520	793	2.198	2.198
	540	813	2.010	2.010
	560	833	2.221	2.221
	580	853	2.100	2.100
C101	600	873	6.990	6.988
	650	923	6.626	6.621
	700	973	6.795	6.737
	750	1023	6.682	6.676
	800	1073	7.025	6.938
	850	1123	6.896	6.785
	900	1173	7.035	7.036

for a quick assessment of the level of oxidation that would be expected upon heat treating the different materials. Table 5.1 presents the change of mass from the heat treatments (*e.g.,* due to oxidation) of the different alloys used in this study.

5.3 Results from Miniaturised Cogging of C101 Alloy

5.3.1 Pre-worked C101 Alloy

The first material tested was copper C101 alloy, the starting microstructure prior to any grain growth heat treatments is presented in Figure 5.3. The presented microstructure is characteristic of pure copper alloy with a preferential alignment of the [011] direction for IPF-ND (out-of-page). The EDS results also output 100% copper as a result, demonstrating that the impurities are of very low quantity, which is expected when compared with Table 4.1. The average Vickers microhardness was measured as 105.4HV for the procured C101 alloy.

This as-received material was then subjected to a grain growth heat treatment of 800 °C for 2 hours in a VFE TAV vacuum furnace. This grain growth heat treatment was carried out so that grain refinement in the following cogging tests can be better visualised, allowing the efficacy of the apparatus to be assessed. The heat treated microstructure can be seen previously in Figures 5.1 and 5.2. Additionally, EBSD data was captured at the same scale as the procured material EBSD data, seen in Figure 5.3 for comparison, this data is presented in Figure 5.4. It is observed that the grain size is much larger than the previous procured EBSD map, with not many grains visible at this scale. From these observations, it is concluded that the desired coarse grain structure was

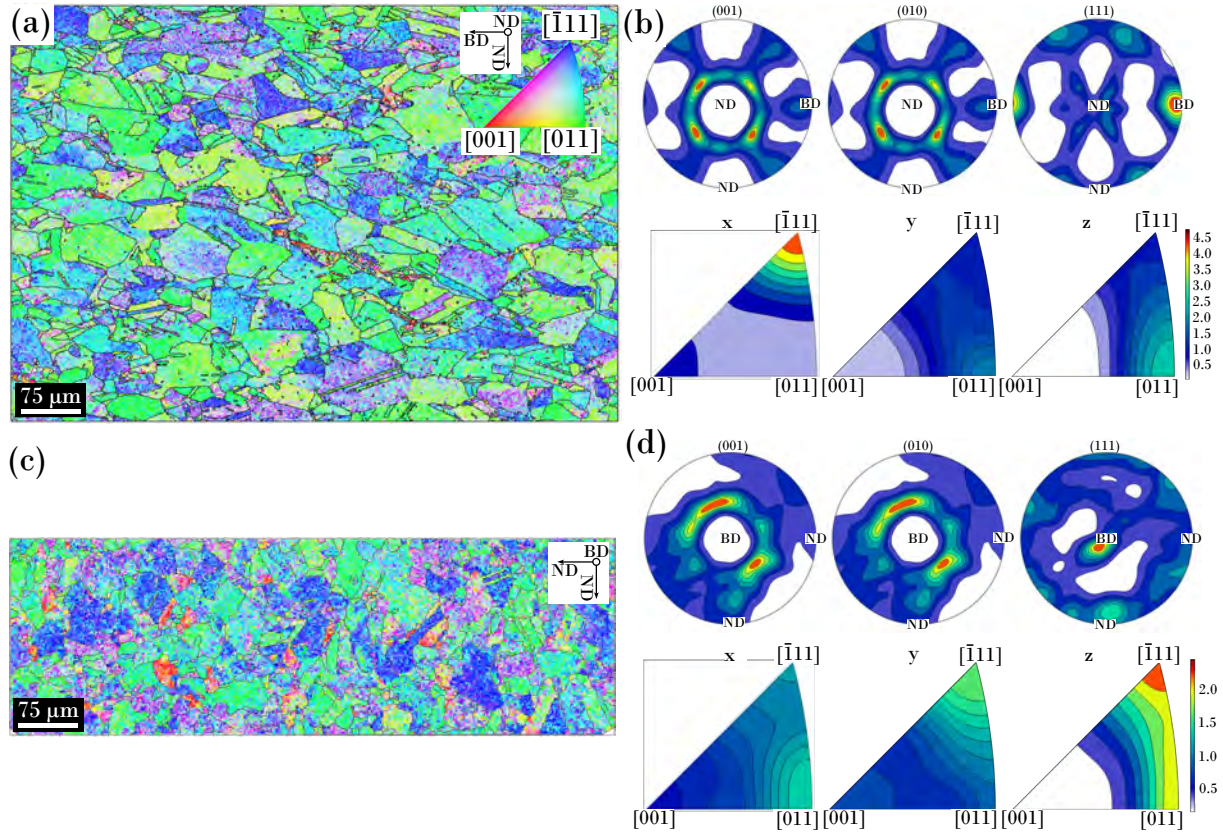

Figure 5.3: EBSD results captured from the as-received C101 alloy material, (a) IPF-ND map (out-of-page) for billet section (b) Pole figures and Inverse pole figure diagrams for ND map (c) IPF-ND map (out-of-page), (d) Pole figures and Inverse pole figure diagrams for transverse (BD) map. Billet Direction (BD), and what would be Cogging Directions (CD) have been labelled as ND, which are 90 degrees from the BD. IPF keys are the same for (a) and (c).

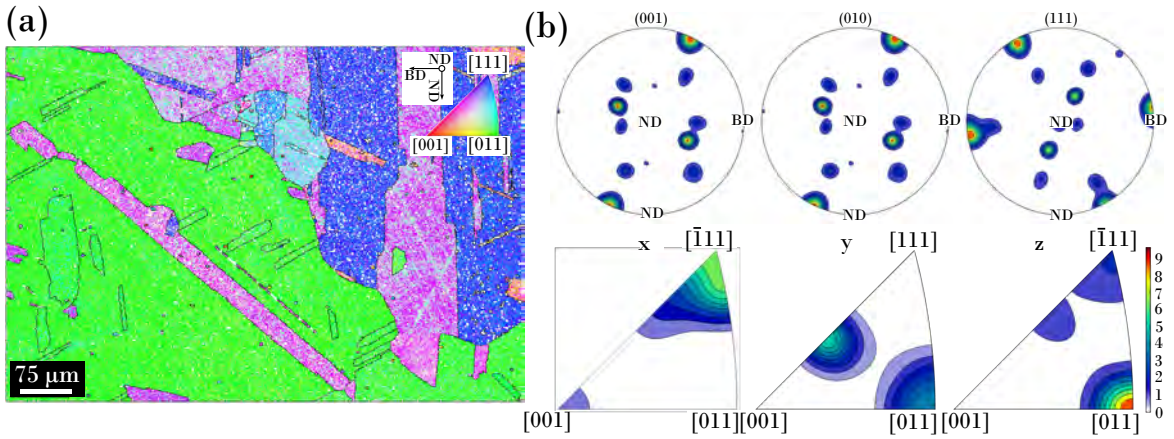

Figure 5.4: EBSD results captured from the heat-treated (800 °C for 2 hours) C101 alloy material (AHT-C101), (a) IPF-ND map (out-of-page) for billet section (b) Pole figures and Inverse pole figure diagrams for ND map.

achieved with the heat treatments carried out, and the material was ready for miniaturised cogging trials.

5.3.2 Miniaturised Cogging of C101 Alloy

Equipment capability was initially tested at room temperature, starting with the benchmark, specimen SP1. Specimen SP1 was cold-worked with 5% incremental deformation (*i.e.,* reduction of cross-sectional height) in the radial direction on both 0° and 90° axes. Between each of these pairs of bites the sample was removed from the holder and measured using electronic calipers, across 3 points of the cogged area and the readings were then averaged. The details of these measurements are provided in Table 5.2, *N.B.* original specimen height measured as 11.59 mm.

Benchmark testing halted after the first bite at 30% as the sample sheared. Understanding of the apparatus operation, material behaviour at room temperature, expected load figures, and tooling capabilities was captured from this first test. Figure 5.5(b) shows specimen SP1 after cold cogging and Figure 5.10(a) shows the light microscopy appearance of the longitudinal cross-section of specimen SP1. Figure 5.10(a) it can be seen that there are visible plastic flow lines towards the edge of the transition zone, and throughout the centre of the cogged zone. Table 5.3 details the specimen results for the C101 copper alloy data-set, comparing target, measured, and calculated height and area reductions respectively.

Deformation resulted from all cogging trials followed a similar overall trend, with the first bite

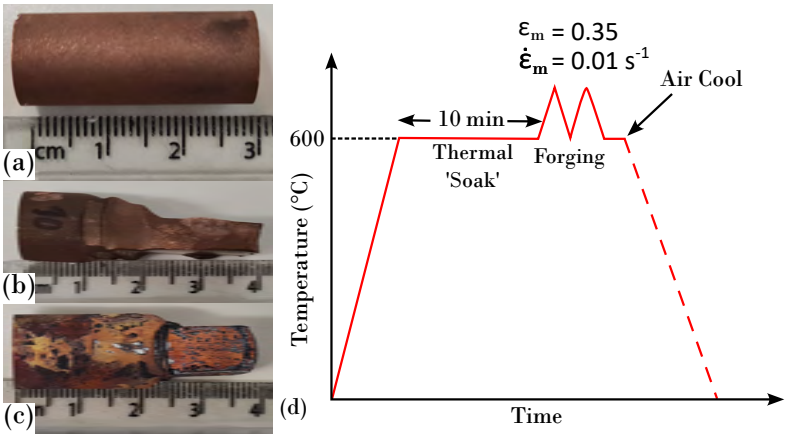

Figure 5.5: (a) Specimen before testing, (b)Benchmark copper C101 specimen SP1 forged at ambient temperature, (c) Copper C101 specimen SP6 forged at elevated temperature (600 °C) and, (d) Schematic overview of the elevated temperature compression tests used in the copper experiments.

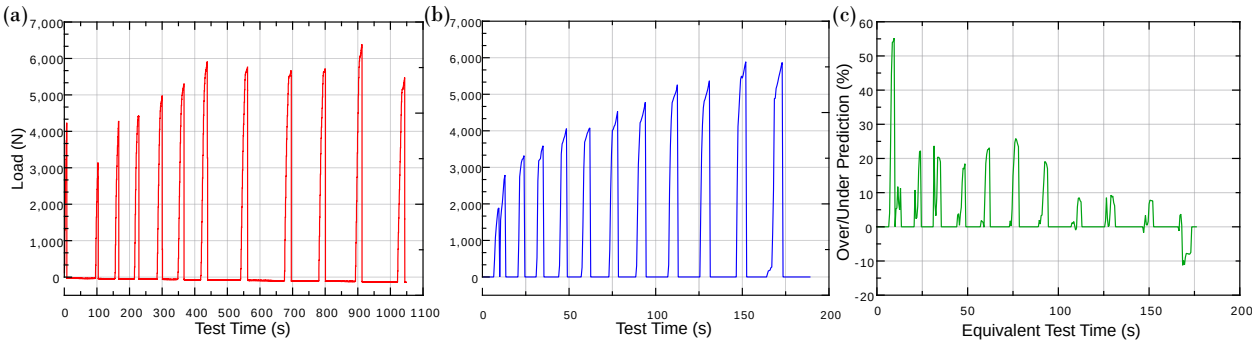

Figure 5.6: (a) Measured load (N) against test time (s) for specimen SP6 during the cogging trial at 600 °C. Data was taken from Zwick/Roell™ load cell during testing, recorded in Zwick™ testXpert III software, (b) The FE predicted graph for load (N) against test time (s) for C101 copper alloy to the same temperature and number of bites and, (c) Graph showing over or under prediction of the model against the captured load data as a percentage against an equivalent test time. Visualised using LabPlot by KDE®.

achieving a higher load than the respective second bite on the perpendicular axis. This can be seen from the load graph data of specimen SP6 in Figure 5.6(a), *N.B.* load cell drift is observed over the course of the cogging trial. The post-analysis load graph output from DEFORM™ FE modelling

Table 5.2: Per-bite target and measured cross-sectional deformation levels for Specimen SP1, deformed at ambient temperature, used as a benchmark for subsequent tests. All measurements made with electronic vernier callipers.

Target Cross-sectional Height (mm)	Measured Cross-sectional Height (mm)	Cross-sectional Height Deviation (mm)	Target Cross-sectional Height Reduction (%)	Input Cross-sectional Height Reduction (%)	Measured Cross-sectional Height Reduction (%)
11.0	11.3±0.2	0.3	5	6	2.2
10.4	10.9±0.2	0.5	10	12	6.3
9.9	10.4±0.2	0.5	15	19	10.5
9.3	10.1±0.2	0.8	20	28	13.2
8.7	9.5±0.2	0.8	25	38	18.4
8.1	7.5±0.2	-0.6	30	47	35.0

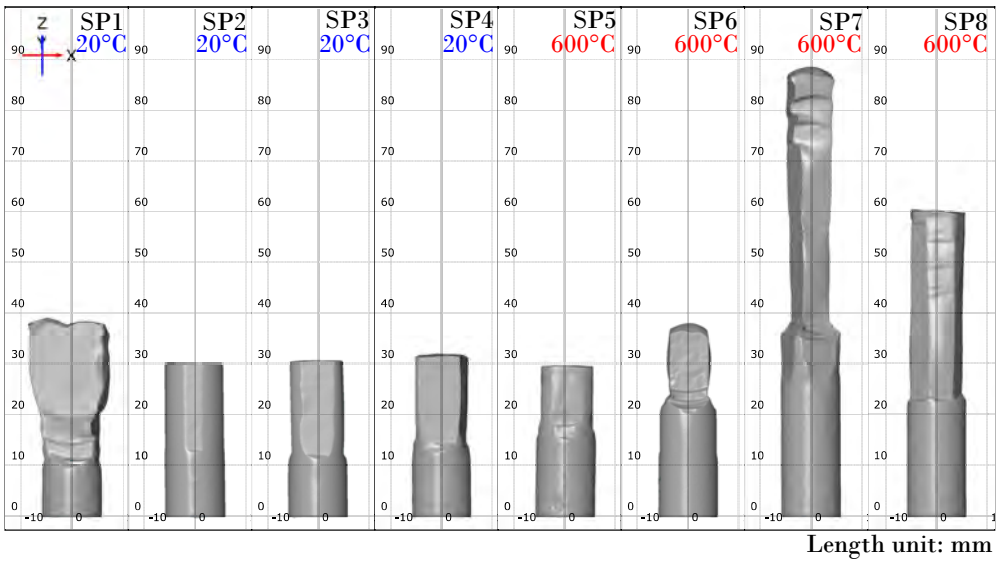

Figure 5.7: 3D GOM photogrammetry scans of copper C101 specimen range highlighting final geometries, parts to same scale.

Table 5.3: Results of geometric assessments for all C101 copper alloy specimens cogged at ambient and elevated temperatures, comparing the target cross-section height reduction, lab measured cross-section height reduction measured with vernier callipers, and the maximum and average cross-section height reductions calculated using sectioned areas from the stub and cogged zones of the 3D GOM scans. Also detailing the geometry, total number of bites, and calculated elongation percentage.

Specimen No.	SP1	SP2	SP3	SP4	SP5	SP6	SP7	SP8
Target X-section Red. (%)	30	5	10	15	15	30	40	10
Measured X-section Red. (%) (±0.2)	35.0	4.7	10.0	13.1	9.7	32.6	41.0	8.1
Avg. Area Red. (%)	29.1	0.4	4.0	8.9	4.8	46.5	52.5	13.1
Max. Area Red. (%) (±1.0)	43.2	7.7	12.7	21.8	14.0	54.7	69.9	24.0
Geometry	□	□	□	□	□	□	□(2)	○
Total No. of Bites	12	2	4	6	6	12	16	8
Elongation (%)	28.4	0.6	2.6	3.5	2.1	23.2	54.9	9.1
Temperature (°C)	20	20	20	20	600	600	600	600

of the material is provided in Figure 5.6(b). It is observed that the test time for the FE predicted load graph seen in Figure 5.6(b) is much shorter, as well as a more uniform increase in load for each set of bite targets. From Figure 5.6(c) it is observed that the model over-predicts the first bite by a significant margin (above 50%), and continues to generally over-predict the subsequent bites in decreasing amounts until the last bite at 30% is under-predicted by 11.3%.

Comparative GOM 3D scan results for each of the C101 specimens can be seen in Figure 5.7. These scans show the final billet geometries, which are representative of billet geometries seen in

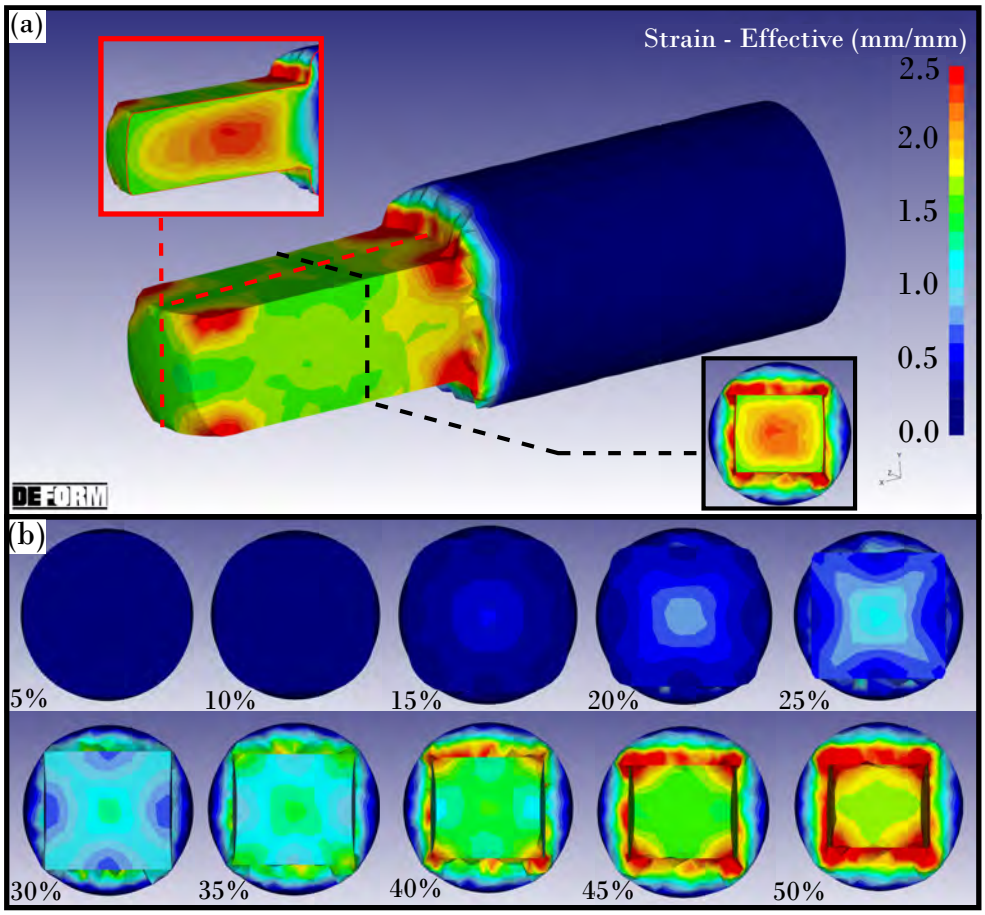

Figure 5.8: (a) The FE predicted effective strain distribution in copper C101 alloy specimen SP6 following cogging trial to 45% deformation (at 600 °C), with the strain distributions on both the longitudinal and transverse cross sections provided, (b) The FE predicted strain distributions on the radial cross-section after each cogging pass up to 10 passes (*i.e.,* 50% strain). The effective strain scalebar is the same for both.

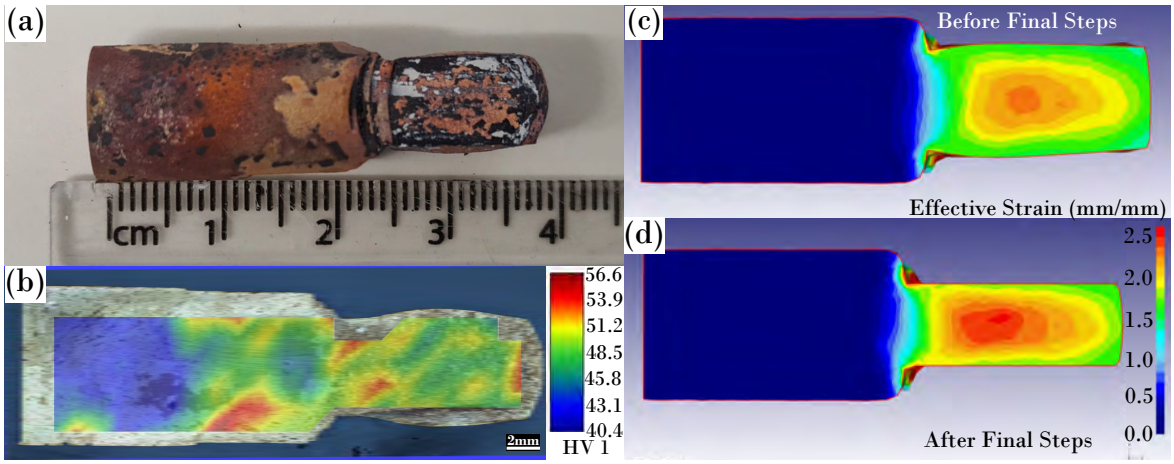

Figure 5.9: (a) A photograph of copper C101 alloy specimen SP6 image after the cogging trial at 600 °C, (b) An optical micrograph of the cross-section of specimen SP6 with overlaid microhardness heat map, (c) + (d) the result of the FE simulation of the open-die forging of copper C101 alloy specimen SP6 to an area reduction within 1.5% of the strain level of the real result, (c) prior to final simulation step straightening and, (d) after final simulation step straightening, both (c) and (d) use the same effective strain scalebar, acquired using DEFORM™ software.

industrial processes [130]. Specimen SP1 is in exception to the expected geometry, as it was the first cold-worked benchmark obtained using the designed experimental apparatus and due to this was repeatedly removed and replaced in the machine for calliper measurements. Figure 5.5(a) and (b) show the specimen geometries before and after being cogged, this geometry was the result of a load-frame auto-stop after detecting shear in the sample.

Specimen SP6, shown after cogging in Figure 5.5(c), is a clear example of the equipment achieving noticeable grain refinement, visible in Figure 5.10(b). 94.59% reduction in grain size between the stub and cogged zones was measured using the mean linear intercept method in ImageJ. The largest grains ($\approx$25 mm^2) in the stub zone can be seen to transition quickly to a refined equiaxed structure in the cogged zone where the average grain size is $\approx$5000 µm^2. Figure 5.8(a) shows the

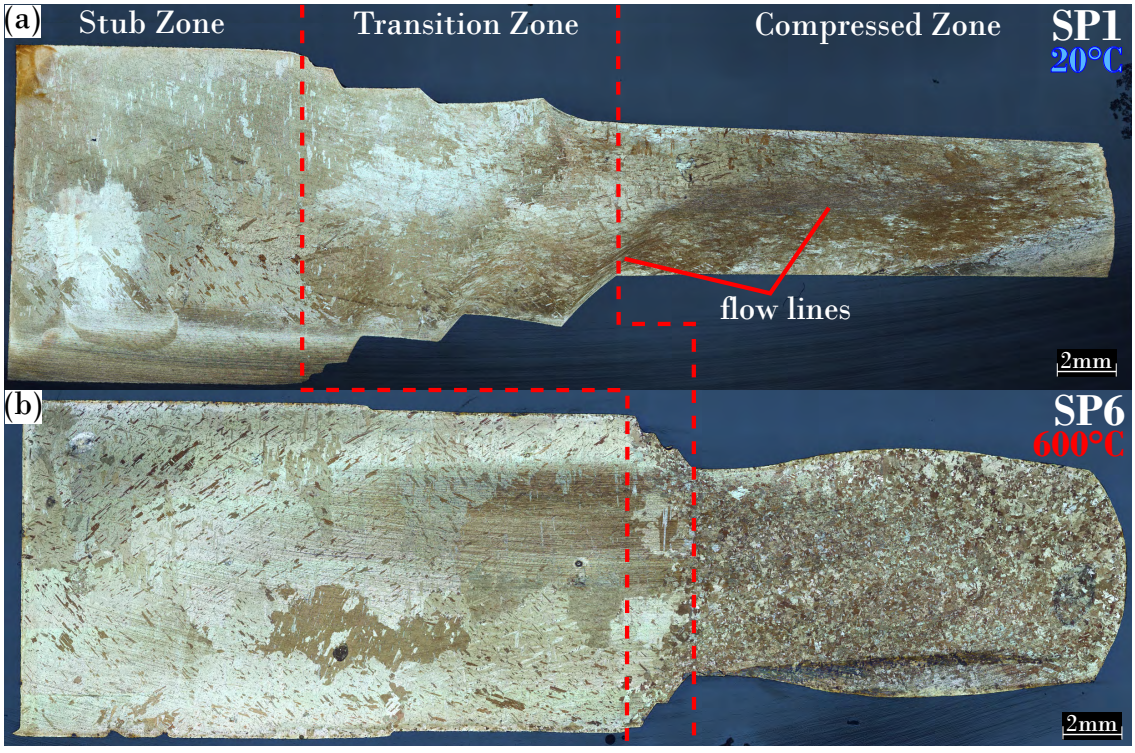

Figure 5.10: Macrographs of the C101 specimens following cogging trials (a) SP1, (b) SP6, both after a 30% nominal reduction in area after cogging), highlighting Stub, Transition, and Cogged zones in both specimens.

strain distribution relative to 45% area reduction, representative of specimen SP6 after deformation, whereas Figure 5.8(b) shows the relative strain distributions through each consecutive series of compressive bites. The FE results presented in 5.8(b) clearly shows the increase in strain imposed with % reduction. The locations close to the sharp corners at front end of the sample and close to coupling (non-deformed section) experience higher strain values. This could be due to influence of tensile stresses building up with the increase in % reduction.

The remaining specimen light microscopy images can be seen in Figure 5.11. These images emphasise the clear difference in recrystallisation and microstructural changes between the cold and hot-worked specimens. Large coarse regions are observed in the ambient temperature cogged specimens, and do not show any signs of refined equiaxed grains that are visible in the hot-worked range. This comparison is clear between specimens SP4 and SP5 in Figure 5.11(c) and (d), as these are of approximately similar cross-section reduction, with temperature as the only variable. In Figure 5.11(f), this contrast is visible between the stub zone and cogged zones, where fine equiaxed grains occupy the majority of the cogged area. However, it can also be seen towards the top end

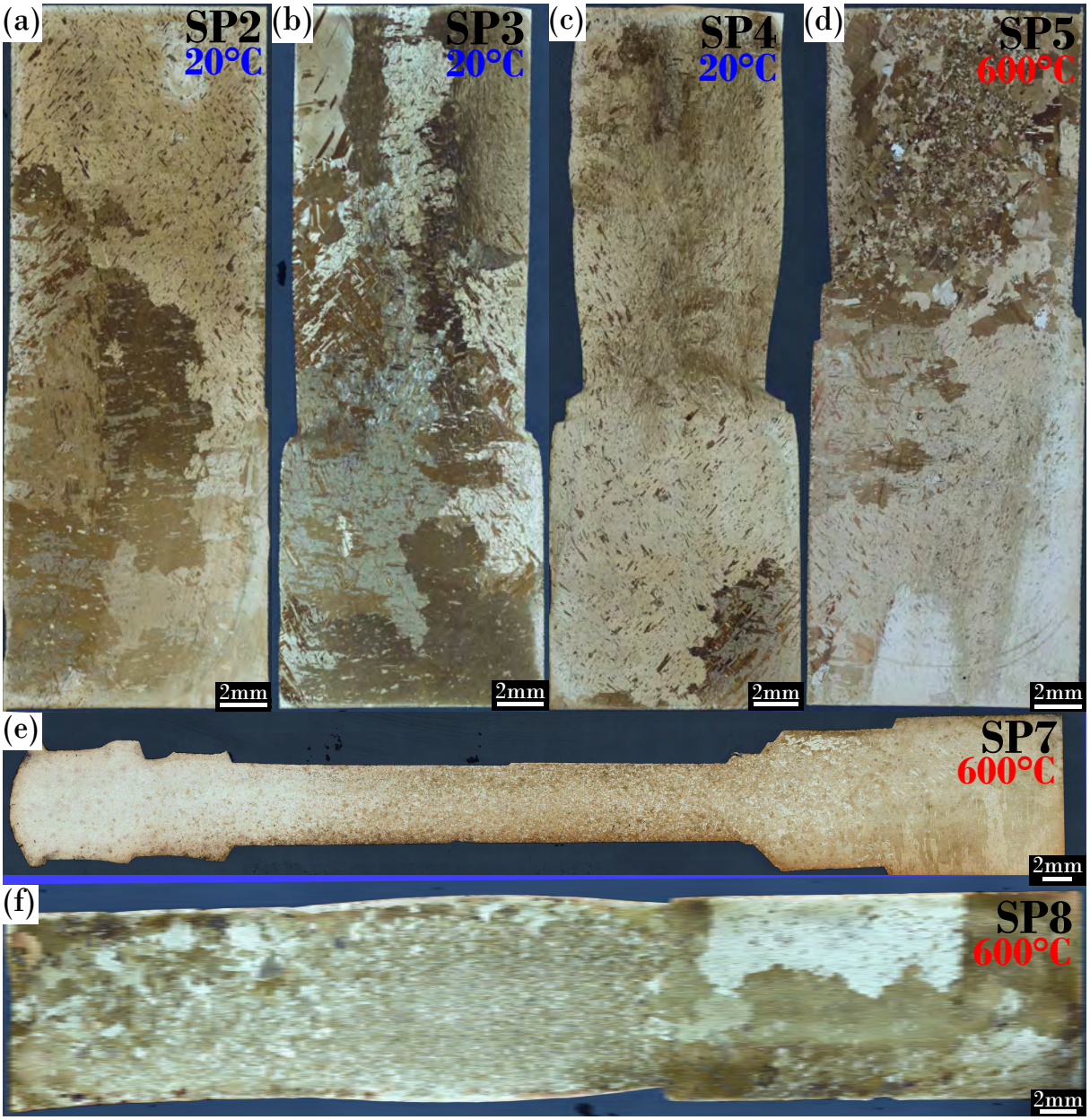

Figure 5.11: Light microscopy macrographs of the C101 specimens following cogging trials (avg. area reduction) (a) SP2 (0.4%), (b) SP3 (4.0%), (c) SP4 (8.9%), (d) SP5 (4.8%), (e) SP7 (52.5%), and (f) SP8 (13.1%).

Table 5.4: Vickers hardness results for C101 alloy deformed at ambient and elevated temperatures, highlighting the average hardness measured in the stub and cogged zones, and the overall percentage increase in hardness.

Specimen No.	SP1	SP2	SP3	SP4	SP5	SP6	SP7	SP8
Temperature (°C)	20	20	20	20	600	600	600	600
Avg. HV (Stub)(±0.5)	53.0	48.1	50.1	54.0	44.2	42.9	45.9	46.4
Avg. HV (Cogged)(±0.5)	131.0	72.2	94.4	113.6	48.7	49.7	48.4	51.8
HV Increase (%)(±1)	147.1	50.1	88.4	110.4	10.1	16	5.5	11.76

(left-side of Figure 5.11(f)) the recrystallised grains have partially grown between bites/passes of the cogging test. This could easily be avoided with future experimentation, as more rigid tooling would assure specimen clearance from sticking - and as this was the first multi-pass octagonal specimen extra time was allowed for alignment checks. This specimen is also interesting as it achieved some of the smallest grain sizes, despite only achieving a GOM measured 13.1% average area reduction. Due to the increased number of bites and bite angles (45° for the octagonal shape), which allows more slip plane systems to be activated, allowing for more dislocations and ultimately more finer recrystallised grains.

Figure 5.9(b) shows the obtained light micrograph of the specimen after cogging (showing evidence of grain refinement, and a barreling effect), along with the FE predicted strain distribution, (*i.e.,* deformed to the same strain level as the cogging trials), in Figure 5.9(c) which corroborates the barreling effect seen in the specimen. This allows correlation of the strain distribution to the observed grain structure refinement, demonstrating the potential predictive capability for microstructures that could be expected after forging. Figure 5.12 shows light optical microscopy appearances of the three zones: stub, transition, and cogged. The micrographs reveal the variation

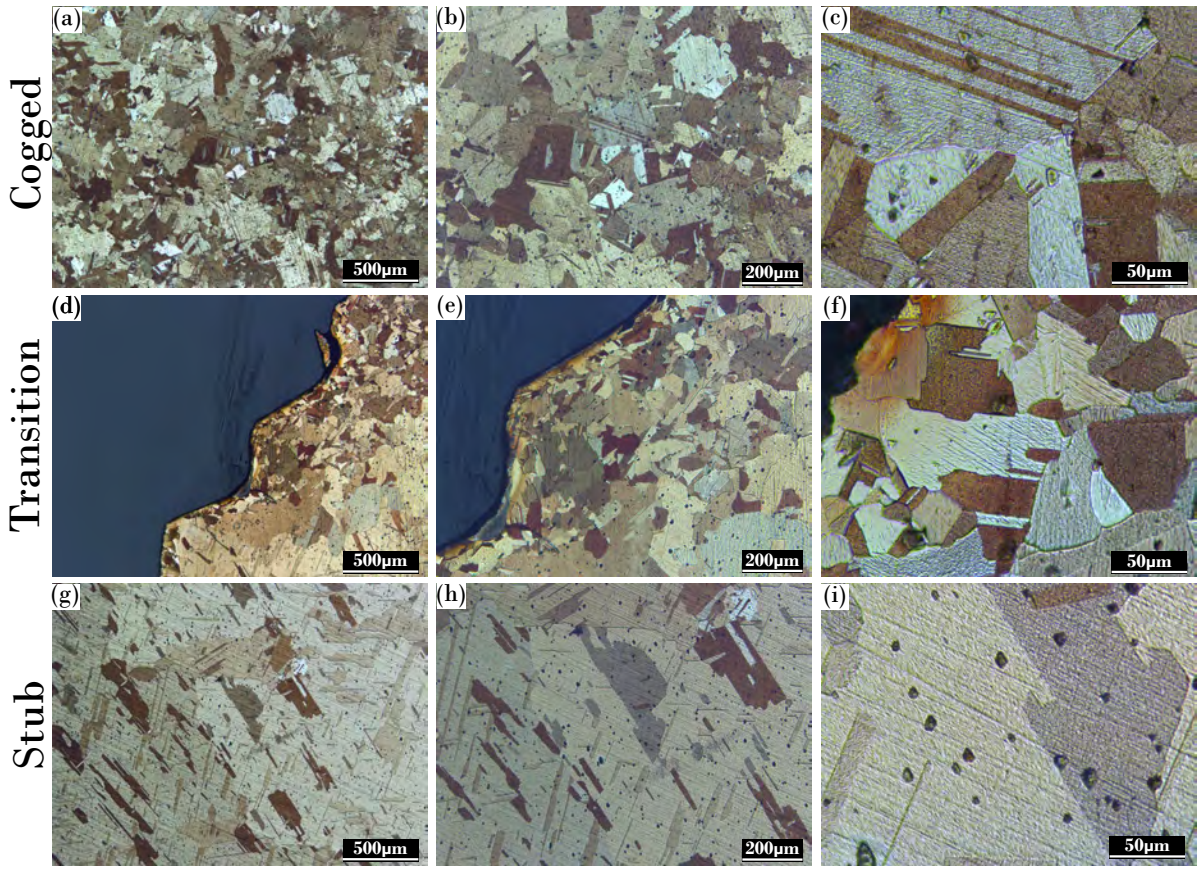

Figure 5.12: Light micrographs taken from different zones of the cross-section of copper C101 alloy specimen SP6 after forging at 3.5×, 7×, 35× magnifications: (a) - (c) Cogged zone, (d) - (f) Transition zone, (g) - (i) Stub zone.

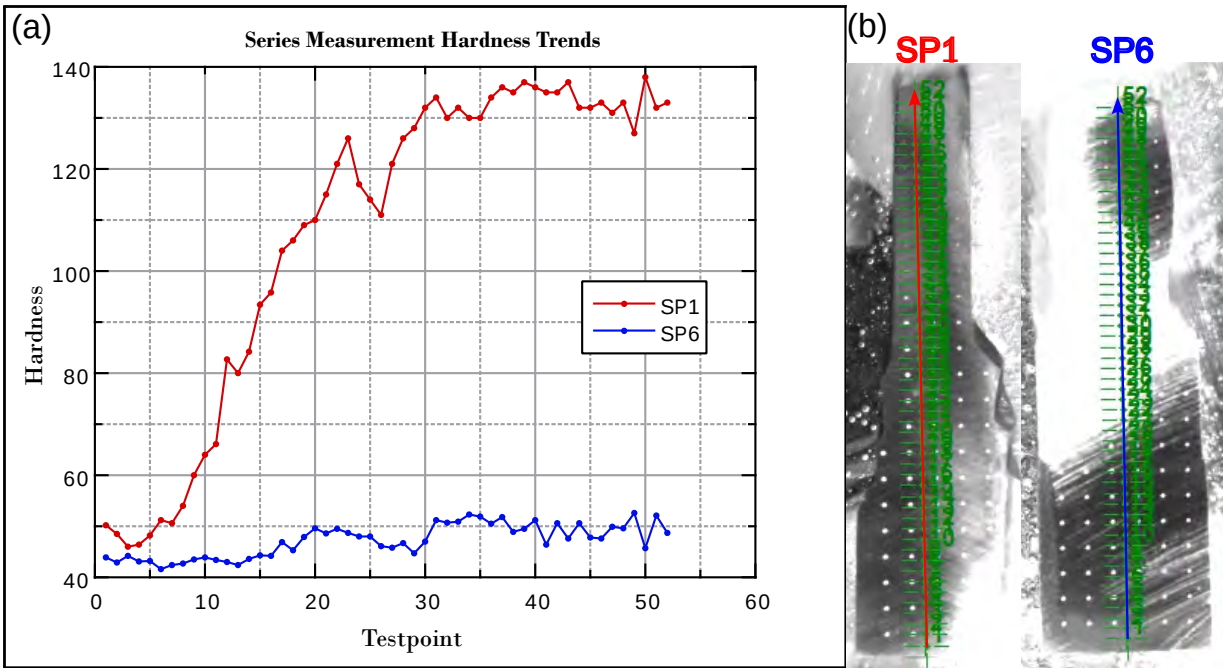

Figure 5.13: (a) Plot of Vickers hardness trend lines for copper C101 alloy specimen SP1 (red) cogged at room temperature, and copper C101 alloy specimen SP6 (blue) cogged at 600 °C. (b) Images of SP1 (red) and SP6 (blue) showing indentation lines and points for hardness testing.

in grain size throughout the specimen cross-section, ranging from a coarse structure in the stub zone, capturing the transition at the edge into the refined equiaxed structure in the cogged zone where the deformation was concentrated.

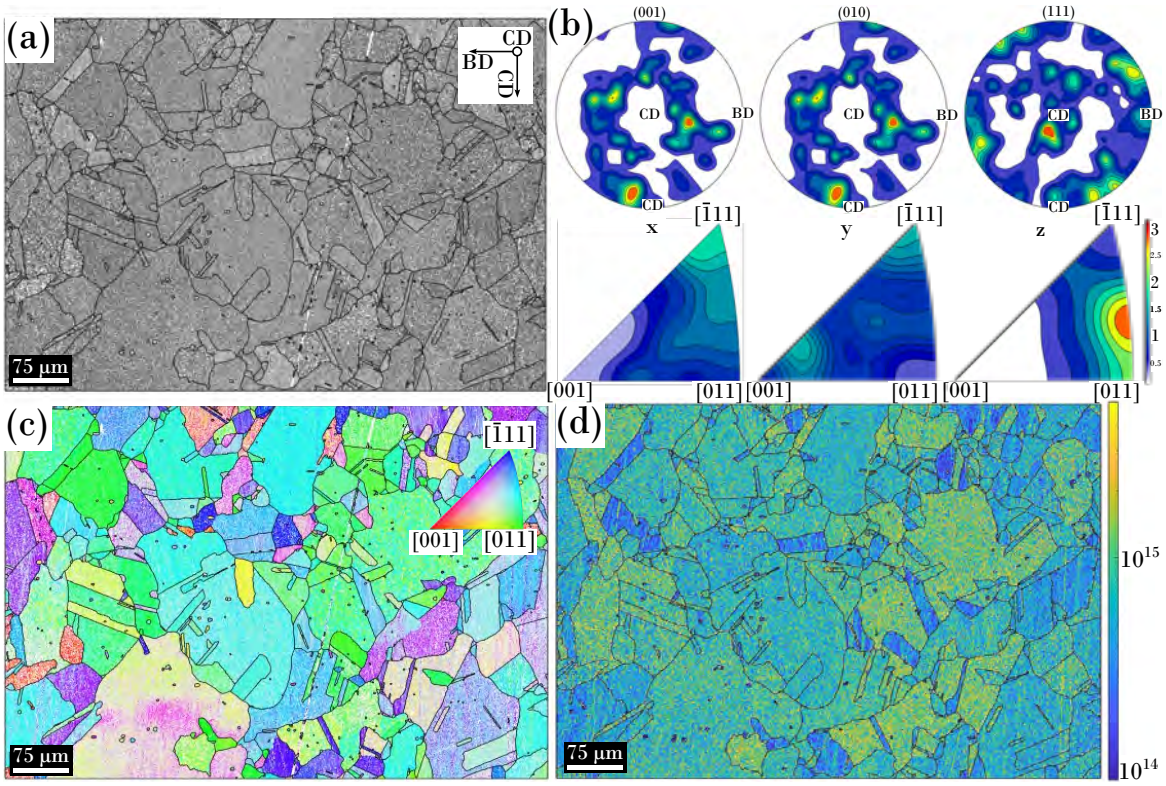

Figure 5.14: EBSD results captured from the cogged zone of copper specimen SP6, deformed at 600 °C to 45.6% reduction in area, equivalent to a nominal strain of $\varepsilon \approx 0.25$; (a) Band contrast map highlighting grain boundaries and with labelled Billet Direction (BD), and Cogging Directions (CD), (b) Pole figures and Inverse pole figure diagrams (c) IPF-CD map (out-of-page), (d) GND density distribution map, colour scale indicates log(GND density in lines/µm^2).

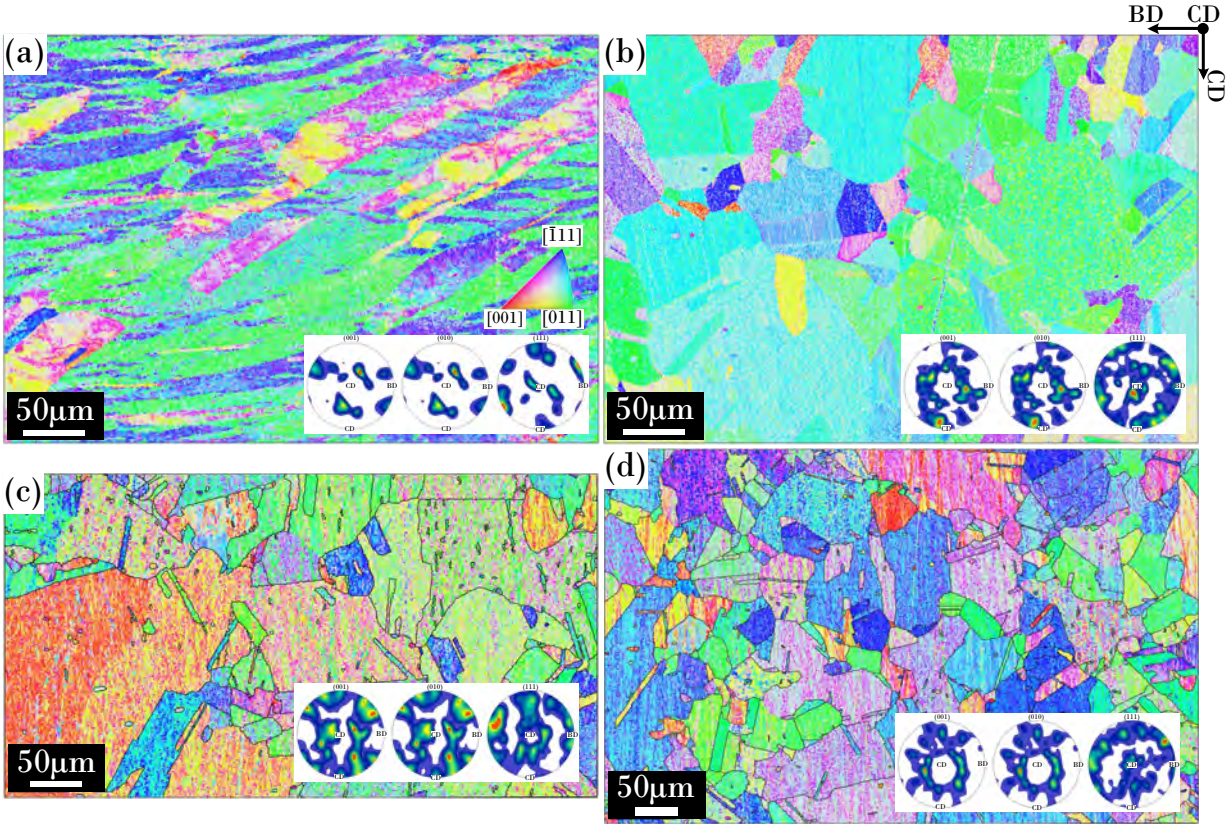

Figure 5.15: EBSD IPF-CD maps (out-of-page) captured from the cogged zone from a range of copper specimens with pole figures, deformed at ambient and elevated temperatures, (a) SP1, (b) SP6, (c) SP7 and, (d) SP8.

Microhardness measurements reveal a noticeable increase in the Vickers hardness values for the samples that have been cold-worked between the stub and the cogged zones, *e.g.,* an increase of 147.1% for specimen SP1. The samples forged at elevated temperature similarly show an increase in hardness between the stub and cogged zones, but with a lower increase of 16% for SP6. The full list of hardness increase values from the stub zone to the cogged zone of each sample can be seen in Table 5.4. It is evident from the data in the table that the cold-worked copper has a much greater average increase in hardness by a factor of ∼9.2. Series measurement trend lines for SP1 and SP6, seen in Figure 5.13, highlights this factor as the area reduction is approximately the same.

The captured EBSD results can be seen in Figure 5.14, where Figure 5.14(a) shows the band contrast output detailing the billet and the cogging directions. The IPF-CD map (out-of-page), seen in Figure 5.14(c), shows a preferential alignment to the [011] direction, which correlates with one of the compression directions. Fine recrystallised grains nucleated within prior grains are also seen. The pole figures and IPF's in Figure 5.14(b) reveal that there is no discernible texture after deformation. From Figure 5.14(d), showing the geometrically necessary dislocations (GND) map of the area, it can be seen that the higher GND energies align with the higher levels of dislocations, in one of the compression directions, which aligns with the preferred [011] orientation seen in Figure 5.14(c). GND maps were calculated using Pantleon's method [347], which uses the curvature tensors captured by EBSD, which are directly related to the dislocation density tensors according to Kröner [348].

From Figure 5.15 it can be observed that the difference between the cold-worked and hot worked C101 alloy is pronounced in terms of the grain shapes. Figure 5.15(a) shows the cold-worked material that remains characteristic of having plastic flow generally in the billet direction(BD) whereas in (b), (c), and (d) this flow tendency is completely lost with the grain structure due to the dynamic recrystallisation at high temperature.

5.3.3 Discussion of Miniaturised Cogging of C101 Alloy

As copper C101 alloy is easily formable, it proved to be an excellent starting material for experimentation on the newly presented apparatus and allowed for the testing of the set-up up to 600 °C. As a single-phase alloy, it allowed for the focus of the characterisation of the material to remain on the grain-size refinement, and capability of the experimental method to be determined accurately. It allowed for the first trials to run smoothly, as the method was iterated and developed in the lab from specimen to specimen, as improvements were made (*e.g.,* improved accounting for tooling losses). Another example of the iteration that these starting trials provided was the ability of testing multiple bites along the length of the specimens in the form of passes. This proved that the designed apparatus captured the capability for the full range of lateral and rotational positioning accuracy. With this control, it allowed for a range of specimens (presented in Figures 5.10 and 5.11) to be tested with a variety of parameters in a short testing window.

Copper specimen SP1 demonstrated that a greater nominal input strain or load would be required to achieve the low strain targets. This trend continued with all future cold-worked sample results, where larger inputs, or initial losses in tooling and elastic material properties require larger compensation. Where accelerated compensation is required as the strain target climbs, there is an unknown yield point in the material and tooling where the compensation values balance. This trend was also observed in samples deformed at elevated temperature, although a decrease in the overall load required was seen. A similar degree of compensation was required for the machine and tooling to achieve the required target strain.

Plastic flow lines can be seen in Figure 5.10(a), which can be expected from localised plastic deformation [349]. Optically, the size of the elongated grains of the cold-worked material was found to be more difficult to determine in the areas with shear bands. This could be indicative of these areas being characterised by ultra-fine nano-sized grains after dynamic loading [350–352]. At the transition zone edges, stretching effects are visible where the grains have been elongated and follow the curvature of the edge. Interestingly, longer samples (*e.g.,* C101 specimen SP8) with multiple passes along the main axis have shown signs of dynamic recrystallisation and grain growth in sections of earlier bites. Re-validating the potential for the studies that could be explored using this experimental method.

Now that Copper C101 has given a foundation to the experimental method, alongside the testing of Aluminium Al6060 alloy, this means that the method can be carried forward for a large range of matrix material testing in the form of open-die forging. Potentially with more added features and capability (*i.e.,* upsetting functionality via tooling upgrades).

5.4 Results from Miniaturised Cogging of Al6060 Alloy

5.4.1 Pre-worked Al6060 Alloy

Alongside the testing of the copper C101 alloy, aluminium Al6060 alloy was tested. The starting microstructure prior to any grain growth heat treatments is presented in Figure 5.16. The presented microstructure is characteristic of a rolled aluminium alloy, with fine elongated grains, with an average grain width of ∼44 µm running along the length of the billet (or rolled) direction. Figure 5.16(b) also shows a strong rolled texture seen in aluminium alloys, shown in the works of Wang *et al.* [353], which would be expected from the procured aluminium alloy. The average Vickers microhardness was measured as 107.2HV. The chemical composition of the aluminium Al6060 alloy is presented Table 4.2.

This procured material was then subjected to a grain growth heat treatment of 580 °C for 2 hours in a VFE TAV vacuum furnace, following the EN 573-3 standard where it is stated for a homogenisation procedure a temperature of 580 °C is employed for at least 2 hours [331]. This

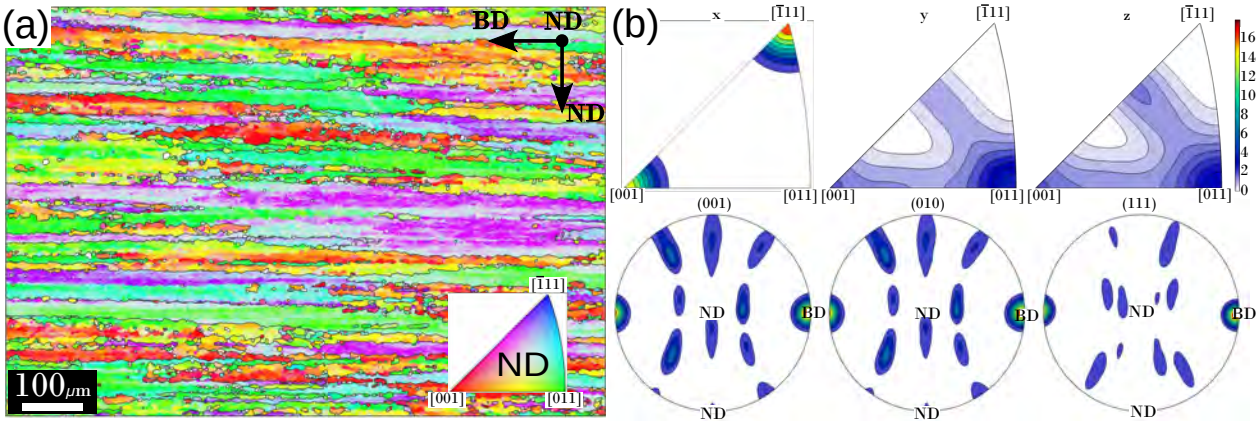

Figure 5.16: EBSD results captured from the as-received hot-rolled Al6060 alloy, (a) IPF-ND (out-of-page) map showing orientation data, and (b) Pole figures and Inverse pole figure diagrams for ND map showing strong texture.

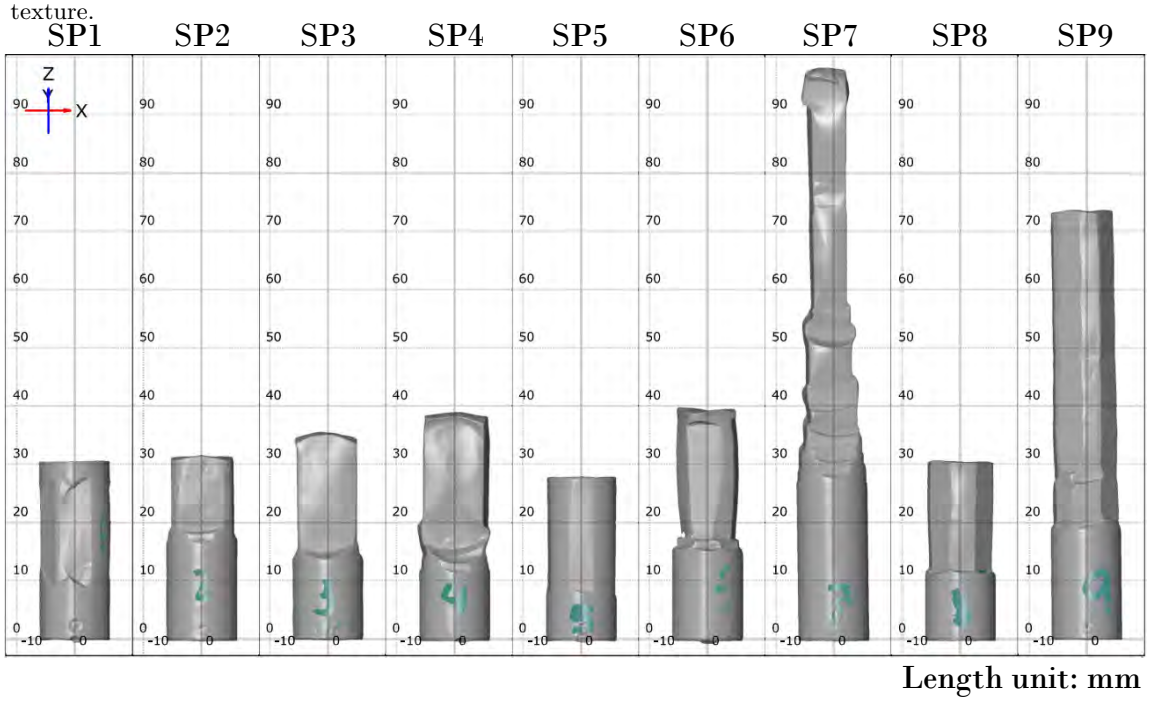

Figure 5.17: 3D GOM photogrammetry scans of aluminium specimen range, cogged at 450 °C, highlighting final geometries, parts to same scale.

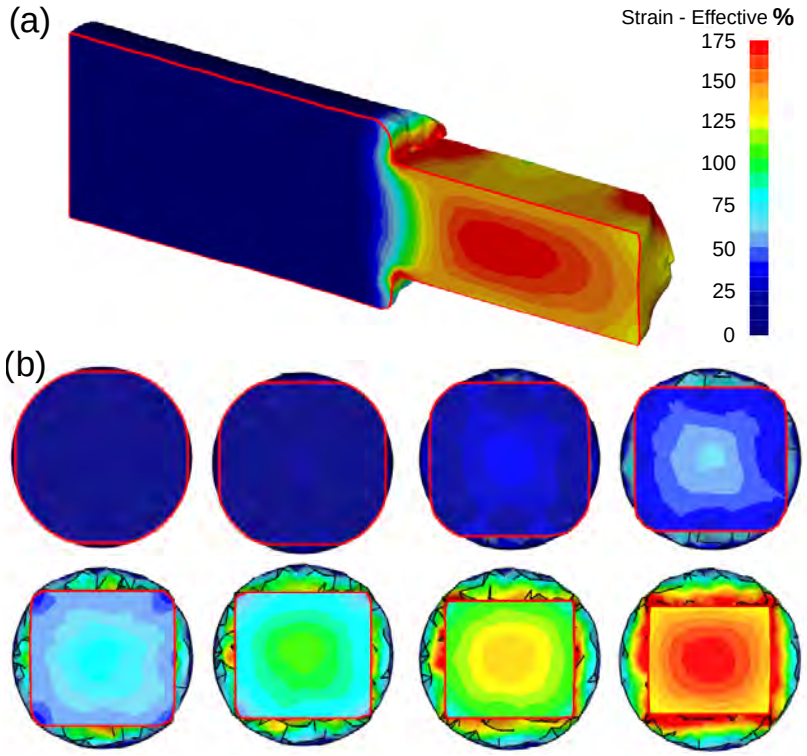

Figure 5.18: (a) The FE predicted effective strain distribution of the aluminium Al6060 alloy following a cogging trial to 40% deformation, (b) The FE predicted strain distributions on the radial cross-section after each cogging pass up to 8 passes (*i.e.,* 40% strain). The effective strain scalebar is the same for both.

grain growth heat treatment was carried out so that grain refinement in the following cogging tests can be better visualised, allowing the efficacy of the apparatus to be assessed. It is observed in the stub zones of Figure 5.20 that the grain size has greatly increased to approximate 1.4mm µm average grain width (approximately 96% increase) from the previous procured material of 44 µm average grain width, with not many grains now visible at this scale. One observation that remains consistent between the pre-cogged and cogged material, is the tendency to form elongated grains along the direction of the billet. From these observations, it is concluded that a coarser grain structure was achieved with the heat treatments carried out, and the material was ready for miniaturised cogging trials.

Table 5.5: Results of geometric assessments for all Al6060 aluminium alloy specimens cogged at 450 °C, comparing the target cross-sectional height reduction, lab measured cross-sectional height reduction measured with vernier callipers, and the maximum and average cross-sectional height reductions calculated using sectioned areas from the stub and cogged zones of the 3D GOM scans. Also detailing the geometry, total number of bites, and calculated elongation percentage.

Specimen No.	SP1	SP2	SP3	SP4	SP5	SP6	SP7	SP8	SP9
Target X-section Red. (%)	10	15	20	25	5	20	40	10	10
Measured X-section Red. (%)	4.7	13.0	19.7	24.6	4.1	10.1	41.7	6.0	9.7
	±0.2	±0.2	±0.2	±0.2	±0.2	±0.2	±0.2	±0.2	±0.2
Avg. Area Red. (%)	2.9	10.6	23.8	34.7	0.9	29.9	52.9	14.0	17.6
Max. Area Red. (%)	3.9	14.3	30.6	41.2	3.0	40.3	69.8	21.9	22
	±1.0	±1.0	±1.0	±1.0	±1.0	±1.0	±1.0	±1.0	±1.0
Geometry	□	□	□	□	□	○	□(2)	○	○(4)
Total No. of Bites	4	6	8	10	2	24	32	12	48
Elongation (%)	3.1	4.7	17.4	28.1	1.1	22.8	59.5	10.0	14.8

5.4.2 Miniaturised Cogging of Al6060 Alloy

Table 5.5 details the specimen results for the Al6060 aluminium alloy data-set, comparing target, measured, and calculated height and area reductions respectively. 3D GOM scan data is presented in Figure 5.17, where the range of finished specimen geometries were captured before being sectioned for characterisation. It can be seen across this Figure and Table 5.5 that multi-pass specimen SP7 achieved a geometrical change similar to an industrial ingot-to-billet conversion (*i.e.,* cogging stage) of superalloys, as described by Reed [1]. Figure 5.19 presents the various load graphs output from the aluminium Al6060 cogging tests. It is observed that the load values are kept relatively low throughout, as none of the bites exceeded 6 kN of force. The same general trends are observed in the load graphs for the cogging of aluminium Al6060 and of the cogging of copper C101 alloys.

Vickers microhardness measurements for the Al6060 aluminium alloys samples are presented in Table 5.6. There is a measureable difference, approximately 60-70%, in the Vickers microhardness

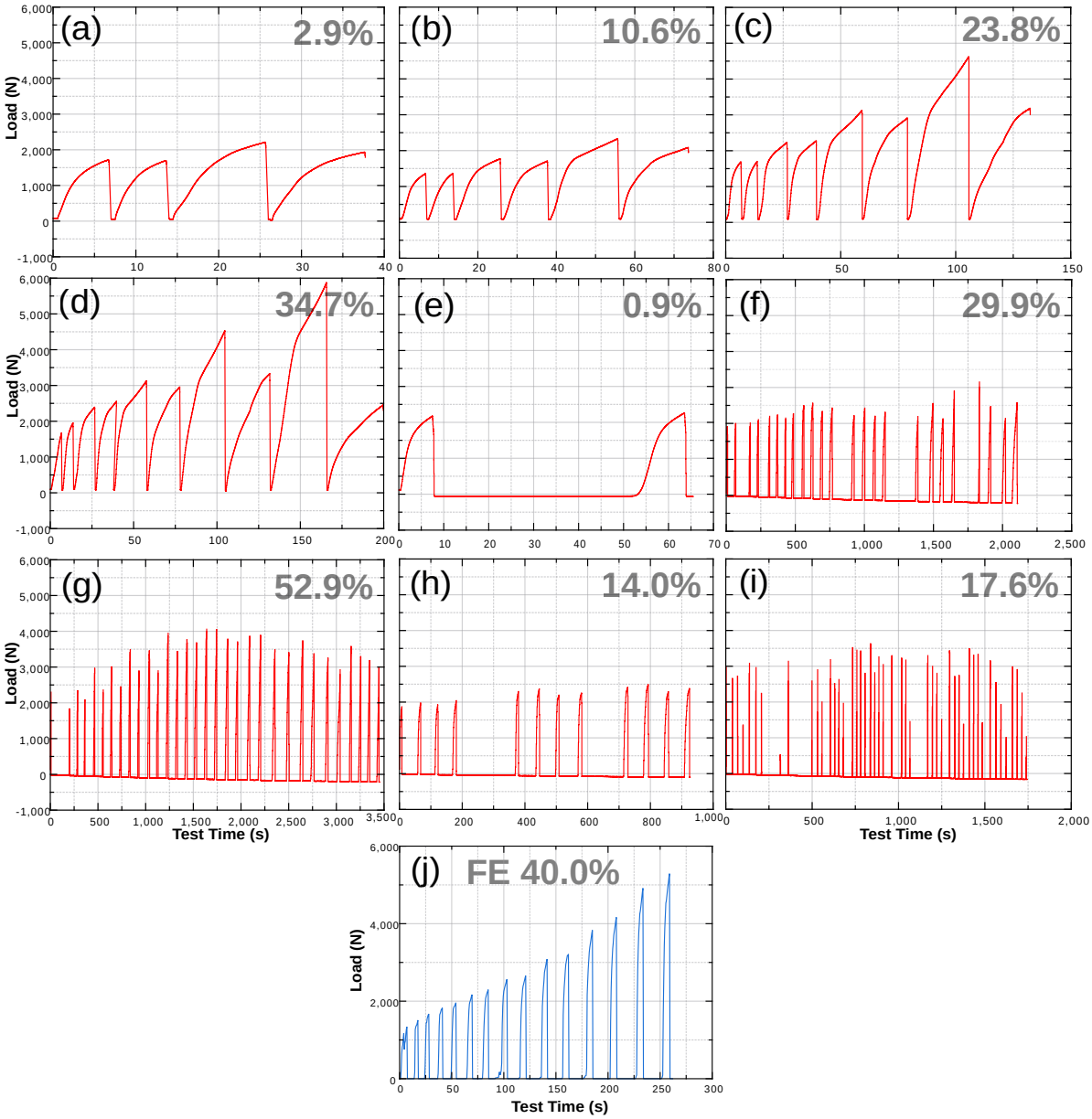

Figure 5.19: Measured load (N) against test time (s) for aluminium specimen range of cogging trials, cogged at 450 °C. (a) SP1 (2.9%), (b) SP2 (10.6%), (c) SP3 (24.8%), (d) SP4 (34.7%), (e) SP5 (0.9%), (f) SP6 (29.9%), (g) SP7 (52.9%), (h) SP8 (14.0%) and (i) SP9 (17.6%) Data was taken from Zwick/Roell™ load cell during testing, recorded in Zwick™ testXpert III software. (j) The FE predicted graph for load (N) against test time (s) for Al6060 aluminium alloy. Visualised using LabPlot by KDE®. All to the same load (y) scale.

Table 5.6: Vickers hardness results for Al6060 alloy deformed at 450 °C, highlighting the average hardness measured in the stub and cogged zones, and the overall percentage increase in hardness.

Specimen No.	SP1	SP2	SP3	SP4	SP5	SP6	SP7	SP8	SP9
Avg. HV (Stub)(±0.5)	44.2	39.7	42.1	42.6	46.8	39.4	40.7	41.8	44.3
Avg. HV (Cogged)(±0.5)	42.1	41.2	41.6	42.2	45.6	40.2	42.0	42.7	43.3
HV Increase (%) (±1)	0.2	3.8	-1.2	-1.0	-2.6	-2.0	3.2	2.2	-2.3

between the procured material to the heat-treated/cogged material. On the other hand, there is no clear difference (*i.e.,* approximately equal increase/decrease, no greater than 3.8%) between the cogged and stub zones of the Al6060 alloy in the cogged specimens.

Figure 5.18 presents the FE predicted strain distributions in the aluminium Al6060 alloy, reaching a maximum of ≈1.75, or 175%, effective strain. This effective strain is calculated through the simulation of multi-directional loading on the material within the DEFORM software package, which is a 1:1 scale of the experiment. The highest strain point is observed to be focused on the centre of the cogged zone, as would be expected. The final geometry that was expected was found to be the same as the other material simulations in the study. The different stages of the cogging simulation can be used to validate the different specimen geometries and strains, allowing the correlation between effective strain and microstructure.

It can be observed in Figure 5.20 that the grains have been refined towards the outer edge of the specimens, in each of the zones. Clear plastic flow characteristics are seen throughout the specimen range. One key impact the micro-cogging had on the microstructure of the aluminium Al6060 alloy specimens, is the width of the columnar grains. This is observed in Figure 5.20, where the stub zone grains are wider than that observed in the cogged zones, with the most refined grains running along the edge of the specimens.

Despite not having a large impact on the morphology of the grains throughout the miniaturised cogging of aluminium alloy Al6060, the grain width reduction was successful. Results of these grain width changes can be seen summarised in Table 5.7.

Table 5.7: Results of grain width measurements for all Al6060 aluminium alloy specimens cogged at 450 °C, measured with ImageJ software using the mean intercept method in the CD direction (perpendicular to the billet direction).

Specimen No. Avg. X-section Red.	SP1 (2.9%)	SP2 (10.6%)	SP3 (24.8%)	SP4 (34.7%)	SP5 (0.9%)	SP6 (29.9%)	SP7 (52.9%)	SP8 (14.0%)	SP9 (17.6%)
Stub Avg. Grain Width (mm)	0.95	1.21	1.17	1.21	1.29	1.30	1.43	1.12	1.61
Cogged Avg. Grain Width (mm)	0.90	0.77	0.51	0.35	1.26	0.72	0.26	0.81	0.80
Avg. Percentage Reduction (±1) (%)	5.2	36.4	56.4	71.1	2.3	44.6	82.0	27.7	50.0

The calculated percentage reductions, seen in Table 5.7, from the mean linear intercept method corroborates the expected grain size change from the average grain size reduction (*i.e.,* deformation levels) of each of the specimens.

From Figure 5.21 it can be observed for specimen SP4 that there are a number of internal sub-boundaries induced from the higher level of deformation (shown with red lines and black arrows). This indicates that the cogging operation performed had an effect on the internal sub-grain structures induced increasing amounts of strain within the grain boundaries when compared to SP5 shown in Figure 5.22 where these boundaries are not clear. This recrystallisation behaviour is seen in other 6000 series aluminium alloys, *e.g.,* Lin *et al.* studied the DRX behaviour of 6082 aluminium alloy during hot deformation [354]. In this study, Lin found through microstructure analysis that the sub-grain structure formed in the original grain and is coarsened by grain boundary migration,

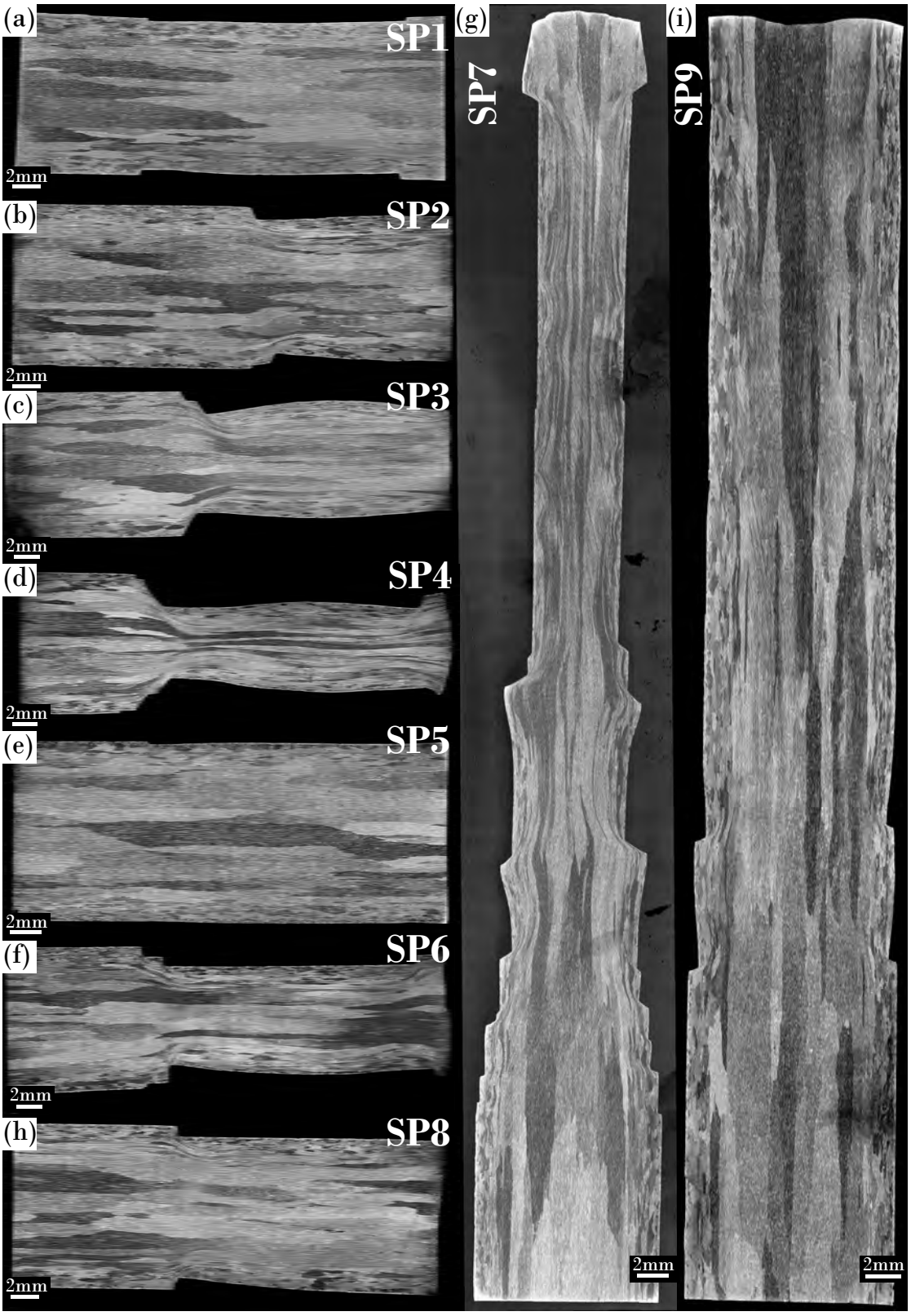

Figure 5.20: Light micrographs of sections from the full Al6060 alloy cogged specimen range deformed at 450 °C, highlighting columnar grains, refined grain edges and plastic flow lines, including; (a) SP1 (2.9%), (b) SP2 (10.6%), (c) SP3 (23.8%), (d) SP4 (34.7%), (e) SP5 (0.9%), (f) SP6 (29.9%), (g) SP7 (52.9%), (h) SP8 (14.0%) and, (i) SP9 (17.6%). All values in brackets display the Avg. Area Reduction of the specimen measured from GOM.

where the orientation difference increased continuously until a LAGB forms, resulting in DRX of the grains. Lin *et al.* concluded that continuous dynamic recrystallisation (CDRX) was likely occurring

throughout hot deformation, which reflects the microstructural data output from this work. It is also observed from the pole figures and inverse pole figures in Figures 5.22(b) and 5.21(b) that the strong rolled texture from the procured aluminium is lost after cogging, as was seen with the C101 alloy after cogging.

5.4.3 DCT 3D Grain Mapping of Al6060

The advanced technique of of X-ray computed tomography (XCT) was chosen for analysis of the mini-billet specimens in this study. The technique of X-ray diffraction contrast tomography (DCT) has the capability to characterise crystallographic microstructure by mapping grains and their crystallographic orientation non-destructively and in three dimensions, and therefore is a powerful tool for understanding many aspects related to damage and deformation mechanisms in polycrystalline materials. DCT utilises the Laue diffraction method [355].

A beamstop is used to attenuate the direct X-ray beam transmitted through the sample, allowing for the collection of diffraction signals with improved sensitivity. Grains diffract the beam onto the other part of the detector. Data acquisition is performed in a symmetric geometry and the diffracted signals appear as line-shaped spots enabling increased diffraction signal strength, and having the capability of many and closely packed diffraction spots to be handled. It is possible for hundreds of grains to be mapped in a single scan. The diffraction patterns are then reconstructed using 3D Grain Mapper software. Further work on improving the minimum detectable grain size is ongoing.

After acquiring the raw and segmented 3D X-ray data, seen in Figure 5.23, and reconstructing it in the 3DGrainMapper software, the data was then loaded and analysed using Dragonfly™ software. With this software it was possible look through the 3D grains in individual slices of the voxels in the x, y, and z directions as well as look at the 3D model of the DCT absorption or orientation data. This allowed for validation through EBSD data collection of the samples. From initial results

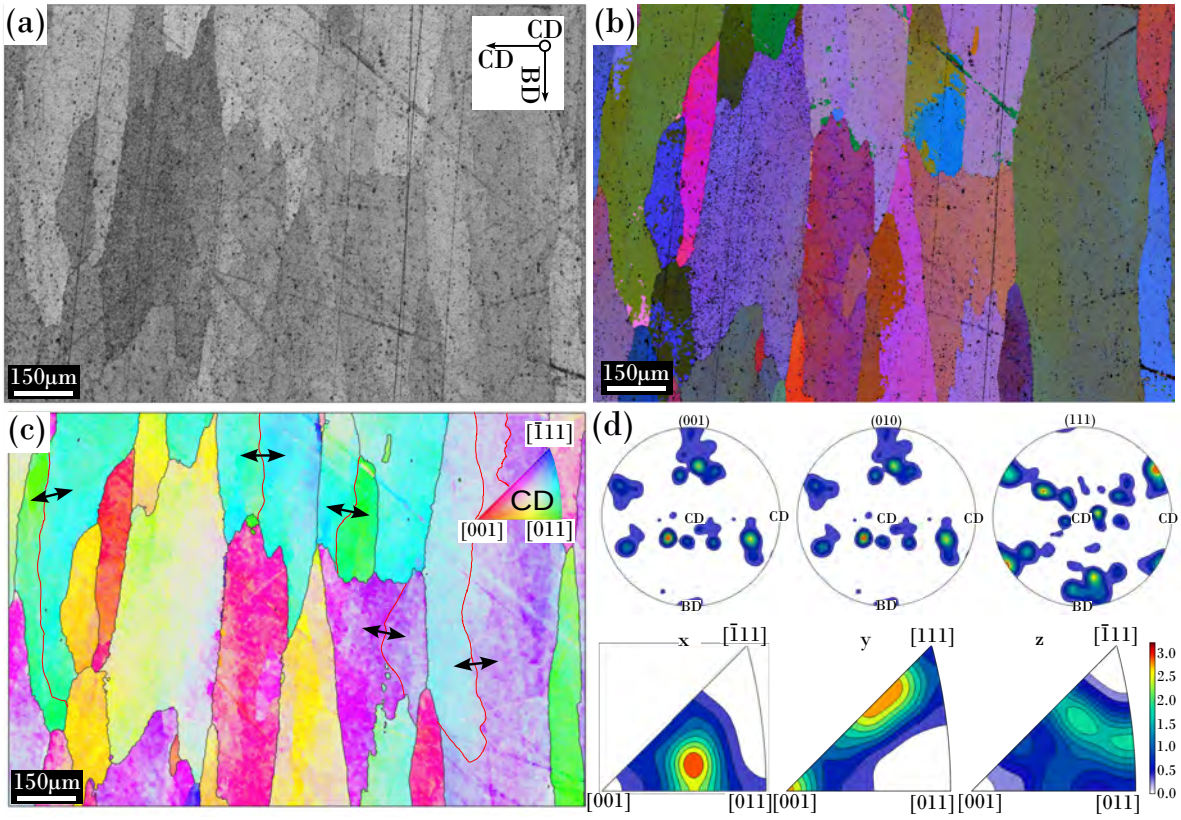

Figure 5.21: EBSD results captured from the cogged zone of aluminium specimen SP4, deformed at 450 °C to 34.7% reduction in area, equivalent to an effective strain of $\varepsilon \approx 1.3$ or 130%; (a) Band contrast map highlighting silica pitting and microscratches, (b) Euler color map of cogged billet section (c) IPF-CD map (out-of-page) of cogged billet section and, (d) Pole figures and Inverse pole figure diagrams for CD map.

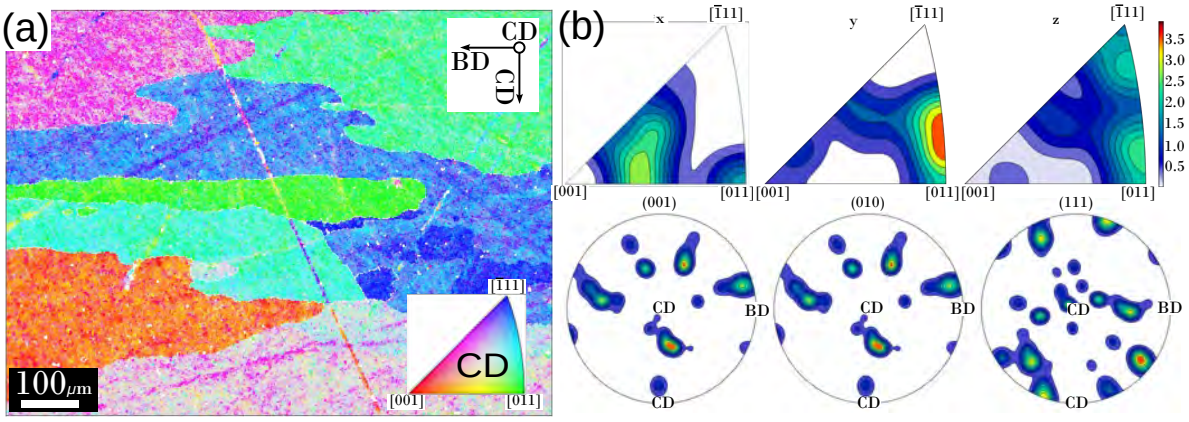

Figure 5.22: EBSD results captured from the cogged zone of aluminium specimen SP5, deformed at 450 °C to 0.9% reduction in area, equivalent to an effective strain of ε <5%; (a) IPF-CD (out-of-page) map showing orientation data, and (b) Pole figures and Inverse pole figure diagrams for CD map showing texture.

comparing just the 3D data output from DCT SP1(2.9%) and SP2(10.6%) it was a result that would be expected from the micro-cogging grain refinement process. *I.e.,* SP1 has much larger, and fewer, grains distributed through the DCT specimen at 2.9% average area reduction (observed in Figure 5.24), and SP2 had a finer grain structure (observed in Figure 5.25) at 10.6% average area reduction. It can be concluded in this case, from these 2 specimens, that the micro-cogging was successful in achieving the desired grain refinement.

From the EBSD data presented in Figure 5.26(b) it can be observed that the grain size of the 3D DCT data captured in Figure 5.24 is corroborated, as both the EBSD images and 3D reconstructed data show a single large grain taking up >80% of the specimen area. Furthermore, it can be seen around this large central grain - that smaller grains make up the edge of the sample in both datasets, further reinforcing the validation of the data. A comparison with the top down view on the DCT sample is also presented in Figure 5.26(c), where slices at different heights in the 3D DCT scan are shown. Due to the preparation of the material, a small (micron-level) surface angle may have been

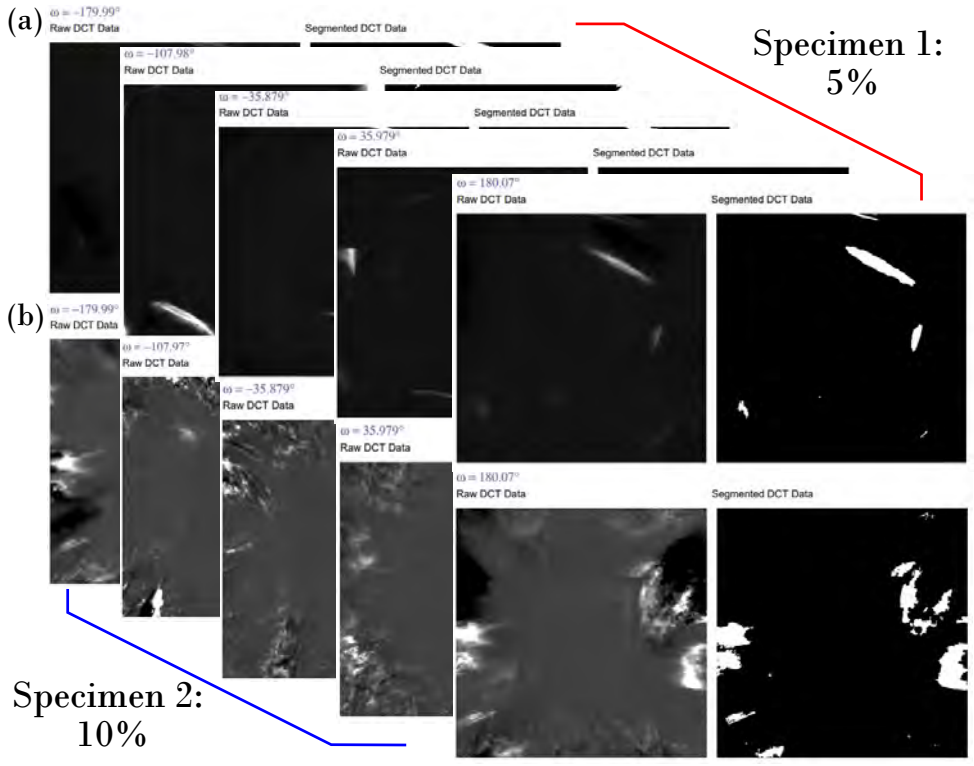

Figure 5.23: Collection of images showing raw DCT X-ray diffraction patterns and Segmented DCT data for (a) SP1 (2.9%) and, (b) SP2 (10.6%).

introduced which may cause a slight difference of visible grains in the EBSD map data compared to the 3D DCT map data. From this data it is also observed that there is some internal sub-boundary strain between the central and top visible grains.

It can be observed from the EBSD data presented in Figure 5.27 corroborates the 3D DCT data captured in Figure 5.25. When compared with Figures 5.24 and the EBSD data presented in 5.26 it is obvious that more grains are visible, which would be expected from the comparison between the two 3D datasets. However, it was expected upon the validation to see even more grains with a smaller grain size. This may also be due to preparation (any small micro-level incline) not showing more grains in the EBSD validation, or any small level of recrystallisation that has occurred between the 3D data capture and the EBSD data capture. It also seems to indicate a closer similarity to the expected grain size and morphology observed from the light microscopy presented in Figure 5.20. Overall this EBSD data, from the presented grain size and morphology, validates the DCT 3D grain mapping method.

5.4.4 Discussion of Miniaturised Cogging of Al6060 Alloy

The trial study of micro-cogging using aluminium Al6060 was successful in gaining insights into the apparatus behaviour and capability. It provided one of the first explorations into the inclusion of elevated temperature testing with the apparatus and was pivotal for beginning the experimental stage. As it easily cold and hot-worked it allowed for the loads on the press to remain relatively low throughout experimentation, ensuring that the tooling was used well below their limits. This meant that the focus could remain on the performance of the apparatus, how well the design fully integrated with the exploitation of the extensometer slot, and the positional accuracy that the electronic controller provided while the method was developed.

A few iterations of coding changes and bug fixes were carried out during testing, to allow for

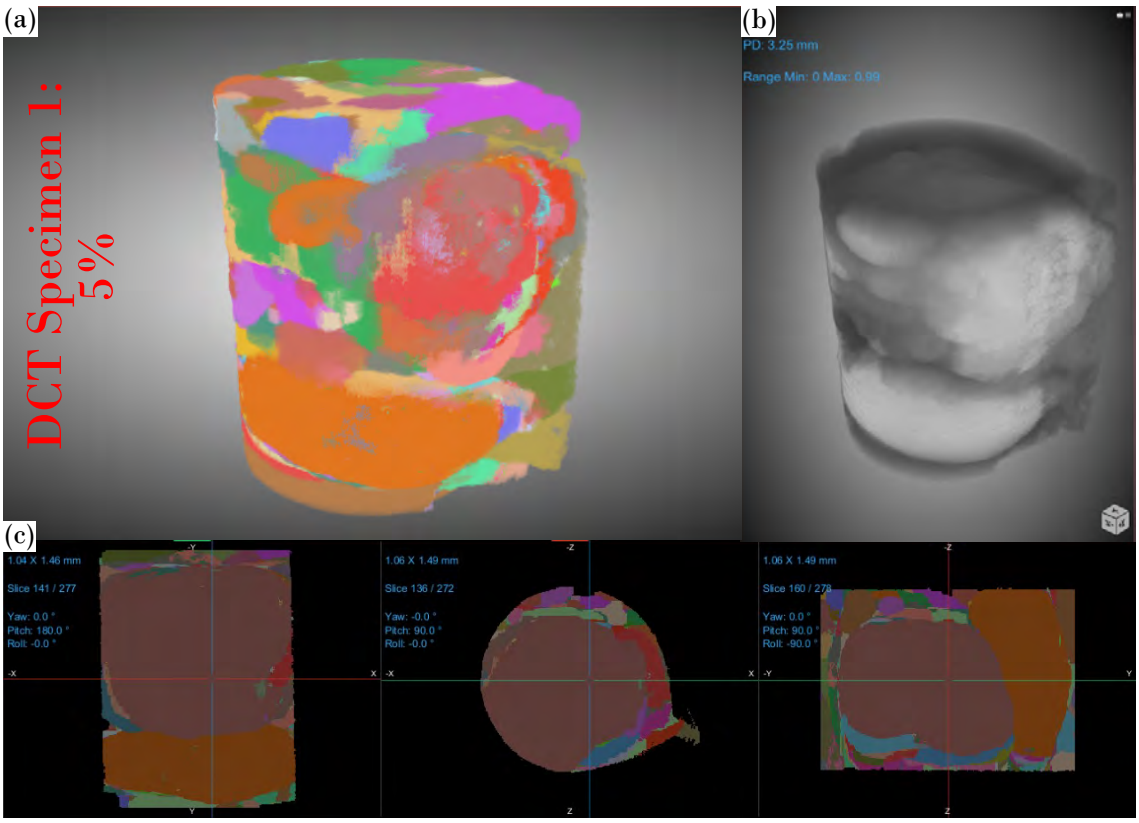

Figure 5.24: Images showing 3D grain reconstruction of X-ray diffraction patterns of SP1 (2.9%) using 3DGrainMapper software visualised in Dragonfly™ software, (a) 3D grain reconstruction showing Euler angle relationship between grains, (b) 3D grain reconstruction of raw DCT data, and (c) x, y, and z centre sections of the 3D reconstruction. Figure shows nominal target cross-section reduction of specimen.

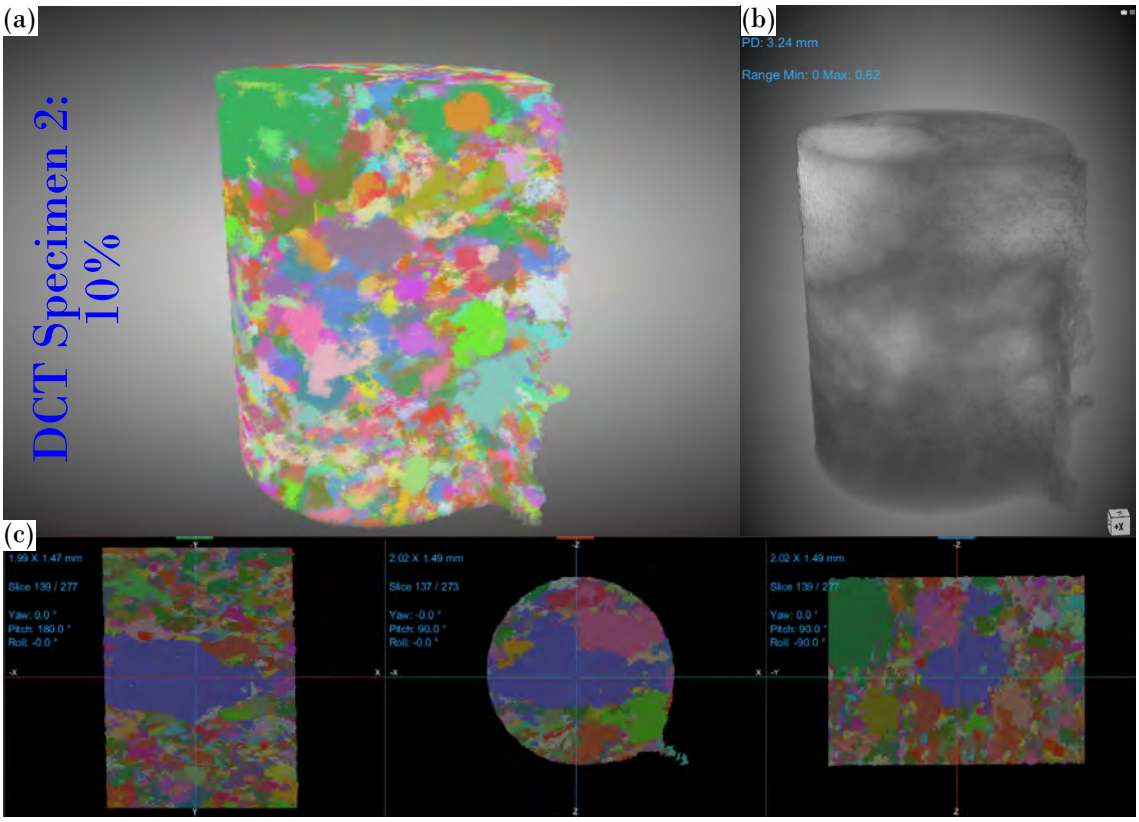

Figure 5.25: Images showing 3D grain reconstruction of X-ray diffraction patterns of SP2 (10.6%) using 3DGrainMapper software visualised in Dragonfly™ software, (a) 3D grain reconstruction showing Euler angle relationship between grains, (b) 3D grain reconstruction of raw DCT data, and (c) x, y, and z centre sections of the 3D reconstruction. Figure shows nominal target cross-section reduction of specimen.

more accurate rotations, or the implementation of driving the motor during compression to avoid slippages, as the first few tests did not have this functionality.

During preparation stages, it was found that aluminium was difficult to work with for a number of reasons. Firstly, as it has a low ageing temperature threshold, and hot-mounting Bakelite curing is carried out at 150 °C, this meant that hot mounting of the specimens once cut was not possible without effecting the microstructure. As the specimens could not be hot-mounted, the alternative cold mounting in epoxy resin was the only option. This led to the issue of conductivity in the SEM. Where, due to the epoxy resin being non-conductive, led to a number of challenges with charging of the aluminium samples under the electron beam. Charging would cause the image to drift and lose focus, making it uneasy to capture high quality EBSD and BSE images of the aluminium. To compound this issue, as aluminium is a relatively soft metal it also had the challenge of avoiding scratches during preparation. Often, with this particular alloy which was found to be particularly soft, large scratches would appear during any stage of the preparation which were often unexplainable. It is suspected that during grinding/polishing, small pieces of epoxy resin would break off in chunks and be dragged across the surface resulting in these scratches. To overcome many of these preparation issues, extensive iteration was carried out with many methods of papers and polishing techniques. It was found that reducing the overall load onto the specimens, as well as avoiding diamond polishing entirely and using only 0.02 µm colloidal silica achieved the best result.

Although the Al6060 alloy microstructure was not impacted as highly by the micro-cogging testing as the C101 alloy microstructure, it can still be observed through Figures 5.22 and 5.21 that the increased effective strain increased the overall internal strain within the sub-grains.

Migration of sub-grain boundaries during hot open-die forging, or cogging, or any form of multi-directional loading of aluminium alloys could be further explored with this experimental method in future studies. The new apparatus presented in this work can be used as a platform for many material and grain kinetic studies for aluminium as well as other materials. Exell and Warrington's

study [356] observed that the sub-grain boundary migration of aluminium contributes significantly to the overall strain rate and that the stress and temperature dependence are in accord with the macroscopic strain rate, and are related to the deformation contribution from fine slip. Fundamental studies of the kinetics on multi-directional loading on old and new materials can be explored much more easily, and cheaply with the employment of this method into a laboratory, rather than the expensive and wasteful alternate routes with large-scale forging.

CDRX is the most common recrystallisation mechanism for both commercially pure Al and Al alloys under hot forming conditions [357]. CDRX is usually observed during torsion, tension, and compression testing up to 0.7 T_m (where T_m is the melting temperature) and has been seen under strain rates ranging from 0.0005 to 10 s^{-1} [358–361].

5.5 Summary

Overall, the miniaturised experimental simulation study of single-phase alloys was successful in allowing for the assessment and validation of the micro-cogging rig design and method in capturing a range of materials and microstructural evolution stages. It was also successful in achieving the desired measurable grain refinement in both copper C101 and aluminium Al6060 alloys, and achieving a range of geometries and recrystallisation in both single-phase alloys tested. The single-phase alloy study was pivotal in assessing and testing the apparatus in operation with the peripheral equipment in the laboratory and validating the method worked as intended. It allowed for the step-up into applying the method into a more commercially influential material, Ti-6Al-4V, which is widely used and of interest to many researchers and industries alike.

In terms of validation, the advanced Lab-DCT technique used in this study corroborated EBSD data captured with an SEM. For the future of advanced alloy processing, it is a powerful method for analysis of grain structures, and holds a lot of potential for further study as the technology

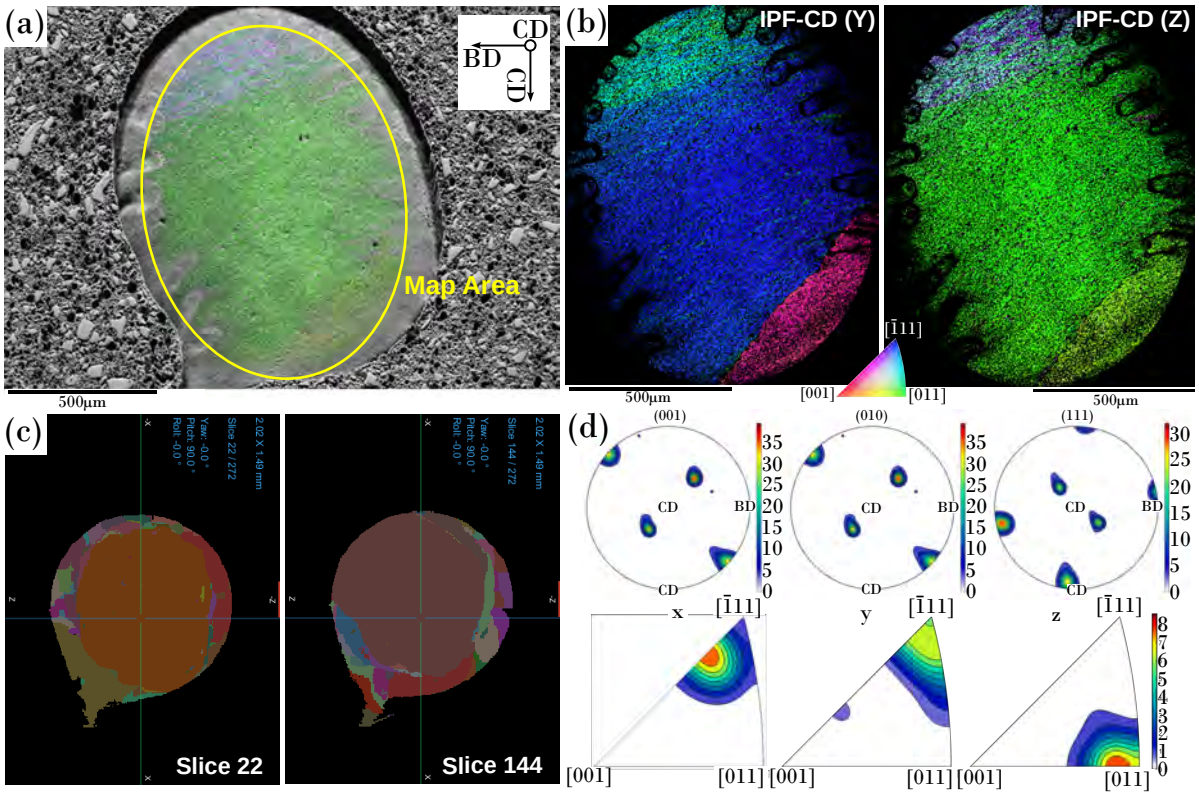

Figure 5.26: (a) Mixed image of tilted DCT specimen 1 (2.9% cross-section reduction) showing the EBSD data map area, (b) EBSD data maps for IPF-CD (Y) and IPF-CD (Z) (out-of-page), (c) DCT 3D grain data slices at different heights of 3D scan for comparison with (b), and (d) Pole figures and Inverse pole figures for the EBSD data maps provided in (b).

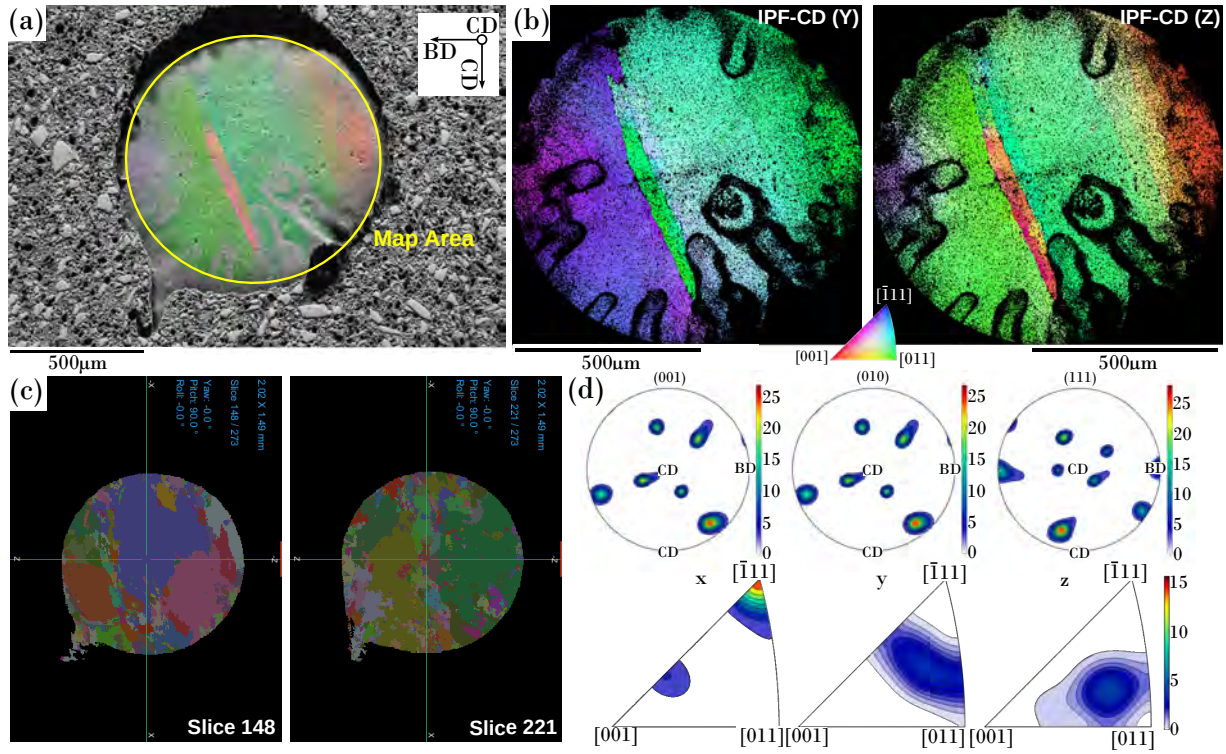

Figure 5.27: (a) Mixed image of tilted DCT specimen 2 (10.6% cross-section reduction) showing the EBSD data map area, (b) EBSD data maps for IPF-CD (Y) and IPF-CD (Z) (out-of-page), (c) DCT 3D grain data slices at different heights of 3D scan for comparison with (b), and (d) Pole figures and Inverse pole figures for the EBSD data maps provided in (b).

improves.

The easily worked materials allowed for a great basis of study and allowed for a publication of the equipment design and method [362], that can be shared, replicated, and improved upon in other materials testing laboratories. This could allow for a large increase in the multi-load testing of metallic materials worldwide, and their inclusion in the development of next generation metallurgical manufacturing digital twins.

Chapter 6 presents and discusses the first experimental proof of concept material results from the novel design, at high temperature, using titanium alloy Ti-6Al-4V, demonstrating the objective of achieving different levels of microstructure evolution and morphology. Furthermore, demonstrating the replication of the cogging process in line with the aim and objectives of the research.

6 Micro Cogging of Dual-Phase Alloy

6.1 Introduction

This study presents the application of a new experimental technique for laboratory-scale simulation of the open-die forging process, known as cogging, an intermediate hot-working process necessary to design an optimised microstructure in the advanced engineering titanium alloy Ti-6Al-4V. Small test-bars of Ti-6Al-4V alloy were subjected to multi-directional cogging operations at elevated temperatures (950 - 1050 °C). Prior to forging, the as-received material underwent heat treatments to coarsen the starting grain structure, to better simulate the industrial-scale intermediate microstructure (*i.e.,* β recrystallised) and to help demonstrate the capability of the apparatus to achieve microstructure modification via globularisation (below β-transus), and recrystallisation (dynamic and static) and recovery mechanisms (above β-transus) within the cogged material. The influences of hot working parameters on deformation localisation, width of α platelets, and globularisation within the resulting microstructure variation have been investigated using light microscopy (LM), Vickers hardness (HV) testing, and electron backscatter diffraction (EBSD). The cogged Ti-6Al-4V alloy specimens underwent various microstructural evolution stages after hot forging, thus demonstrating the success of the designed miniaturised open-die forging apparatus for high temperature experimentation and characterisation studies. This will be suitable for low-cost small-scale trials to determine the key process parameters affecting the onset of microstructure evolution during open-die forging (*e.g.,* ingot-to-billet conversion) of the Ti-6Al-4V alloy, prior to large-scale trials which are rather more expensive.

Building on the previous chapters study detailing design and effectiveness of the apparatus in achieving desired microstructure evolution (*e.g.,* grain-refinement) in a single-phase alloy [362], this study provides proof that there is capability of capturing different levels of microstructural evolution in alloys of high research and commercial interest. Specifically, the capability of hot forging titanium alloys was a requirement that guided a number of design decisions with regard to the load frame capacity, specimen size with respect to available furnace volume, as well as the material choice and geometry of tooling. One key evaluation of the new apparatus is investigating its capability to breakdown intermediate β-recrystallised material with lamellar structure to a globularised α microstructure, which is a microstructural evolution explored in the works of Semiatin *et al.* [363], Souza *et al.* [364] and Sabban *et al.* [365]. Globularisation of the α-phase originates from strain localisation on the grain boundaries of deformed α lamellae within an $\alpha+\beta$ structure. This localised strain causes a build-up of micro-defects, *i.e.,* sub-boundary dislocations, which then creates a channel of dislocations for solute diffusion which can generate thermal interface grooving in the α platelet/lamellae which leads to globularised α grains, which is described and visualised well in Zhang *et al.*'s work [366].

This chapter aims to demonstrate the opportunity of a new experimental method in capturing multiple levels of microstructure evolution in Ti-6Al-4V through numerous miniaturised open-die forging tests, meanwhile reaching new temperature capability, which will then be investigated through different characterisation techniques. FE modelling will additonally be used to determine stress, strain, and expected load from the micro-cogging (*i.e.,* open-die forging) operations.

6.2 Results

The commercial $\alpha+\beta$ alloy Ti-6Al-4V was selected as the specimen material for the high temperature forging trials. The nominal chemical composition of the material is provided in Table 4.3. As an $\alpha+\beta$ alloy, Ti-6Al-4V can have differing volume fractions of α and β phases, depending on heat treatment and the contents of interstitial elements (primarily oxygen). The procured Ti-6Al-4V average Vickers microhardness was measured to be 364HV across the longitudinal section and 376

across the transverse section.

6.2.1 Pre-worked Ti-6Al-4V Alloy

The alloy was procured as a 12 mm hot-rolled round bar. Anti-oxidising glass coatings were applied to sections of the alloy bar before being subjected to a heat treatment in a VFE TAV TPHF horizontal vacuum furnace for 2 hours at 1100 °C followed by air-cooling. This heat treatment above the β-transus (about 1000 °C) was performed to grow the β grains drastically, so as to replicate the β recrystallised condition, which is typically the microstructure processed at industrial-scale during open-die forging. This material will henceforth be referred to as "as-heat-treated" (AHT). The AHT bar sections were subsequently cut into shorter test specimens, 28-35 mm in length. The effect of heat treatment from the procured material to the AHT state is presented in Figure 6.1, where the initial fully equiaxed microstructure of approximately 85% globularised α + 15% transformed β (*i.e.,* secondary-α) transitioned through a β recystallised microstructure to an α lamellar structure with an average prior-β grain size of 700 µm. The billet (BD) and the cogging (CD) directions are denoted to highlight the directions along which the open-die forging was conducted.

6.2.2 Heat Treatment Study on Ti-6Al-4V

This short section continues on from the heat treatment study found in the previous chapter and will evaluate the microstructure characterisation results of the Ti-6Al-4V specimens. Table 5.1 in the previous chapter highlights the heat treatments carried out on the Ti-6Al-4V material as part of the heat treatment study on the procured material. All heat treatments in this section were

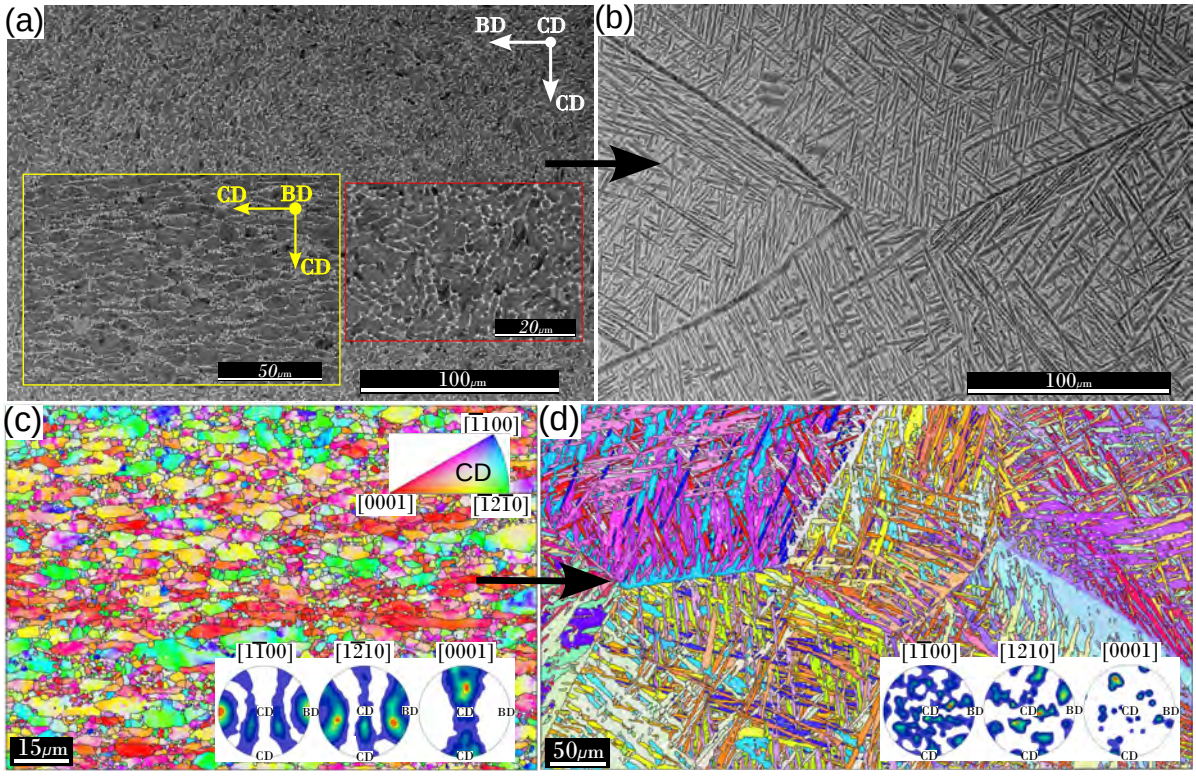

Figure 6.1: (a) Backscatter electron images of procured Ti-6Al-4V material prior to heat treatment showing a fine microstructure, a higher magnification image highlighted in red, and an image showing the transverse microstructure highlighted in yellow (b) Backscatter image of AHT microstructure, showing α colonies within prior β grain boundaries, (c) EBSD IPF-CD map (out-of-page) of procured Ti-6Al-4V material prior to heat treatment, highlighting a hot-rolled microstructure with clear texture observed in pole figures, (d) EBSD IPF-CD map (out-of-page) of AHT Ti-6Al-4V material, highlighting a microstructure of α lath colonies within prior β grain boundaries with no discernible texture observed in the pole figures. Orientation directions are the same unless highlighted in blue, IPF-CD (out-of-page) key is the same for (c) and (d).

conducted over a 1 hour duration.

Figure 6.2 presents light micrographs from the heat treatments of Ti-6Al-4V, in the range of 900-1100 °C. It is observed from Figure 6.2(a) that 900 °C annealed the procured microstructure into a fully-equiaxed microstructure as it was 50 - 100 °C below the β-transus. Similarly, 950 °C, seen in Figure 6.2(b) had a similar result as it remains below the β-transus, resulting in a bi-modal structure. These microstructures are desired for further secondary processing in Ti-6Al-4V. However, as the aim of this study is return to a lamellar structure to simulate the primary processing (*i.e.,* ingot-to-billet conversion) stage, therefore the heat treatment temperature was raised and tested above the β-transus. Figure 6.2(c) - (e) present the light micrography results from the 1000 °C, 1050 °C, and 1100 °C heat treatment trials. It is observed from these micrographs, that these temperatures were sufficient in achieving the desired microstructure for simulating the cogging process.

Carrying forward the results from this study, 2 hours at 1100 °C was the final selected heat treatment for this study to ensure large β-grain growth, in which the α laths form colonies. In the future, different starting microstructures could be generated and tested using this method.

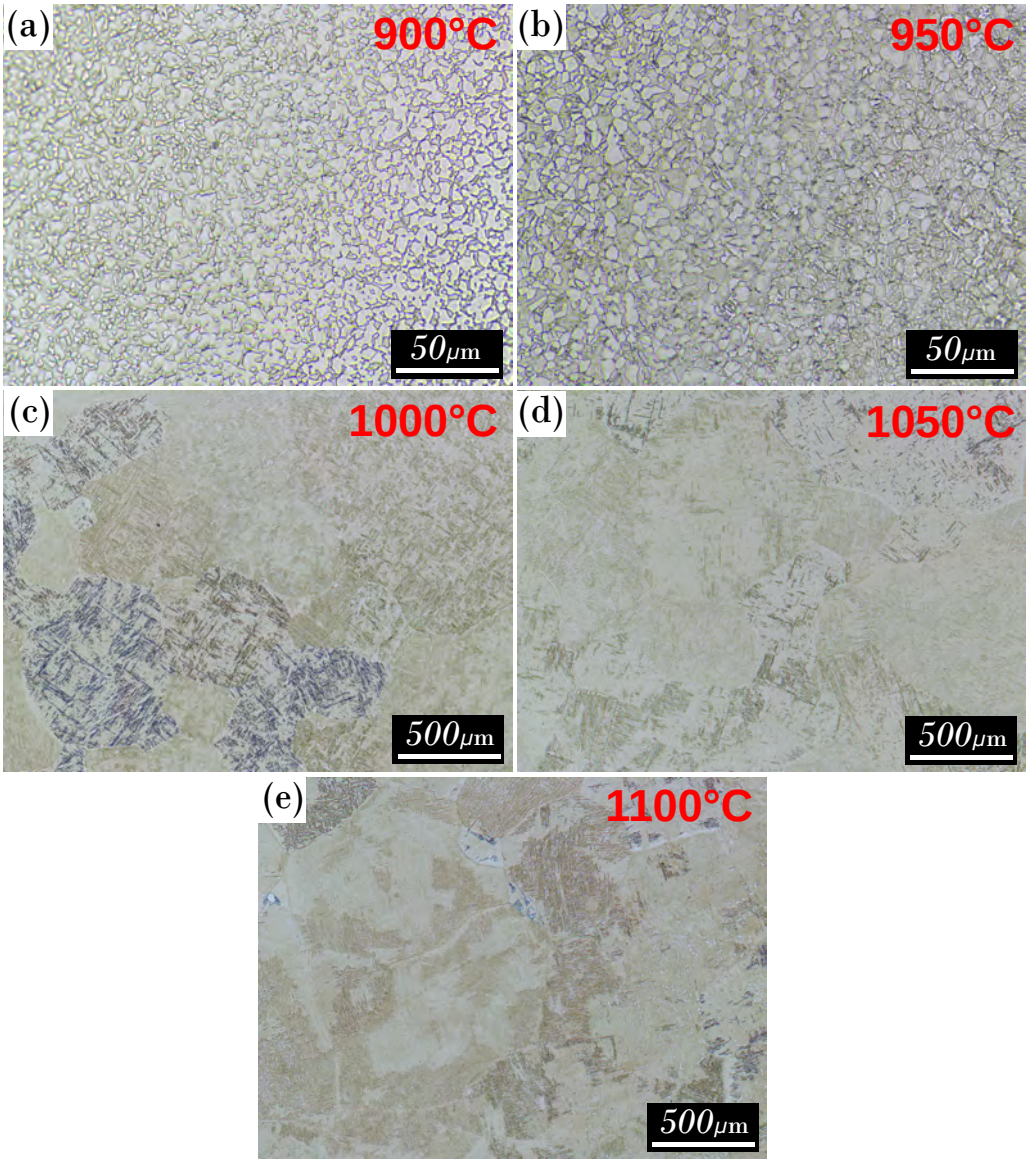

Figure 6.2: Light macrographs of Ti-6Al-4V titanium alloy heat treated material sections, (a) 900 °C, (b) 950 °C, (c) 1000 °C, (d) 1050 °C, (e) 1100 °C.

6.2.3 Miniaturised Cogging of Ti-6Al-4V Alloy

The open-die forging was carried out on a 250 kN Zwick/Roell™ Amsler Z250 load frame equipped with a Severn Thermal Solutions SF2113 Split Tube Furnace (SF) using a CU2113 Eurotherm™ temperature control system, and the Zwick™ testXpert III software. The manipulation of the specimens was carried out using the miniaturised open-die forging manipulator developed in house and integrated with the tensile test machine, details of which are explained elsewhere. [362]. Specimens were first mounted into the manipulator coupling and then aligned through the extensometer slot of the SF. Specimen positioning was then adjusted remotely prior to heating and the remaining gaps in the SF extensometer slot were filled with ceramic wool for thermal insulation. This set-up can be seen in Figure 6.3. The specimens were then heated to 950 °C within the SF and "soaked" for 10 minutes to ensure a homogeneous and stable temperature distribution. A pre-load of 20 N was applied at the end of the soak time, to aid against specimen slipping. The specimens were then repeatedly deformed in 5% cross-section height reduction increments (*i.e.,* in the CD) using a controlled step program. Between each deformation, or "bite", the specimen was rotated 90° (except where specified otherwise) to simulate the cogging (*i.e.,* open-die forging) operation. The manipulator rods were marked at 0° in vision of the operator to track specimen rotation between bites, an example of this is presented in Figure 6.3(b). The test matrix for all the cogging operations conducted on the Ti-6Al-4V specimens are provided previously in Table 4.6.

The final cogged geometry target for specimen SP7 was for a reduction of 25% in nominal cross-section in CD, corresponding to a macroscopic true strain(ε_m) of 0.22, with a measured cross-head displacement rate of 0.12 mm/s.The specimen was then withdrawn from the split furnace and allowed to air cool. A schematic diagram of the thermomechanical procedure for the forging tests is shown in Figure 6.4(a).

Following forging, the 3D geometries of the specimens were captured using the GOM ATOS TripleScan III non-contact rotary table scanner. GOM Suite software was used to measure cross-section reduction for each sample using section areas taken every 1 mm along the sample. The average cross-section reduction was then calculated from the difference in area between sections in the stub zone against the cogged zone. A detailed description of the manufacture and assembly of the experimental set-up and tooling is provided in Chapter 3.

Table 6.1 presents the geometric results from the open-die forging of the mini-billets, highlighting the differences in cross-section reduction targets against the measured cross-section reductions in the lab and using 3D GOM scan data. Deformation results from all cogging trials followed a similar overall trend. This can be seen from the load graph data presented in Figure 6.7(a), *N.B.* minimal load cell drift is observed over the course of the cogging trial. The post-analysis load graph output from DEFORM™ FE modelling of the nominal material processing is provided in Figure 6.7(l). It is

Table 6.1: Geometric assessments for all Ti-6Al-4V specimens cogged at elevated temperatures, comparing the target cross-sectional height reduction (X-section height red.), lab measured cross-sectional height reduction measured with Vernier callipers, and the maximum and average cross-sectional area reductions calculated using sectioned areas from the stub and cogged zones of the 3D GOM scans. Also detailing the geometry, total number of bites, and calculated elongation percentage.

Specimen No.	SP1	SP2	SP3	SP4	SP5	SP6	SP7	SP8	SP9	SP10	SP11
Target X-section Height Red. (%)	5	10	10	10	15	20	25	5	10	10	15/30
Measured X-section Height Red. (%)	3.8	6.2	0.6	10.8	12.9	14.5	13.4	2.4	8.9	9.0	18.3
Avg. Area Reduction (%)	1.3	2.3	0.2	4.2	8.1	10.8	12.2	0.1	7.3	3.6	13.1
Max. Area Reduction (%)	1.4	3.9	0.3	4.8	8.1	11.0	15.4	0.4	7.4	3.9	15.1
Geometry	□	□	□	□	□	□	□	○	○	□	□
Total No. of Bites	2	4	4	6	6	8	10	4	8	4	12
Elongation (%)	0.7	1.3	0.5	4.1	2.2	5.0	7.1	0.6	5.9	4.0	10.3
Temperature (°C)	950	950	950	950	950	950	950	950	950	950	950/ 1050

observed that the test time for the FE predicted load graph seen in Figure 6.7(b) is much shorter, as well as a more uniform increase in load for each set of bite targets. *N.B.* Specimen SP3 was off-centre during alignment (due to new methods being tested for in-situ alignment) which led to it slipping relative to the dies during compression, this is reflected in Figure 6.7(c). A final observation is the large decrease in required load seen in Figure 6.7(j) due to the temperature increase from 950 to 1050 °C for cogging above the β-transus, the period of cooling and reheating has been removed from this load graph.

The elevated temperature testing in this study was carried out at 950 and 1050 °C. To extend the longevity of the Nimonic-90 platens, boron nitride suspension was used as a lubricant and

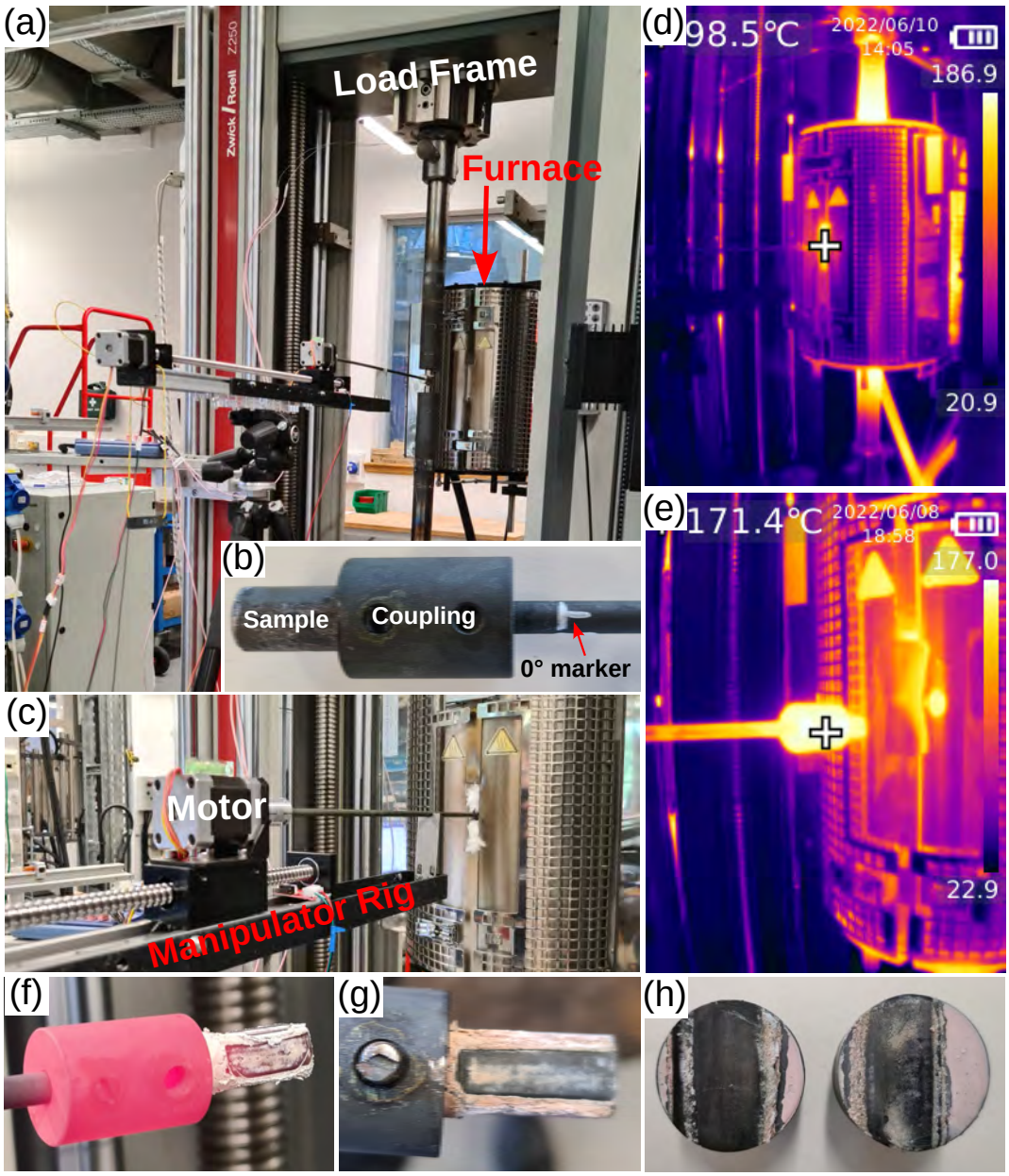

Figure 6.3: Collection of images from experimentation, presenting; (a) the test apparatus during alignment within Zwick/Roell™ Z250 load frame prior to testing, (b) a close-up of sample in coupling, highlighting a 0° rotation marker, (c) close-up of the apparatus manipulator during high temperature testing. Thermal camera image of split-tube furnace taken; (d) during testing highlighting heat escaping through insulated extensometer slot and, (e) after testing and during cooling, highlighting the effective heat dissipation from the sample and coupling along the manipulator rod. Captured using the Uni-T UTi690B Professional Thermal Imager (-20 to 550 °C). Images showing test specimen mounted within the manipulator coupling, highlighting removal of lubricant during specimen deformation; (f) immediately after removal from the furnace after forging and, (g) after air cooling, (h) Nimonic®-90 superalloy custom dies after testing.

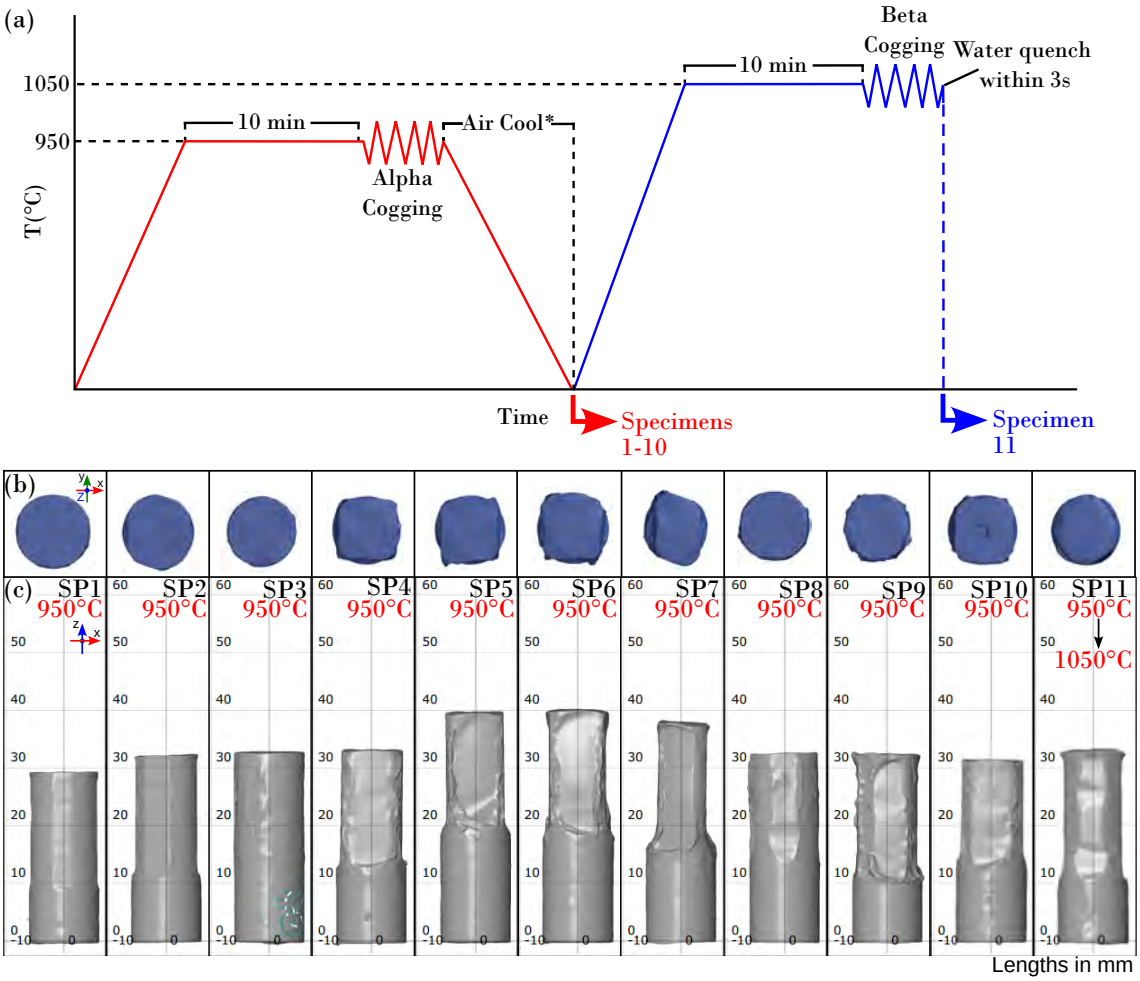

Figure 6.4: (a) Schematic representation of the sub-transus (950 °C) processing and the super-transus (1050 °C) processing used in this study. 3D GOM photogrammetry scans of the specimen range highlighting the final forged geometries, showing (b) plan (blue) and, (c) elevation views (grey). Parts to same scale.

anti-stick agent. Images showing the tooling dies, rods, and couplings after testing are shown in Figure 6.3(f) - (h), demonstrating the effect of repeated compressions on the lubricant across the dies and specimens. Additionally, thermal images captured during and after testing of the tooling are presented in Figure 6.3(d) - (e), showing minimal heat conduction along the length of the manipulator rod. This demonstrates that there is sufficient distance between the SF and electrical components of the cogging apparatus.

A thermal conductivity range of 6.9-18.0 W/mK for Ti-6Al-4V was used as a function of temperature for heating operations of the workpiece as suggested by DEFORM™ which are values corroborated in Kim & Lee's work [334], with a convection coefficient of 0.02 N/s/mm/°C. For the deformation operations, a friction coefficient of 0.3 between the dies and the sample was implemented, as per the software's suggested values for lubricated hot forging. Additionally, the deformation conditions were set up with no heat transfer with the environment, die, and workpiece temperature fixed at 950 °C. A Taylor-Quinney factor of 0.9 was used [335, 336], which is a good approximation of the fraction of mechanical work converted into heat during deformation. [337–339] A mesh with 16,000 tetrahedral elements was generated for the workpiece geometry. The movement speed of the lower die during the experimental compression tests was recorded, and the measured value was used as an input for the FEM simulation.

The model for this study was first set up for nominal cogging conditions, assuming all rotations and compressions were perfect 5% incremental bites throughout with no slippage or sticking, shown in Figure 6.5(a). A second model was set up post experimentation for Specimen SP7, which during testing had a sticking complication. This sticking was due to numerous factors, including the large

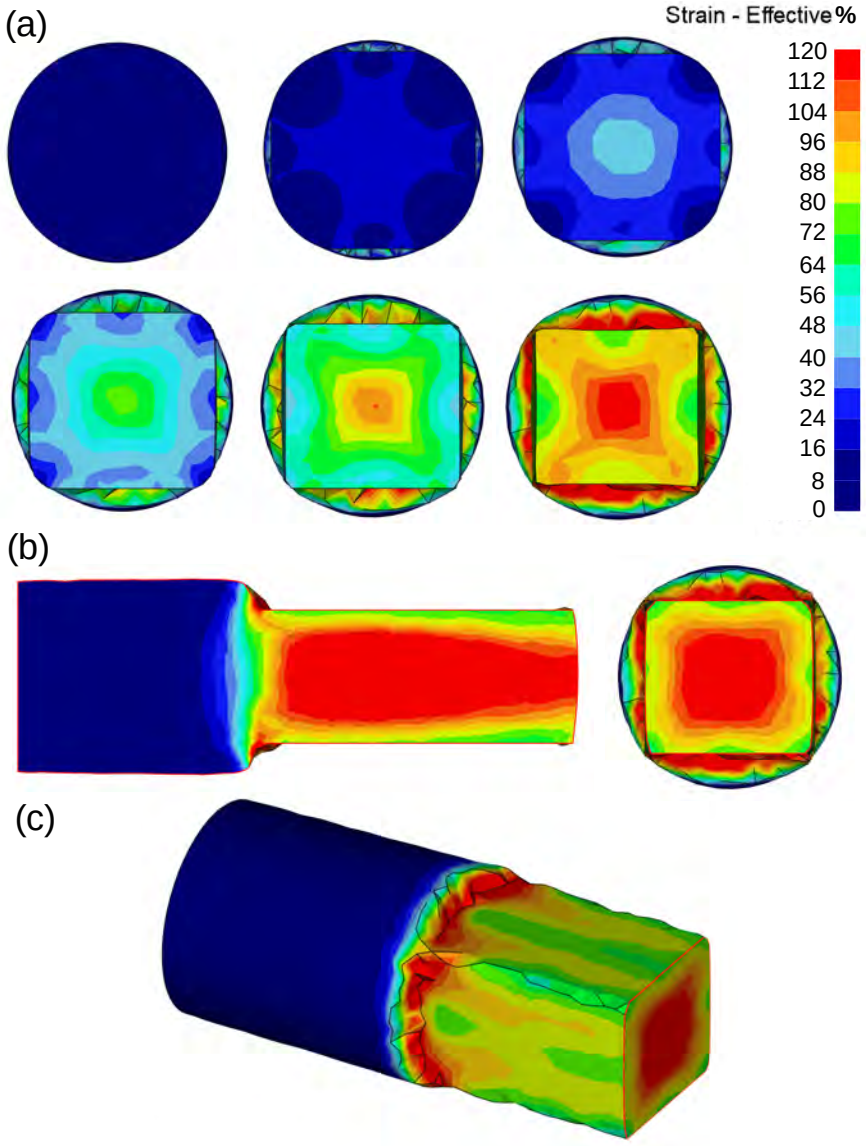

Figure 6.5: The results of FE simulation presenting (a) the nominal strain distributions on the radial cross-section after each 5% cogging pass up to 6 passes (*i.e.,* 30% cross-section reduction), (b) the strain distributions on both the longitudinal and transverse cross sections of Ti-6Al-4V specimen following cogging testing to 30% cross-section reduction and, (c) effective strain distribution in 3D isometric view. The effective strain scalebar is the same for all plots.

number of bites, which resulted in the final rotation being interrupted. The final compression was repeated in the first compression direction. Therefore, this element was carried forward into the model and the simulation repeated, these results can be seen in Figure 6.6.

The specimens dimensions predicted by the model were compared with the actual dimensions of the deformed specimens after compression. The model was set up to replicate the same compression levels of the various samples up to a macroscopic true strain(ε_m) of 0.26. The results of FE models match the geometry of the deformed parts, and for Specimen SP7 predict a final cross-section of 8.5 mm in one direction, which was within 2% of the measured diameter of 8.3 mm. This validates the chosen values of heat transfer coefficient, friction coefficient, and suggests that the strain distribution is reasonably accurate.

Comparative GOM 3D scan results for each of the Ti-6Al-4V specimens can be seen in Figure 6.4(b)-(c). These scans show the final billet geometries, which are representative of billet geometries seen in industrial processes [130]. *N.B.* A thin layer of boron nitride lubricant can be seen on the 3D GOM scans across the samples, which has caused observed ridges. Figure 6.9 presents

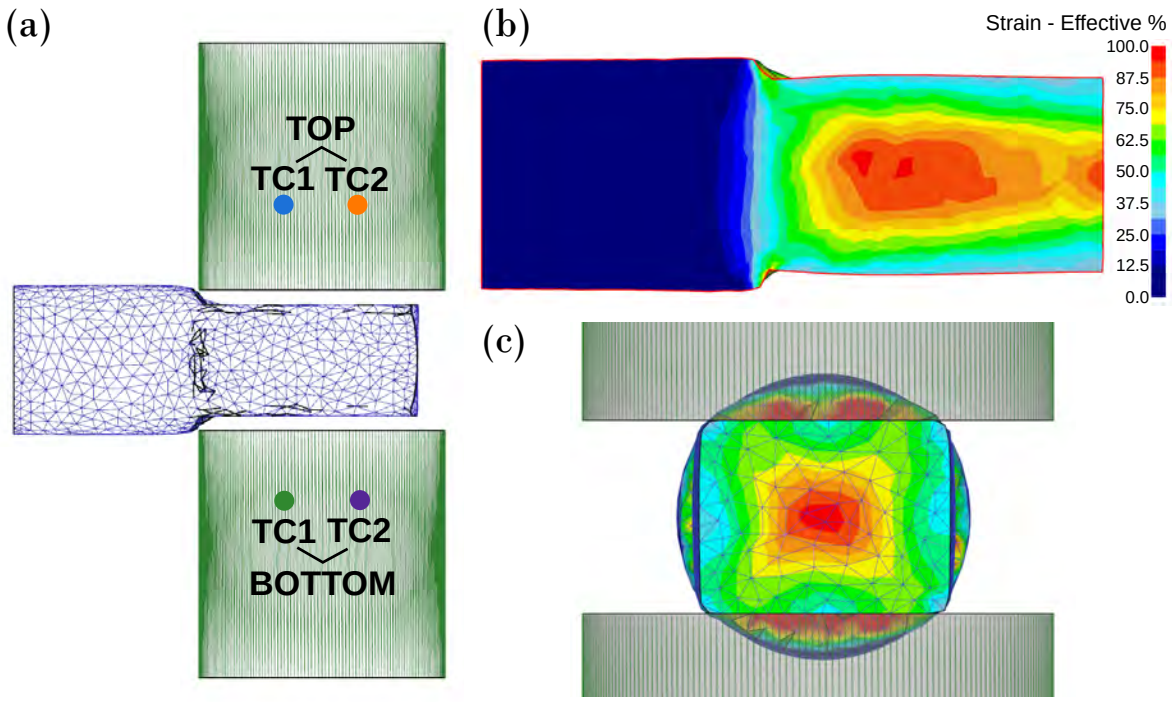

Figure 6.6: Results of FE simulation of Specimen SP7; (a) an illustration of the FE mesh for the workpiece and dies at 25% reduction with repeated final compression in the CD at 0° rotation, also highlighting representative thermocouple placements for reference in Figure 6.10, (b) strain distributions on the longitudinal cross-section following cogging to 25% reduction with repeated final compression in the CD at 0° rotation, (c) strain distributions on the transverse end, including mesh on the specimen and dies.

light macrographs of the full miniaturised open-die forging titanium specimen range, where the variation in achieved geometries is highlighted. It can also be observed the difference in morphology between the centre of specimen SP11 compared with the other specimens due to the different testing temperatures. Another observation from Figure 6.9 is the emphasised barrelling effect seen in specimen SP7 compared to the other specimens due to the higher strain, and final compression direction (*i.e.,* final strain path).

Microhardness measurements reveal a noticeable increase in the Vickers hardness for all samples at the edges that have been exposed to air while forging, *e.g.,* an average increase of 10 to 20% across all samples. This increase in Vickers hardness is due to the formation of oxygen-rich alpha-case at the surface of the samples forged at elevated temperature. It is evident from the captured Vickers hardness maps and lines that overall there is no clear change from the forging itself. This could be indicative of an increase in strength with no measurable change in ductility within the more highly strained specimens, as the grain size decreases while the hardness values remain the same.

The FE results shown in Figures 6.5 and 6.6 highlight the strain distributions expected over the specimens range. The 30% target was selected as this is just beyond the upper limit of the current Ti-6Al-4V data-set, and is the upper limit of cross-section reduction seen in industrially cogged billets due to their size.

Figure 6.8 presents electron-backscatter micrographs from the three separate zones within specimen SP7 where changes in morphology are observed. These observations are shown at three separate magnifications, where the original lamellar/α-platelet structure of the AHT material in the stub zone is seen to breakdown and form rounded globularised α-grains. Internal localised strain is observed within the larger α lamellae seen at the transition zone edges of the specimen, indicating lamella breakdown *i.e.,* the first stage of globularisation.

Figure 6.10 presents results from specimen SP10, which was used as an exploratory sample to investigate the level of adiabatic heating released in the centre of the sample during compression. This was achieved by machining a small hole in the end of the sample to place a thermocouple

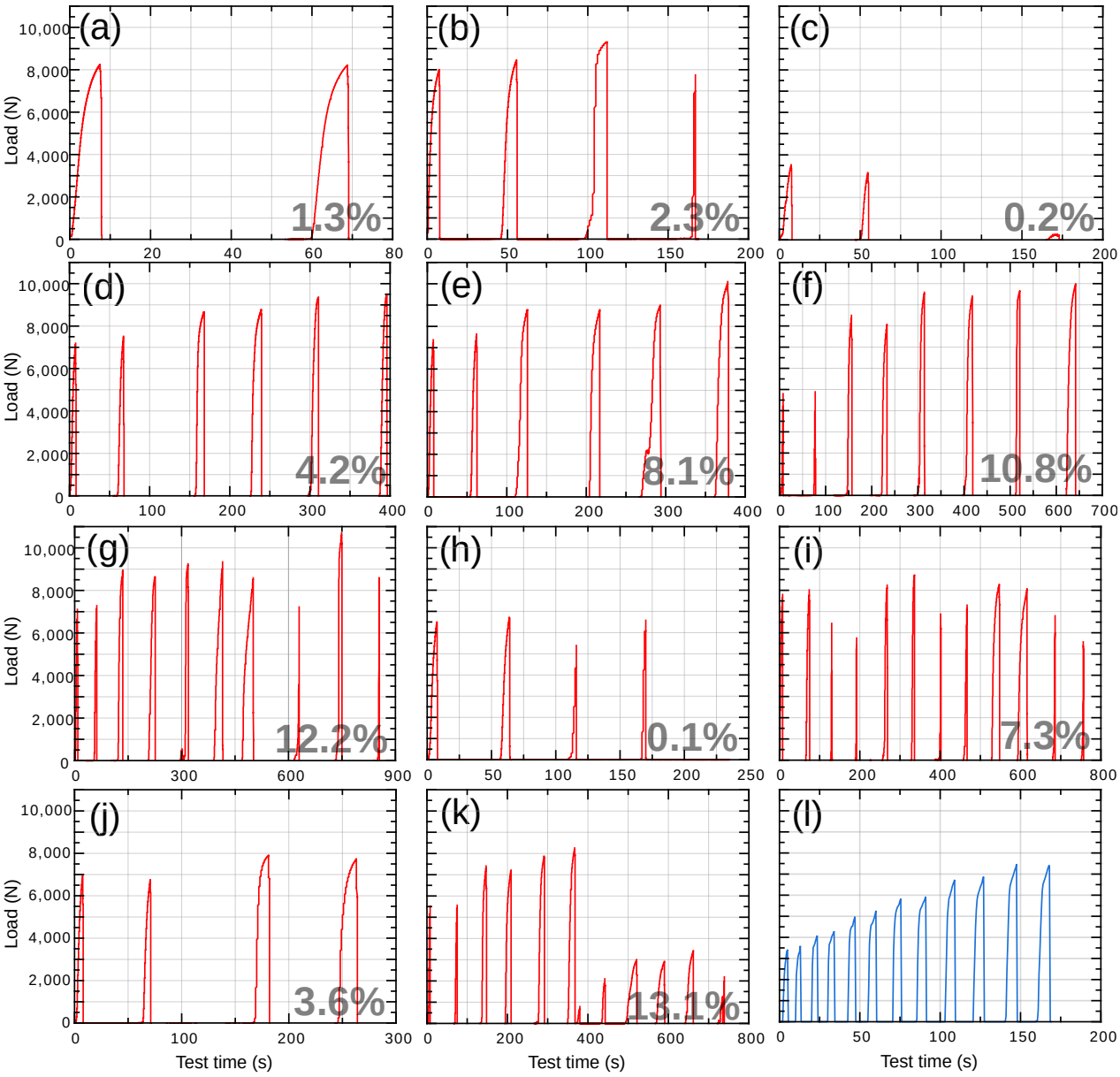

Figure 6.7: Measured load (N) against test time (s) during cogging tests for specimens; (a) SP1 (5%), (b) SP2 (10%), (c) SP3 (10%), (d) SP4 (10%), (e) SP5 (15%), (f) SP6 (20%), (g) SP7 (25%), (h) SP8 (5%), (i) SP9 (10%), (j) SP10 (10%), (k) SP11 (15/30%). Data was taken from Zwick/Roell™ load cell during testing, recorded in Zwick™ testXpert III software . The values on the plots are the measured deformation %, compared to the target deformation % stated in brackets in the caption for each specimen, (l) The FE predicted graph for load (N) against number of steps for Ti-6Al-4V alloy to the same number of bites. All plots are to the same y-axis scale and visualised using LabPlot by KDE®.

into the end of the specimen that was to be forged. Figure 6.10(c) shows a light micrograph of the specimen with the thermocouple hole visible in the cogged zone, with an overlaid Vickers microhardness map. A noticeable increase in hardness is observed at the edge of the specimen, where the α-case has formed through diffusion with the hot air of the furnace. The band contrast map seen in Figure 6.10(a) is also indicated. This band contrast reveals another example of the large volume of α-case generated at the edges of the sample exposed to air during forging, as well as the numerous fine α-lamellae that formed from the initial β recrystallisation heat treatment. Lastly, Figure 6.10(b) shows the plot of temperature (°C) against time (ms) which highlights the small increase in temperature ($\sim$3 °C) which is about double the increase measured by the set of thermocouples elsewhere in the furnace.

The initial lamellar structure of the AHT material that was created during the β recrystallisation

heat treatment remains to be seen in the cogged zone of specimen SP1, shown in Figure 6.11(a), as the local strain induced in the billet is too low to have had significant impact on the microstructure. Figure 6.11(b) - (d) reveal two stages of globularisation in each micrograph, where both long platelets with grooving and fully globularised equiaxed grains are observed, showing the mechanisms operating for globularisation are orientation dependent. It is also indicative that at low strain level, a high level of globularisation can be achieved through the multi-directional loading activation of different slip systems. Figures 6.11(e) and (f) demonstrate some fully globularised/equiaxed grains as the strain level was sufficient for achieving 28% α globularisation. Globularisation mechanisms of titanium alloys with lamellar colonies are described in Zhang *et al.*'s work [366].

A final exploratory test was the forging of specimen SP11. This specimen was the first advancement into forging above 1000 °C using the miniaturised setup. Testing the temperature limitations of the tooling was one key output from this test. However, it also allowed the investigation into the β cogging of the Ti-6Al-4V alloy at this scale. Figure 6.12 presents three magnification levels of EBSD IPF-CD (out-of-page) map data that show a widmanstätten (or basketweave) structure, in Figure 6.12(d) this structure is observed along the centre of the specimen in the BD, understandably where some diffusion was allowed to occur due to the higher temperature retention of the core, and thus slower cooling rate. On the other hand, the outer regions of the specimen are observed to be martensitic, where the water-quenching did not allow time for diffusion, which aligns with Bignon *et al.*'s study on martensite formation in titanium alloys [367]. This was due to the rapid

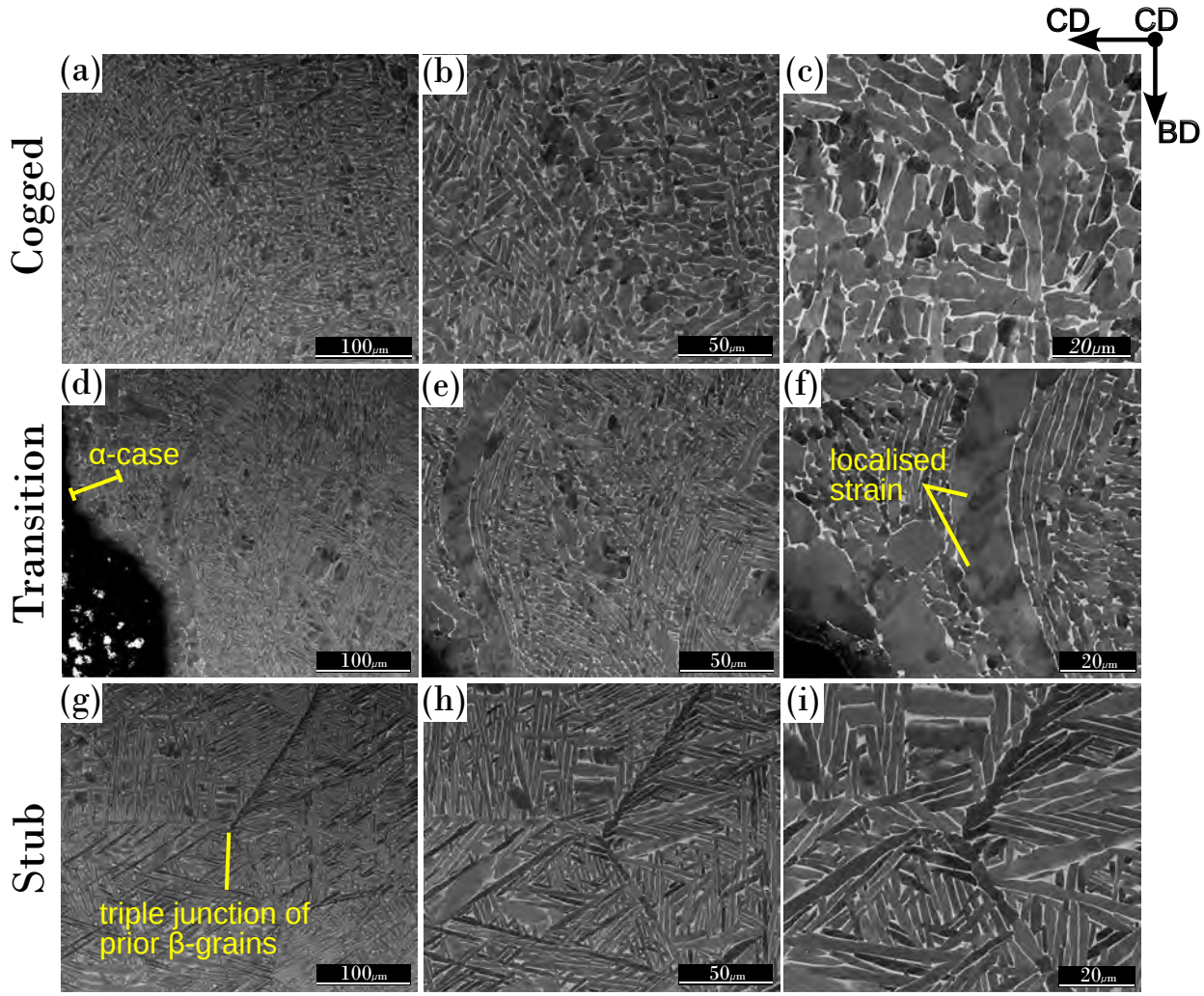

Figure 6.8: Backscatter electron images taken from different zones of the cross-section of specimen SP7 after forging at three magnification levels: (a) - (c) Cogged zone, (d) - (f) Transition zone, (g) - (i) Stub zone. The images highlight the effect of cogging, using the manipulation apparatus, on the microstructure obtained at different strain zones within a single specimen.

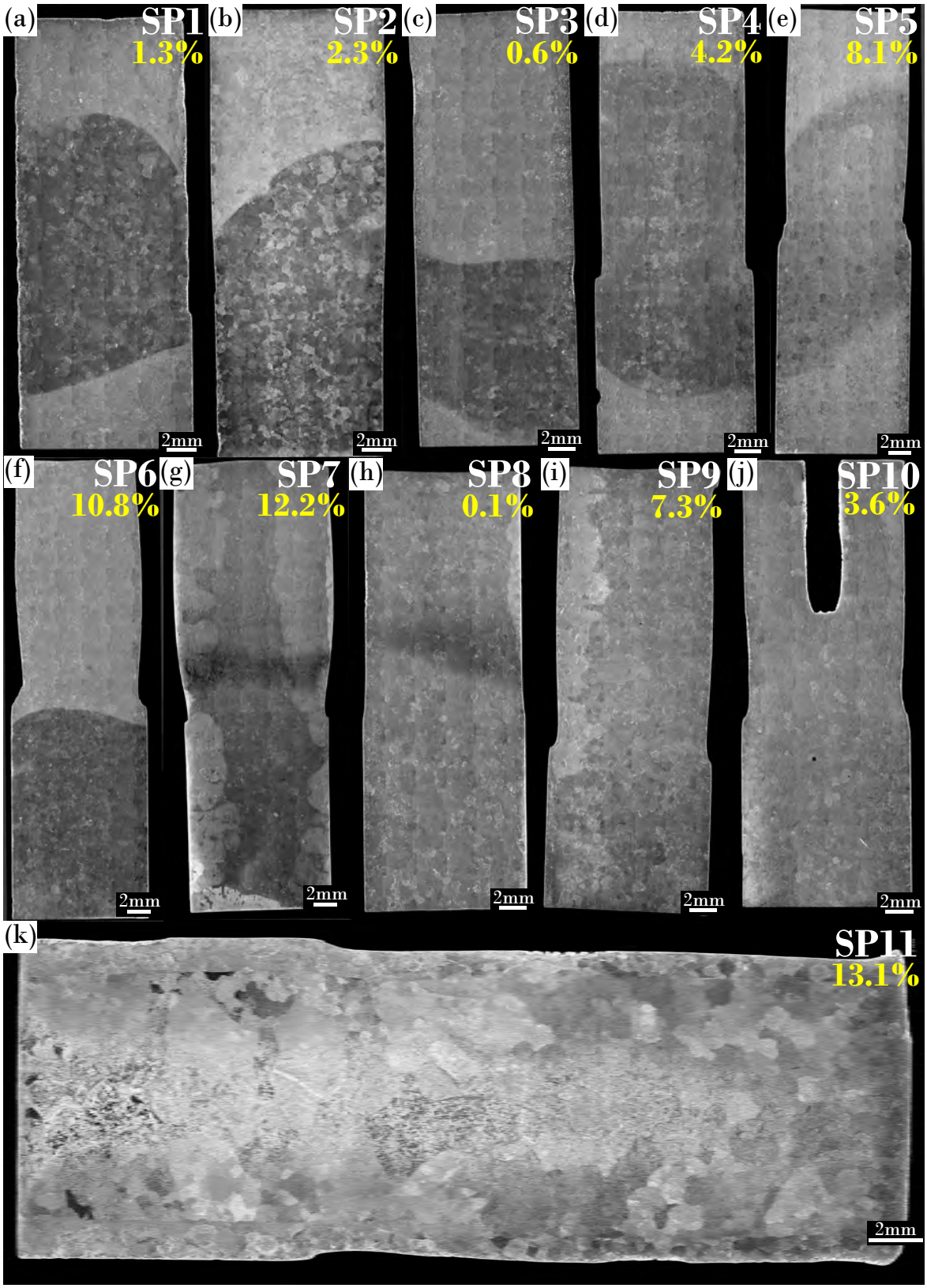

Figure 6.9: Light macrographs of sections from the full Ti-6Al-4V alloy cogged specimen range, highlighting varied microstructural evolution stages, α-case layer along the edges, including; (a) SP1, (b) SP2, (c) SP3, (d) SP4, (e) SP5, (f) SP6, (g) SP7, (h) SP8, (i) SP9, SP10 and, SP11. All % values in the image represent the Avg. Area Reduction of the specimen measured from GOM.

cooling from above the β-transus after forging, which inhibited the growth and recrystallisation of secondary α grains. It is also clear within the presented pole figures that no discernible texture can

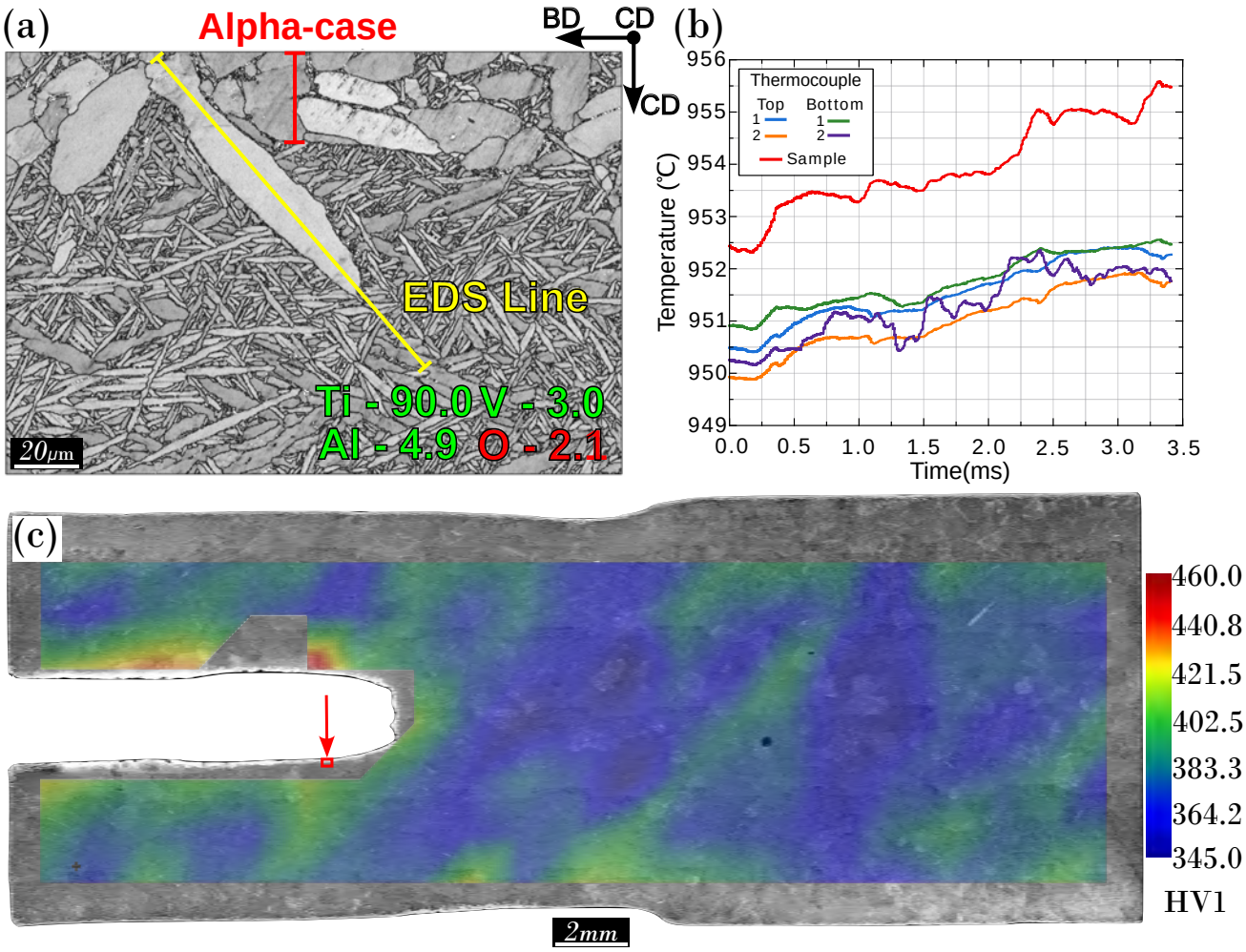

Figure 6.10: (a) A band contrast micrograph of Specimen SP10 taken from the internal face edge of the thermocouple hole showing large α lamellae, (b) Temperature($^{\circ}$C) against time(ms) from thermocouples in the sample and top and bottom dies during compression (representative thermocouple placements shown in Figure 6.6) and, (c) light micrograph of Specimen SP10 showing the location from which (a) was captured and overlaid with a Vickers microhardness map.

still be observed after deformation. The prior β-grain structure is also visible within Figure 6.12(c), where the α-colonies would nucleate from the grain boundaries.

For all samples examined in this work, the extent of microstructural transformation becomes more important with increasing deformation and local effective strain. After two orthogonal deformation steps of 5%, *i.e.,* in specimen SP1, the initial microstructure of the AHT material that was created during the β-recrystallisation heat treatment remains unaffected, as shown in Figure 6.11(a). At higher levels of deformation, for example in specimens SP4, SP5, and SP6, where the effective strain in the cogged zone reaches between 0.25 and 0.9, some deformed alpha laths and segmentation are observed, as shown in Figure 6.11(b) - (d); but these occurrences remain isolated. Sample SP7 underwent the highest amount of deformation, *i.e.,* effective strain of 1.37 in the cogged zone, and displayed the most deformed microstructure. Many alpha laths are broken up into smaller equiaxed grains, observed in Figure 6.11(e); and as a result, the globularised fraction (fraction of grains with aspect ratio lower than 2) raised to 28%. However, full globularisation was not achieved in this sample and some initial alpha lamellae remain.

Parent beta grain reconstruction (PBGR), presented in Figure 6.13, was carried out using the MTEX Toolbox which recovers the parent grains from the measured child grains using the Burgers orientation relationship [368]. This aligns the (110) plane of the β phase (*i.e.,* BCC crystal structure) with the (0001) plane of the α-phase (*i.e.,* HCP crystal structure) and the $[1\bar{1}1]$ direction of the

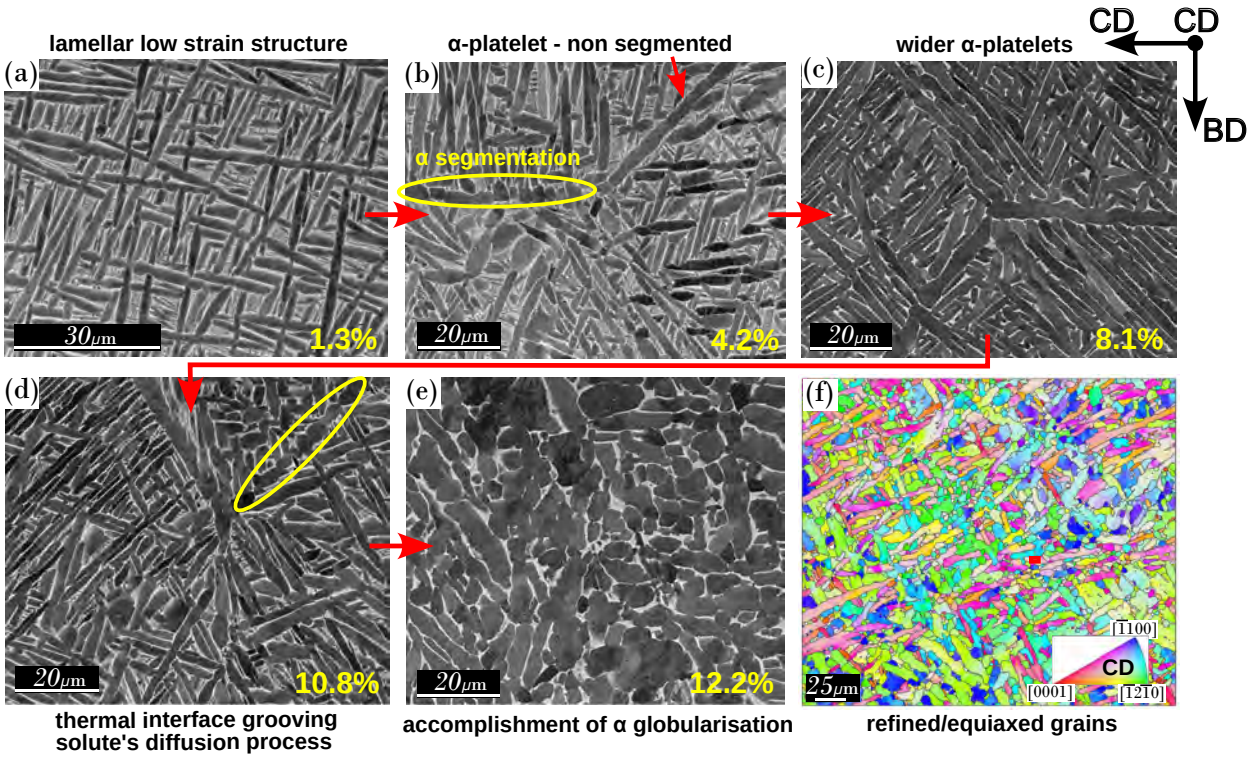

Figure 6.11: Microstructure appearances of the Ti-6Al-4V specimens underwent different levels of globularisation with increased average cross-section reduction (*i.e.,* strain), denoted in caption brackets, (a) SP1 (1.3%), (b) SP4 (4.2%), (c) SP5 (8.1%), (d) SP6 (10.8%), (e) SP7 (12.2%), and (f) EBSD IPF-CD (out-of-page) map showing segmented α and equiaxed grain orientations of Specimen SP7 (12.2%).

β phase with the [2110] direction of the α-phase. It can be observed that the success of the software in recovering the parent grains is influenced by both the temperature and localised strain in the material. Figures 6.13(a)-(b) display that a clear reconstruction is obtained if there is no plastic strain, or if there is deformation above the β-transus, whereas in Figures 6.13 (c)-(e), the reconstruction becomes increasingly interrupted with α-platelets whose orientations differ significantly from their neighbours within the same α-colonies. These interruptions become more frequent as the cross-section reduction, and hence level of strain, increases. This trend continued with specimen SP7, although the prior-β grains could be discerned visually from EBSD IPF maps, the computation of the PBGR was less effective to discern some parent grains, with a greater failure rate.

Figure 6.14 shows a comparison of the different shape parameters seen between low strain specimen SP2 (2.3% cross-section reduction) and the most highly deformed (12.2% cross-section reduction) specimen SP7 EBSD data. It can be clearly seen that the difference in secondary α shape, also displayed in Figure 6.14(g)-(h) is the α size distributions between the low strain and high strain material. The equivalent perimeter is defined as the perimeter of a circle with the same area as the grain and is always smaller than the actual perimeter of the grain. Therefore, the ratio between grain perimeter and equivalent perimeter, known as the shape factor, is always greater than one. Figure 6.14(c)-(d) shows the shape factor, *i.e.,* how different each grain is from a circle. Similarly, Figure 6.14 (e)-(f) displays the discrepancy between the actual grain shape again a circle using the perimeter (P) and equivalent perimeter(P_e) in a simple calculation:

$$\frac{P - P_e}{P} \tag{6.1}$$

this plots asymmetric grains as values close to zero and oblong or irregular convex grains will get values up to 0.5.

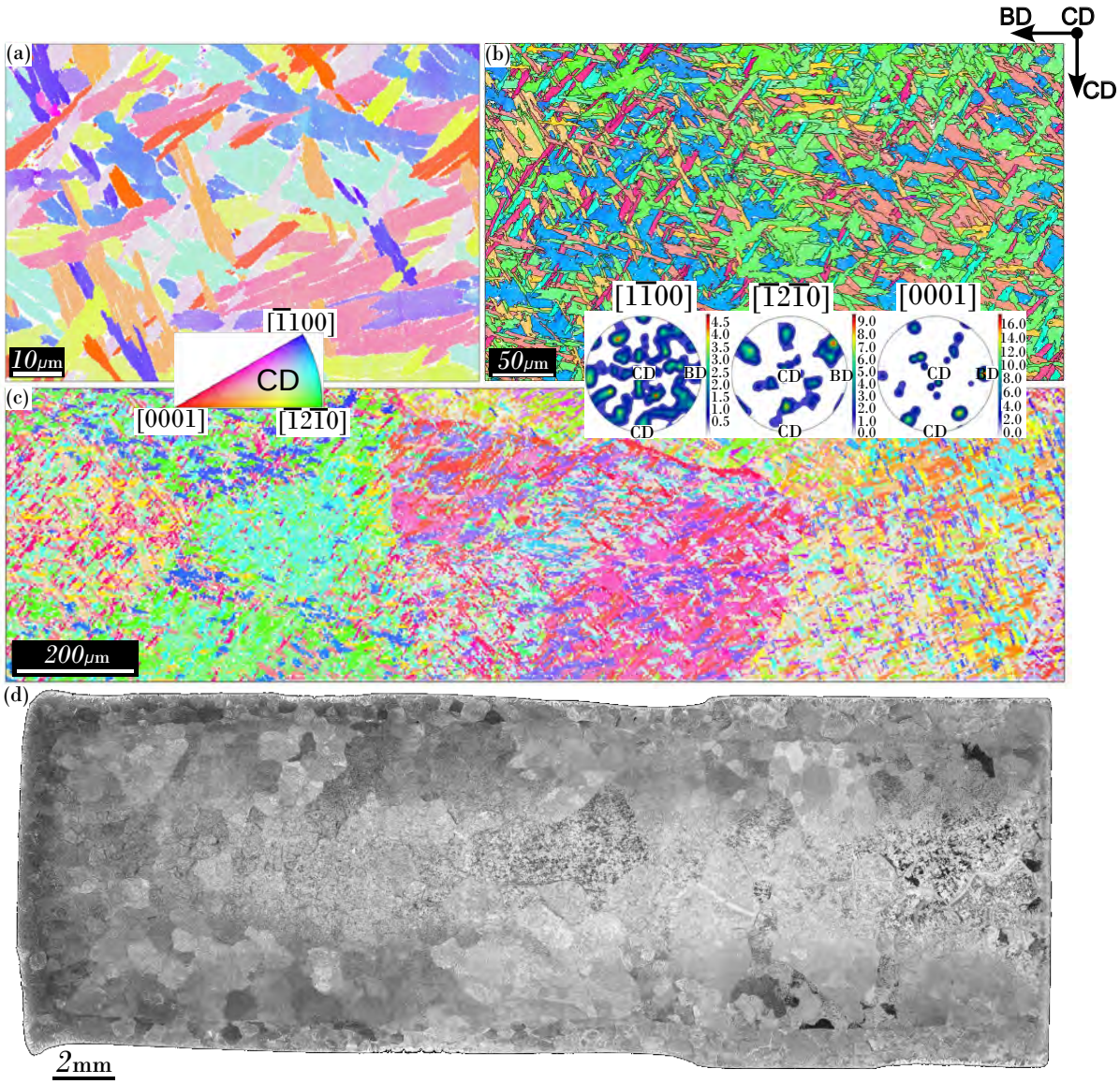

Figure 6.12: EBSD IPF-CD (out-of-page) maps for Specimen SP11, which underwent 2-stage cogging operations (below and above β-transus), including (a)97.5×66.6, (b) 487.2×334.8 and, (c)1826.0×504.0 μm map sizes all within the cogged zone, also showing polefigures that demonstrate no clear texture (c). IPF-CD (out-of-page) key is the same for all EBSD images. (d) Light macrograph of Specimen SP11 showing the macro-structure of martensite towards the specimen edges with an central widmanstätten (basketweave) structure.

6.3 Discussion

The presented pilot studies using the described new apparatus have successfully demonstrated the ability to characterise and control microstructural evolution during small scale open-die forging (*i.e.,* micro-cogging) of Ti-6Al-4V dual-phase alloy, as previously demonstrated on copper C101 [362] alloy (*i.e.,* at lower temperatures). Notably, the studies have proven and assessed the capability of this small-scale set-up to achieve a high degree of α-globularisation. This is exciting, as globularisation kinetics in Ti-6Al-4V remain of high research interest, as seen in the work of Ouyang *et al.* with the experimental and numerical simulation study of lamellar globularisation for titanium TC21 alloy [369], and also seen in the work of Jin *et al.* with additively manufactured Ti-6Al-4V [370]. With the increased throughput of testing that this apparatus can offer, this means research on this topic could be accelerated.

While it must be acknowledged that, a 1:1 scale comparison with industrial ingot-to-billet con-

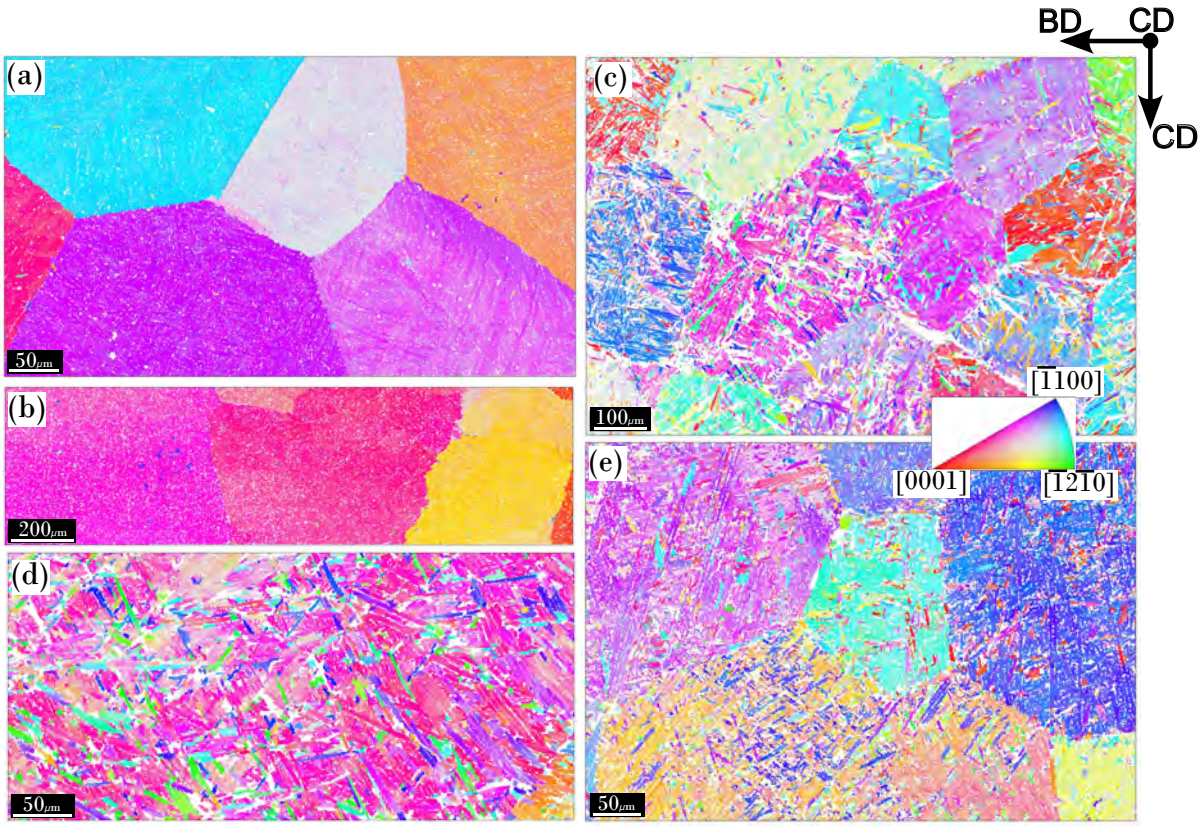

Figure 6.13: Parent β grain reconstruction (PBGR) obtained from EBSD map data of (a) the AHT material, (b) Specimen SP11, (cogged to 13.1% cross-section reduction) above β-transus, (c) Specimen SP5 (cogged to 8.1% cross-section reduction) at 950 °C, (d) Specimen SP6 (cogged to 10.8% cross-section reduction) at 950 °C and, (e) Specimen SP9 (7.3% cross-section reduction) to a octagonal geometry at 950 °C. IPF-CD (out-of-page) key is the same for all maps.

version, is impossible to replicate at this scale, *i.e.,* due to the industrial billet grains being centimetres in scale [371], the developed apparatus and methodology can still provide a useful tool for the simulation and testing of industrial scale processing parameters and measuring their impact on the existing material and structures. Specifically, the apparatus is capable of replicating the conditions and microstructural evolution during the later stages of ingot-to-billet conversion when some degree of microstructure refinement has already been achieved, *e.g.,* multi-directional forging of Ti-6Al-4V by Zhang *et al.* [372]. Furthermore, the comparative simplicity and low-cost of the equipment, assuming existing access to suitable load frame/press and furnace, the methodology and tooling can be upscaled and modified for studying larger test specimens with coarser microstructures. Overall, the parameters that can be assessed with this equipment offer attractive benefits to industrial ingot-to-billet manufacturers as they can save largely on cost, material, labour, and time.

This method can also offer researchers an avenue for metallurgical processing studies. To date, especially in Ti-6Al-4V, ingot-to-billet conversion has been limited due to the large costs involved in producing specimens for characterisation and study. The high degree of control under isothermal conditions on offer with this method is significant, as it is distinctly relevant to the high thermal mass ingots found in industrial ingot-to-billet conversion. The relatively slow cross-head displacement of 0.12 mm/s, with the aim for a low nominal strain rate of 0.01s^{-1} ($\dot{\varepsilon_m}$) used in this study is also representative of industrial ingot-to-billet conversion , as low strain rates are typical due to the large size of the ingots. Typically, higher strain rates are only observed in closed-die operations. However, strain rate is not a limitation of the equipment or method. Higher bites per minute, and strain rates can be explored in future studies with the employment of the apparatus with various load cells, similar to the study by Niu *et al.* [371] where the $0.01\,\text{s}^{-1}$ is used but also varied up $1\,\text{s}^{-1}$.

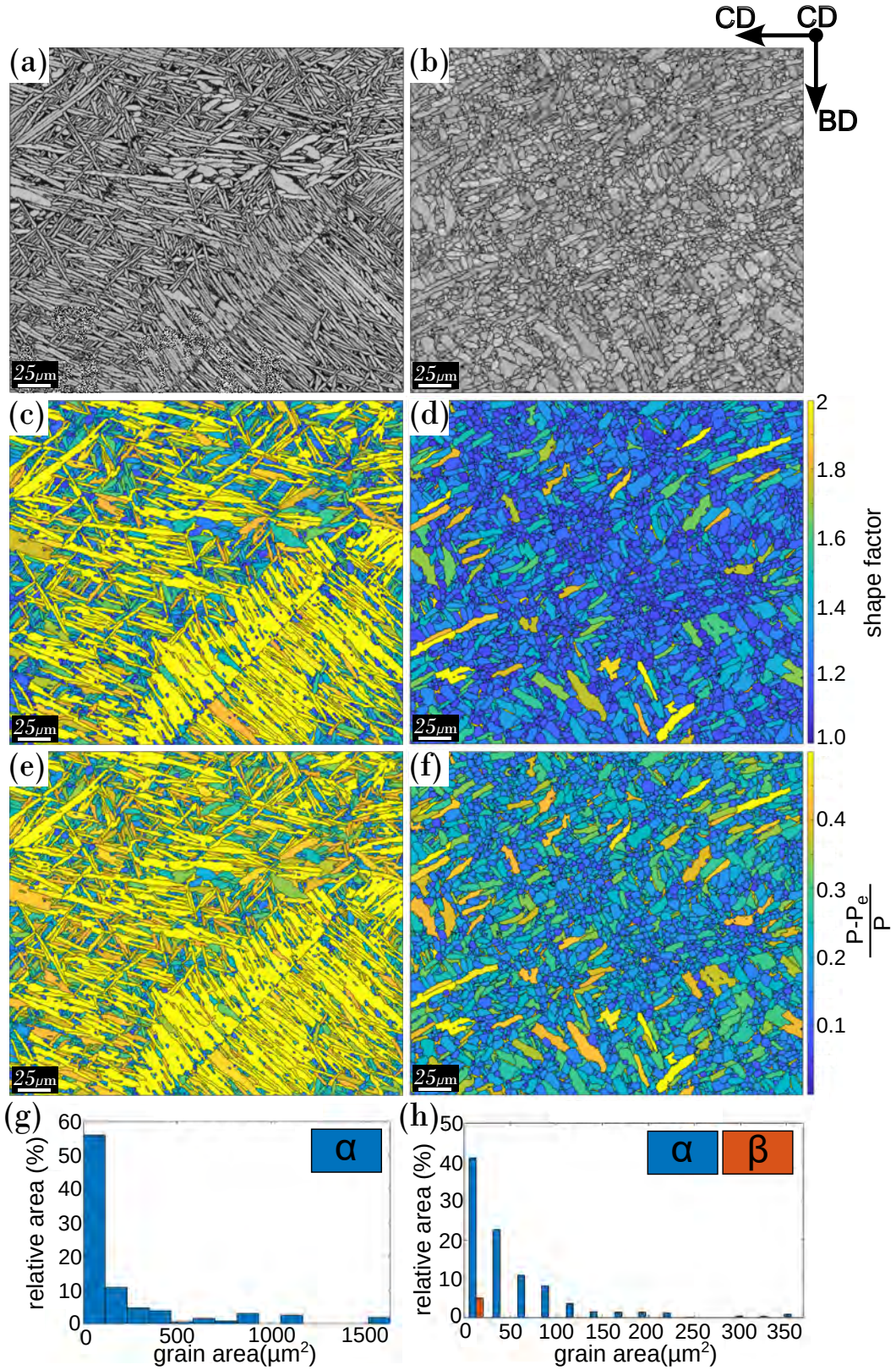

Figure 6.14: Processed EBSD data output from cogged zones of: **LEFT** Specimen SP2 (2.3% cross-section reduction) in comparison with **RIGHT** Specimen SP7 (12.2% cross-section reduction) , (a) - (b) band contrast images with grain boundaries, (c) - (d) shape factor plots, (e) - (f) plots of the relative difference between the perimeter and equivalent perimeter and, (g) - (h) plots of grain size distributions. Calculated and visualised using the MTEX Toolbox in MATLAB®.

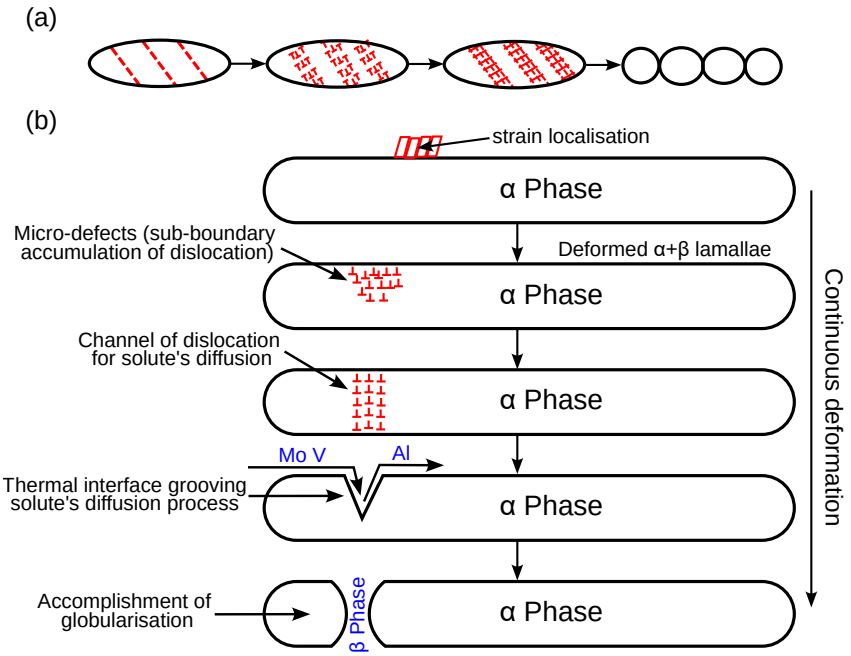

Figure 6.15: (a) Shearing mechanism of globularisation [373], and (b) unified globularisation mechanism by coupling multiple factors. Adapted from Zhang *et al.* [366].

The influence of prior-β processing on the evolution of microstructure during $\alpha + \beta$ forging was examined by Lahiri *et al.* [374] Air cooling the heat-treated β phase resulted in lamellar structures with a homogeneous morphology and distribution of crystallographic orientations. However, deformation above the β-transus temperature led to the formation of elongated β grains, which affected the nucleation and growth of the α-phase during cooling [374, 375]. Consequently, this alteration modified the morphology and orientation distribution of the lamellae and had an impact on the globularisation process. The presence of shorter and non-randomly oriented lamellae within the deformed prior-β grains led to higher rates of spheroidisation. Additionally, the direction of $\alpha + \beta$ forging in relation to β upsetting was found to be significant, as seen evidenced in Zhao *et al.*'s work [375]. It was observed in Zhao *et al.*'s work that higher rates of globularisation were achieved when two perpendicular directions were applied. This method could be applied to examine these phenomena closely at comparatively low cost.

Dyja *et al.* [376] studied the optimal angles of tilt in cogging through FEM and a series of upsetting and cogging trials. Another strength of this new set-up is that it could be directly applied to validating and optimising compression angles such as these. This inclusion of micro-upsetting with the apparatus, alongside micro-cogging, could be a major benefit of the apparatus that can lead to an overall increase in future material and open-die forging schedule optimisation studies. Similarly, in Zhang *et al.*'s [372] work a similar style of 60% upsetting between 90° rotations was employed for the multi-directional isothermal forging, the new set-up method will allow for the geometry of the forged components to be more akin to those in industrial ingot-to-billet conversion.

During cogging processes, it is often necessary to conduct reheating steps to maintain the desired temperature distribution throughout the specimen. In the studies reviewed, short reheating times were used due to the small size of the specimens. For instance, Ari-Gur and Semiatin [377] and Kim *et al.* [293] used annealing times of 3 minutes and 10 minutes respectively between forging steps. Although these short annealing times had minimal impact on the microstructure, a slight grain coarsening was observed after multiple deformation and reheating cycles [293]. However, in industrial cogging operations, the reheating time for a bar is significantly longer, often lasting several hours. This prolonged reheating period has the potential to induce microstructural changes that can influence subsequent process steps. Nevertheless, these potential effects have not been thoroughly investigated. Cooling rates from above the β-transus also has an overall effect on the

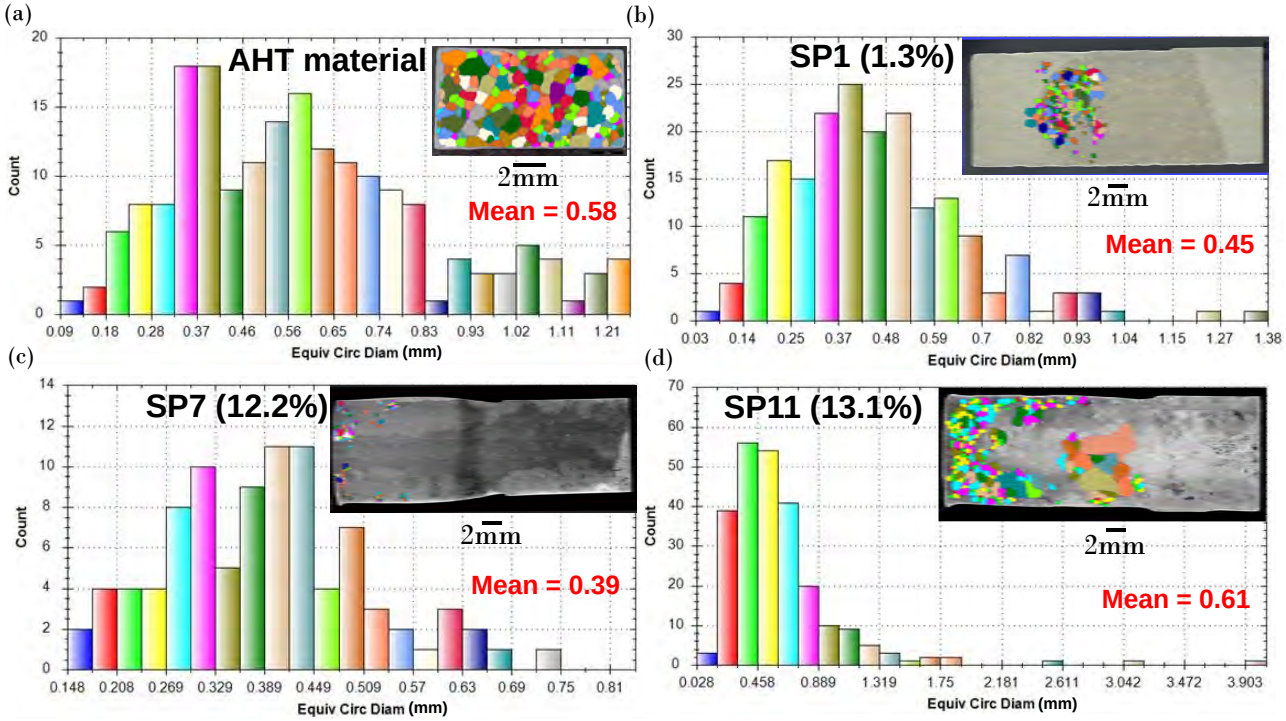

Figure 6.16: Collection of histograms with fixed bin width presenting grain count against equivalent circular diameter, captured from a representative area/cogged zone of: (a) AHT material, (b) Specimen SP1 (1.3%), (c) Specimen SP7 (12.2%), and (d) Specimen SP11.

level of globularisation that can be achieved after $\alpha + \beta$ processing. Due to the isothermal nature of the present study, the reheating of the component was not a significant point of study but could play a role in future work with the apparatus.

One outcome from this work is the small-scale reproducibility and inexpensive set-up that could be easily standardised and used in materials testing labs across the globe to accelerate data capture and understanding of materials evolution. This study has aimed to prove the applicability of this new method at a higher temperature ensuring value for materials of commercial interest. Design iteration for improvement of this method could yield highly beneficial rewards for materials engineers due to the higher rate and lower cost of materials and energy that constitutes testing of a batch of materials.

β-processing cogging is an important stage of the thermomechanical processing of Ti-6Al-4V. More specifically, reducing the β grain size from the coarse as-cast structure is a critical process requirement. Figure 6.16 presents fixed bin width histograms from an example dataset (*i.e.,* AHT, SP1, SP7, and SP11) of how the presented set-up can be used to study the control and measurement of β grain size reduction. It can be observed from Figure 6.16, that the mean β grain equivalent circular diameter is reduced from 0.58 mm in the AHT material to 0.45 mm and 0.39 mm in Specimens SP1 and SP7 respectively. The mean β grain equivalent circular diameter in Specimen SP11, presented in Figure 6.16(d) was increased to 0.61 mm, this was influenced by the large Widmanstätten grain structure in the centre of the specimen, due to temperature and time allowing for diffusion.

Another advantage that small-scale open-die forging can offer is the ability to target study specific microstructural phenomena. As an example, this study showed that the cogging of small samples using the described new apparatus, with increments of 5% deformation was successful in inducing globularisation in Ti-6Al-4V material with lamellar initial microstructure. The specimens displayed an increasing level of microstructural transformation with deformation increments. Mechanisms of globularisation at high temperature involve the formation of α/α boundaries within the laths due to localised shear and buckling, and continuous dynamic recrystallisation followed by the penetration of beta phase along these α/α boundaries ultimately leading to fragmentation of α laths into smaller globular grains [282, 300, 378–381]. In agreement with these mechanisms, progressive

breaking up of α laths into smaller grains was observed with increasing deformation (Figure 6.11).

Investigations on the modelling of globularisation has received significant attention. Some studies developed an empirical model based on Avrami's equation [382, 383] due to their simplicity and low computational demand. Others used physically based models actually capturing the microstructural mechanisms responsible for evolution in microstructure, this can be seen in the works of Sun *et al.* [384], Babu *et al.* [385], and Gao *et al.* [386]. An in-house model was developed based on the dislocation density model from Sun *et al.* [384], presented in equations 6.2 to 6.5. The dislocation rate takes into consideration work hardening, dynamic recovery, static recovery, and dynamic globularisation; and these mechanisms are represented by the four terms in equations 6.2 to 6.5 respectively. Globularisation occurs only when the dislocation density is higher than a critical value dependent on process parameters. The globularisation rate is dependent on the dislocation density, temperature, grain size, and a parameter γ that varies with dislocation density and level of globularisation. This model was calibrated using large-scale multi-axial forging experiments on Ti-6Al-4V from Fabris [387].

It was then implemented as a user subroutine into Finite Element software DEFORM™ and executed alongside the process modelling simulations. Predictions from this model for the experimental conditions in this work are presented in Figure 6.17. The predicted values are in line with the experimental levels of globularisation. *N.B.* The first two experimental data points are $> 0\%$ globularisation due to the measurement method, where α-laths orientated in the out-of-page image plane result in a grain aspect ratio of < 2, meaning the true % globularisation is closer in correlation with the model results for < 0.3 effective strain.

The discrepancies in results between the model prediction and experimental measurements can be due to model calibration and any differences in strain distribution between these two scales, *i.e.,* variations due non-isothermal and isothermal conditions (*e.g.,* tooling rigidity, different losses of heat and internal tooling strain, *etc.*). However, the correlation indicates that microstructural trends observed at small-scale (from experimentation) in this work are similar to those experienced at larger scale (from modelling), and that the described apparatus can help accelerate research thanks to its increased throughput of testing, and lower material requirement. Additionally, it proves the new apparatus presented in this work may be used for calibration of future material models, where the user can capitalise on the advantages of scaled down experimentation.

$$\dot{\rho} = k_1\sqrt{\rho}\dot{\varepsilon} - k_2\rho\dot{\varepsilon}^m exp\left(\frac{-Q_s}{RT}\right) - k_3\rho^n exp\left(\frac{-Q_s}{RT}\right) - \frac{k_4\rho\dot{S}}{(1-S)} \tag{6.2}$$

$$\dot{S} = \frac{\beta_1\gamma\rho exp\left(\frac{-Q_b}{RT}\right)}{d} \tag{6.3}$$

$$\rho_{cr} = \beta_2\left[\dot{\varepsilon}exp\left(\frac{Q_z}{RT}\right)\right]^{\lambda_1} \tag{6.4}$$

$$\gamma = (0.1+S)^q(1-S)\frac{\rho}{\rho_{cr}} \tag{6.5}$$

Table 6.2: Geometric material constants for the dislocation density model.

K_1	K_2	K_3	K_4	Q_s	Q_z	Q_b	m	n	β_1	β_2	λ_1	q
4.1×10^8	410	0.1	0.01	27,500	150,000	150,000	0.833	1	0.324	4.5×10^{13}	0.0398	1.168

The parameters of this globularisation model were determined from experimental data [387] using a genetic algorithm optimisation approach in Microsoft Excel and are presented in Table 6.2.

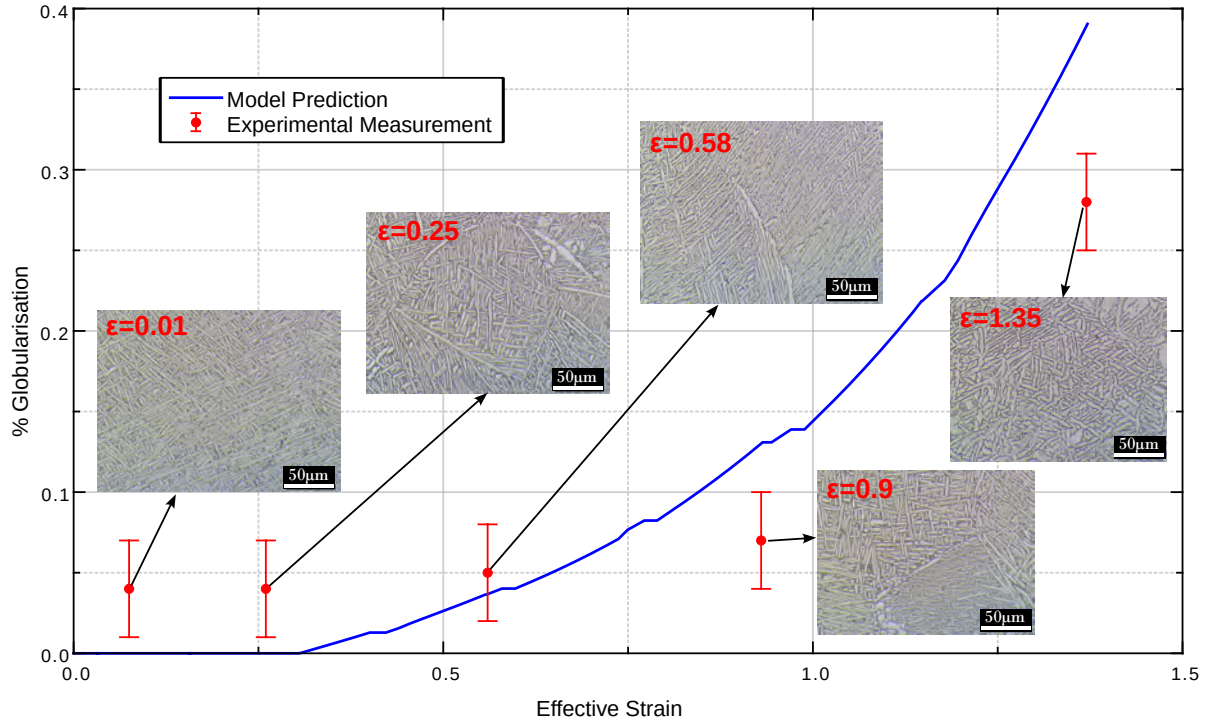

Figure 6.17: Predicted and experimental globularised fractions for Specimens SP1 to SP7.

The experimental data used for calibration is from multiaxial forging trials on large samples, so the prediction should be more accurate for trials similar to an industrial cogging process scale.

ρ is the dislocation density (m^{-2}), Q_s, Q_b, Q_s are activation energies (J/mol/K), ρ_{cr} is the critical dislocation density (m^{-2}), S is the globularised fraction, γ is the mobile fraction of grain boundaries, R is the ideal gas constant (8.314 J/mol), k_1, k_2, k_3, k_4, n, m, p, q, β_1, β_2, and λ_1 are constants.

Globularisation kinetics are known to be dependent on the processing route and strain path [294, 297, 388]; and slower kinetics were observed during multi-axial forging compared to uniaxial compression trials [301, 389]. However, the mechanisms of microstructural evolution related to the strain path during cogging are not well understood. The described new apparatus was successfully used to introduce some level of globularisation (28%) in a small-scale Ti-6Al-4V sample via a cogging schedule; and it can be utilised to further explore the effect of process parameters such as strain increment and angle between deformation directions, on globularisation.

Macrozones in $\alpha + \beta$ titanium are millimetre long clusters of α grains with close to the same or the same crystallographic orientation [390]. These macrozones are known to have a negative effect on the fatigue performance of the alloy. What remains unknown with these features is how to sufficiently break them down at an industrial scale, owing to the large primary β grain size. Huang *et al.*'s work [321] investigated the formation and evolution of macrozones in Ti-6242S alloy during TMP and found that the formation of macrozones is related to the evolution of primary α (*i.e.*, α_p) and β grains. The new set-up presented in this work would allow for further understanding of macrozone evolution using less material. However, with the novelty of the set-up, some design challenges remain for high temperature testing (*i.e.*, $\geq$950 °C). One should be mindful of these experimental nuances and resolving them would greatly enhance the reliability and repeatability of the tests.

Firstly, the isothermal conditions and repeat passes progressively remove lubricant from the sample during the experiments. This increases the risk and likelihood that the test-specimen will stick to the dies for longer test runs that require larger numbers of bites. This problem is exacerbated when the starting mini-billet geometry is rectilinear rather than cylindrical. Possible solutions could

include a high-temperature lubricant delivery system or the use of highly sintered ceramic dies.

Another consideration would be the "flying-blind" nature of the current method at higher forging temperatures (600 °C) using split tube furnaces. Lower temperature tests on copper and aluminium alloys used an environmental chamber, which had an observation window that facilitated convenient monitoring of the specimen position and its in-situ adjustment. An improved set up could feature a high-temperature viewport or fibre-optic imaging of the specimen position.

Tribology is another consideration, for tool operating life is crucial in bulk metal forming which can be affected by many factors in the system including the machine, tool, and workpiece [391]. Hot forging dies are subjected to a range of cyclic thermal, mechanical, chemical, and tribological loads. Various parameters during hot forging including the friction and lubrication conditions can influence the final billet geometry and microstructure. For these tests a combination of a glass coating and boron nitride lubricant was used, which due to the isothermal conditions was found to have an increased sticking effect as the number of bites increased. It was found as part of a following study with square starting cross-sections that both a higher cross-section reduction in a single bite, as well as the increased surface area influenced this sticking factor. Short checks had to be introduced to ensure that the specimens were free from die sticking before rotation.

This study provides positive evidence that the presented laboratory equipment can be used to study open die forging/cogging of commercial alloys which are of high research interest. The desired capability of hot forging of titanium alloys informed the experiment design decisions: the load frame capacity, specimen size with respect to available furnace volume, and the choice and geometry of the tooling materials. Overall, this study has acted as a reinforcement that miniaturised cogging can be used to inform upstream to more costly intermediate and larger research scale testing and help provide data for development of microstructure-sensitive CPFE models, which could be used to advance digital-twin development for the next generation of data-driven metallurgical manufacturing.

6.4 Summary

This study has investigated the capability of a new laboratory-scale apparatus in the open-die forging of Ti-6Al-4V alloy below and above β-transus used in ingot-to-billet conversion of material for high-value component manufacturing. The following conclusions can be obtained:

1. Various levels of microstructural evolution stages of Ti-6Al-4V were successfully captured through precise apparatus control and analysed through various characterisation techniques.

2. Validation of experimental data was performed through FE modelling, demonstrating apparatus capability for data generation in future advanced digital-twin development.

3. Globularisation of α in Ti-6Al-4V was achieved through small scale multi-directional open-die forging, *i.e.,* micro-cogging, with newly designed apparatus.

4. Experimental microstrucutral data was applied and validated through α globularisation model based upon dislocation density models.

5. Increased temperature capability of the apparatus successfully validated.

As this was the commercial material proof of concept study, it was highly successful in showing the capability of the novel design. It has showed that it can withstand multiple high temperature tests and that the experimental open-die forging (*i.e.,* cogging) testing of superalloys is within reach after some tooling improvements.

Chapter 7 presents the conclusions of this research work. From the initial design work and method development, to the different proof of concept material studies presented throughout Chapters 5 and 6. In addition, it highlights the many future opportunities that this work has opened.

7 Conclusions
and Recommendations for Further Work

This work has designed and manufactured an original experimental method for laboratory material compression testing, based upon the miniaturisation of the large industrial grain refinement open-die forging method known as cogging. The new experimental methods capabilities were then assessed through proof of concept testing of single- and dual-phase alloys at a range of temperatures and strain levels. A series of microstructure characterisation methods and simulations were employed to record and analyse the success of the method in achieving varying levels of microstructural evolution and grain refinement. First, the conclusions from this body of work are presented; then, a collection of avenues for potential design improvements and further work is discussed.

7.1 Conclusions

The following conclusions can be drawn from this PhD thesis.

A large quantity of literature is available on the technology and mechanisms that occur during the processing routes of advanced engineering alloys. The background and advancements of triple melting procedures to purify the metal, heat treatments, and different further processing stages are all important to understand the history of each component being manufactured, to ensure the material properties will be fit for purpose. Equally, it is critical to recognise the significance of the mechanics and kinetics undergone by the material during processing, from the macro to micro scales. Literature surrounding experimental cogging, or experimental open-die forging, to date has been limited by factors such as quantity, and cost of material required for studies on large multi-tonne presses. This has lead to most cogging studies being completed through improvements to modelling and simulation, however, not all situations can be evaluated using simulation alone. Ultimately, requiring a need for an experimental validation technique to be linked to informed models in the future.

This study has generated a novel experimental laboratory technique for exploring the parameters and mechanisms surrounding ingot-to-billet conversion in high-value engineering components manufacture. It has successfully demonstrated that a comparatively inexpensive apparatus can be constructed using readily available mechatronics components with a very limited number of custom-made high temperature parts, and used for this purpose with a conventional uni-axial load frame typically available in most materials testing laboratories. Furnaces mounted on the load frame were used to achieve isothermal conditions for both the workpiece specimens and tooling, which compensated for their small thermal masses compared to that of industry-manufactured billets. Design considerations and decisions made early in the conceptualisation of the physical apparatus, as well as the software design, were made with a focus on safety, environment, performance (control and accuracy), and size constraints (furnace limitations), see *Appendix C*.

The first high-temperature cogging trials carried out on C101 copper alloy have been used to develop the foundation for a testing methodology and have shown the ability of the approach to achieve significant grain refinement via recrystallisation and recovery. An average grain size reduction, refinement from $\sim 25\,\mathrm{mm}^2$ down to $\sim 5000\,\mu\mathrm{m}^2$, has been demonstrated in a specimen deformed to 46.5% of its original cross sectional area. In conjunction with modern characterisation techniques, the proposed apparatus and methodology could provide a cost-effective way of investigating the phenomenology of microstructural evolution during complex multi-step forging processes, such as cogging and upsetting operations during ingot-to-billet conversion. Microhardness measurements revealed a noticeable increase in the Vickers hardness values for the C101 alloy samples that were cold-worked between the stub and the cogged zones, *i.e.,* increase in hardness by a factor of ~ 9.2.

The second cogging trials for investigating the capability of the experimental apparatus were performed using aluminium Al6060 alloy. The apparatus was successful in achieving grain-width reduction in the elongated grains subjected to compression. The highest grain width reduction was

seen in aluminium Al6060 Specimen SP7 by a significant average percentage reduction of 82(±1)%, from the measured average of 1.43 mm in the stub (non-deformed) zone to 0.26 mm in the cogged zone. There is a measureable difference, approximately 60-70%, in the Vickers microhardness between the procured material to the heat-treated/cogged material. However, there was no distinct difference in hardness (*i.e.,* approximately equal increase/decrease, no greater than 3.8%) between the cogged and stub zones of the Al6060 alloy in the cogged specimens.

In terms of validation, the advanced Lab-DCT technique used in this study corroborated EBSD data captured with an SEM. For the future of advanced alloy processing, it is a powerful method for analysis of grain structures, and holds a lot of potential for further study as the technology improves. The easily worked single-phase materials allowed for a great basis of study and allowed for a publication of the equipment design and method [362].

This final proof of concept study carried out at high temperature (950 - 1050 °C) investigated the capability of the laboratory-scale apparatus in the open-die forging/cogging of Ti-6Al-4V alloy in an effort to simulate the ingot-to-billet conversion of a commercial material used for high-value component manufacturing. The following conclusions can be derived from this high temperature proof of concept investigation:

1. The experimental apparatus and testing methodology were successfully applied to forging of a dual-phase aerospace titanium alloy Ti-6Al-4V. Various stages of microstructural evolution in Ti-6Al-4V have been successfully captured through precise control of multi-directional compressive deformation.

2. FE modelling has been used to evaluate the stress-state and plastic strain within the forged specimens, demonstrating apparatus capability for data generation in future advanced digital-twin development. The simulated forgings matched well the 3D geometries and cross-section reductions measured from the test specimens using GOM scans.

3. The small scale multi-directional open die forging (cogging) experiments have demonstrated the ability to achieve globularisation of the α phase in Ti-6Al-4V. Manual analyses and EBSD data processing have shown the degree of globularisation to depend on the overall level of plastic strain sustained by the specimens. This is consistent with existing understanding of the phenomenon and its mechanisms. JMAK type behaviour is evident in the experimental data, but would need further experimental verification.

4. Some correlation has been observed between the evolution of α-globularisation captured from the new experimental technique and an α-globularisation model calibrated from larger-scale forging trials. Further calibration of the model parameters could improve the overall match of the model with the experimental data trend.

5. In contrast to our original pilot study using the miniature cogging apparatus, an increased temperature capability has been successfully validated. There is good potential for applying the described equipment and techniques to the study of materials with even higher temperature capabilities, such as namely superalloys, if some of the outlined limitations are overcome and tooling materials are upgraded.

6. The experimental approach combined with complementary simulations and larger scale experiments could be instrumental in the development of future digital twins for open die forging, which could enable data-driven real-time process optimisation in industry.

7. Microhardness changes revealed a noticeable increase in the Vickers hardness for all samples at the edges that have been exposed to air while forging, *e.g.,* an average increase of 10 to 20% across all samples, due to the formation of oxygen-rich alpha-case. It is evident from the captured Vickers hardness maps and lines that overall there is no signficant changes from the cogging itself.

The new insights gained from miniaturised testing may help inform more costly intermediate-scale testing and provide data for development of new plasticity models, which could be used to develop digital twins for the next-generation of digital metallurgical manufacturing. While the presented pilot investigation has its limitations, notably the extent of applicability to industry-scale, there is ample opportunity for further refinement of the methodology and its use in the identification of possible size-effects, so this investigation aspires to provide a platform for further scientific research and discussion.

7.2 Recommendations for Further Work

7.2.1 Design Considerations

There are a number of design considerations and improvements that can be made to the prototype cogging rig design.

One key fault of designing for compatibility and adjustability for use across different load frame devices is the sacrifice of ease of alignment. Laboratory use of the prototype revealed that the initial alignment can be easily imbalanced. Especially between compression stages, and unloads. As these periods within testing often displaced the manipulator rod through relaxation contact or sticking.

Greater investment in robust components and more focused adaptation of pre-existing equipment fixtures and features, could further improve the efficacy and robustness of the apparatus design. A key recommendation for further exploration to solve this issue would be into designing the rig centred around the most modern extensometer add-ons to the Zwick™ tensile and compression machines. This fixture would allow for permanent ease of alignment in the first stages of experimentation. The design focus would need to surround the compensation in the z-axis, as currently this is accounted for with the flexion present in the manipulator rod. A more sophisticated set-up would be beneficial to be able to calculate and adjust for specimen displacement and the material expansion and relaxation during testing.

Another complication observed in the high temperature testing utilising the prototype rig was the difficulty of lubrication when compressing to higher reduction sizes. As the reduction size or load increased on the material the risk of the material sticking to the platens increased. As well as the direct correlation between the number of compressions and rotations once at temperature. As the number of compressions increased, so did the likelihood of the sample sticking to the platens, as the lubricant was also being incrementally removed.

Designing for portability was one major benefit of this method as it could be used with any load frame system using the current tripod-mounted configuration. However, some load frames provide existing external mounts, allowing for rig mounting to the pre-existing extensiveness fixtures, *e.g.,* mounting arms available on some Zwick/Roell™ load frames, typically used for extensometers. This would allow for more consistent specimen alignment and also reduce the alignment time, allowing a faster specimen turnover. In addition, increasing the holding torque on the sample via the use of more powerful stepper motors (*e.g.,* NEMA23) would further increase the resistance to slippage. The addition of a third motor system would aid to compensate for the vertical displacement of the specimen during compression, rather than relying on deflection of the long manipulator rod to accommodate this displacement. It would also help fine position adjustments.

Another consideration would be to address the "flying-blind" nature of the method at higher forging temperatures (greater than 600 °C) using tube furnaces, *i.e.,* not being able to use environmental chamber viewing windows. A small form factor optical fibre-optic camera solution, or high temperature viewport, could provide an invaluable additional degree of workpiece position control during operation. It would allow the state of the specimen after each bite to be evaluated and adjustments to be made accordingly. Alongside this system, an in-situ lubrication injection system could prove highly beneficial, if not a necessity, when studying greater levels of strain during hot forging at temperatures exceeding 900 °C. Exploration of the use of graphite films may also of be

interest, as this could provide an excellent solution to the issue of tool sticking. As the isothermal conditions and repeat passes remove lubricant from the sample, the risk of sticking increases the longer the test runs. In-situ lubrication is used in many larger scale research and industry to not only ensure die/workpiece separation and lower friction, but also to act as a thermal insulator.

Routine programs can be created alongside the load frame control software (*e.g.,* Zwick™ testXpert III) to fully automate each process. Addition of optically isolated BNC connections was primarily done to automate this process. However was never tested due to external circumstances and early-stage nature of this work. This change could increase positional accuracy, and throughput of testing.

A final consideration is in the design of the coupling tooling. Currently, grub screws are used to hold the sample and manipulator rod in place. This works well for the manipulator rod. However, as specimens need to be repeatedly inserted and removed from this coupling, this design may not be optimal for high temperature applications due to the reduced longevity of the grub screws. The thermal expansion and oxidation that may occur, can lead to seizure of the workpiece inside the barrel of the specimen holder. Inclusion of a capped pin/pin system, or lock-and-key design, could eliminate this issue, at the expense of more complex sample and holder machining that would be required.

7.2.2 Future Studies

It is crucial at this stage to emphasise the many new potential research avenues that the success of this research has opened. It is clear through both the design work, the proof of concept studies, and through the publications already made using the key design output [302, 362], that this new method can be utilised for numerous material studies in the future. As a new experimental method, it is just the beginning of where it could potentially lead for metallurgists and industry alike as there are hundreds of alloys that could potentially be studied, investigating parameters such as strain, strain rate, temperature *etc.* Even as the apparatus is iteratively improved and the method honed to remove uncertainties and generally standardise the components, it could grow to have many copies of the same apparatus for studying open-die forging processes across the country and worldwide. It could also be a starting point for new alloys being developed, for a cost-effective method for exploring processing before commiting to larger scale study and development.

Furthermore, beyond the scope of materials studies it can be further used to experiment with varying the die geometry in conjunction with varying strain rates, which may not be representative of the early ingot-to-billet cogging stage, however can allow for the apparatus to provide insights into parameters of other forging techniques. The exploitation of the extensometer slot for other similar forging techniques could also be explored in the future, *e.g.,* is it possible to incorporate upsetting steps between the cogging bites, as part of the design?

Collaboration and significant investment in the future of the apparatus has been secured by the Advanced Forming Research Centre from the Tier 1 partner, Aubert and Duval, with other industrial partners beginning to take an interest. As part of this investment, a CORE work package was created for the assessment of the Micro Future Forge's capability for miniaturised superalloy cogging. This will involve design upgrades to the environmental chamber/furnace to reach even higher temperatures with stable control, upgrades to tooling to improve the die-life, with considerations for the inclusion of cooling and lubrication injection. The aim is to use the upgraded "Micro Future Forge 2.0" to carry out experiments on at least one polycrystalline superalloy, characterise the microstructure of the specimens, and assess the performance of the upgraded rig. Another target is to perform a second cogging trial using strain rates and strokes per minute that closely match industrial conditions, and reassess the microstructure characterisation and the performance of the apparatus.

Further to the aforementioned work package, that is currently underway, additional studies may take the form of future PhD projects in the case of further scope improvements to furnace

integration, or standardisation in the lab. Equally, these may take the form of a standalone work package in the research centre for staff to undertake.

Microstructure modelling evolution is of great technical significance to the microstructure tailoring and optimisation of TMP. Therefore, more in-depth simulation studies should also be considered, where the relation of parameter effects between the industrial scale and the laboratory scale can be further explored. A more direct link and understanding between the two scales would allow for the new experimental method to be catapulted forward into the forefront of the future of materials processing and testing due to the many advantages that it brings over larger scale testing. *I.e,* it is faster, more cost-effective, uses less material, is more enviromentally friendly by using less power, can make use of off-cuts/waste from larger ingots, requires less operators in the lab, so overall less labour cost than operating larger furnaces and forges.

There are a great number of possibilities for the future success of the miniaturised cogging equipment, and the research paths that could continue to be opened up and scoped for further development. This work has been the first, of what is hoped to be many doctorate and general research studies, underpinning the large investment made at the Advanced Forming Research Centre and the National Manufacturing Institute of Scotland's new FutureForge. The development of this device, and the FutureForge, are both a step in the right direction with the industry wide push for a more informed and data-centred approach to manufacturing.

Overall, the studies included in this work aim to set a foundation for many future studies using the methodology and equipment designed and discussed herein. The platform that has been set can allow for a variety of miniaturised forging studies across materials testing laboratories that have an interest in studying the parameters and mechanisms seldom examined in open-die forging processes. Used in conjuction with upsetting processes, characterisation techniques, and simulation studies, the presented methodology aims to help contribute to the development of next generation metallurgical digital twins for manufacture of advanced alloys.

Bibliography

[1] Roger C. (Roger Charles) Reed. *The superalloys : fundamentals and applications*. Cambridge University Press, Cambridge, 2006.

[2] Robert E. Schafrik and S. Walston. Challenges for high temperature materials in the new millennium. *Superalloys*, pages 3–9, 2008.

[3] S.R. Hegde, R.M. Kearsey, and J.C. Beddoes. Designing homogenization–solution heat treatments for single crystal superalloys. *Materials Science and Engineering: A*, 527(21):5528–5538, 2010.

[4] Bei jiang Zhang, Guang pu Zhao, Wenyun Zhang, Shuo Huang, and Shifu Chen. Investigation of high performance disc alloy gh4065 and associated advanced processing techniques. *Acta Metallurgica Sinica*, 51:1227–1234, 2015.

[5] James C Williams and Edgar A Starke. Progress in structural materials for aerospace systems11the golden jubilee issue—selected topics in materials science and engineering: Past, present and future, edited by s. suresh. *Acta Materialia*, 51(19):5775–5799, 2003. The Golden Jubilee Issue. Selected topics in Materials Science and Engineering: Past, Present and Future.

[6] Srinivasan Chandrashekar, Rajaram Nagappa, Lalitha Sundaresan, and N.Ramani. Technology & innovation in china - a case study of single crystal superalloy development for aircraft turbine blades. Technical report, National Institute of Advanced Studies, 11 2011.

[7] R. F. Decker. The evolution of wrought age-hardenable superalloys. *JOM*, 58(9):32–36, 2006.

[8] Marcos Pérez, Christian Dumont, Olivier Nodin, and Sebastien Nouveau. Impact of forging direction on the recrystallization behaviour of nickel base superalloy AD730 billet material at subsolvus temperatures. *Materials Characterization*, 146:169–181, 2018.

[9] Alok Choudhury. State of the art of superalloy production for aerospace and other application using vim/var or vim/esr. *ISIJ International*, 32(5):563–574, 1992.

[10] Matthew Donachie and Stephen Donachie. *Superalloys: A Technical Guide, 2nd Edition*. ASM Technical Books, 01 2002.

[11] Ramesh Singh. 1 - introduction. In Ramesh Singh, editor, *Applied Welding Engineering (Third Edition)*, pages 3–5. Butterworth-Heinemann, third edition edition, 2020.

[12] A. H. W. Ngan and R. E. Smallman. *Physical Metallurgy and Advanced Materials Engineering*. Elsevier Ltd., 2007.

[13] G.E. Dieter. *Mechanical Metallurgy*. Createspace Independent Pub, 2014, 1961.

[14] Harald Scholz, Ulrich Biebricher, and Henrik Franz. STATE OF THE ART IN VAR AND ESR PROCESSES A COMPARISON. In , 2014.

[15] Jeanette M. Moyer, Laurence A. Jackman, Charles B. Adasczik, R. M. Davis, R. Forbes-Jones, Teledyne Allvac, and Oviya P. ADVANCES IN TRIPLE MELTING. In , 1998.

[16] Rui Tang, Dong Zhe Wang, Yan Mo, Qu Bo He, An Zhong Zhao, Deng Hua Chen, and Hai Ding Liu. Effect of triple smelting process on the purity and microstructure of 9cr18mo bearing steel. *Materials Science Forum*, 914:132–139, 2018.

[17] Nandagopal M, Parameswaran P, Vijayanand V. D, Laha K, and Mathew M. D. Influence of steel melting processes on tensile properties of 14cr-15ni-ti stainless steel. *High temperature materials and processes*, 30(3):229–232, 2011.

[18] Aaron Teske. High-tech melting processes improve aerospace materials. *Industrial Heating*, 80(11):45–49, November 2012.

[19] Qu Bo He, Dong Zhe Wang, An Zhong Zhao, Rui Tang, Hai Ding Liu, Deng Hua Chen, and Yan Mo. Effect of triple smelting process on the purity and microstructure of 9cr18mo bearing steel. In *Functional Materials Technology and Industry Forum IX*, volume 914 of *Materials Science Forum*, pages 132–139. Trans Tech Publications Ltd, 3 2018.

[20] R. T. Holt and W. Wallace. Impurities and trace elements in nickel-base superalloys. *International Metals Reviews*, 21(1):1–24, 1976.

[21] A. K. Jena and M. C. Chaturvedi. The role of alloying elements in the design of nickel-base superalloys. *Journal of Materials Science*, 19(10):3121–3139, 1984.

[22] G. Lutjering and J. G. Williams. *Titanium*. Springer-Verlag, Berlin, Heidelberg, 2003.

[23] Niraj Nayan, Govind, K. Suseelan Nair, M.C Mittal, and K.N Sudhakaran. Studies on al–cu–li–mg–ag–zr alloy processed through vacuum induction melting (vim) technique. *Materials science and engineering*, 454:500–507, 2007.

[24] Guoxing Qiu, Dongping Zhan, Changsheng Li, Min Qi, Zhouhua Jiang, and Huishu Zhang. Development of a micro-scale y–zr–o oxide-dispersion-strengthened steel fabricated via vacuum induction melting and electro-slag remelting. *Nuclear engineering and technology*, 51(6):1589–1595, 2019.

[25] Hubert Matysiak, Malgorzata Zagorska, Joel Andersson, Alicja Balkowiec, Rafal Cygan, Marcin Rasinski, Marcin Pisarek, Mariusz Andrzejczuk, Krzysztof Kubiak, and Krzysztof J. Kurzydlowski. Microstructure of haynes® 282® superalloy after vacuum induction melting and investment casting of thin-walled components. *Materials*, 6(11):5016–5037, 2013.

[26] Y.J Duan, B Chen, Y.C Ma, and K Liu. Kinetics of al evaporation from liquid u-al alloys in vacuum induction melting. *Journal of materials science and technology*, 31(4):423–426, 2015.

[27] P. G Min and V. E Vadeev. Vacuum induction furnace melting technology for high-temperature composite material based on nb–si system. *Metallurgist (New York)*, 63(7-8):878–884, 2019.

[28] James Mathew. X-ray computed tomography studies on porosity distribution in vacuum induction cast al-7si alloys. *JOM: The Journal of The Minerals, Metals and Materials Society (TMS)*, 73(12):3866–3873, December 2021.

[29] Erin T. McDevitt. Vacuum induction melting and vacuum arc remelting of co-al-w-x gamma-prime superalloys. *MATEC Web of Conferences*, 14:2001, 2014.

[30] Yu Feng. Vacuum induction melting furnace observation window, 2020.

[31] Chen Wei, Liu Guanwei, Song Jiubao, Zhu Qibin, Lin Liqun, Zhang Qiuming, Zhu Ming, Fu Guobao, Yang Hongxing, Lu Bingsen, Xiong Wuwen, Wang Huanyu, Jiang Shengyun, and Huang Huiqing. Novel vacuum induction melting furnace, 2019.

[32] K. O. Yu and J. A. Domingue. Control of solidification structure in var and esr processed alloy 718 ingots. *Superalloys*, pages 33–48, 1989.

[33] David C Drennen, Curtis Maitland Jackson, and Herbert Julius Wagner. *The development of melting and casting procedures for nitinol nickel-base alloys*, volume 69. Battelle Memorial Institute, 1968.

[34] Delin Li. Comparing pipeline steel melted in vacuum and air induction furnaces. *Modern Casting*, 110(8):31–36, August 2020.

[35] K Kamyshnykova and J Lapin. Vacuum induction melting and solidification of tial-based alloy in graphite crucibles. *Vacuum*, 154:218–226, 2018.

[36] Yi Tan, Shiqiang Ren, Shuang Shi, Shutao Wen, Dachuan Jiang, Wei Dong, Ming Ji, and Shihai Sun. Removal of aluminum and calcium in multicrystalline silicon by vacuum induction melting and directional solidification. *Vacuum*, 99:272–276, 2014.

[37] Kun Qian, Bo Chen, Long Zhang, Zhanhui Du, and Kui Liu. Kinetics study of nitrogen removal from liquid in718 alloy during vacuum induction melting. *Vacuum*, 179:109521, 2020.

[38] Unknown Author. Vacuum induction melting (vim). *Edwards Vacuum Company*, 2020.

[39] S. Viswanathan. Vacuum Induction Melting. In *Casting*. ASM International, 12 2008.

[40] Simbarashe Fashu, Mykhaylo Lototskyy, Moegamat Davids, Lydia Pickering, Vladimir Linkov, Sun Tai, Tang Renheng, Xiao Fangming, Pavel Fursikov, and Boris Tarasov. A review on crucibles for induction melting of titanium alloys. *Materials and Design*, 186:108295, 10 2019.

[41] ES Machlin. Kinetics of vacuum induction refining-theory. *Transactions of the American Institute of Mining and Metallurgical Engineers*, 218(2):314–326, 1960.

[42] Jafar Safarian and Merete Tangstad. Vacuum refining of molten silicon. *Metallurgical and Materials Transactions B*, 43(6):1427–1445, 2012.

[43] Jafar Safarian and Merete Tangstad. Kinetics and mechanism of phosphorus removal from silicon in vacuum induction refining. *High Temperature Materials and Processes*, 31(1):73 – 81, 2012. Cited by: 23.

[44] ZHOU HONGQIANG, WANG KAIMING, and ZHAO GUANGZHOU. Horizontal vacuum induction melting furnace, 2020.

[45] Chen Xiaodong and Sun Baoyu. Double-crucible vacuum melting rapid-settling equipment, 2015.

[46] Shen Yaohui and Zhang Yipeng. Four-chamber horizontal continuous vacuum induction melting and casting furnace, 2018.

[47] Zheng Zhi, Liu Enze, Ning Likui, and Tong Jian. Horizontal centrifugal cast tube of vacuum induction machine, 2016.

[48] Min Wang. Formation mechanism of microstructural non-uniformity in the hot working of commercial-scale electro-slag remelted alloy 690 ingots. *Metallurgical andMaterials Transactions. Part A*, 51(8):3996–4008, August 2020.

[49] Louis W Lherbier and GK Bhat. *Proceedings of the 1986 Vacuum Metallurgy Conference on Speciality Metals Melting and Processing: Pittsburgh, Pennsylvania, June 9-11, 1986*. Iron & Steel Society, 1987.

[50] Armin Paar, Reinhold Schneider, Peter Zeller, Gerhard Reiter, Stefan Paul, and Paul Würzinger. Effect of electrical parameters on type and content of non-metallic inclusions after electro-slag-remelting. *steel research international*, 85(4):570–578, 2014.

[51] R. A. Wood. Status of electroslag processing for production of large rotor forgings. final report. Technical report, Battelle Columbus Laboratories, 1978.

[52] SI Kuchuk-Yatsenko, Yu V Shvets, Ea Dumchev, Vi Shvets, Ya I Mikitin, Sd Taranenko, and NN Nikitina. Flash-butt welding of railway frogs with rail ends using an intermediate insert. *The Paton Welding J*, 1:2–4, 2005.

[53] R Schumann, U Biebricher, and H Scholz. Features-inert gas esr produces clean, homogeneous large forging ingots-enclosing the esr furnace eliminates unwanted atmosphere/melt/slag reactions, producing cleaner ingots having tighter. *Industrial Heating*, 68(4):39–44, 2001.

[54] Rafael A Mesquita. *Tool steels: Properties and performance*. CRC press, 2016.

[55] Rafael Agnelli Mesquita and Reinhold SE Schneider. Tool steel quality and surface finishing of plastic molds. *Exacta*, 8(3):307–318, 2010.

[56] Walter Eric Duckworth and Geoffrey Hoyle. Electroslag refining. *Chapman and Hall, London. 1969, 178 P*, 1969.

[57] Geoffrey Hoyle. Electroslag processes: principles and practice. *Applied Science Publishers, xiv+ 215, 22 x 14, illustrated(pounds sterling 25. 00)*, 1982.

[58] W Holzgruber and E Plockinger. Electroslag remelting, a new process for improving the quality of high-grade steels. *Berg Huttenmann Monatsh Montan Hochsch Leoben*, 113(3):83–93, 1968.

[59] W Holzgruber and E Plockinger. Metallurgical and technological foundations of electroslag re-melting of steel. *Stahl Eisen*, 88(12):638–648, 1968.

[60] F Ayman, A Azza, EF Hoda, and E Mamdouh. Behaviour of precipitates and inclusions during esr of nitrogen alloyed and conventional aisi m41 high speed steels. *Steel Grips*, 4(4):298–304, 2006.

[61] Jun Gil Yang and Joo Hyun Park. Distribution behavior of aluminum and titanium between nickel-based alloys and molten slags in the electro slag remelting (esr) process. *Metallurgical and materials transactions. B, Process metallurgy and materials processing science*, 48(4):2147–2156, 2017.

[62] V.V. Satya Prasad. Production of cu–cr alloys by in situ reduction of chromium oxide during electro slag crucible melting (escm). *Materials and Manufacturing Processes*, 16(2):209–218, March 2001.

[63] A Pribulová, P Futáš, A Kmita, D Márasová, and M Holtzer. Impact of electro slag remelting on 14 109 steel properties. *Archives of metallurgy and materials*, 62(1):181–185, 2017.

[64] Scholz Harald, Franz Henrik, Biebricher Ulrich, and Kilzer Thomas. Electro-slag remelting installation, 2018.

[65] Rayan Bhar, Alain Jardy, Pierre Chapelle, and Vincent Descotes. 3d numerical simulation of the var consumable electrode melting process. *Metallurgical and Materials Transactions B*, 51(6):2492–2503, 2020.

[66] Laurentiu Nastac. A multiscale transient modeling approach for predicting the solidification structure in var-processed alloy 718 ingots. *Metallurgical and Materials Transactions B*, 45(1):44–50, 2014.

[67] Gerd Lütjering and James C. Williams. *Titanium matrix composites*. Springer, 2007.

[68] G Ghazal, A Jardy, P Chapelle, and Y Millet. On the dissolution of nitrided titanium defects during vacuum arc remelting of ti alloys. *Metallurgical and Materials Transactions B*, 41(3):646–659, 2010.

[69] Ebrahim Karimi-Sibaki, Abdellah Kharicha, Menghuai Wu, Andreas Ludwig, and Jan Bohacek. A parametric study of the vacuum arc remelting (var) process: effects of arc radius, side-arcing, and gas cooling. *Metallurgical and Materials Transactions B*, 51(1):222–235, 2020.

[70] Jiajun Cui, Baokuan Li, Zhongqiu Liu, Fengsheng Qi, Jianxiang Xu, and Ji Zhang. Comparative investigation on ingot evolution and product quality under different arc distributions during vacuum arc remelting process. *Journal of materials research and technology*, 18:3991–4006, 2022.

[71] P-O Delzant, B Baque, P Chapelle, and A Jardy. On the modeling of thermal radiation at the top surface of a vacuum arc remelting ingot. *Metallurgical and Materials Transactions B*, 49(3):958–968, 2018.

[72] EN Kondrashov, MI Musatov, A Yu Maksimov, AE Goncharov, and LV Konovalov. Calculation of the molten pool depth in vacuum arc remelting of alloy vt3-1. *Journal of Engineering Thermophysics*, 16(1):19–25, 2007.

[73] Hongchao Kou, Yingjuan Zhang, Pengfei Li, Hong Zhong, Rui Hu, Jinshan Li, and Lian Zhou. Numerical simulation of titanium alloy ingot solidification structure during var process based on three-dimensional cafe method. *Rare Metal Materials and Engineering*, 43(7):1537–1542, 2014.

[74] A Kermanpur, DG Evans, RJ Siddall, PD Lee, and M McLean. Effect of process parameters on grain structure formation during var of inconel alloy 718. *Journal of materials science*, 39(24):7175–7182, 2004.

[75] RC Atwood, PD Lee, RS Minisandram, and RM Jones. Multiscale modelling of microstructure formation during vacuum arc remelting of titanium 6-4. *Journal of materials science*, 39(24):7193–7197, 2004.

[76] Yuan Sheng Huang, Mao Sheng Yang, Jing She Li, and Li Guo Bai. Vacuum arc remelting process of high-alloy bearing steel and multi-scale control of solidification structure. In *Materials Science Forum*, volume 817, pages 826–836. Trans Tech Publ, 2015.

[77] Yadong Wang, Lifeng Zhang, Jian Zhang, Yang Zhou, Tingyao Liu, Ying Ren, and Dongbin Jiang. Simulation of solidification structure during vacuum arc remelting using cellular automaton finite element method. *Steel research international*, 93(1):2100408–n/a, 2022.

[78] FJ Zanner, LA Bertram, C Adasczik, and T O'Brien. Observations of melt rate as a function of arc power, co pressure, and electrode gap during vacuum consumable arc remelting of inconel 718. *Metallurgical Transactions B*, 15(1):117–125, 1984.

[79] Alain Jardy, Pierre Chapelle, Ashish Malik, Jean-Pierre Bellot, Hervé Combeau, and Bernard Dussoubs. Arc behaviour and cathode melting process during var: an experimental and numerical study. *ISIJ international*, 53(2):213–220, 2013.

[80] Dmytro Zagrebelnyy and Matthew John M Krane. Segregation development in multiple melt vacuum arc remelting. *Metallurgical and Materials Transactions B*, 40(3):281–288, 2009.

[81] X Xu, W Zhang, and PD Lee. Tree-ring formation during vacuum arc remelting of inconel 718: Part ii. mathematical modeling. *Metallurgical and Materials Transactions A*, 33(6):1805–1815, 2002.

[82] Lang Yuan, Georgi Djambazov, Peter D Lee, and Koulis Pericleous. Multiscale modeling of the vacuum arc remelting process for the prediction on microstructure formation. *International Journal of Modern Physics B*, 23(06n07):1584–1590, 2009.

[83] EN Kondrashov, A Yu Maksimov, and LV Konovalov. Quasi-steady-state characteristics of solidification of alloys made from vt3-1 alloy during vacuum arc remelting. *Russian Journal of Non-Ferrous Metals*, 49(1):23–27, 2008.

[84] L Fernando Carvajal and GE Geiger. An analysis of the temperature distribution and the location of the solidus, mushy, and liquidus zones for binary alloys in remelting processes. *Metallurgical and Materials Transactions B*, 2(8):2087–2092, 1971.

[85] LA Bertram, PR Schunk, SN Kempka, F Spadafora, and R Minisandram. The macroscale simulation of remelting processes. *JOM*, 50(3):18–21, 1998.

[86] Matthieu Revil-Baudard, Alain Jardy, Hervé Combeau, Faustine Leclerc, and Véronique Rebeyrolle. Solidification of a vacuum arc-remelted zirconium ingot. *Metallurgical and Materials Transactions B*, 45(1):51–57, 2014.

[87] Vincent Descotes, Thibault Quatravaux, Jean-Pierre Bellot, Sylvain Witzke, and Alain Jardy. Titanium nitride (tin) germination and growth during vacuum arc remelting of a maraging steel. *Metals (Basel)*, 10(4):541, 2020.

[88] Seongi Lee and Kwangmin Lee. Microstructure and mechanical properties of equiatomic and non-equiatomic timotanbv high entropy alloys prepared using vacuum arc remelting. *Archives of metallurgy and materials*, 65(4):1311–1315, 2020.

[89] HJ Klein and JW Pridgeon. Effective electroslag remelting of superalloys. *TheMinerals, Metals and Materials Society*, pages 25–31, 1972.

[90] Zou Qin and Cao Rui. Vacuum arc remelting furnace, 2016.

[91] Wang Shipu, Zhao Changhong, and Li Ming. Bracket for placing crystallizer of vacuum arc remelting furnace, 2020.

[92] Patel Ashish D, Phillips James Leroy, Sensenig Jeremy L, and McFarland Robert James. Compact coil assembly for a vacuum arc remelting system, 2020.

[93] W.D. Callister. *Materials Science and Engineering: An Introduction, 7th Edition Wiley Plus Set*. Wiley Plus Products. Wiley, 2006.

[94] H. Jazaeri and F. J. Humphreys. The transition from discontinuous to continuous recrystallization in some aluminium alloys: II - annealing behaviour. *Acta materialia*, 52(11):3251–3262, 2004.

[95] Rodney Boyer. *Titanium and Its Alloys: Metallurgy, Heat Treatment and Alloy Characteristics*. 12 2010.

[96] Wongyu Seo, Daeho Jeong, Dongjun Lee, Hyokyung Sung, Yongnam Kwon, and Sangshik Kim. Effects of cooling rate and stabilization annealing on fatigue behavior of beta-processed ti-6al-4v alloys. *Metals and materials international*, 23(4):648–659, 2017.

[97] Hassanen Jaber, János Kónya, Klaudia Kulcsár, and Tünde Kovács. Effects of annealing and solution treatments on the microstructure and mechanical properties of ti6al4v manufactured by selective laser melting. *Materials*, 15(5):1978, 2022.

[98] Ali Hemmasian Ettefagh, Congyuan Zeng, Shengmin Guo, and Jonathan Raush. Corrosion behavior of additively manufactured ti-6al-4v parts and the effect of post annealing. *Additive manufacturing*, 28:252–258, 2019.

[99] Mohammad Reza Jandaghi, Abdollah Saboori, Luca Iuliano, and Matteo Pavese. On the effect of rapid annealing on the microstructure and mechanical behavior of additively manufactured stainless steel by laser powder bed fusion. *Materials science & engineering. A, Structural materials : properties, microstructure and processing*, 828:142109, 2021.

[100] M. R Stoudt, E. A Lass, D. S Ng, M. E Williams, F Zhang, C. E Campbell, G Lindwall, and L. E Levine. The influence of annealing temperature and time on the formation of δ-phase in additively-manufactured inconel 625. *Metallurgical and materials transactions. A, Physical metallurgy and materials science*, 49(7):3028–3037, 2018.

[101] Ludmila Kučerová, Karolina Burdová, Štěpán Jeníček, and Iveta Chena. Effect of solution annealing and precipitation hardening at 250 °c–550 °c on microstructure and mechanical properties of additively manufactured 1.2709 maraging steel. *Materials science & engineering. A, Structural materials : properties, microstructure and processing*, 814:1, 2021.

[102] Yun-Lai Deng, Li Wan, Li-Hui Wu, Yun-Ya Zhang, and Xin-Ming Zhang. Microstructural evolution of al–zn–mg–cu alloy during homogenization. *Journal of materials science*, 46(4):875–881, 2010.

[103] Agnieszka Tomaszewska, Grzegorz Moskal, Damian Migas, Marta Mikuskiewicz, and Tomasz Maciag. Thermal parameters determination of co–al–w as-cast alloy homogenization by dta analysis. *Journal of thermal analysis and calorimetry*, 134(1):157–164, 2018.

[104] Xiaofeng Wang, Mingxing Guo, Lingyong Cao, Jinru Luo, Jishan Zhang, and Linzhong Zhuang. Effect of heating rate on mechanical property, microstructure and texture evolution of al–mg–si–cu alloy during solution treatment. *Materials Science and Engineering: A*, 621:8–17, 2015.

[105] Guosheng Peng, Kanghua Chen, Songyi Chen, and Huachan Fang. Evolution of the second phase particles during the heating-up process of solution treatment of al–zn–mg–cu alloy. *Materials Science and Engineering: A*, 641:237–241, 2015.

[106] M. S. Zedalis and M. E. Fine. Precipitation and ostwald ripening in dilute ai base-zr-v alloys. *Metallurgical Transactions A*, 17(12):2187–2198, 1986.

[107] JD Robson and PB Prangnell. Dispersoid precipitation and process modelling in zirconium containing commercial aluminium alloys. *Acta Materialia*, 49(4):599–613, 2001.

[108] JD Robson. Optimizing the homogenization of zirconium containing commercial aluminium alloys using a novel process model. *Materials Science and Engineering: A*, 338(1-2):219–229, 2002.

[109] JD Robson and PB Prangnell. Modelling al3zr dispersoid precipitation in multicomponent aluminium alloys. *Materials Science and Engineering: A*, 352(1-2):240–250, 2003.

[110] Min Jia, Ziqiao Zheng, and Zhu Gong. Microstructure evolution of the 1469 al–cu–li–sc alloy during homogenization. *Journal of alloys and compounds*, 614:131–139, 2014.

[111] M. Osman, O. Engler, K. Karhausen, L. Löchte, and A. J. McLaren. Effect of homogenisation conditions on recrystallisation in the al-mg-mn alloy aa5454, 2007.

[112] D.A. Porter and K.E. Easterling. *Phase Transformations in Metals and Alloys*. Chapman & Hall, 1992.

[113] Cong Li, Jian Chen, Wei Li, and Jianghua Chen. A comparative investigation on the microstructural features in ti-6al-4me(cr,mo) alloys of annealing conditions. *Journal of alloys and compounds*, 734:75–80, 2018.

[114] Y.H Gao, J Kuang, J.Y Zhang, G Liu, and J Sun. Tailoring precipitation strategy to optimize microstructural evolution, aging hardening and creep resistance in an al–cu–sc alloy by isochronal aging. *Materials science & engineering. A, Structural materials : properties, microstructure and processing*, 795:139943, 2020.

[115] Kenji Matsuda, S Ikeno, H Gamada, K Fujii, Y Uetani, T Sato, and A Kamio. High-resolution electron microscopy on the structure of guinier-preston zones in an al-1.6 mass pct mg2si alloy. *Metallurgical and Materials Transactions A*, 29(4):1161–1167, 1998.

[116] J Buha, RN Lumley, AG Crosky, and K Hono. Secondary precipitation in an al–mg–si–cu alloy. *Acta Materialia*, 55(9):3015–3024, 2007.

[117] Mohamed Intan Fadhlina, Seung Won Lee, and Zenji Horita. Strengthening of al 6061 alloy by high-pressure torsion through grain refinement and aging. In *Materials Science Forum*, volume 765, pages 408–412. Trans Tech Publ, 2013.

[118] MW Zandbergen, Q Xu, A Cerezo, and GDW Smith. Study of precipitation in al–mg–si alloys by atom probe tomography i. microstructural changes as a function of ageing temperature. *Acta Materialia*, 101:136–148, 2015.

[119] Guy Hillel. Direct observation of initial stages of precipitation hardening process in commercial al 6061 alloy. *Journal of Materials Science*, 57(22):10395–10407, June 2022.

[120] SJ Andersen, HW Zandbergen, J Jansen, Chresten TrÆholt, U Tundal, and O Reiso. The crystal structure of the β" phase in al–mg–si alloys. *Acta Materialia*, 46(9):3283–3298, 1998.

[121] G. A. Edwards, K. Stiller, G. L. Dunlop, and M. J. Couper. The precipitation sequence in al–mg–si alloys. *Acta materialia*, 46(11):3893–3904, 1998.

[122] Gangshu Shen, Gracious Ngaile, and Taylan Altan. *Cold and Hot Forging: Fundamentals and Applications.* ASM International, 2004.

[123] Heinz Tschaetsch. *Metal Forming Practise: Processes ; Machines ; Tools.* Springer-Verlag, Berlin, Heidelberg, 1. aufl. edition, 2006.

[124] M. Chandrasekaran. 9 Forging of metals and alloys for biomedical applications. In Mitsuo Niinomi, editor, *Metals for Biomedical Devices*, Woodhead Publishing Series in Biomaterials, pages 235–250. Woodhead Publishing, 2010.

[125] P. Skubisz, J. Sinczak, and S. Bednarek. Forgeability of mg-al-zn magnesium alloys in hot and warm closed die forging. *Journal of materials processing technology*, 177(1-3):210–213, 2006.

[126] R. Gupta. Effect of variants of thermomechanical working and annealing treatment on titanium alloy ti6al4v closed die forgings. *Journal of Materials Engineering & Performance*, 25(6):2551–2563, June 2016.

[127] Jasleen Kaur, B. S. Pabla, and S. S. Dhami. Optimization and comparison of deformation during closed die forging of different parts. In *Advances in intelligent systems and computing*, volume 698 of *Advances in Intelligent Systems and Computing*, pages 469–480. Springer Singapore, Singapore, 2018.

[128] H. J. Marczinski. Axial closed-die rolling, an economic hot-forming method due to high precision and flexibility. *Journal of Materials Processing Technology*, 34(1-4):495–502, 1992.

[129] Yong Zheng, Dong Liu, Yanhui Yang, Zhe Zhang, Xiaolong Li, and Runqiang Zhang. Microstructure evolution of Ti-6Al-4V with periodic thermal parameters during axial closed die rolling process. *Journal of alloys and compounds*, 735:996–1009, 2018.

[130] S. L. Semiatin. Open-Die Forging. In L. Semiatin, editor, *Metalworking: Bulk Forming*, volume 14A, pages 99–110. ASM International, 01 2005.

[131] D. Recker, M. Franzke, and G. Hirt. Fast models for online-optimization during open die forging. *CIRP annals*, 60(1):295–298, 2011.

[132] P. H. Kim, M. S. Chun, J. J. Yi, and Y. H. Moon. Pass schedule algorithms for hot open die forging. *Journal of Materials Processing Technology*, 130-131:516–523, 2002. AFDM 2002 S.I.

[133] K. V. Durga Rajesh, Tanya Buddi, and Himanshu Mishra. Finite element simulation of ti-6al-4v billet on open die forging process under different temperatures using deform-3d. *Advances in materials and processing technologies (Abingdon, England)*, ahead-of-print(ahead-of-print):1–10, 2021.

[134] S.K. Biswas and B.W. Rooks. Application of a computer simulation technique to estimate load and energy in axisymmetric closed die forging. In *13th International Machine Tool Design Research Conference*, pages 90 – 11, Birmingham, UK, 1972. computer simulation technique;estimate load and energy;axisymmetric closed die forging;forming hammer;work restricted forging machine;forging characteristics;deformation;stress distribution;die filling;step;by step;simulation technique;.

[135] E. Appleton. Experimental study into the use of an industrial robot as a manipulator for open die forging of light work-pieces. In *Water Resources and Environmental Engineering Research Report*, pages 709–728, 1979.

[136] B. Aksakal, F. H. Osman, and A. N. Bramley. Analysis for the automation of small batch manufacturing using open die forging. *CIRP Annals*, 42(1):273–278, 1993.

[137] Andrea Di Schino. Open die forging process simulation: a simplified industrial approach based on artificial neural network. *AIMS Materials Science*, 8(5):685–697, 2021.

[138] S. L. Semiatin. Rotary Forging. In *Metalworking: Bulk Forming*. ASM International, 01 2005.

[139] Marcos Perez. Analysis of innovative incremental cold forming process for the manufacturing of aerospace rotating parts. In *Proceedings of the International Manufacturing Science and Engineering Conference 2017*, 06 2017.

[140] Xinghui Han and Lin Hua. Effect of size of the cylindrical workpiece on the cold rotary-forging process. *Materials & Design*, 30(8):2802–2812, 2009.

[141] Xiaobin Deng, Lin Hua, Xinghui Han, and Yanli Song. Numerical and experimental investigation of cold rotary forging of a 20CrMnTi alloy spur bevel gear. *Materials & Design*, 32(3):1376–1389, 2011.

[142] J. Nowak, L. Madej, S. Ziolkiewicz, A. Plewinski, F. Grosman, and M. Pietrzyk. Recent development in orbital forging technology. *International Journal of Material Forming*, 1(1):387–390, 2008.

[143] Xinghui Han and Lin Hua. Comparison between cold rotary forging and conventional forging. *Journal of Mechanical Science and Technology*, 23(10):2668, 2009.

[144] P. M. Standring. Characteristics of rotary forging as an advanced manufacturing tool. *Proceedings of the Institution of Mechanical Engineers, Part B: Journal of Engineering Manufacture*, 215(7):935–945, 2001.

[145] Shijian Yuan, Xiaohong Wang, Gang Liu, and Decheng Chou. The precision forming of pin parts by cold-drawing and rotary-forging. *Journal of Materials Processing Technology*, 86(1-3):252–256, 1999.

[146] J. J. Sheu and C. H. Yu. The die failure prediction and prevention of the orbital forging process. *Journal of Materials Processing Technology*, 201(1-3):9–13, 2008.

[147] J. J. Sheu and C. H. Yu. The cold orbital forging die and process design of a hollow-ring gear part. In *Proceedings of the 35th International Matador Conference*, pages 111–114. Springer, 2007.

[148] Paranjayee Mandal, Himanshu Lalvani, and Martin Tuffs. Cold rotary forging of Inconel 718. *Journal of Manufacturing Processes*, 2019.

[149] M. Furukawa, Z. Horita, M. Nemoto, and T. G. Langdon. Review: Processing of metals by equal-channel angular pressing. *Journal of Materials Science*, 36(12):2835–2843, 2001.

[150] Miroslav Plancak, Dragivsa Vilotic, Milentije Stefanovic, Dejan Movrin, and Igor Kavcmarvcik. Orbital Forging - A Plausible Alternative for Bulk Metal Forming. 2012.

[151] P. M. Standring, J. R. Moon, and E. Appleton. Plastic deformation produced during indentation phase of rotary forging. *Metals Technology*, 7(1):159–166, 1980.

[152] P. M. Standring. The significance of nutation angle in rotary forging. In *In proceedings of 6th ICTP Congress, Nuremberg, Germany, pp. 1739-1744*, 1999.

[153] Qiu Jin, Zhiqiang Gu, and Jian Hua. Preform designing approach in cold orbital forging of flange gear. *Advances in Mechanical Engineering*, 10:168781401880862, 10 2018.

[154] G. Liu, S. Yuan, M. Zhang, and L. Chi. Numerical analysis on rotary forging mechanism of a flange. *Journal of Material Science and Technology*, 2001.

[155] Xinghui Han and Lin Hua. Plastic deformation behaviors of cold rotary forging under different contact patterns by 3d elastic-plastic fe method. *Materials Transactions*, 50(8):1949–1958, 2009.

[156] Marcos Pérez. Microstructural and texture evolution of Jethete M152 flanged-test pieces during cold rotary forging. *Journal of Materials Processing Technology*, 252:582–594, 2018.

[157] Marius Herrmann, Christian Schenck, and Bernd Kuhfuss. Dry rotary swaging with structured tools. *Procedia CIRP*, 40:653–658, 2016. 13th Global Conference on Sustainable Manufacturing – Decoupling Growth from Resource Use.

[158] Z. M. Xie, R. Liu, S. Miao, T. Zhang, X. P. Wang, Q. F. Fang, C. S. Liu, and G. N. Luo. Effect of high temperature swaging and annealing on the mechanical properties and thermal conductivity of w-y2o3. *Journal of nuclear materials*, 464:193–199, 2015.

[159] Radim Kocich and Lenka Kuncicka. Effect of swaging temperature on deformation behaviour of w93ni6co1 tungsten heavy alloy. *Key Engineering Materials*, 865:91–96, 2020.

[160] Henning Hasselbruch, Marius Herrmann, A. Mehner, Bernd Kuhfuss, and Hans Zoch. Incremental dry forging - interaction of w-dlc coatings and surface structures for rotary swaging tools. *Procedia Manufacturing*, 8:541–548, 12 2017.

[161] Jannica Heinrichs and Staffan Jacobson. Laboratory test simulation of aluminium cold forming - influence from PVD tool coatings on the tendency to galling. *Surface and Coatings Technology*, 204(21-22):3606–3613, 2010.

[162] Xin Chen, Chuming Liu, Shunong Jiang, Zhiyong Chen, and Yingchun Wan. Fabrication of nanocrystalline high-strength magnesium lithium alloy by rotary swaging. *Advanced engineering materials*, 24(1):2100666–n/a, 2022.

[163] Tao Wang, Ruizhi Wu, Milin Zhang, Li Li, Jinghuai Zhang, and Jiqing Li. Effects of calcium on the microstructures and tensile properties of mg-5li-3al alloys. *Materials Science And Engineering A Structural Materials Properties Microstructure and Processing*, 528(18):5678–5684, JUL 15 2011.

[164] T. Al. Samman. Comparative study of the deformation behavior of hexagonal magnesium lithium alloys and a conventional magnesium az31 alloy. *Acta Materialia*, 57(7):2229–2242, 2009.

[165] Martin Lentz, Manuela Klaus, Irene J. Beyerlein, Milovan Zecevic, Walter Reimers, and Marko Knezevic. In situ x-ray diffraction and crystal plasticity modeling of the deformation behavior of extruded mgli(al) alloys: An uncommon tension-compression asymmetry. *Acta Materialia*, 86:254–268, 2015.

[166] Jinghuai Zhang, Li Zhang, Zhe Leng, Shujuan Liu, Ruizhi Wu, and Milin Zhang. Experimental study on strengthening of mg-li alloy by introducing long-period stacking ordered structure. *Scripta Materialia*, 68(9):675–678, MAY 2013.

[167] Jian-Yih Wang. Mechanical properties of room temperature rolled mglialzn alloy. *Journal of Alloys and Compounds*, 485(1-2):241–244, OCT 19 2009.

[168] Tianzi Wang, Haipeng Zheng, Ruizhi Wu, Jinliang Yang, Xudong Ma, and Milin Zhang. Preparation of fine-grained and high-strength mg-8li-3al-1zn alloy by accumulative roll bonding. *Advanced Engineering Materials*, 18(2):304–311, FEB 2016.

[169] Xiaoqiang Li, Chunlong Cheng, Qichi Le, Xiong Zhou, Qiyu Liao, Xingrui Chen, Yonghui Jia, and Ping Wang. Ex-situ ebsd analysis of yield asymmetry, texture and twinning development in mg-5li-3al-2zn alloy during tensile and compressive deformation. *Journal of Alloys and Compounds*, 805:947–956, OCT 15 2019.

[170] Yan Tang, Qichi Le, Weitao Jia, Li Fu, Xuan Liu, and Jianzhong Cui. Microstructure evolution and strengthening mechanism study of mg-li alloys during deformation and heat treatment. *Materials Science And Engineering A Structural Materials Properties Microstructure and Processing*, 704:344–359, SEP 17 2017.

[171] Yan Tang, Qichi Le, R. D. K. Misra, Guanqiao Su, and Jianzhong Cui. Influence of extruding temperature and heat treatment process on microstructure and mechanical properties of three structures containing mg-li alloy bars. *Materials Science And Engineering A Structural Materials Properties Microstructure and Processing*, 712:266–280, JAN 18 2018.

[172] Yan Tang, Qichi Le, Weitao Jia, Xuan Liu, and Jianzhong Cui. Influences of warm rolling and annealing processes on microstructure and mechanical properties of three parent structures containing mg-li alloys. *Materials Science And Engineering A Structural Materials Properties Microstructure and Processing*, 711:1–11, JAN 10 2018.

[173] Furong Cao, Guoqiang Xue, and Guangming Xu. Superplasticity of a dual phase dominated mglialznsr alloy processed by multidirectional forging and rolling. *Materials Science And Engineering A Structural Materials Properties Microstructure and Processing*, 704:360–374, SEP 17 2017.

[174] Y. Zeng, B. Jiang, Q. R. Yang, G. F. Quan, J. J. He, Z. T. Jiang, and F. S. Pan. Effect of li content on microstructure, texture and mechanical behaviors of the as-extruded mg-li sheets. *Materials Science And Engineering A Structural Materials Properties Microstructure and Processing*, 700:59–65, JUL 17 2017.

[175] Hanwu Dong, Fusheng Pan, Bin Jiang, Ruihong Li, and Xiaoyong Huang. Mechanical properties and deformation behaviors of hexagonal mgli alloys. *Materials & Design*, 65:42–49, JAN 2015.

[176] Fei Guo, Luyao Jiang, Yanlong Ma, Lei Liu, Zhen Zhang, Mingbo Yang, Dingfei Zhang, and Fusheng Pan. Strengthening a dual phase mgli alloy by strain induced phase transformation at room temperature. *Scripta Materialia*, 179:16–19, APR 2020.

[177] D. K. Xu, L. Liu, Y. B. Xu, and E. H. Han. The strengthening effect of icosahedral phase on as-extruded mg-li alloys. *Scripta Materialia*, 57(3):285–288, AUG 2007.

[178] Qian Su, Jie Xu, Yugiao Li, Jae Ik Yoon, Debin Shan, Bin Guo, and Hyoung Seop Kim. Microstructural evolution and mechanical properties in superlight mg-li alloy processed by high-pressure torsion. *Materials*, 11(4), APR 2018.

[179] Yun Zou, Lehao Zhang, Yang Li, Hongtao Wang, Jiabin Liu, Peter K. Liaw, Hongbin Bei, and Zhongwu Zhang. Improvement of mechanical behaviors of a superlight mg-li base alloy by duplex phases and fine precipitates. *Journal of Alloys and Compounds*, 735:2625–2633, FEB 25 2018.

[180] Hui Fu, Bincheng Ge, Yunchang Xin, Ruizhi Wu, Carlos Fernandez, Jianyu Huang, and Qiuming Peng. Achieving high strength and ductility in magnesium alloys via densely hierarchical double contraction nanotwins. *Nano Letters*, 17(10):6117–6124, OCT 2017.

[181] Qiuming Peng, Yong Sun, Bingcheng Ge, Hui Fu, Qun Zu, Xiaozhi Tang, and Jianyu Huang. Interactive contraction nanotwins-stacking faults strengthening mechanism of mg alloys. *Acta Materialia*, 169:36–44, MAY 1 2019.

[182] Song Tang, Tongzheng Xin, Wanqiang Xu, David Miskovic, Gang Sha, Zakaria Quadir, Simon Ringer, Keita Nomoto, Nick Birbilis, and Michael Ferry. Precipitation strengthening in an ultralight magnesium alloy. *Nature Communications*, 10, MAR 1 2019.

[183] Anastasiya Toenjes, Svetlana Ishkina, Christian Schenck, Axel Von Hehl, Hans-Werner Zoch, and Bernd Kuhfuss. Eccentric rotary swaging variants. *MATEC Web of Conferences*, 190:15003, 2018.

[184] M. Plancak, A. Bramley, and F. Osman. Non-conventional cold extrusion. *Journal of Materials Processing Technology*, 34(1):465–472, 1992.

[185] Mladomir Milutinovic, Miodrag Hadzistevic, Dejan Movrin, and Igor Vrba. Non conventional methods for shaping plastics parts. *Mat. Plast*, 48:222, 2011.

[186] L Mujica Roncery, I Lopez-Galilea, B Ruttert, S Huth, and W Theisen. Influence of temperature, pressure, and cooling rate during hot isostatic pressing on the microstructure of an sx ni base superalloy. *Materials & Design*, 97:544–552, 2016.

[187] Qing Teng, Qingsong Wei, Pengju Xue, Chao Cai, Hui Chen, Hongxia Chen, and Yusheng Shi. Effects of processing temperatures on fgh4097 superalloy fabricated by hot isostatic pressing: Microstructure evolution, mechanical properties and fracture mechanism. *Materials science & engineering. A Structural materials : properties, microstructure and processing*, 739:118–131, 2019.

[188] Daniele Marini, David Cunningham, and Jonathan Corney. A review of flow forming processes and mechanisms. Trans Tech Publications Ltd, 2015.

[189] F. J. Humphreys and M. Hatherly. In F.J. Humphreys and M. Hatherly, editors, *Recrystallization and Related Annealing Phenomena (Second Edition)*, pages 333–378. Elsevier, Oxford, second edition edition, 2004.

[190] J. A. Ewing and Walter Rosenhain. Bakerian Lecture: The Crystalline Structure of Metals. *Philosophical Transactions of the Royal Society of London. Series A, Containing Papers of a Mathematical or Physical Character*, 193:353–375, 1900.

[191] D. Hull and D. J. Bacon. Chapter 3 - Movement of Dislocations. In D. Hull and D.J. Bacon, editors, *Introduction to Dislocations (Fifth Edition)*, pages 43–62. Butterworth-Heinemann, Oxford, fifth edition edition, 2011.

[192] William D. Callister. *Materials science and engineering : an introduction*. John Wiley & Sons, New York, 2007.

[193] R Le Hazif, P Dorizzi Et, and J.P Poirier. Glissement {110} ⟨110⟩ dans les metaux de structure cubique a faces centrees. *Acta Metallurgica*, 21(7):903–911, 1973.

[194] M. L. Kronberg and F. H. Wilson. $Trans.AIME$. 1949.

[195] H. V. Atkinson. Overview no. 65: Theories of normal grain growth in pure single phase systems. *Acta Metallurgica*, 36(3):469–491, 1988.

[196] Koenraad G. F. Janssens, David Olmsted, Elizabeth A. Holm, Stephen M. Foiles, Steven J. Plimpton, and Peter M. Derlet. Computing the mobility of grain boundaries. *Nature Materials*, 5(2):124–127, 2006.

[197] Blas Pedro Uberuaga, Louis J. Vernon, Enrique Martinez, and Arthur F. Voter. The relationship between grain boundary structure, defect mobility and grain boundary sink efficiency. *Scientific Reports*, 5(1):9095, 2015.

[198] M. Winning, A.D. Rollett, G. Gottstein, D.J. Srolovitz, A. Lim, and L.S. Shvindlerman. Mobility of low-angle grain boundaries in pure metals. *Philosophical Magazine*, 90(22):3107–3128, 2010.

[199] Hao Zhang, Mikhail I. Mendelev, and David J. Srolovitz. Mobility of Σ 5 tilt grain boundaries: Inclination dependence. *Scripta Materialia*, 52(12):1193–1198, 2005.

[200] A. Bolognesi, M. Berliocchi, M. Manenti, A. Di Carlo, P. Lugli, K. Lmimouni, and C. Dufour. Effects of grain boundaries, field-dependent mobility, and interface trap states on the electrical characteristics of pentacene tft. *IEEE Transactions on Electron Devices*, 51(12):1997–2003, 2004.

[201] David L. Olmsted, Elizabeth A. Holm, and Stephen M. Foiles. Survey of computed grain boundary properties in face-centered cubic metals—ii: Grain boundary mobility. *Acta Materialia*, 57(13):3704–3713, 2009.

[202] W. C. Leslie, J. T. Michalak, and F. W. Aul. Iron and its dilute solid solutions. *New York: Interscience*, page 119, 1963.

[203] Anthony W. Thompson. Substructure strengthening mechanisms. *Metallurgical Transactions A*, 8(6):833–842, 1977.

[204] R. J. McElroy and Z. C. Szkopiak. Dislocation - substructure - strengthening and mechanical - thermal treatment of metals. *International Metallurgical Reviews*, 17(1):175–202, 1972.

[205] J. J. Jonas, D. R. Axelrad, and J. L. Uvira. On substructure strengthening and the high temperature deformation of cubic metals. Technical report, McGill University Montreal, 1968.

[206] Doris Kuhlmann-Wilsdorf. A critical test on theories of work-hardening for the case of drawn iron wire. *Metallurgical Transactions*, 1(11):3173–3179, 1970.

[207] H. J. McQueen and E. Evangelista. Substructures in aluminium from dynamic and static recovery. *Czechoslovak Journal of Physics B*, 38(4):359–372, 1988.

[208] Hsun Hu. Direct observations on annealing of a si-fe crystal in electron microscope. *Transactions of the Metallurgical Society of AIME*, 224(1):75, 1962.

[209] James C. M. Li. Possibility of subgrain rotation during recrystallization. *Journal of Applied Physics*, 33(10):2958–2965, 1962.

[210] D. Moldovan, D. Wolf, S. R. Phillpot, and A. J. Haslam. Role of grain rotation during grain growth in a columnar microstructure by mesoscale simulation. *Acta Materialia*, 50(13):3397 – 3414, 2002. Cited by: 93.

[211] H. M. Chan and F. J. Humphreys. Effect of particle stimulated nucleation on orientation of recrystallized grains. *Metal science*, 18(11):527–530, 1984.

[212] R. F. & American Institute of Mining Mehl and Metallurgical Engineers. A brief history of the science of metals. *New York: American Institute of Mining and Metallurgical Engineers.*, 1948.

[213] J.E. Burke and D. Turnbull. Recrystallization and grain growth. *Progress in Metal Physics*, 3:220–292, 1952.

[214] Keith J. Laidler. The development of the arrhenius equation. *J. Chem. Educ.*, 61(6):494, June 1984.

[215] W. A. Anderson and R. F. Mehl. Recrystallization of aluminum in terms of the rate of nucleation and the rate of growth. *Trans. Aime*, 161:140, 1945.

[216] O Haase and E Schmid. Über den gleitwiderstand von metallkristallen (on the sliding resistance of metal crystals). *Zeitschrift für Physik*, 33(1):413–428, 1925.

[217] J. D. Embury, W. J. Poole, and E. Koken. Some views on the influence of strain path on recrystallization. *Scripta Metallurgica et Materialia*, 27(11):1465–1470, 1992.

[218] Eva Lindh, Bevis Hutchinson, and Shinjiro Ueyama. Effect of redundant deformation on recrystallisation behaviour of copper. *Scripta metallurgica et materialia*, 29(3):347–352, 1993.

[219] D. Juul Jensen. Growth rates and misorientation relationships between growing nuclei/grains and the surrounding deformed matrix during recrystallization. *Acta Metallurgica et Materialia*, 43(11):4117–4129, 1995.

[220] A. N. Kolmogorov. A study of the equation of diffusion with increase in the quantity of matter, and its application to a biological problem. *Moscow University Bulletin of Mathematics*, 1:1–25, 1937.

[221] WA Johnson and KF Mehl. Calorimetric study of precipitation kinetics of al-cu-mg and al-cu-mg-0.06 wt% sn alloys. *Trans TMS AIME*, 135:416, 1939.

[222] Melvin Avrami. Kinetics of phase change. i general theory. *The Journal of chemical physics*, 7(12):1103–1112, 1939.

[223] M. Fanfoni and M. Tomellini. The johnson-mehl-avrami-kohnogorov model: A brief review. *Il Nuovo Cimento D*, 20(7):1171–1182, 1998.

[224] A. A. Ridha and W. B. Hutchinson. Recrystallisation mechanisms and the origin of cube texture in copper. *Acta metallurgica*, 30(10):1929–1939, 1982.

[225] J. Hjelen, R. Ørsund, and E. Nes. On the origin of recrystallization textures in aluminium. *Acta metallurgica et materialia*, 39(7):1377–1404, 1991.

[226] M. Somerday and F. J. Humphreys. Recrystallisation behaviour of supersaturated al–mn alloys part 1–al–1.3 wt-% mn. *Materials science and technology*, 19(1):20–29, 2003.

[227] R. A. Vandermeer and B. B. Rath. Modeling recystallization kinetics in a deformed iron single crystal. *Metallurgical Transactions A*, 20(3):391–401, 1989.

[228] R.D. Knutsen, C.I. Lang, and J.A. Basson. Discontinuous cellular precipitation in a cr–mn–n steel with niobium and vanadium additions. *Acta Materialia*, 52(8):2407–2417, 2004.

[229] Fengxiang Lin, Yubin Zhang, Andrew Godfrey, and Dorte Juul Jensen. Twinning during recrystallization and its correlation with the deformation microstructure. *Scripta Materialia*, 219:114852, 2022.

[230] H. Gleiter. The formation of annealing twins. *Acta Metallurgica*, 17(12):1421–1428, 1969.

[231] H. Gleiter, S. Mahajan, and K.J. Bachmann. The generation of lattice dislocations by migrating boundaries. *Acta Metallurgica*, 28(12):1603–1610, 1980.

[232] P. J. Goodhew. Annealing twin formation by boundary dissociation. *Metal Science*, 13(3-4):108–112, 1979.

[233] Peter Streitenberger and Dana Zöllner. von Neumann-Mullins-type evolution equations for triple and quadruple junction controlled grain growth. *Scripta Materialia*, 109:52–55, 2015.

[234] John Von Neumann. Metal interfaces. *American Society for Metals, Cleveland*, 108, 1952.

[235] W. Mullins, W. Two-dimensional motion of idealized grain boundaries. *Journal of Applied Physics*, 27(8):900–904, 1956.

[236] Ola Hunderi and Nils Ryum. A note on the von Neumann-Mullins equation. *Scripta Materialia*, 53(6):719 – 722, 2005. Cited by: 7.

[237] Tadao. Watanabe. Approach to Grain Boundary Design for Strong and Ductile Polycrystals. *Res Mechanica: International Journal of Structural Mechanics and Materials Science*, 11(1):47 – 84, 1984. Cited by: 835.

[238] Tadao. Watanabe. Grain boundary engineering: historical perspective and future prospects. *Journal of materials science*, 46(12):4095–4115, 2011.

[239] Yaodong Xuanyuan, Hongjun Li, Ming Huang, Yinbiao Yan, and Sen Yang. Tuning the microstructure and mechanical properties of tial-based alloy through grain boundary engineering. *Journal of Materials Research and Technology*, 18:5370–5379, 2022.

[240] M. Shimada, H. Kokawa, Z. J. Wang, Y. S. Sato, and I. Karibe. Optimization of grain boundary character distribution for intergranular corrosion resistant 304 stainless steel by twin-induced grain boundary engineering. *Acta Materialia*, 50(9):2331–2341, 2002.

[241] Qingqing Sun, Jinhua Han, Jiaxing Li, Fahe Cao, and Shuai Wang. Tailoring hydrogen embrittlement resistance of pure Ni by grain boundary engineering. *Corrosion Communications*, 6:48–51, 2022.

[242] Nadia Souaï, Nathalie Bozzolo, Loic Nazé, Yvan Chastel, and R Logé. About the possibility of grain boundary engineering via hot-working in a nickel-base superalloy. *Scripta materialia*, 62(11):851–854, 2010.

[243] Lizhen Tan, K Sridharan, TR Allen, Randy K Nanstad, and David A McClintock. Microstructure tailoring for property improvements by grain boundary engineering. *Journal of Nuclear Materials*, 374(1-2):270–280, 2008.

[244] V. Randle. Mechanism of twinning-induced grain boundary engineering in low stacking-fault energy materials. *Acta Materialia*, 47(15):4187–4196, 1999.

[245] Christopher A. Schuh, Mukul Kumar, and Wayne E. King. Analysis of grain boundary networks and their evolution during grain boundary engineering. *Acta Materialia*, 51(3):687–700, 2003.

[246] Mukul Kumar, Adam J. Schwartz, and Wayne E. King. Microstructural evolution during grain boundary engineering of low to medium stacking fault energy fcc materials. *Acta Materialia*, 50(10):2599–2612, 2002.

[247] C. M. Sellars. Recrystallization of metals during hot deformation. *Philosophical Transactions of the Royal Society of London. Series A, Mathematical and Physical Sciences*, 288(1350):147–158, 1978.

[248] R. A. Petković, M. J. Luton, and J. J. Jonas. Recovery and recrystallization of carbon steel between intervals of hot working. *Canadian metallurgical quarterly*, 14(2):137–145, 1975.

[249] R. A. Petkovic Djaic and J. J. Jonas. Static recrystallization of austenite between intervals of hot working. *J Iron Steel Inst*, 210(4):256–261, 1972.

[250] Zhou Xu, Guo-Rong Zhang, and Taku Sakai. Effect of carbon content on static restoration of hot worked plain carbon steels. *ISIJ international*, 35(2):210–216, 1995.

[251] T. Sakai, M. Ohashi, K. Chiba, and J. J. Jonas. Recovery and recrystallization of polycrystalline nickel after hot working. *Acta Metallurgica*, 36(7):1781–1790, 1988.

[252] Taku Sakai, Andrey Belyakov, Rustam Kaibyshev, Hiromi Miura, and John J. Jonas. Dynamic and post-dynamic recrystallization under hot, cold and severe plastic deformation conditions. *Progress in materials science*, 60:130–207, 2014.

[253] Shunyu Liu and Yung C. Shin. Additive manufacturing of ti6al4v alloy: A review. *Materials & Design*, 164:107552, 2019.

[254] Dirk Herzog, Vanessa Seyda, Eric Wycisk, and Claus Emmelmann. Additive manufacturing of metals. *Acta Materialia*, 117:371–392, 2016.

[255] Runze Huang, Matthew Riddle, Diane Graziano, Joshua Warren, Sujit Das, Sachin Nimbalkar, Joe Cresko, and Eric Masanet. Energy and emissions saving potential of additive manufacturing: the case of lightweight aircraft components. *Journal of cleaner production*, 135:1559–1570, 2016.

[256] Werner Kritzinger, Matthias Karner, Georg Traar, Jan Henjes, and Wilfried Sihn. Digital twin in manufacturing: A categorical literature review and classification. *Ifac-PapersOnline*, 51(11):1016–1022, 2018.

[257] R. R. Hart, B. C. Wonsiewicz, and G. Y. Chin. High strength copper alloys by thermomechanical treatments. *Metallurgical Transactions*, 1(11):3163–3172, 1970.

[258] Khaled Al-Fadhalah. Effect of thermomechanical processing on the flow stress of copper. *Kuwait journal of science & engineering*, 38, 06 2011.

[259] L.G. Peterson, E.R. Kimmel, and R.A. Queeney. Thermomechanical processing, microstructure and properties of a copper-1.0 vol. *Materials Science and Engineering*, 16(1):107–113, 1974.

[260] Emad Scharifi, Ruben Knoth, and Ursula Weidig. Thermo-mechanical forming procedure of high strength Aluminum sheet with improved mechanical properties and process efficiency. *Procedia Manufacturing*, 29:481–489, 2019. "18th International Conference on Sheet Metal, SHEMET 2019" "New Trends and Developments in Sheet Metal Processing".

[261] Gerhard Welsch, Rodney Boyer, and E. W. Collings. *Materials properties handbook: titanium alloys*. ASM international, 1993.

[262] Matthew J. Donachie. *Titanium: a technical guide*. ASM international, 2000.

[263] S. L. Semiatin. An overview of the thermomechanical processing of α/β titanium alloys: Current status and future research opportunities. *Metallurgical & Materials Transactions. Part A*, 51(6):2593–2626, June 2020.

[264] N. S. Weston and M. Jackson. FAST-forge - A new cost-effective hybrid processing route for consolidating titanium powder into near net shape forged components. *Journal of Materials Processing Technology*, 243:335–346, 2017.

[265] R. Ding, Z. X. Guo, and A. Wilson. Microstructural evolution of a ti-6al-4v alloy during thermomechanical processing. *Materials Science and Engineering: A*, 327(2):233–245, 2002.

[266] A. Coyne-Grell, J. Blaizot, S. Rahimi, I. Violatos, S. Nouveau, C. Dumont, A. Nicolaÿ, and N. Bozzolo. Recrystallization mechanisms and associated microstructure evolution during billet conversion of a gamma-gamma' nickel based superalloy. *Journal of Alloys and Compounds*, 916:165465, 2022.

[267] A. Coyne-Grell, J. Blaizot, S. Rahimi, I. Violatos, S. Nouveau, C. Dumont, A. Nicolaÿ, and N. Bozzolo. Evolution of γ' precipitation during the early stages of industrial forging of a nickel-based superalloy. *Metallurgical and Materials Transactions A: Physical Metallurgy and Materials Science*, 54(5):2022 – 2036, 2023. Cited by: 0; All Open Access, Green Open Access, Hybrid Gold Open Access.

[268] Marcin Kukuryk. Numerical analysis of strains and stresses in the hot cogging process. *Journal of Applied Mathematics and Computational Mechanics*, 17:45–52, 09 2018.

[269] J. R. Cho, C. Y. Park, and D. Y. Yang. Investigation of the cogging process by three-dimensional thermo-viscoplastic finite element analysis. *Proceedings of the Institution of Mechanical Engineers, Part B: Journal of Engineering Manufacture*, 206(4):277–286, 1992.

[270] Jianxin Dong, Linhan Li, Haoyu Li, Maicang Zhang, and Zhihao Yao. Effect of extent of homogenization on the hot deformation recrystallization of superalloy ingot in cogging process. *Acta Metall Sin*, 51(10):1207, 2015.

[271] GP Kang, KH Lee, and SU Lee. Computer simulation of microstructure evolution during hot forging of waspaloy. In *Proceedings of the Korean Society for Technology of Plasticity Conference*, pages 53–56. The Korean Society for Technology of Plasticity, 2007.

[272] Qian Bai, Jian-guo Lin, T. A. Dean, D. S. Balint, T. Gao, and Z. Zhang. Modelling of dominant softening mechanisms for ti-6al-4v in steady state hot forming conditions. *Materials Science and Engineering: A*, 559:352–358, 2013.

[273] F. Roters, P. Eisenlohr, L. Hantcherli, D. D. Tjahjanto, T. R. Bieler, and D. Raabe. Overview of constitutive laws, kinematics, homogenization and multiscale methods in crystal plasticity finite-element modeling: Theory, experiments, applications. *Acta Materialia*, 58(4):1152–1211, 2010.

[274] Paul M. Souza, Giribaskar Sivaswamy, Luke Bradley, Andrew Barrow, and Salaheddin Rahimi. An innovative constitutive material model for predicting high temperature flow behaviour of inconel 625 alloy. *Journal of Materials Science*, 57(44):20794–20814, 2022.

[275] Paul M. Souza, Giribaskar Sivaswamy, Liza Hall, and Salaheddin Rahimi. An analysis of the forgeability of ti-10v-2fe-3al β titanium alloy using a combined estrin mecking and avrami material constitutive model. *International Journal of Mechanical Sciences*, 216:106975, 2022.

[276] H. M. Flower. Microstructural development in relation to hot working of titanium alloys. *Materials Science and Technology*, Nov 1990.

[277] Vydehi Arun Joshi. *Titanium alloys: an atlas of structures and fracture features*. Crc Press, 2006.

[278] R. R. Boyer. An overview on the use of titanium in the aerospace industry. *Materials Science and Engineering: A*, 213(1):103–114, 1996. International Symposium on Metallurgy and Technology of Titanium Alloys.

[279] Ian Polmear, David StJohn, J. F. Nie, and Ma Qian. *Light Alloys : Metallurgy of the Light Metals*. 03 2017.

[280] G. Lütjering. Influence of processing on microstructure and mechanical properties of $(\alpha + \beta)$ titanium alloys. *Materials Science and Engineering: A*, 243(1):32–45, 1998.

[281] M. Peters, J. Hemptenmacher, J. Kumpfert, and C. Leyens. *Structure and Properties of Titanium and Titanium Alloys*, chapter 1, pages 1–36. John Wiley & Sons, Ltd, 2003.

[282] Chao Li, Xiao-yong Zhang, Ke-chao Zhou, and Chaoqun Peng. Relationship between lamellar α evolution and flow behavior during isothermal deformation of ti-5al-5mo-5v-1cr-1fe near β titanium alloy. *Materials Science and Engineering: A*, 558:668–674, 12 2012.

[283] F. H. Froes. *Titanium: Physical Metallurgy, Processing, and Applications*. ASM International, 2015.

[284] Pan Deng, Dachun Liu, Xiumin Chen, Wenlong Jiang, Lingxin Kong, and Liang Li. Carbochlorination mechanism of low-grade titanium slag: Ab initio molecular dynamic simulation. *Journal of Materials Research and Technology*, 17:459–466, 2022.

[285] George Chen, Derek Fray, and Tom Farthing. Direct electrochemical reduction of titanium dioxide to titanium in molten calcium chloride. *Nature*, 407:361–4, 10 2000.

[286] S. Suwas and N.P. Gurao. 3.05 - development of microstructures and textures by cross rolling. In Saleem Hashmi, Gilmar Ferreira Batalha, Chester J. Van Tyne, and Bekir Yilbas, editors, *Comprehensive Materials Processing*, pages 81–106. Elsevier, Oxford, 2014.

[287] Qing-Shan Yang, Bin Jiang, Zu-Jian Yu, Qing-Wei Dai, and Su-Qin Luo. Effect of extrusion strain path on microstructure and properties of az31 magnesium alloy sheet. *Acta Metallurgica Sinica (English Letters)*, 28(10):1257–1263, 2015.

[288] Tao Tang, Yichuan Shao, Dayong Li, Liming Peng, Yinghong Peng, Shaorui Zhang, and Peidong Wu. Polycrystal plasticity simulation of extrusion of a magnesium alloy round bar: Effect of strain path non-uniformity. *Journal of Alloys and Compounds*, 730:161–181, 2018.

[289] S. B. Davenport and R. L. Higginson. Strain path effects under hot working: an introduction. *Journal of Materials Processing Technology*, 98(3):267–291, 2000.

[290] S. Gardner, W. Li, M. Coleman, and R. Johnston. The effects of thermomechanical history on the microstructure of a nickel-base superalloy during forging. *Materials Science and Engineering: A*, 668:263–270, 2016.

[291] Gennady Salishchev, Sergey Mironov, and Sergey Zherebtsov. Mechanisms of submicrocrystalline structure formation in titanium and two-phase titanium alloy during warm severe processing. *Materials Physics and Mechanics*, 11:152–158, 04 2006.

[292] N. Gurao, S. Sethuraman, and Satyam Suwas. Evolution of texture and microstructure in commercially pure titanium with change in strain path during rolling. *Metallurgical and Materials Transactions A*, 44, 03 2012.

[293] Jin Kim, Kyung-Tae Park, In Shim, and Soon Hong. Globularization behavior of eli grade ti6al4v alloy during non-isothermal multi-step forging. *Materials Transactions - MATER TRANS*, 49:215–223, 01 2008.

[294] A. A. Korshunov, F. U. Enikeev, M. I. Mazurski, G. A. Salishchev, O. V. Dmitriev, A. V. Muravlev, and P. V. Chistyakov. Grain-structure refinement in titanium alloy under different loading schedules. *Journal of Materials Science*, 31(17):4635–4639, 1996.

[295] R. Poths, B. Wynne, William Rainforth, J. Beynon, Giuliano Angella, and S. Semiatin. Effect of strain reversal on the dynamic spheroidization of ti-m-4v during hot deformation. *Metallurgical and Materials Transactions A-physical Metallurgy and Materials Science - METALL MATER TRANS A*, 35:2993–3001, 09 2004.

[296] S. Semiatin, J. Brown, T. Brown, D. DeLo, Thomas Bieler, and J. Beynon. Strain-path effects during hot working of ti6al4v with a colony-alpha microstructure. *Metallurgical and Materials Transactions A-physical Metallurgy and Materials Science - METALL MATER TRANS A*, 32:1556–1559, 06 2001.

[297] K. Muszka, M. Lopez-Pedrosa, Klaudiusz Raszka, Matthew Thomas, William Rainforth, and B. Wynne. The impact of strain reversal on microstructure evolution and orientation relationships in ti-6al-4v with an initial alpha colony microstructure. *Metallurgical and Materials Transactions A*, 45, 12 2014.

[298] S.V. Zherebtsov, G.A. Salishchev, R.M. Galeyev, O.R. Valiakhmetov, S.Yu. Mironov, and S.L. Semiatin. Production of submicrocrystalline structure in large-scale ti–6al–4v billet by warm severe deformation processing. *Scripta Materialia*, 51(12):1147–1151, 2004.

[299] Thomas R Bieler and S.L Semiatin. The origins of heterogeneous deformation during primary hot working of ti–6al–4v. *International Journal of Plasticity*, 18(9):1165–1189, 2002.

[300] S. Mironov, M. Murzinova, S. Zherebtsov, G. A. Salishchev, and S. L. Semiatin. Microstructure evolution during warm working of ti-6al-4v with a colony-α microstructure. *Acta Materialia*, 57(8):2470–2481, 2009.

[301] Digvijay Sheed, Bhagawati Kashyap, and Rajkumar Singh. Study of globularization in ti-6al-4v alloy during non-isothermal multiple forging and annealing. 04 2015.

[302] David Connolly, Mathieu Fabris, Giribaskar Sivaswamy, Salaheddin Rahimi, and Vassili Vorontsov. Miniaturised experimental simulation and combined modelling of open-die forging of ti-6al-4v titanium alloy. *Journal of Materials Research and Technology*, 30:3622–3639, 2024.

[303] A. Tomlinson, J. D. Stringer, et al. Spread and elongation in flat tool forging. *J. Iron Steel Inst*, 193:157–162, 1959.

[304] Matjaž Knap, Goran Kugler, Heinz Palkowski, and Radomir Turk. Prediction of material spreading in hot open-die forging. *Steel research international*, 75(6):405–410, 2004.

[305] Nieschwitz, Ecken, and Siemer. Pass schedule calculation program "Comforge" for open-die forging plants. *MPT- Metallurgical Plant and Technology*, 11(5):54–68, 1988.

[306] Schmidt R. Fister W. Computer-aided program forging for axissymetric hammer forging. *Steel and Iron*, 106(22):1213–1218, 1986.

[307] W. Schmitz. Forgebase - a tool for optimization of the open-die forging process. In *Proceedings of the 15th International Forgemasters Meeting, Kobe, Japan*, pages 26–29, 2003.

[308] Martin Wolfgarten, Dirk Rosenstock, Fridtjof Rudolph, and Gerhard Hirt. New approach for the optimization of pass-schedules in open-die forging. *International Journal of Material Forming*, 12(6):973 – 983, 2019. Incremental forming process;Influencing parameters;Mechanical properties and reliabilities;Micro-structure evolutions;Open die forging;Optimization algorithms;Pass schedule;Quality characteristic;.

[309] D. Huang, W.T. Wu, Dave Lambert, and S.L. Semiatin. Computer simulation of microstructure evolution during hot forging of waspaloy and nickel alloy 718. *Microstructure Modeling and Prediction During Thermomechanical Processing*, pages 137–146, 01 2001.

[310] E. Siemer, P. Nieschwitz, and R. Kopp. Quality-optimized process control in open-die forging. *Stahleisen*, page pp. 383–387, 1986.

[311] D. Recker, M. Franzke, G. Hirt, R. Rech, and K. Steingießer. Grain size prediction during open die forging processes. *La Metallurgia Italiana*, 2010.

[312] Dirk Rosenstock, Dominik Recker, Martin Franzke, Gerhard Hirt, Dieter Sommler, Klaus-J Steingießer, Andreas Tewes, Ralf Rech, Bodo Gehrmann, Stefan Kirchhoff, et al. Online visualization during open die forging and optimization of pass schedules. *Steel Research International*, 85(9):1348–1354, 2014.

[313] Dylan Agius, Abdullah Al Mamun, Chris A. Simpson, Christopher Truman, Yiqiang Wang, Mahmoud Mostafavi, and David Knowles. Microstructure-informed, predictive crystal plasticity finite element model of fatigue-dwells. *Computational Materials Science*, 183:109823, 2020.

[314] Li Miaoquan, Chen Dunjun, Xiong Aiming, and Long Li. An adaptive prediction model of grain size for the forging of ti–6al–4v alloy based on fuzzy neural networks. *Journal of Materials Processing Technology*, 123(3):377–381, 2002.

[315] Zhichao Sun, Xiaoqun Wang, Jue Zhang, and He Yang. Prediction and control of equiaxed α in near-β forging of ta15 ti-alloy based on bp neural network: For purpose of tri-modal microstructure. *Materials Science and Engineering: A*, 591:18–25, 2014.

[316] B. Schulz, T. Leitner, M. Hafok, and S. Primig. Advancements in processing of ni-based superalloys by microstructure engineering via discontinuous γ' break-down. *Materialia*, 31:101873, 2023.

[317] K. Ashok Reddy. Non-destructive testing, evaluation of stainless steel materials. *Materials Today: Proceedings*, 4(8):7302–7312, 2017.

[318] J.R. Deepak, V.K. Bupesh Raja, D. Srikanth, H. Surendran, and M.M. Nickolas. Non-destructive testing (ndt) techniques for low carbon steel welded joints: A review and experimental study. *Materials Today: Proceedings*, 44:3732–3737, 2021.

[319] Elena Jasiūnienė, Liudas Mažeika, Vykintas Samaitis, Vaidotas Cicėnas, and David Mattsson. Ultrasonic non-destructive testing of complex titanium/carbon fibre composite joints. *Ultrasonics*, 95:13–21, 2019.

[320] Isaac Segovia Ramírez, Fausto Pedro García Márquez, and Mayorkinos Papaelias. Review on additive manufacturing and non-destructive testing. *Journal of Manufacturing Systems*, 66:260–286, 2023.

[321] Long Huang, Zhichao Sun, Jing Cao, and Zhikun Yin. The formation and evolution of macrozone in ti-6242s alloy during thermo-mechanical processing. *Journal of Alloys and Compounds*, 861:158533, 2021.

[322] Navya Prakash, Dorothea Nieberl, Monika Mayer, and Alfons Schuster. Learning defects from aircraft ndt data. *NDT & E International*, 138:102885, 2023.

[323] M. Ward. Metal forming and forging – finding a new place within high value manufacturing through advanced, industrial scale research. *Ironmaking & Steelmaking*, 42(4):252–258, 2015.

[324] Salah Rahimi, Ioannis Violatos, Bradley Wynne, and Martin Jackson. Digital twins for high-value components. *Materials World*, 30(6):38–41, June 2022.

[325] Paul L. Blackwell. From materials characterisation to pre-production validation : from materials characterisation to pre-production validations to providing processing solutions to industry. In *International Conference on New Forming Technology*, CHN, August 2015.

[326] A. Iturbe, E. Giraud, E. Hormaetxe, A. Garay, G. Germain, K. Ostolaza, and P. J. Arrazola. Mechanical characterization and modelling of Inconel 718 material behavior for machining process assessment. *Materials Science and Engineering: A*, 682:441–453, 2017.

[327] SpecialMetals. Inconel® alloy 718, 2007.

[328] SpecialMetals. Nimonic® alloy 90, 2004.

[329] T. W. Gibbs and H. W. Wyatt. Short-Time Tensile Properties of Type 316 Stainless Steel at Very High Temperatures. *Journal of Basic Engineering*, 83(4):481–488, 12 1961.

[330] Copper and copper alloys - plate, sheet, strip and circles for general purposes - part 2: Sheet and strip, 1997.

[331] Aluminium and aluminium alloys - chemical composition and form of wrought products - part 3: Chemical composition and form of products, September 2019.

[332] Tiffany A. Dux. Forging of Aluminum Alloys[1]. *Aluminum Science and Technology*, 11 2018.

[333] S. H. Huang, S. X. Chai, X. S. Xia, Q. Chen, and D. Y. Shu. Compression deformation behavior and processing map of pure copper. *Strength of Materials*, 48(1):98–106, 2016.

[334] Dong-Hyeon Kim and Choon-Man Lee. Experimental investigation on machinability of titanium alloy by laser-assisted end milling. *Metals*, 11:1552, 09 2021.

[335] Geoffrey Ingram Taylor and H. Quinney. The latent energy remaining in a metal after cold working. *Proceedings of the Royal Society of London. Series A Containing Papers of a Mathematical and Physical Character*, 143(849):307–326, 1934.

[336] Mykola Kulakov, Salaheddin Rahimi, and S. Lee Semiatin. Effect of deformation heating on microstructure evolution during hot forging of ti-6al-4v. *Metallurgical and Materials Transactions A*, 53(2):407–419, 2022.

[337] D. Rittel, L. H. Zhang, and S. Osovski. The dependence of the Taylor-Quinney coefficient on the dynamic loading mode. *Journal of the Mechanics and Physics of Solids*, 107:96–114, 2017.

[338] Hashem M. Mourad Charles K. C. Lieou and Curt A. Bronkhorst. Strain localization and dynamic recrystallization in polycrystalline metals: Thermodynamic theory and simulation framework. *International Journal of Plasticity*, 119:171–187, 2019.

[339] G. C. Soares and M. Hokka. The Taylor-Quinney coefficients and strain hardening of commercially pure titanium, iron, copper, and tin in high rate compression. *International Journal of Impact Engineering*, 156:103940, 2021.

[340] Rahul Jain, Surjya K. Pal, and Shiv B. Singh. 5 - Numerical modeling methodologies for friction stir welding process. In J. Paulo Davim, editor, *Computational Methods and Production Engineering*, Woodhead Publishing Reviews: Mechanical Engineering Series, pages 125–169. Woodhead Publishing, 2017.

[341] Florian Bachmann, Ralf Hielscher, and Helmut Schaeben. Grain detection from 2d and 3d EBSD data - Specification of the MTEX algorithm. *Ultramicroscopy*, 111(12):1720–1733, 2011.

[342] D. G. Brandon. The structure of high-angle grain boundaries. *Acta metallurgica*, 14(11):1479–1484, 1966.

[343] International Organization for Standardization (ISO). Metallic materials: Vickers hardness test, ISO 6507-1:2018, 2018.

[344] Philip J. Withers, Charles Bouman, Simone Carmignato, Veerle Cnudde, David Grimaldi, Charlotte K. Hagen, Eric Maire, Marena Manley, Anton Du Plessis, and Stuart R. Stock. X-ray computed tomography. *Nature Reviews Methods Primers*, 1(1):18, 2021.

[345] Abdul J. Jerri. The shannon sampling theorem - its various extensions and applications: A tutorial review. *Proceedings of the IEEE*, 65(11):1565–1596, 1977.

[346] Shinji Kumai, Yoshimasa Takayama, Takayuki Tsuchida, Shoichi Hirosawa, Kenji Matsuda, Tatsuo Sato, Hideo Yoshida, and Yoko Urata. ICAA11 - The 11th international conference on aluminium alloys. *Keikinzoku/Journal of Japan Institute of Light Metals*, 59(2):95–99, February 2009.

[347] W. Pantleon. Resolving the geometrically necessary dislocation content by conventional electron backscattering diffraction. *Scripta Materialia*, 58(11):994–997, 2008.

[348] E. Kroner. Dislocations and continuum mechanics. *Appl. Mech. Rev*, 15(8):599–606, 1962.

[349] Qing Wang, Peng Yang, Baorui Zhang, Hui Fan, Xuexia Xu, Wenbin Li, Xiaoliang Fan, Jinfeng Wang, and Haimin Ding. Microstructure and texture evolution of cold rolled 1070 al alloy during the subsequent annealing treatment. *Results in Physics*, 13:102178, 2019.

[350] Anuj Mishra, M. Martin, N. N. Thadhani, B. K. Kad, Edward A. Kenik, and M. A. Meyers. High-strain-rate response of ultra-fine-grained copper. *Acta materialia*, 56(12):2770–2783, 2008.

[351] L. E. Murr, A. C. Ramirez, S. M. Gaytan, M. I. Lopez, E. Y. Martinez, D. H. Hernandez, and E. Martinez. Microstructure evolution associated with adiabatic shear bands and shear band failure in ballistic plug formation in ti-6al-4v targets. *Materials Science and Engineering: A*, 516(1-2):205–216, 2009.

[352] Dengke Yang, Yang An, Pavel Cizek, and Peter Hodgson. Development of adiabatic shear band in cold-rolled titanium. *Materials Science and Engineering: A*, 528(12):3990–3997, 2011.

[353] Qing Wang, Peng Yang, Baorui Zhang, Hui Fan, Xuexia Xu, Wenbin Li, Xiaoliang Fan, Jinfeng Wang, and Haimin Ding. Microstructure and texture evolution of cold rolled 1070 al alloy during the subsequent annealing treatment. *Results in Physics*, 13:102178, 2019.

[354] Hai bo Lin. Dynamic recrystallization behavior of 6082 aluminum alloy during hot deformation. *Advances in Mechanical Engineering*, 13(9):16878140211046107, 2021.

[355] José Luis Amorós. *The laue method*. Elsevier, 2012.

[356] S. F. Exell and D. H. Warrington. Sub-grain boundary migration in aluminium. *The Philosophical Magazine: A Journal of Theoretical Experimental and Applied Physics*, 26(5):1121–1136, 1972.

[357] Jiaxin Lv, Jing-Hua Zheng, Victoria A. Yardley, Zhusheng Shi, and Jianguo Lin. A review of microstructural evolution and modelling of aluminium alloys under hot forming conditions. *Metals*, 10(11), 2020.

[358] David Canelo-Yubero, Zsolt Kovács, J.F. Thierry Simonet Fotso, Domonkos Tolnai, Norbert Schell, Istvan Groma, and Cecilia Poletti. In-situ characterization of continuous dynamic recrystallization during hot torsion of an al-si-mg alloy. *Journal of Alloys and Compounds*, 822:153282, 2020.

[359] M C Poletti, T Simonet-Fotso, D Halici, D Canelo-Yubero, F Montheillet, D Piot, Z Kovács, N Schell, and D Tolnai. Continuous dynamic recrystallization during hot torsion of an aluminum alloy. *Journal of Physics: Conference Series*, 1270(1):012049, aug 2019.

[360] S. Gourdet and F. Montheillet. An experimental study of the recrystallization mechanism during hot deformation of aluminium. *Materials Science and Engineering: A*, 283(1):274–288, 2000.

[361] H. E. Hu, L. Zhen, L. Yang, W. Z. Shao, and B. Y. Zhang. Deformation behavior and microstructure evolution of 7050 aluminum alloy during high temperature deformation. *Materials Science and Engineering: A*, 488(1):64–71, 2008.

[362] David Connolly, Giribaskar Sivaswamy, Salaheddin Rahimi, and Vassili Vorontsov. Miniaturised experimental simulation of open-die forging. *Journal of Materials Research and Technology*, 26:3146–3161, 2023.

[363] S.L Semiatin, V Seetharaman, and I Weiss. Flow behavior and globularization kinetics during hot working of ti-6al-4v with a colony alpha microstructure. *Materials Science and Engineering: A*, 263(2):257–271, 1999.

[364] Paul M. Souza, Giribaskar Sivaswamy, Aurik Andreu, and Salaheddin Rahimi. A novel cyclic thermal treatment for enhanced globularisation kinetics in ti-6al-4v alloy: Experimental, constitutive and fe based analyses. *Journal of Alloys and Compounds*, 898:162859, 2022.

[365] Rushikesh Sabban, Sumit Bahl, Kaushik Chatterjee, and Satyam Suwas. Globularization using heat treatment in additively manufactured ti-6al-4v for high strength and toughness. *Acta Materialia*, 162:239–254, 2019.

[366] Jian Zhang, Hongwei Li, and Mei Zhan. Review on globularization of titanium alloy with lamellar colony. *Manufacturing Review*, 7:18, 01 2020.

[367] Madeleine Bignon, Emmanuel Bertrand, Pedro E. J. Rivera-Díaz del Castillo, and Franck Tancret. Martensite formation in titanium alloys: Crystallographic and compositional effects. *Journal of Alloys and Compounds*, 872:159636, 2021.

[368] Vivian Tong, Sudha Joseph, Abigail Ackerman, David Dye, and T. Britton. Using transmission kikuchi diffraction to characterise α variants in an $\alpha + \beta$ titanium alloy. *Journal of Microscopy*, 267, 01 2017.

[369] Delai Ouyang, Xia Cui, Xixin Lan, Xingcai Wan, and Longteng Pan. Experimental study and numerical simulation of lamellar globularization for tc21 titanium alloy during multidirectional forging. *Materials Research Express*, 9(8), 2022. Average grain size;Fe simulation;Globularization;Globularization mechanism;Key factors;Lamellar globularization;Multidirectional forging;SEM-EDS;Single pass;TC21 titanium alloys;.

[370] Yu Jin, Yanqin Zhang, Guowei Zhao, and Wei Li. Kinetics and crystallography of globularization in the additively manufactured ti-6al-4v. *Results in Engineering*, 18:101140, 2023.

[371] Liqun Niu, Qi Zhang, Bo Wang, Bin Han, Hao Li, and Tangjie Mei. A modified hansel-spittel constitutive equation of ti-6al-4v during cogging process. *Journal of Alloys and Compounds*, 894:162387, 2022.

[372] Z. X. Zhang, S. J. Qu, A. H. Feng, and J. Shen. Achieving grain refinement and enhanced mechanical properties in ti-6al-4v alloy produced by multidirectional isothermal forging. *Materials Science and Engineering: A*, 692:127–138, 2017.

[373] F. Pilehva, A. Zarei-Hanzaki, S. Moemeni, and A. R. Khalesian. High-temperature deformation behavior of a ti-6al-7nb alloy in dual-phase ($\alpha+ \beta$) and single-phase (β) regions. *Journal of Materials Engineering and Performance*, 25:46–58, 2016.

[374] Indranil Lahiri, Debrupa Lahiri (Mondal), and S. Bhargava. Effect of prior β processing on superplasticity of ($\alpha + \beta$) thermomechanically treated ti–6al–4v alloy. *Materials and Manufacturing Processes*, 18(4):621–635, 2003.

[375] A. M. Zhao, H. Yang, X. G. Fan, P. F. Gao, R. Zuo, and M. Meng. The flow behavior and microstructure evolution during ($\alpha+\beta$) deformation of β wrought ta15 titanium alloy. *Materials & Design*, 109:112–122, 2016.

[376] H. Dyja, A. A. Tukibay, and S. A. Mashekov. The influence of technological conditions of the process of cogging in flat dies on the quality of two-phase titanium alloys. *Archives of Metallurgy and Materials*, 61(2A):671 – 676, 2016. Cogging;Effective stress;Flat dies;Stress strain state;Tilting;.

[377] P. Ari-Gur and S. L. Semiatin. Evolution of microstructure, macrotexture and microtexture during hot rolling of ti-6al-4v. *Materials Science and Engineering: A*, 257(1):118–127, 1998.

[378] I. Weiss, F. H. Froes, D. Eylon, and G. E. Welsch. Modification of alpha morphology in ti-6al-4v by thermomechanical processing. *Metallurgical Transactions A*, 17(11):1935–1947, 1986.

[379] Tadashi Furuhara, B. Poorganji, H. Abe, and T. Maki. Dynamic recovery and recrystallization in titanium alloys by hot deformation. *Jom*, 59:64–67, 2007.

[380] N. Stefansson and S. L. Semiatin. Mechanisms of globularization of ti-6al-4v during static heat treatment. *Metallurgical and Materials Transactions A*, 34(3):691–698, 2003.

[381] S. Zherebtsov, M. Murzinova, G. Salishchev, and S. L. Semiatin. Spheroidization of the lamellar microstructure in ti–6al–4v alloy during warm deformation and annealing. *Acta Materialia*, 59(10):4138–4150, 2011.

[382] Hong-Wu Song, Shi-Hong Zhang, and Ming Cheng. Dynamic globularization kinetics during hot working of a two phase titanium alloy with a colony alpha microstructure. *Journal of Alloys and Compounds*, 480(2):922–927, 2009.

[383] Kai xuan Wang, Wei dong Zeng, Yong qing Zhao, Yi tao Shao, and Yi gang Zhou. Prediction of dynamic globularization of ti-17 titanium alloy with initial lamellar microstructure during hot compression. *Materials Science and Engineering: A*, 527(23):6193–6199, 2010.

[384] Z.C. Sun, H. Yang, G.J. Han, and X.G. Fan. A numerical model based on internal-state-variable method for the microstructure evolution during hot-working process of ta15 titanium alloy. *Materials Science and Engineering: A*, 527(15):3464–3471, 2010.

[385] Bijish Babu and Lars-Erik Lindgren. Dislocation density based model for plastic deformation and globularization of ti-6al-4v. *International Journal of Plasticity*, 50:94–108, 2013.

[386] Pengfei Gao, He Yang, Xiaoguang Fan, and Shuai Zhu. Unified modeling of flow softening and globularization for hot working of two-phase titanium alloy with a lamellar colony microstructure. *Journal of Alloys and Compounds*, 600:78–83, 2014.

[387] M. Fabris. *Evolution of Globularisation in Ti-6Al-4V Alloy During Secondary Cogging Operations Under Industrial Scale Conditions*. University of Strathclyde, 2022.

[388] X.G. Fan, H.J. Zheng, Y. Zhang, Z.Q. Zhang, P.F. Gao, M. Zhan, and J. Liu. Acceleration of globularization during interrupted compression of a two-phase titanium alloy. *Materials Science and Engineering: A*, 720:214–224, 2018.

[389] Bipin Kedia, I. Balasundar, and T. Raghu. Globularisation of alpha lamellae in titanium alloy : Effect of strain, strain path and starting microstructure. *Transactions of the Indian Institute of Metals*, 71, 04 2018.

[390] Azdine Nait-Ali, Samuel Hémery, and Mikael Gueguen. How macrozone size and morphology influence yield in titanium alloys investigated using fast Fourier transform-based crystal plasticity simulations. *International Journal of Solids and Structures*, 216:1–16, 2021.

[391] B.-A. Behrens, A. Bouguecha, I. Lüken, J. Mielke, and M. Bistron. 5.11 - tribology in hot forging. In Saleem Hashmi, Gilmar Ferreira Batalha, Chester J. Van Tyne, and Bekir Yilbas, editors, *Comprehensive Materials Processing*, pages 211–234. Elsevier, Oxford, 2014.

Appendices

Appendix A: Engineering Drawings

These engineering drawings are a collation of all custom design and manufactured components that have been highlighted in Chapter 4: Equipment Design.

The engineering drawings are presented as one collected appendix on seperate pages.

PLEASE TURN OVER.

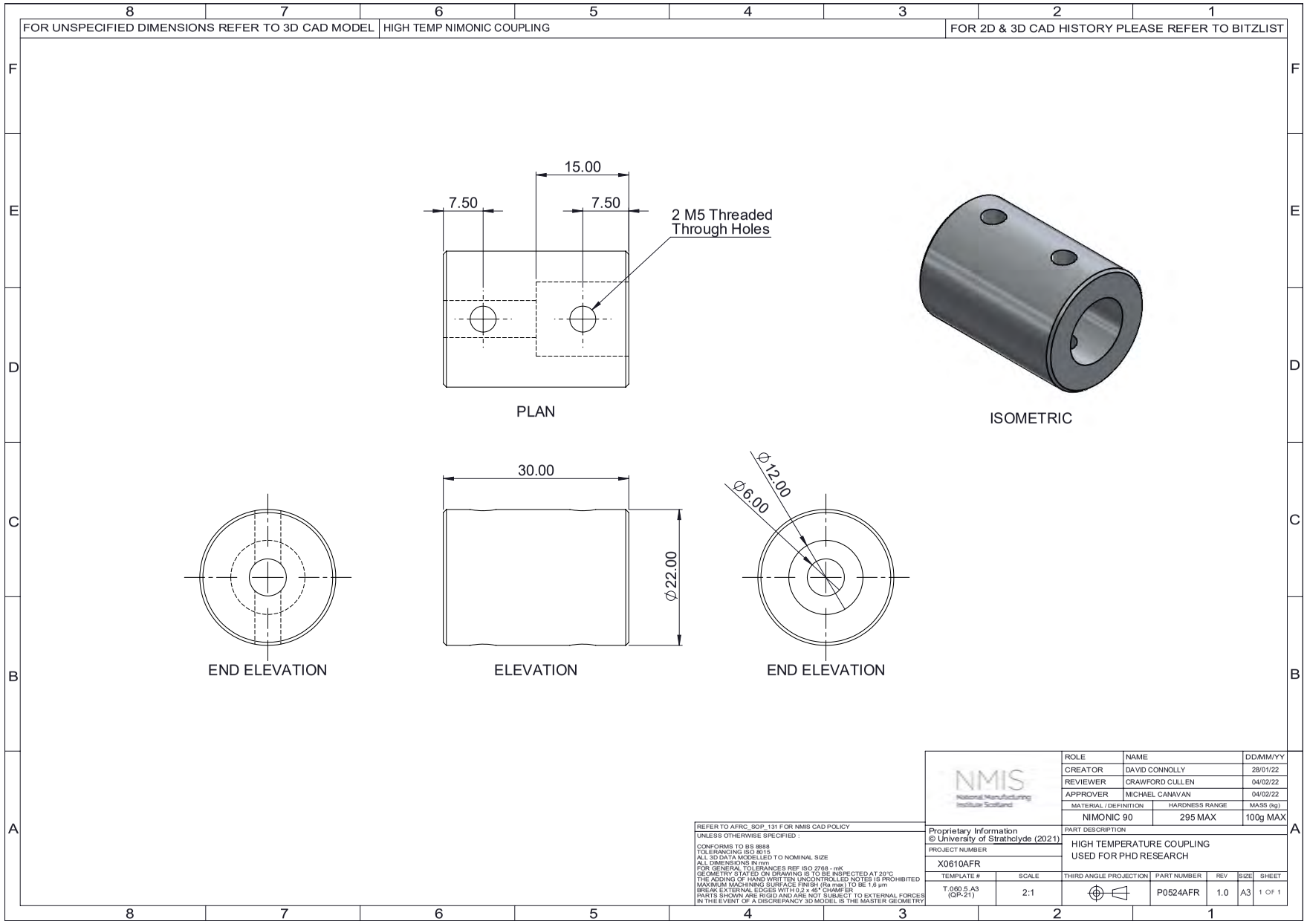

Figure 7.1: CAD Enginnering drawing for type 316 stainless steel and Nimonic®-90 high temperature coupling.

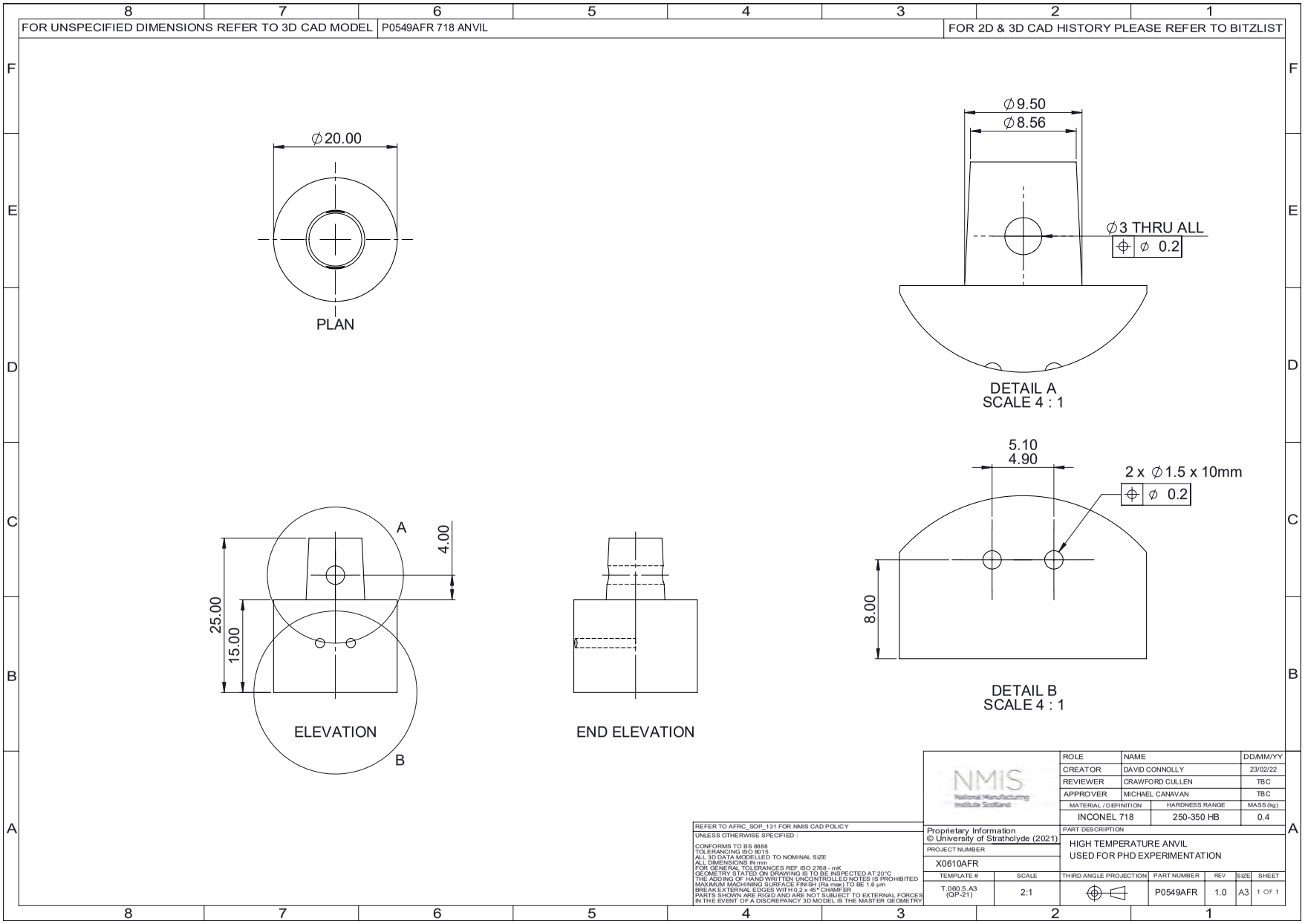

Figure 7.2: CAD Enginnering drawing for IN718 alloy, and Nimonic®-90 nickel-based superalloy high temperature dies.

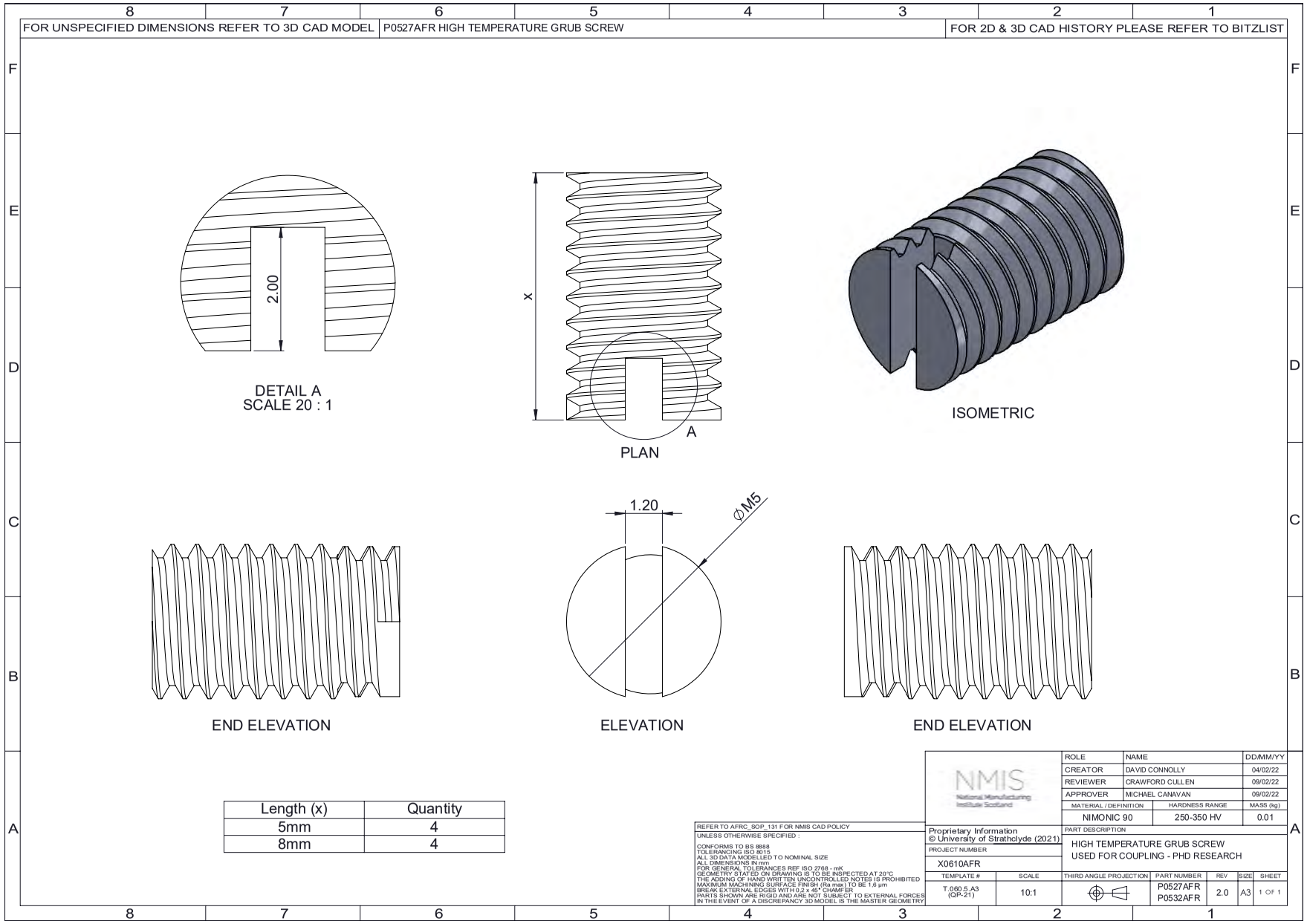

Figure 7.3: CAD Enginnering drawing for Nimonic®-90 high temperature grub screws used with the Nimonic®-90 manipulator rod and coupling.

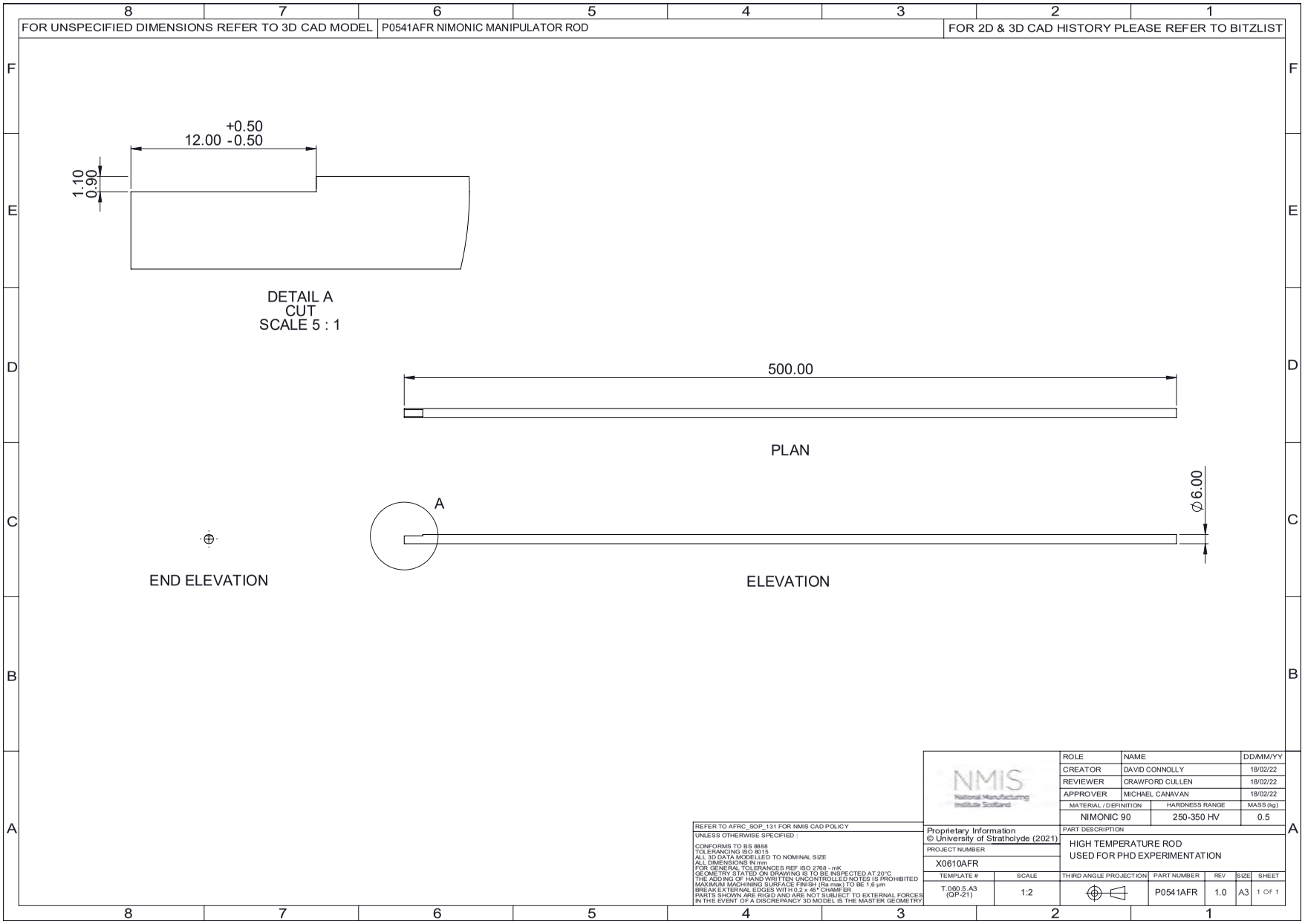

Figure 7.4: CAD Enginnering drawing for Nimonic®-90 high temperature grub screws used with the Nimonic®-90 manipulator rod and coupling.

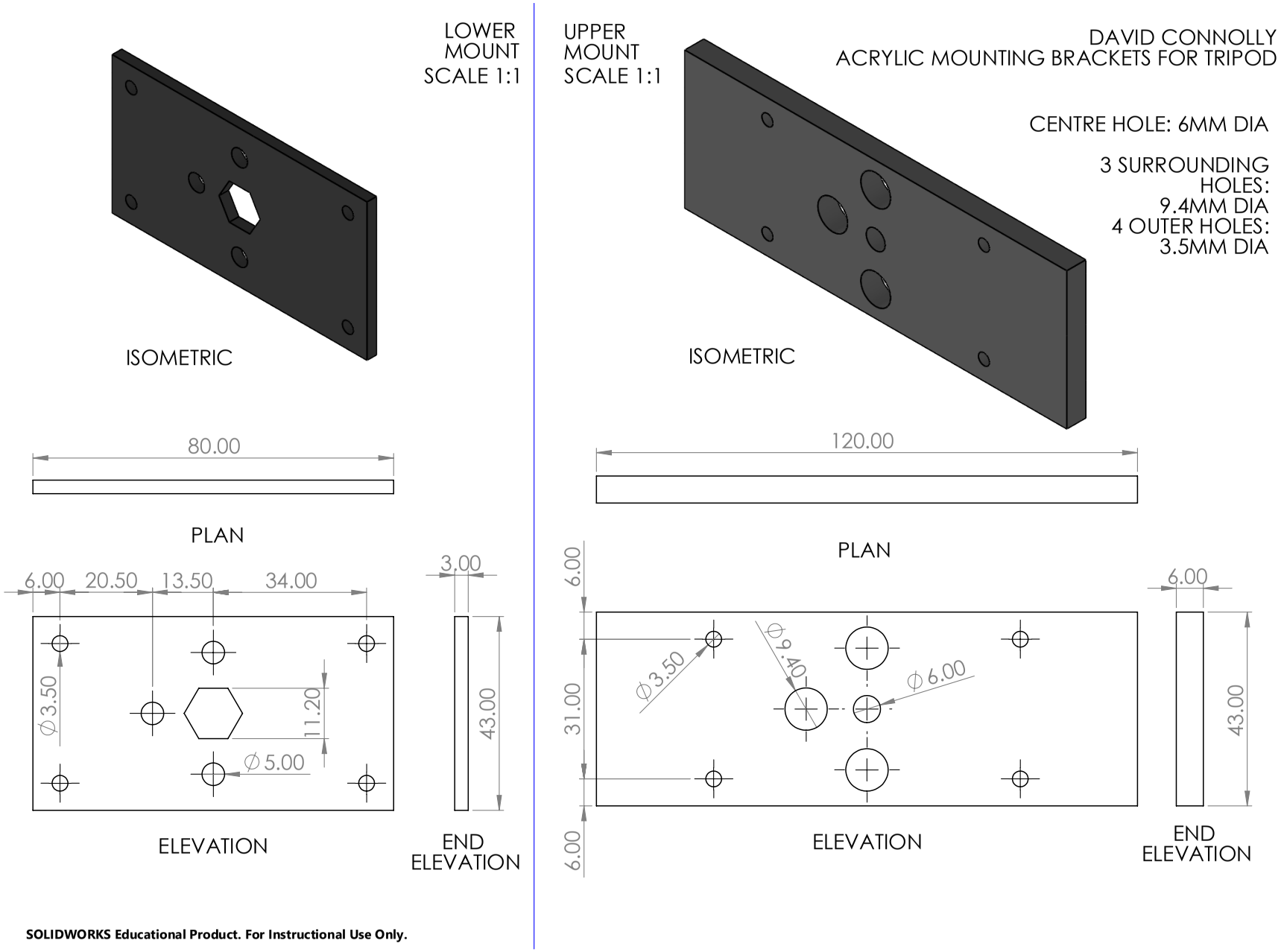

Figure 7.5: CAD Enginnering drawing for Manfrotto™ tripod mount adaptor subassembly of acrylic components for manipulator arm.

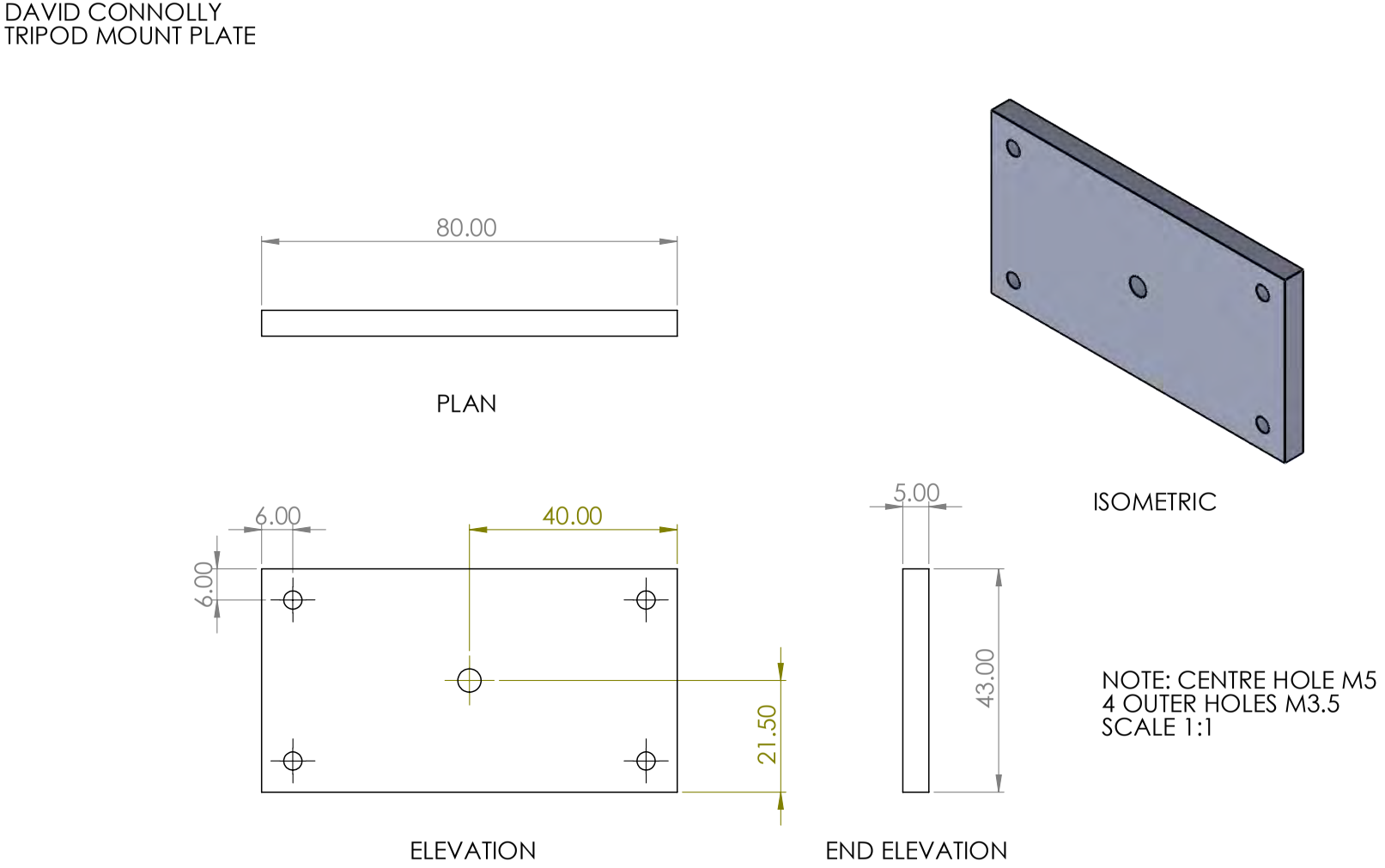

Figure 7.6: CAD Enginnering drawing for Manfrotto™ tripod mount of metal plate as part of adaptor subassembly for manipulator.

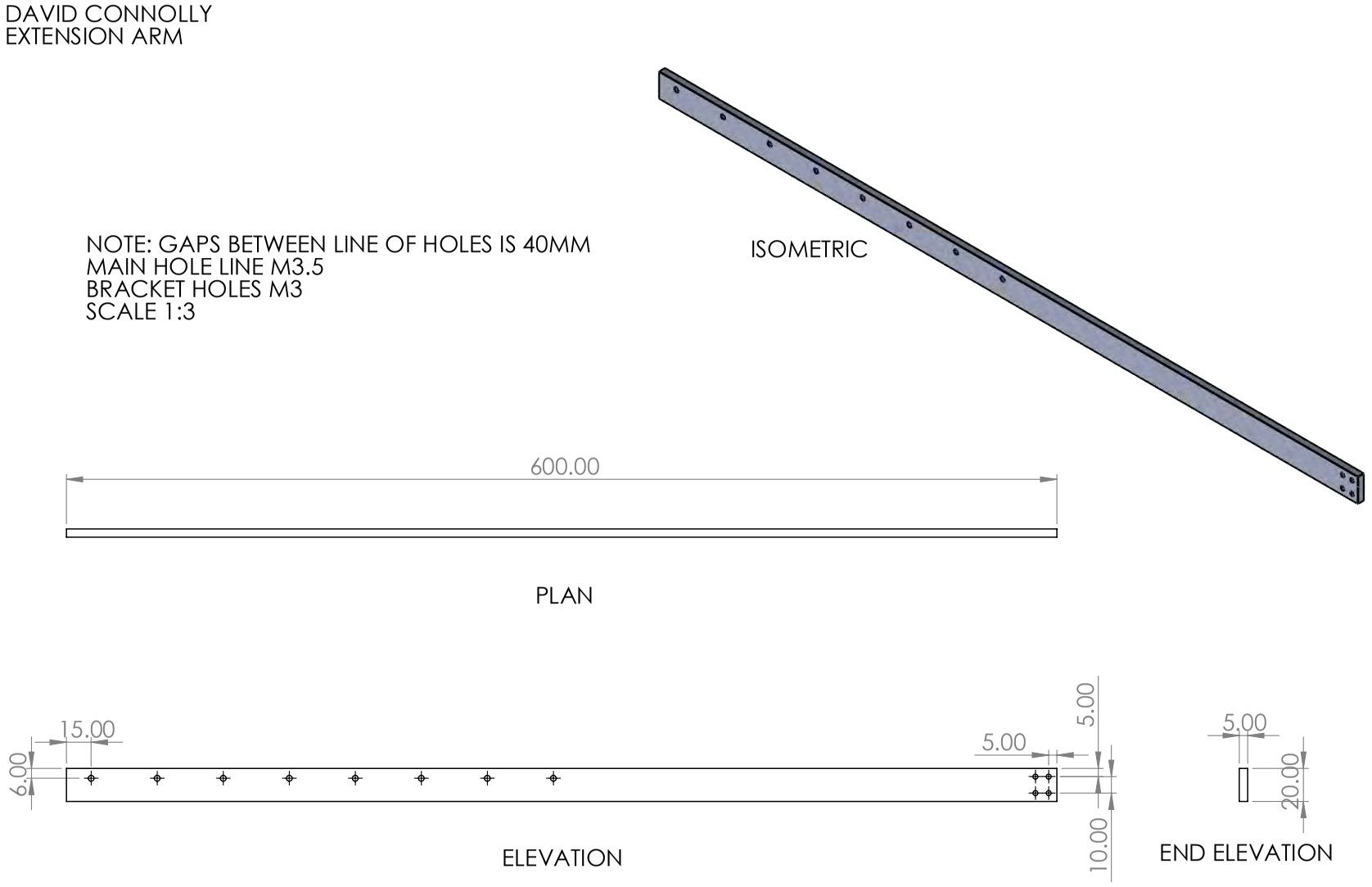

Figure 7.7: CAD Enginnering drawing for type 316 steel manipulator arm extension.

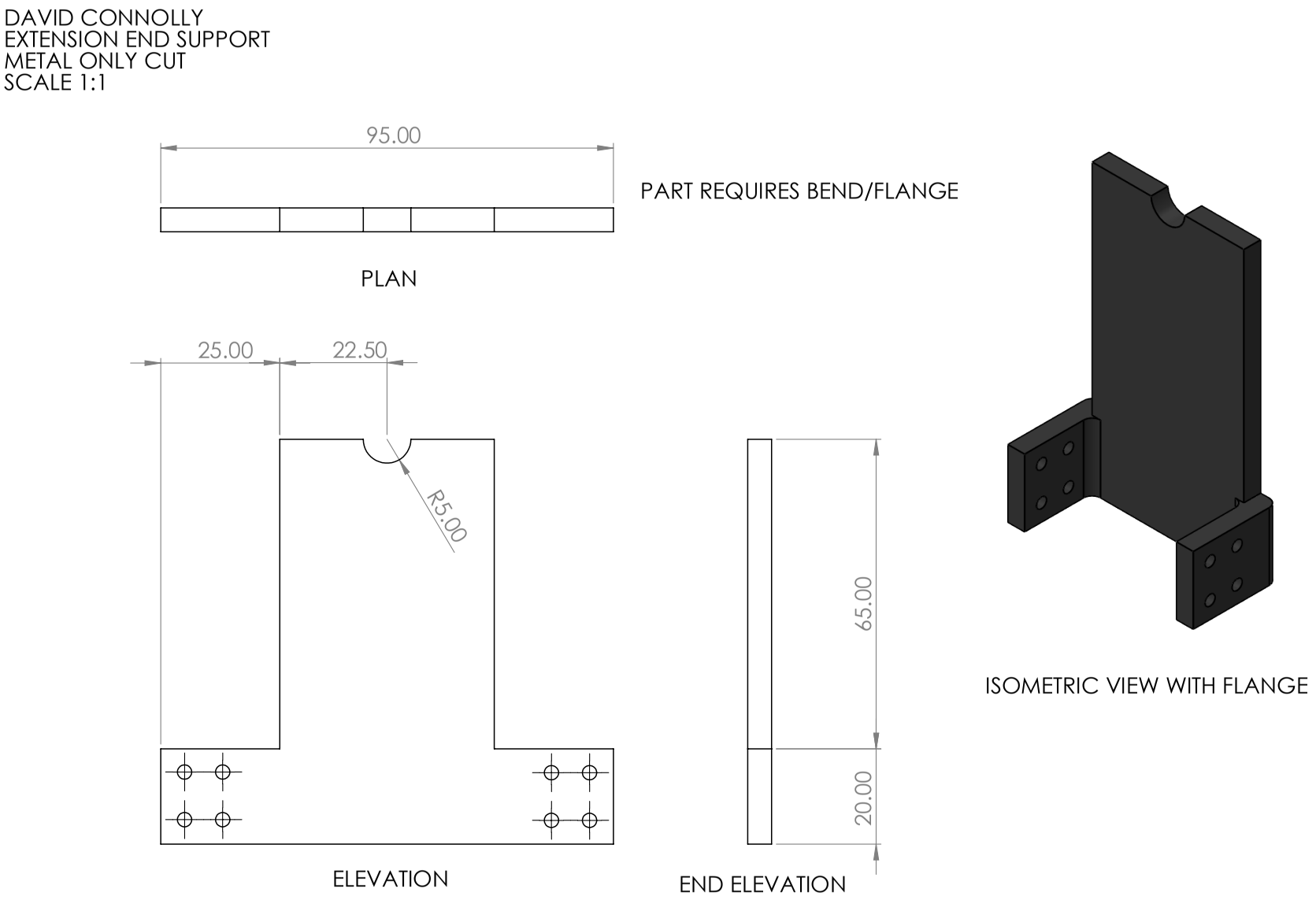

Figure 7.8: CAD Enginnering drawing for type 316 steel manipulator arm extension end bracket.

Appendix B: Arduino Code

```
1 //Included Libraries
2 #include <Wire.h>                // Library to use the convenient i2c communication
      protocol
3 #include <LiquidCrystal_I2C.h> // Library to control a character LCD via i2c bus
4
5 //Pin definitions for x-axis (translational) motor
6 #define xDir     34       // x-axis direction pin
7 #define xStep    35      // x-axis step pin
8 #define xSleep   36     // x-axis sleep pin
9 #define xStop1   40    // x-axis end-stop 1 QQQ Rear stop
10 #define xStop2   41   // x-axis end-stop 2 QQQ Forward stop
11
12 //Pin definitions for z-axis (rotational) motor
13 #define zDir     42     // z-axis direction pin
14 #define zStep    43    // z-axis step pin
15 #define zSleep   44   // z-axis sleep pin
16
17 //Pin definitions for Joystick
18 #define xJoyPin        A8       // x-axis analog joystick pin
19 #define zJoyPin        A9      // z-axis analog joystick pin
20 #define joyButtonPin   48     // joystick button pin
21
22 //Pin definitions for keypad
23 #define DOWN     4       // down button pin
24 #define LEFT     5      // left button pin
25 #define UP       6     // up button pin
26 #define RIGHT    7    // right button pin
27 #define SELECT   8   // select button pin
28
29 #define FORGE_SEND       22   //Pin to SEND signals to the zwick press
30 #define FORGE_RECEIVE    24   //Pin to RECEIVE signals from the zwick press
31
32 /* ******************* GLOBAL VARIABLES ********************** */
33
34 // Cogging experiment automation parameter variables
35 int noOfOperations;                    //Required for cogging automation - returns to
       initial position
36 int passCounter =           1;         //Integer set for how many times the workpiece
       is pressed
37 unsigned long stepSpeed =    1000;     //Integer set to vary the speed of the motor
      during automation (tied to hammerTime)
38 unsigned long hammerTime =  1000000;  //Integer set to vary the time between motor
      movements during automation (tied to stepSpeed)
39 int withdraw;                         //Integer for setting logic of
      withdrawEnabledFlag between 1 or 0, true or false
40 int reverse;                          //Integer for setting logic of
      reverseOperation between 1 or 0, true or false
41 int Xsteps = 200;                     //Base set for Xsteps 200 being one full
      rotation, set for how
42 int Zsteps = 50;
43
44 // Stepper motor control variables
45 unsigned long currentMicros;                    //Sets the current micros to keep
      count
46 unsigned long previousMicros = 0;                //Originally sets the previous
      micros count to 0 and is carried and changed through the code
47 unsigned long microsBetweenStepsManual = 1000;   //Sets the very fast step speed of
      the motor for continuous movement
48 unsigned long microsBetweenManualHammer = 1000;  //Long Integer set the speed of the
       motor turns when buttons are pressed in 4th option
```

```
49 bool pulseXOn = LOW;                                    //Boolean for Pulse of X motor
50 bool pulseZOn = LOW;                                    //Boolean for Pulse of Z motor
51
52 // System state flags
53 bool rigAlignmentFlag =       false;  //True when RIG ALIGNMENT option is chosen in
       main menu and enables the Joystick
54 bool experimentSetupFlag =    false;  //True when EXPERIMENT SETUP is chosen in main
        menu
55 bool runExperimentFlag =      false;  //True when RUN EXPERIMENT is chosen in main
       menu
56 bool manualOperationFlag =    false;  //True when EXPERIMENT SETUP is chosen in main
        menuand enables Joystick
57 bool setupCompleteFlag =      false;  //True when all questions completed allowing
       experiment program to begin
58 bool experimentCompleteFlag = false;  //True once experiment cycle has been
       completed and exits back to main menu
59 bool specimenInsertedFlag =   false;  //False when specimen is not inserted into
       working area
60 bool specimenWithdrawnFlag =  false;  //True when specimen is withdrawn all the way
       to rear end-stop
61 bool withdrawEnabledFlag =    false;  //Option to withdraw specimen at end of
       program (true) or leave in place (false)
62 bool questionOneFlag =        true;  //True once the NO OF PASSES (EVENTS) question
       has been completed for automation
63 bool questionTwoFlag =        false;  //True once the SPEED question has been
       completed for automation
64 bool questionThreeFlag =      false;  //True once the Zsteps angle for hammering
       steps has been set
65 bool questionFourFlag =       false;  //True once the Xsteps withdrawing number of
       steps has been set
66 bool questionFiveFlag =       false;  //True once question is completed to be
       reverse to original direction cogging
67 bool coggingDirection =       false;  //True once question is selected to be reverse
        to original direction cogging
68 bool questionSixFlag =        false;  //True once the WITHDRAW question has been
       completed for automation
69 bool questionSevenFlag =      false;  //True once the previous question has been
       completed to go to confirm settings
70 bool finishedFlag =           false;  //This is true once the first experiment cycle
        is complete
71
72 //Main menu items shown on LCD screen
73 String  menuItems[] = {"RIG-ALIGNMENT","EXPERIMENT-SETUP","RUN-EXPERIMENT","MANUAL-
       OPERATION"};
74 int     noOfMenuItems = sizeof(menuItems)/sizeof(String); // Count number of menu
       items in above string array
75
76 // Navigation button variables
77 unsigned long keyPadPressTime = 0;
78 int savedDistance = 0;
79
80 // LCD menu control variables
81 bool  lcdRefreshFlag = false;     // LCD is refreshed if false
82 bool  menuRefreshFlag = false;    // Main menu is redrawn if false
83 bool  cursorRefreshFlag = false;  // Cursor is retdrawn if false
84 int   cursorPosition = 0;         // Cursor position on LCD (between 0 and 3 on 20x4
        LCD)
85
86 // Dummy counter variables to use in for loops etc.
87 int i;
88
89 // Create custom characters for the menu display
90 byte menuCursor[8] = { // Cursor chevron
```

```
  B01000, //  *
  B00100, //   *
  B00010, //    *
  B00001, //     *
  B00010, //    *
  B00100, //   *
  B01000, //  *
  B00000  //
};

// Set up the I2C LCD screen (i2c address, characters per line, no. of lines)
LiquidCrystal_I2C lcd(0x27,20,4);
//
```

```
// Initial setup
//
```

```
void setup() {

  // Begin serial monitor at 9600 baud
  Serial.begin(9600);

  //Initialise the LCD screen and turn on backlight
  lcd.init();
  lcd.backlight();

  //Create custom menu characters
  lcd.createChar(0, menuCursor); // selection cursor

  //Set the motor pins as OUTPUTS & endstop pins as INPUTS
  pinMode(xStep,  OUTPUT); // X-Axis motor step pin
  pinMode(xDir,   OUTPUT); // X-Axis motor direction pin
  pinMode(xSleep, OUTPUT); // X-Axis motor sleep pin
  pinMode(xStop1, INPUT);  // Endstop 1 pin
  pinMode(xStop2, INPUT);  // Endstop 2 pin
  pinMode(zStep,  OUTPUT); // Z-Axis motor step pin
  pinMode(zDir,   OUTPUT); // Z-Axis motor direction pin
  pinMode(zSleep, OUTPUT); // Z-Axis motor sleep pin

  //Set the button pins as as inputs with internal pullups
  pinMode(DOWN,   INPUT_PULLUP);  // DOWN   (4)
  pinMode(LEFT,   INPUT_PULLUP);  // LEFT   (5)
  pinMode(UP,     INPUT_PULLUP);  // UP     (6)
  pinMode(RIGHT,  INPUT_PULLUP);  // RIGHT  (7)
  pinMode(SELECT, INPUT_PULLUP);  // SELECT (8)
  //RESET is linked directly on the board

  pinMode(FORGE_SEND,    OUTPUT); //Pin 22
  pinMode(FORGE_RECEIVE, INPUT);  //Pin 24

  // Set up joystick button pin as input with internal pullup
  pinMode(joyButtonPin, INPUT_PULLUP);

  //Sleep both motors initially (LOW to enable, HIGH to disable)
  digitalWrite(xSleep, HIGH);
  digitalWrite(zSleep, HIGH);

}
//
```

```
148 //Main microcontroller loop
149 //
    ------------------------------------------------------------------------------

150 void loop() {
151
152   // Draw main menu and cursor on LCD avoiding flicker (i.e. unnecessary LCD
        refreshing)
153
154   if (menuRefreshFlag == false) { // Check if refresh is needed
155     mainMenuDraw();               // Draw the main menu options
156     menuRefreshFlag = true;       // Mark menu state as refreshed
157   }
158
159   if (cursorRefreshFlag == false) { // Check if refresh is needed
160     drawCursor();                   // Draw the cursor chevron symbol
161     cursorRefreshFlag = true;       // Mark cursor state as refreshed
162   }
163
164   // Operate main menu using input buttons
165
166   operateMainMenu();                // Gets input from buttons and returns choice
        flag
167
168   // If RIG ALIGNMENT menu option is chosen
169
170   while (rigAlignmentFlag == true) { // Check if RIG ALIGNMENT menu option is chosen
171     rigAlignment();                  // Run rig alignment function
172   }
173
174   // If EXPERIMENT SETUP menu option is chosen
175
176   while (experimentSetupFlag == true) { // Check if EXPERIMENT SETUP menu option is
        chosen
177     experimentSetup();// Run experiment setup function
178     if (setupCompleteFlag == true){
179       break;
180     }
181   }
182
183   // If RUN EXPERIMENT menu option is chosen
184
185   while (runExperimentFlag == true) { // Check if RUN EXPERIMENT menu option is
        chosen
186
187     if(setupCompleteFlag == false){
188       digitalWrite(zSleep,LOW);
189
190       if (digitalRead(LEFT) == LOW) {      // If LEFT button is pressed
191         runExperimentFlag =      false;
192         setupCompleteFlag =      false;
193         experimentCompleteFlag = false;
194         exitMain();
195         digitalWrite(xSleep, HIGH);
196         digitalWrite(zSleep, HIGH);
197         break;
198       }
199     }
200
201     if(setupCompleteFlag == true) {   // Check if experiment program setup is
          complete
202
203       while(specimenInsertedFlag == false) {
```

```
204         insertSpecimen();
205       }
206
207       if(specimenInsertedFlag == true && experimentCompleteFlag == false){
208       for(int u = 0; u <= passCounter; u++) {
209         runExperiment();
210
211         if(u >= passCounter  && withdrawEnabledFlag == true){
212           withdrawSpecimen();
213           experimentCompleteFlag = true;
214         }
215
216         while(u >= passCounter && withdrawEnabledFlag == false){
217           experimentCompleteFlag = true;
218           digitalWrite(xSleep, HIGH);
219           digitalWrite(zSleep, HIGH);
220           break;
221         }
222         if(experimentCompleteFlag == true){
223           experimentCompleted();
224           break;
225         }
226       }
227     }
228   }
229   if (finishedFlag == true){
230      break;
231   }
232  }
233
234   // If MANUAL OPERATION menu option is chosen
235
236   while (manualOperationFlag == true) {
237     manualOperation(); // Run manual operation function
238   }
239
240 }
241 //
    ---------------------------------------------------------------------------

242 // Draw the menu items based on menuItems string array
243 //
    ---------------------------------------------------------------------------

244 void mainMenuDraw() {
245
246   lcd.clear();
247
248   for (i = 0; i < 4; i++) {
249     lcd.setCursor(1, i);
250     lcd.print(menuItems[i]);
251   }
252 }
253 //
    ---------------------------------------------------------------------------

254 // Draw the cursor based on cursorPosition variable
255 //
    ---------------------------------------------------------------------------

256
257 void drawCursor() {
258   for (i = 0; i < 4; i++){
```

```
259     lcd.setCursor(0, i);
260     lcd.print("-");
261   }
262   lcd.setCursor(0, cursorPosition);
263   lcd.write(byte(0));
264 }
265
266 //
```

```
267 // Used when LEFT button is pressed for collection of flags to exit to Main Menu
268 //
```

```
269
270 void exitMain(){
271   keyPadPressTime =        millis();  // Update last press time
272   manualOperationFlag =    false;     // End MANUAL OPERATION
273   specimenWithdrawnFlag = false;      //True when specimen is withdrawn all the way
          to rear end-stop
274   withdrawEnabledFlag =    false;     //Option to withdraw specimen at end of program
          (true) or leave in place (false)
275   rigAlignmentFlag =       false;     // End RIG ALIGNMENT
276   lcdRefreshFlag =         false;     // Mark LCD for refresh next time a sub-menu is
          loaded
277   menuRefreshFlag =        false;     // Request main menu to be loaded
278   cursorRefreshFlag =      false;     // Request cursor refresh
279 }
280
281 void exitSimple(){
282   keyPadPressTime =        millis();  // Update last press time
283   lcdRefreshFlag =         false;     // Mark LCD for refresh next time a sub-menu is
          loaded
284   cursorRefreshFlag =      false;     // Request cursor refresh
285 }
286 //
```

```
287 // Main menu navigation
288 //
```

```
289 void operateMainMenu() {
290
291   if (millis() >= keyPadPressTime + 300) { // Only do this at time intervals to
          debounce the button presses
292
293     if (digitalRead(RIGHT) == LOW) { // RIGHT button pressed
294       keyPadPressTime = millis();
295       if (cursorPosition == 0) {        // Rig alignment
296         rigAlignmentFlag = true;
297       } else if (cursorPosition == 1) { // Experiment setup
298         experimentSetupFlag = true;
299         questionOneFlag = true;
300         setupCompleteFlag = false;
301       } else if (cursorPosition == 2) { // Run experiment
302         runExperimentFlag = true;
303       } else if (cursorPosition == 3) { // Manual operation
304         manualOperationFlag = true;
305       }
306
307     } else if (digitalRead(UP) == LOW) { // UP button pressed
308       cursorRefreshFlag = false;
```

```
309       keyPadPressTime = millis();
310       if (cursorPosition > 0 && cursorPosition <= noOfMenuItems - 1){
311         cursorPosition = cursorPosition - 1;
312       } else if (cursorPosition == 0){
313         cursorPosition = noOfMenuItems - 1;
314       }
315
316     } else if (digitalRead(DOWN) == LOW) { // DOWN button pressed
317       cursorRefreshFlag = false;
318       keyPadPressTime = millis();
319       if (cursorPosition >= 0 && cursorPosition < noOfMenuItems - 1){
320         cursorPosition = cursorPosition + 1;
321       } else if (cursorPosition == noOfMenuItems - 1){
322        cursorPosition = 0;
323       }
324     }
325   }
326 }
327 //
```

```
328 // RIG ALIGNMENT function called in the main loop
329 //
```

```
330 void rigAlignment() {
331
332   // Set LCD to RIG ALIGNMENT screen
333   if (lcdRefreshFlag == false) {
334     lcd.clear();
335     lcd.setCursor(1, 0);
336     lcd.print("JOYSTICK-ACTIVE!");
337     lcd.setCursor(1, 1);
338     lcd.print("ALIGN-MACHINE-AXES");
339     lcd.setCursor(1, 3);
340     lcd.print("EXIT:-PRESS-<LEFT>");
341     lcdRefreshFlag = true;
342   }
343
344   microsBetweenStepsManual = 500;     // x motor
345   microsBetweenManualHammer = 1000;   // y motor
346
347   // Sleep x-axis motor if joystick is in central position and quit RIG ALIGNMENT if
        LEFT button is pressed
348   while (analogRead(xJoyPin) >= 400 && analogRead(xJoyPin) <= 600) {
349
350     if (digitalRead(xStop1) == LOW) { // Check end-stop
351         digitalWrite(xSleep,HIGH);        // Disable x-stepper if end-stop triggered
352         break;                            // End while loop
353     }
354
355   if (millis() >= keyPadPressTime + 300) {          //Rotates Top Motor 90 degrees
356   if (digitalRead(SELECT) == LOW){
357   digitalWrite(zDir, HIGH);
358   digitalWrite(zSleep,LOW);
359   for (int i = 0; i < 50; i++){
360     digitalWrite(zStep,HIGH);
361     digitalWrite(zStep,LOW);
362     currentMicros = micros();
363     while(micros() < currentMicros + 1000){
364                                                 }
365   }
366     delay(250);
```

```
367     digitalWrite(zSleep,HIGH);
368       }
369   }
370
371   if (millis() >= keyPadPressTime + 300) {
372   if (digitalRead(DOWN) == LOW){
373   digitalWrite(zDir, LOW);
374   digitalWrite(zSleep,LOW);
375   for (int i = 0; i < 50; i++){
376     digitalWrite(zStep,HIGH);
377     digitalWrite(zStep,LOW);
378     currentMicros = micros();
379     while(micros() < currentMicros + 1000){
380                                                 }
381   }
382     delay(250);
383     digitalWrite(xSleep,HIGH);
384       }
385   }
386
387   if (millis() >= keyPadPressTime + 300) {
388   if (digitalRead(UP) == LOW){
389   digitalWrite(xDir, LOW);
390   digitalWrite(xSleep,LOW);
391   for (int i = 0; i < 50; i++){
392     digitalWrite(xStep,HIGH);
393     digitalWrite(xStep,LOW);
394     currentMicros = micros();
395     while(micros() < currentMicros + 1000){
396                                                 }
397   }
398     delay(250);
399     digitalWrite(xSleep,HIGH);
400       }
401   }
402
403         digitalWrite(xSleep, HIGH);
404         if (millis() >= keyPadPressTime + 300) {    // Only do this at time
              intervals to debounce the button presses
405
406         if (digitalRead(LEFT) == LOW) {      // If LEFT button is pressed
407         exitMain();
408         digitalWrite(xSleep, HIGH);
409         digitalWrite(zSleep, HIGH);
410         //break;                             // End while loop (i.e. exit to main
              menu)
411       }
412      }
413     }
414
415 // Move specimen forward along x if joystick tilted
416  while (analogRead(xJoyPin) >= 600) {
417
418         if (digitalRead(xStop1) == LOW) { // Check end-stop
419         digitalWrite(xSleep,HIGH);        // Disable x-stepper if end-stop triggered
420         break;                            // End while loop
421     }
422
423         digitalWrite(xSleep,LOW); // Enable x-stepper motor
424         digitalWrite(xDir, HIGH); // Set x-stepper direction (HIGH = CCW / LOW = CW)
425         manualXStep();            // Run x-stepper function
426
427         if (digitalRead(LEFT) == LOW) {         // If LEFT button is pressed
```

```
428         exitMain();
429         digitalWrite(xSleep, HIGH);
430         digitalWrite(zSleep, HIGH);
431         break;                          // End while loop (i.e. exit to main menu)
432       }
433   }
434
435   // Move specimen backwards along x if joystick tilted
436   while (analogRead(xJoyPin) <= 400) {
437
438         if (digitalRead(xStop2) == LOW){ // Check end-stop
439         digitalWrite(xSleep,HIGH);       // Disable x-stepper if end-stop triggered
440         break;                           // End while loop
441     }
442
443         digitalWrite(xSleep,LOW); // Enable x-stepper motor
444         digitalWrite(xDir, LOW);  // Set x-stepper direction (HIGH = CCW / LOW = CW)
445         manualXStep();            // Run x-stepper function
446
447         if (digitalRead(LEFT) == LOW) {         // If LEFT button is pressed
448         exitMain();
449         digitalWrite(xSleep, HIGH);
450         digitalWrite(zSleep, HIGH);
451         break;                          // End while loop (i.e. exit to main menu)
452       }
453   }
454
455   while (analogRead(zJoyPin) >= 400 && analogRead(zJoyPin) <= 600) {
456
457         digitalWrite(zSleep, HIGH);
458
459         if (digitalRead(LEFT) == LOW) {         // If LEFT button is pressed
460         exitMain();
461         digitalWrite(xSleep, HIGH);
462         digitalWrite(zSleep, HIGH);
463         break;                          // End while loop (i.e. exit to main menu)
464       }
465   }
466
467   while (analogRead(zJoyPin) >= 600) {
468
469         digitalWrite(zSleep,LOW);
470         digitalWrite(zDir, HIGH);  // (HIGH = anti-clockwise / LOW = clockwise)
471         manualZStep();
472
473         if (digitalRead(LEFT) == LOW) {         // If LEFT button is pressed
474         exitMain();
475         digitalWrite(xSleep, HIGH);
476         digitalWrite(zSleep, HIGH);
477         break;                          // End while loop (i.e. exit to main menu)
478       }
479         }
480
481   while (analogRead(zJoyPin) <= 400) {
482
483         digitalWrite(zSleep,LOW);
484         digitalWrite(zDir, LOW);  // (HIGH = anti-clockwise / LOW = clockwise)
485         manualZStep();
486
487         if (digitalRead(LEFT) == LOW) {         // If LEFT button is pressed
488         exitMain();
489         digitalWrite(xSleep, HIGH);
490         digitalWrite(zSleep, HIGH);
```

```
491         break;                          // End while loop (i.e. exit to main menu)
492       }
493     }
494  }
495 //
```

```
496 // EXPERIMENT SETUP function called in the main loop
497 //
```

```
498 void experimentSetup () {
499
500   // PRINT PAGE 1 - NUMBER OF PASSES - (passCounter)
501   if (lcdRefreshFlag == false && questionOneFlag == true) {
502     lcd.clear();
503     lcd.setCursor(1, 0);
504     lcd.print("NO. OF PASSES");
505     lcd.setCursor(1, 1);
506     lcd.print("= ");
507     lcd.setCursor(18, 1);
508     lcd.print(passCounter);
509     lcd.setCursor(1, 2);
510     lcd.print("SET: <UP/DOWN>");
511     lcd.setCursor(1, 3);
512     lcd.print("SAVE: <RIGHT>");
513     lcdRefreshFlag = true;
514   }
515
516   while(lcdRefreshFlag == true && questionOneFlag == true){
517   if (millis() >= keyPadPressTime + 300) { // Only do this at time intervals to
        debounce the button presses
518
519     if (digitalRead(RIGHT) == LOW) {         // RIGHT button pressed
520       keyPadPressTime = millis();
521       questionOneFlag = false;
522       questionTwoFlag = true;
523       lcdRefreshFlag = false;
524     } else if (digitalRead(UP) == LOW) { // UP button pressed
525       keyPadPressTime = millis();
526       passCounter = passCounter + 1;
527       lcdRefreshFlag = false;
528     } else if (digitalRead(DOWN) == LOW) { // DOWN button pressed
529       keyPadPressTime = millis();
530       passCounter = passCounter - 1;
531       lcdRefreshFlag = false;
532     } else if (digitalRead(LEFT) == LOW) { // LEFT button pressed
533       experimentSetupFlag = false;
534       questionOneFlag = true;
535       exitMain();                                // Exits
            experimentSetupFunctionkeyPadPressTime = millis();
536     }
537
538     if (passCounter >= 5) {
539       passCounter = 1;
540     } else if (passCounter <= 0) {
541       passCounter = 4;
542     }
543   }
544 }
545
546   // PRINT PAGE 2 - SET STEP ANGLE = STRAIN RATE/SPEED OF MOTORS QUESTION
547   if (lcdRefreshFlag == false && questionTwoFlag == true) {
```

```
548     lcd.clear();
549     lcd.setCursor(1, 0);
550     lcd.print("SPEED/HAMMERTIME");
551     lcd.setCursor(1, 1);
552     lcd.print("=");
553     lcd.setCursor(3, 1);
554     lcd.print(stepSpeed);
555     lcd.setCursor(10,1);
556     lcd.print(hammerTime);
557     lcd.setCursor(1, 2);
558     lcd.print("SET:<UP/DOWN>");
559     lcd.setCursor(1, 3);
560     lcd.print("SAVE:<RIGHT>");
561     lcdRefreshFlag = true;
562   }
563
564     while(lcdRefreshFlag == true && questionTwoFlag == true){
565     if (millis() >= keyPadPressTime + 300) { // Only do this at time intervals to
          debounce the button presses
566
567     if (digitalRead(RIGHT) == LOW) {         // RIGHT button pressed
568       keyPadPressTime = millis();
569       questionTwoFlag = false;
570       questionThreeFlag = true;
571       lcdRefreshFlag = false;
572     } else if (digitalRead(UP) == LOW) { // UP button pressed
573       keyPadPressTime = millis();
574       stepSpeed = stepSpeed + 1000;
575       hammerTime = stepSpeed * 1000;
576       lcdRefreshFlag = false;
577     } else if (digitalRead(DOWN) == LOW) { // DOWN button pressed
578       keyPadPressTime = millis();
579       stepSpeed = stepSpeed - 1000;
580       hammerTime = stepSpeed * 1000;
581       lcdRefreshFlag = false;
582     } else if (digitalRead(LEFT) == LOW) { // LEFT button pressed
583       questionOneFlag = true;
584       questionTwoFlag = false;
585       cursorRefreshFlag = false;
586       lcdRefreshFlag = false;
587     }
588
589     if (stepSpeed > 5000) {
590       stepSpeed = 1000;
591     } else if (stepSpeed < 1000) {
592       stepSpeed = 5000;
593     }
594
595     if (hammerTime > 5000000) {
596       hammerTime = 1000000;
597     } else if (hammerTime < 1000000) {
598       hammerTime = 5000000;
599     }
600   }
601 }
602
603   // PRINT PAGE 3 - Zsteps
604   if (lcdRefreshFlag == false && questionThreeFlag == true) {
605     lcd.clear();
606     lcd.setCursor(1, 0);
607     lcd.print("ROTATION-ANGLE");
608     lcd.setCursor(1, 1);
609     lcd.print("=");
```

```
610     lcd.setCursor(1, 2);
611     lcd.print("SET:-<UP/DOWN>");
612     lcd.setCursor(1, 3);
613     lcd.print("SAVE:-<RIGHT>");
614     lcdRefreshFlag = true;
615   }
616
617   while(lcdRefreshFlag == true && questionThreeFlag == true){
618   if (millis() >= keyPadPressTime + 300) { // Only do this at time intervals to
          debounce the button presses
619
620     if (digitalRead(RIGHT) == LOW) {          // RIGHT button pressed
621       keyPadPressTime = millis();
622       questionThreeFlag = false;
623       questionFourFlag = true;
624       lcdRefreshFlag = false;
625     } else if (digitalRead(UP) == LOW) { // UP button pressed
626       keyPadPressTime = millis();
627       Zsteps = Zsteps + 10;
628       lcdRefreshFlag = false;
629     } else if (digitalRead(DOWN) == LOW) { // DOWN button pressed
630       keyPadPressTime = millis();
631       Zsteps = Zsteps - 10;
632       lcdRefreshFlag = false;
633     } else if (digitalRead(LEFT) == LOW) { // LEFT button pressed
634       keyPadPressTime = millis();
635       questionTwoFlag = true;
636       questionThreeFlag = false;
637       cursorRefreshFlag = false;
638       lcdRefreshFlag = false;
639     }
640
641     if (Zsteps >= 101){
642       Zsteps = 25;
643       noOfOperations = 8;
644     } else if (Zsteps <= 0){
645       Zsteps = 100;
646       noOfOperations = 2;
647     }
648     if (Zsteps == 30){
649       Zsteps = 25;
650       noOfOperations = 8;
651     }
652     if (Zsteps == 15){
653       Zsteps = 20;
654       noOfOperations = 10;
655     }
656     if (Zsteps == 35){
657       Zsteps = 40;
658       noOfOperations = 5;
659     }
660     if (Zsteps == 60){
661       Zsteps = 100;
662       noOfOperations = 2;
663     }
664     if (Zsteps == 90){
665       Zsteps = 50;
666       noOfOperations = 4;
667     }
668
669   if (Zsteps == 10){
670       lcd.setCursor(13, 1);
671       lcd.print("18-DEG");
```

```
672     } else if(Zsteps == 20){
673       lcd.setCursor(13, 1);
674       lcd.print("36 DEG");
675     } else if(Zsteps == 25){
676       lcd.setCursor(13, 1);
677       lcd.print("45 DEG");
678     } else if (Zsteps == 40){
679       lcd.setCursor(14, 1);
680       lcd.print("72 DEG");
681     } else if (Zsteps == 50){
682       lcd.setCursor(13, 1);
683       lcd.print("90 DEG");
684     } else if (Zsteps == 100){
685       lcd.setCursor(13, 1);
686       lcd.print("180 DEG");
687     }
688   }
689 }
690
691   // PRINT PAGE 4 - Xsteps
692   if (lcdRefreshFlag == false && questionFourFlag == true) {
693     lcd.clear();
694     lcd.setCursor(1, 0);
695     lcd.print("STEP BACK DIST");
696     lcd.setCursor(1, 1);
697     lcd.print("= ");
698     lcd.setCursor(1, 2);
699     lcd.print("SET: <UP/DOWN>");
700     lcd.setCursor(1, 3);
701     lcd.print("SAVE: <RIGHT>");
702     lcdRefreshFlag = true;
703   }
704
705   while(lcdRefreshFlag == true && questionFourFlag == true){
706   if (millis() >= keyPadPressTime + 300) { // Only do this at time intervals to
        debounce the button presses
707
708     if (digitalRead(RIGHT) == LOW) {         // RIGHT button pressed
709       keyPadPressTime = millis();
710       questionFourFlag = false;
711       questionFiveFlag = true;
712       lcdRefreshFlag = false;
713     } else if (digitalRead(UP) == LOW) { // UP button pressed
714       keyPadPressTime = millis();
715       Xsteps = Xsteps + 100;
716       lcdRefreshFlag = false;
717     } else if (digitalRead(DOWN) == LOW) { // DOWN button pressed
718       keyPadPressTime = millis();
719       Xsteps = Xsteps - 100;
720       lcdRefreshFlag = false;
721     } else if (digitalRead(LEFT) == LOW) { // LEFT button pressed
722       keyPadPressTime = millis();
723       questionThreeFlag = true;
724       questionFourFlag = false;
725       cursorRefreshFlag = false;
726       lcdRefreshFlag = false;
727     }
728
729     if (Xsteps >= 401) {
730       Xsteps = 100;
731     } else if (Xsteps <= 99) {
732       Xsteps = 400;
733     }
```

```
734
735   if (Xsteps == 100) {
736       lcd.setCursor(15, 1);
737       lcd.print("2mm");
738     } else if (Xsteps == 200){
739       lcd.setCursor(15, 1);
740       lcd.print("4mm");
741     } else if (Xsteps == 300){
742       lcd.setCursor(15, 1);
743       lcd.print("6mm");
744     } else if (Xsteps == 400){
745       lcd.setCursor(15, 1);
746       lcd.print("8mm");
747     }
748   }
749 }
750
751 // PRINT PAGE 5 - WITHDRAW QUESTION
752   if (lcdRefreshFlag == false && questionFiveFlag == true) {
753     lcd.clear();
754     lcd.setCursor(1, 0);
755     lcd.print("COGGING-DIRECTION");
756     lcd.setCursor(1, 1);
757     lcd.print("=-");
758     lcd.setCursor(1, 2);
759     lcd.print("SET:-<UP/DOWN>");
760     lcd.setCursor(1, 3);
761     lcd.print("SAVE:-<RIGHT>");
762     lcdRefreshFlag = true;
763   }
764
765     while(lcdRefreshFlag == true && questionFiveFlag == true){
766     if (millis() >= keyPadPressTime + 300) { // Only do this at time intervals to
          debounce the button presses
767
768     if (digitalRead(RIGHT) == LOW) {         // RIGHT button pressed
769       keyPadPressTime = millis();
770       questionFiveFlag = false;
771       questionSixFlag = true;
772       lcdRefreshFlag = false;
773       menuRefreshFlag = false;           // Request main menu to be loaded
774       cursorRefreshFlag = false;         // Request cursor refresh
775     } else if (digitalRead(UP) == LOW) { // UP button pressed
776       keyPadPressTime = millis();
777       reverse = reverse + 1;
778       lcdRefreshFlag = false;
779     } else if (digitalRead(DOWN) == LOW) { // DOWN button pressed
780       keyPadPressTime = millis();
781       reverse = reverse - 1;
782       lcdRefreshFlag = false;
783     } else if (digitalRead(LEFT) == LOW) { // LEFT button pressed
784       keyPadPressTime = millis();
785       questionFourFlag = true;
786       questionFiveFlag = false;
787       cursorRefreshFlag = false;
788       lcdRefreshFlag = false;
789     }
790
791     if (reverse >= 2){
792       reverse = 0;
793     } else if (reverse < 0){
794       reverse = 1;
795     }
```

```
796
797       if (reverse == 1) {
798         specimenInsertedFlag = true;
799         coggingDirection = true;
800         lcd.setCursor(12, 1);
801         lcd.print("INSERT");
802       } else {
803         specimenInsertedFlag = false;
804         coggingDirection = false;
805         lcd.setCursor(12, 1);
806         lcd.print("REVERSE");
807       }
808     }
809   }
810
811   // PRINT PAGE 6 - WITHDRAW QUESTION
812   if (lcdRefreshFlag == false && questionSixFlag == true) {
813     lcd.clear();
814     lcd.setCursor(1, 0);
815     lcd.print("WITHDRAW SPECIMEN");
816     lcd.setCursor(1, 1);
817     lcd.print("= ");
818     lcd.setCursor(1, 2);
819     lcd.print("SET: <UP/DOWN>");
820     lcd.setCursor(1, 3);
821     lcd.print("SAVE: <RIGHT>");
822     lcdRefreshFlag = true;
823   }
824
825     while(lcdRefreshFlag == true && questionSixFlag == true){
826     if (millis() >= keyPadPressTime + 300) { // Only do this at time intervals to
          debounce the button presses
827
828     if (digitalRead(RIGHT) == LOW) {         // RIGHT button pressed
829       keyPadPressTime = millis();
830       questionSixFlag = false;
831       questionSevenFlag = true;
832       lcdRefreshFlag = false;
833       menuRefreshFlag = false;            // Request main menu to be loaded
834       cursorRefreshFlag = false;          // Request cursor refresh
835     } else if (digitalRead(UP) == LOW) { // UP button pressed
836       keyPadPressTime = millis();
837       withdraw = withdraw + 1;
838       lcdRefreshFlag = false;
839     } else if (digitalRead(DOWN) == LOW) { // DOWN button pressed
840       keyPadPressTime = millis();
841       withdraw = withdraw - 1;
842       lcdRefreshFlag = false;
843     } else if (digitalRead(LEFT) == LOW) { // LEFT button pressed
844       keyPadPressTime = millis();
845       questionFiveFlag = true;
846       questionSixFlag = false;
847       cursorRefreshFlag = false;
848       lcdRefreshFlag = false;
849     }
850
851     if (withdraw >= 2){
852     withdraw = 0;
853     } else if (withdraw < 0){
854       withdraw = 1;
855     }
856
857       if (withdraw == 1) {
```

```
858         withdrawEnabledFlag = true;
859         lcd.setCursor(15, 1);
860         lcd.print("TRUE");
861       } else {
862         withdrawEnabledFlag = false;
863         lcd.setCursor(15, 1);
864         lcd.print("FALSE");
865      }
866    }
867  }
868
869    //PRINT PAGE 7 CONFIRM SETTINGS - OUT OF WHILE LOOP
870    if (lcdRefreshFlag == false && questionSevenFlag == true) {
871      lcd.clear();
872      lcd.setCursor(1, 0);
873      lcd.print("CONFIRM SETTINGS?");
874      lcd.setCursor(1, 1);
875      lcd.print("-");
876      lcd.setCursor(1, 2);
877      lcd.print("SET: <LEFT>");
878      lcd.setCursor(1, 3);
879      lcd.print("CONFIRM: <RIGHT>");
880      lcdRefreshFlag = true;
881    }
882
883      if (millis() >= keyPadPressTime + 300) { // Only do this at time intervals to
           debounce the button presses
884
885      if (digitalRead(RIGHT) == LOW) {         // RIGHT button pressed
886        keyPadPressTime = millis();
887        questionSevenFlag = false;
888        menuRefreshFlag = false;           // Request main menu to be loaded
889        cursorRefreshFlag = false;         // Request cursor refresh
890        setupCompleteFlag = true;
891        lcdRefreshFlag = false;
892      }  else if (digitalRead(LEFT) == LOW) { // LEFT button pressed
893        keyPadPressTime = millis();
894        questionSixFlag = true;
895        questionSevenFlag = false;
896        cursorRefreshFlag = false;
897        lcdRefreshFlag = false;
898      }
899    }
900 }
901
902 //
```

```
903 // RUN EXPERIMENT function called in the main loop
904 //
```

```
905 void runExperiment() {
906
907   currentMicros = micros();
908
909   if (lcdRefreshFlag == false && runExperimentFlag == true) {
910     lcd.clear();
911     lcd.setCursor(1, 0);
912     lcd.print("RUNNING EXPERIMENT");
913     lcd.setCursor(1, 1);
914     lcd.print("-");
915     lcd.setCursor(1, 2);
```

```
916       lcd.print("LEFT: <EXIT>");
917       lcd.setCursor(1, 3);
918       lcd.print("SELECT: <WITHDRAW>");
919       lcdRefreshFlag = true;
920     }
921
922   if(specimenWithdrawnFlag == true) {
923       return;
924       }
925
926   if(digitalRead(SELECT) == LOW){
927       withdrawSpecimen();
928       }
929
930   if(digitalRead(LEFT) == LOW){
931       digitalWrite(xSleep, HIGH);
932       digitalWrite(zSleep, HIGH);
933       runExperimentFlag = false;
934       exitMain();
935       }
936
937       digitalWrite(xSleep,HIGH);
938       digitalWrite(zSleep,HIGH);
939       digitalWrite(zDir,HIGH);
940    for(int a = 0; a <= noOfOperations; a++) {
941       autoZStep(Zsteps);
942       currentMicros = micros();
943      /* while(micros() < currentMicros + hammerTime){
944                                                       } */
945       digitalWrite(FORGE_SEND, HIGH);    //This might need reversed to LOW after test
              as they may be considered HIGH then need to be brought LOW similar to
              endstops.
946       while(digitalRead(FORGE_RECEIVE == LOW)){   //This is a wait until the
              FORGE_RECEIVE pin receives a pulse (this should be sent once the platens have
               retracted
947        if(digitalRead(SELECT) == LOW){
948       withdrawSpecimen();
949       }
950       if(digitalRead(RIGHT) == LOW){
951       break;
952       }      /*
953       if(digitalRead(FORGE_RECEIVE == HIGH)){
954       break;
955       }        */
956                                             }
957       }
958
959       if (coggingDirection == true){
960         digitalWrite(xDir,LOW);
961       }
962       else if (coggingDirection == false){
963         digitalWrite(xDir,HIGH);
964       }
965       autoXStep(Xsteps);
966       currentMicros = micros();
967       while(micros() < currentMicros + hammerTime){
968                                                       }
969       }
970 //
```

```
971 // MANUAL OPERATION function called in the main loop
972 //
```

```
973 void manualOperation() {
974
975 currentMicros = micros();
976
977   if (lcdRefreshFlag == false) {
978     lcd.clear();
979     lcd.setCursor(1, 0);
980     lcd.print("MANUAL ROTATION");
981     lcd.setCursor(1, 2);
982     lcd.print("ROTATE:<SELECT>");
983     lcd.setCursor(1, 3);
984     lcd.print("EXIT: PRESS <LEFT>");
985     lcdRefreshFlag = true;
986   }
987
988
989   if (millis() >= keyPadPressTime + 300) {
990   if (digitalRead(SELECT) == LOW){
991   digitalWrite(zDir, HIGH);
992   digitalWrite(zSleep,LOW);
993   for (int i = 0; i < 50; i++){
994     digitalWrite(zStep,HIGH);
995     digitalWrite(zStep,LOW);
996     currentMicros = micros();
997     while(micros() < currentMicros + 1000){
998                                                 }
999   }
1000    delay(250);
1001    digitalWrite(zSleep,HIGH);
1002      }
1003  }
1004
1005  if (millis() >= keyPadPressTime + 300) {
1006  if (digitalRead(DOWN) == LOW){              //Withdraws specimen 0.1mm
1007  digitalWrite(zDir, LOW);
1008  digitalWrite(zSleep,LOW);
1009  for (int i = 0; i < 50; i++){
1010    digitalWrite(zStep,HIGH);
1011    digitalWrite(zStep,LOW);
1012    currentMicros = micros();
1013    while(micros() < currentMicros + 1000){
1014                                                }
1015  }
1016    delay(250);
1017    digitalWrite(xSleep,HIGH);
1018      }
1019  }
1020
1021  if (millis() >= keyPadPressTime + 300) {
1022  if (digitalRead(UP) == LOW){                //Inserts specimen 0.1mm
1023  digitalWrite(xDir, LOW);
1024  digitalWrite(xSleep,LOW);
1025  for (int i = 0; i < 500; i++){
1026    digitalWrite(xStep,HIGH);
1027    digitalWrite(xStep,LOW);
1028    currentMicros = micros();
1029    while(micros() < currentMicros + 1000){
1030                                                }
1031  }
1032    delay(250);
1033    digitalWrite(xSleep,HIGH);
```

```
1034        }
1035    }
1036
1037      digitalWrite(xSleep, HIGH);
1038      if (millis() >= keyPadPressTime + 300) {     // Only do this at time intervals to
              debounce the button presses
1039
1040        if (digitalRead(LEFT) == LOW) {      // If LEFT button is pressed
1041          exitMain();
1042          digitalWrite(xSleep, HIGH);
1043          digitalWrite(zSleep, HIGH);
1044        //  break; // End while loop (i.e. exit to main menu)
1045       }
1046      }
1047    }
1048
1049
1050 //
       ---------------------------------------------------------------------------

1051 // Auto x-axis stepping
1052 //
       ---------------------------------------------------------------------------

1053   void autoXStep(int Xsteps) {
1054      digitalWrite(xSleep,LOW);
1055    for (int i = 0; i < Xsteps; i++){
1056      digitalWrite(xStep,HIGH);
1057      digitalWrite(xStep,LOW);
1058      currentMicros = micros();
1059      while(micros() < currentMicros + stepSpeed){
1060                                                  }
1061   }
1062      digitalWrite(xSleep,HIGH);
1063 }
1064 //
       ---------------------------------------------------------------------------

1065 // Auto z-axis stepping
1066 //
       ---------------------------------------------------------------------------

1067   void autoZStep(int ZSteps) {
1068      digitalWrite(zSleep,LOW);
1069    for (int i = 0; i < Zsteps; i++){
1070      digitalWrite(zStep,HIGH);
1071      digitalWrite(zStep,LOW);
1072      currentMicros = micros();
1073      while(micros() < currentMicros + stepSpeed){
1074                                                  }
1075    }
1076      digitalWrite(zSleep,HIGH);
1077 }
1078 //
       ---------------------------------------------------------------------------

1079 // Manual x-axis stepping
1080 //
       ---------------------------------------------------------------------------

1081 void manualXStep() {
1082
1083    currentMicros = micros();
```

```
1084
1085    if (currentMicros - previousMicros >= microsBetweenStepsManual) {
1086      previousMicros = currentMicros;
1087      if (pulseXOn == LOW) {
1088        pulseXOn = HIGH;
1089      } else {
1090        pulseXOn = LOW;
1091      }
1092      digitalWrite(xStep,pulseXOn);
1093    }
1094  }
1095  //
```

```
1096  // Manual z-axis stepping
1097  //
```

```
1098  void manualZStep() {
1099
1100    currentMicros = micros();
1101
1102    if (currentMicros - previousMicros >= microsBetweenManualHammer) {
1103      previousMicros = currentMicros;
1104      if (pulseZOn == LOW) {
1105        pulseZOn = HIGH;
1106      } else {
1107        pulseZOn = LOW;
1108      }
1109      digitalWrite(zStep,pulseZOn);
1110    }
1111  }
1112  //
```

```
1113  // Insert the test specimen into a pre-defined working area (e.g. press)
1114  //
```

```
1115  void insertSpecimen() {
1116
1117    microsBetweenStepsManual = 1000;
1118    microsBetweenManualHammer = 1000;
1119
1120    if (lcdRefreshFlag == false) {
1121      lcd.clear();
1122      lcd.setCursor(2, 1);
1123      lcd.print("INSERTING");
1124      lcd.setCursor(2, 2);
1125      lcd.print("SPECIMEN-");
1126      lcdRefreshFlag = true;
1127    }
1128
1129    while (digitalRead(xStop2) == true) {
1130          digitalWrite(xSleep,LOW);
1131          digitalWrite(xDir, LOW);   // (HIGH = anti-clockwise / LOW = clockwise)
1132          manualXStep();
1133
1134       if (digitalRead(xStop2) == false) {
1135          digitalWrite(xSleep,HIGH);
1136          specimenInsertedFlag = true;
1137          exitSimple();
1138          break;
```

```
1139          }
1140    }
1141 }
1142 //
     ------------------------------------------------------------------------------

1143 // Withdraw specimen until end-stop is engaged
1144 //
     ------------------------------------------------------------------------------

1145 void withdrawSpecimen() {
1146
1147   microsBetweenStepsManual = 1000;
1148   microsBetweenManualHammer = 1000;
1149   lcdRefreshFlag = false;
1150
1151   if (lcdRefreshFlag == false) {
1152     lcd.clear();
1153     lcd.setCursor(2, 1);
1154     lcd.print("WITHDRAWING");
1155     lcd.setCursor(2, 2);
1156     lcd.print("SPECIMEN-");
1157     lcdRefreshFlag = true;
1158   }
1159
1160   while (digitalRead(xStop1) == true) {
1161         digitalWrite(xSleep,LOW);
1162         digitalWrite(xDir, HIGH);  // (HIGH = anti-clockwise / LOW = clockwise)
1163         manualXStep();
1164
1165      if (digitalRead(xStop1) == false) {
1166         digitalWrite(xSleep,HIGH);
1167         specimenWithdrawnFlag = true;
1168         lcdRefreshFlag = false;
1169         break;
1170         }
1171
1172      if (millis() >= keyPadPressTime + 300) {    // Only do this at time intervals
          to debounce the button presses
1173       if (digitalRead(LEFT) == LOW) {         // If LEFT button is pressed
1174         exitMain();
1175         digitalWrite(xSleep, HIGH);
1176         digitalWrite(zSleep, HIGH);
1177         break;                          // End while loop (i.e. exit to main menu)
1178       }
1179     }
1180   }
1181 }
1182
1183 void experimentCompleted(){
1184   lcdRefreshFlag = false;
1185
1186   if (lcdRefreshFlag == false) {
1187     lcd.clear();
1188     lcd.setCursor(2, 1);
1189     lcd.print("EXPERIMENT");
1190     lcd.setCursor(2, 2);
1191     lcd.print("COMPLETE");
1192     lcdRefreshFlag = true;
1193   }
1194   currentMicros = micros();
1195     while(micros() < currentMicros + 3000000){
1196                                             }
```

```
1197        runExperimentFlag =        false;
1198        setupCompleteFlag =        false;
1199        experimentCompleteFlag = false;
1200        finishedFlag = true;
1201        exitMain();
1202    }
```

Appendix C: Product Design Specification

1. PERFORMANCE

Must replicate the motion and degrees of freedom of a cogging operation in industry, within a miniaturised lab scale. Must be operable and compatible within Lab 3 Zwick 150/250kN presses and clam shell furnace. Must be designed to hold samples stable undergoing torque forces. Must be user programmable and manually adjustable for alignment.

2. ENVIRONMENT

To be operable in the lab in the temperature range of 10°C - 1050°C. Must ensure adequate space between high temperature furnace and electronic components.

3. SERVICE LIFE

To remain in service for duration of research studies Oct 2019-2022 minimum, can remain for future studies Oct 2022 onwards.

4. MAINTENANCE

Range of Allen keys required for maintenance of rig extension, requires tightening before use. Motors and control box to be regularly tested to check for loose wiring.

5. TARGET COST

Cost to be minimised under research budget. £1000 estimated material/component cost.

6. COMPETITION

Unique rig motion and user operation design. No competition of note, novel research product.

7. SHIPPING

Product not planned to be shipped out with UK for any research purposes. When in transit, discrete components must be disconnected and disassembled, and carefully transferred between research premises by car. If to be to be taken on flights, special case for transport should be found.

8. PACKAGING

Product to have no packaging. Research product.

9. QUANTITY

One rig to be manufactured and assembled. Multiple manipulator rods to be purchased and used.

10. MANUFACTURING

One rig to be manufactured. Assembled at home. Components and tooling manufactured using a combination of electric discharge machining (EDM), conventional milling/cutting/bending, and laser cutting.

11. SIZE

Approximate maximum dimensions: 3m x 0.5m x 0.2m

12. WEIGHT

Rig to be able to be disassembled into discrete components and easily portable.

- Actuator Sub Assembly.
- Tripod.
- Electronic Controller.
- Range of tooling.

13. AESTHETICS

To be presentable as a piece of lab equipment, to be clean.

14. MATERIALS

Stainless Steel manipulator and couplings. Nimonic-90 manipulator, coupling, and dies for high temperature testing. Inconel 718 alloy used for die material used in room and elevated temperature testing. Actuator made up of a mixture of steels and acrylic/plastic standard and non-standard components.

15. PRODUCTION LIFE SPAN

To be used for duration of research studies. – To be improved with new PhD iterations, including tooling upgrades for superalloy testing.

16. STANDARDS + SPECIFICATIONS

Non-standard compression testing equipment. Future development opportunity for standardisation of equipment and method.

17. ERGONOMICS

To be easy to disassemble and transport. Control box – man/machine interface, must be simple and easy to use.

18. CUSTOMER

Users of rig, students/researchers. Aubert & Duval main customer has shown interest.

19. QUALITY/RELIABILITY

Proven quality and reliability in reproducible/repeatable testing for a range of results in material microstructural evolution and grain refinement.

20. SHELF-LIFE

Shelf-life 20+ years expected.

21. PROCESSES

Compatible with Zwick machines and be able to communicate signals between software.

22. TIME-SCALES

Room temperature experimentation – April/May 2022 High temperature experimentation – July 2022

23. TESTING

Consistent testing to be carried out with motors and components to ensure no loose connections. Numbers of tests carried out in isolated testing cases. Further testing done during in-service – due to short timespan required for results.

24. SAFETY

Risk Assessment completed and available for user and assembly of product. End-stops, circuit breaker buttons, and fuses introduced throughout control box for rig for several layers of security.

25. COMPANY CONSTRAINTS

N/A

26. MARKET CONSTRAINTS

N/A.

27. PATENTS, LITERATURE, PRODUCT DATA

No patents currently sought or required. Literature and product data published to date: • D.J. Connolly, G. Sivaswamy, S. Rahimi, and V. Vorontsov. Miniaturised Experimental Simulation of Ingot-to-Billet Conversion. (2023) Submitted for publication in the Journal of Materials Research and Technology. • D.J. Connolly, G. Sivaswamy, S. Rahimi, and V. Vorontsov. Miniaturised Experimental Simulation of Ingot-to-Billet Conversion of Ti-6Al-4V. (2023) Submitted for publication in the Journal of Materials Research and Technology.

28. POLITICAL & SOCIAL IMPLICATIONS

N/A.

29. LEGAL

Product designed for research purposes only.

30. INSTALLATION

Portable design, short set-up time (approx. 10-15 minutes) can be installed with any Zwick-/Roell load frame/furnace combination. Tooling installed through extensometer slot of furnace/environmental chamber.

31. DOCUMENTATION/TRAINING

SOP and RA completed for operation of the apparatus in the lab environment. To be used in conjunction with RA/SOP for Zwick/Roell load frames.

32. DISPOSAL

All components recyclable.